TAMPEREEN TEKNILLINEN YLIOPISTO
TAMPERE UNIVERSITY OF TECHNOLOGY
Julkaisu 715 • Publication 715

Philipp Beierer

Experimental and Numerical Analysis of the Hydraulic Circuit of a High Pressure Common Rail Diesel Fuel Injection System

Tampere 2007

Tampereen teknillinen yliopisto. Julkaisu 715
Tampere University of Technology. Publication 715

Philipp Beierer

Experimental and Numerical Analysis of the Hydraulic Circuit of a High Pressure Common Rail Diesel Fuel Injection System

Thesis for the degree of Doctor of Technology to be presented with due permission for public examination and criticism in Konetalo Building, Auditorium K1702, at Tampere University of Technology, on the 21st of December 2007, at 12 noon.

Tampereen teknillinen yliopisto - Tampere University of Technology
Tampere 2007

ISBN 978-952-15-1901-7 (printed)
ISBN 978-952-15-1918-5 (PDF)
ISSN 1459-2045

Beierer, P., **Experimental and Numerical Analysis of the Hydraulic Circuit of a High Pressure Common Rail Diesel Fuel Injection System**, Tampere, 2007, 198 p.
Tampere: Tampere University of Technology, Finland, 2007.
Keywords: fluid transients, high pressure hydraulics, fuel injection, hydraulic circuit properties, experimental measurements, numerical simulation

ABSTRACT

This thesis deals with the analysis of fluid transients in the hydraulic circuit of a high pressure common rail diesel fuel injection system for light vehicle applications. The injection process triggers flow and pressure pulsations that have an adverse effect on the predictability of subsequent fuel injections. To achieve maximum fuel efficiency during the combustion process it is mandatory to meter the amount of injected fuel precisely.

Firstly, a brief review of modelling techniques for analysing fluid transient problems is provided. The basic governing equations are presented as a second step. The individual terms are discussed and evaluated in respect of their importance for modelling the present system.

Experimental measurements are conducted on a hydraulic test bench. The input parameters are defined by injection specific parameters and the geometry of the connection line between rail and injector. The main output parameters are based on the pressure histories at various locations, the oscillation frequency of the main perturbation, and the amount of injected fuel per injection.

To extend the range of analysed parameters, a one-dimensional simulation model is used to describe the complete system characteristics. Additionally, local flow phenomena are modelled by means of three-dimensional simulations. The agreement between measurements and simulations is good. The results show that the fluid transients in the system are strongly dependent on the analysed input parameters. In this work, the individual correlations are pointed out and evaluated. Finally, the simulation models are utilised to analyse parameters that are not accessible by measurements and to study theoretically different measures to minimise unwanted flow and pressure oscillations as much as possible.

PREFACE

This study was carried out at the Institute of Hydraulics and Automation (IHA) at Tampere University of Technology (TUT).

I would like to express my sincere gratitude to Professor Kalevi Huhtala, who has acted as supervisor of this work. He provided me with valuable guidance throughout the years and encouraged me during the more difficult times of this research. I also wish to express my gratitude to Professor Matti Vilenius, Head of the Institute, for providing excellent facilities for completing this study.

I am grateful to all personal of IHA for their support. Special thanks go to Timo Leino, Max Lakkonen (nowadays at Fogtech GmbH & Co KG), and Terho Nykänen (nowadays at Alte Oy) for their friendship and the many fruitful discussion we had about hydraulics and everyday topics. I am grateful also to Janne Uusi-Heikkilä for never getting tired of helping me resolve the IT problems. The laboratory team (Markku Rytimaa, Markku Pakarinen, Seppo Joonala, Juha Kukkohovi) deserve particular mention, as they did an outstanding job for the experimental test bench.

I wish to express my sincere gratitude to the preliminary examiners D.Sc (Tech) Jyrki Kajaste (Helsinki University of Technology) and Professor Kevin Edge (University of Bath, England) for their valuable comments on my thesis.

The support of Shawn Harnish (Gamma Technologies Inc.) is highly appreciated for resolving code related issues. The Finnish IT Centre for Science (CSC) is also thanked for providing the hardware and software for performing the three-dimensional CFD calculations.

In addition, I am grateful to my new employer, Sandvik Mining and Construction Oy, and particularly Pauli Lemmetty, for giving me the time needed to finalize this thesis.

This study has been partly funded by the Graduate School of Concurrent Mechanical Engineering (GSCME), headed by Professor Erno Keskinen, and the Finnish Funding Agency for Technology and Innovation (TEKES). This financial support is gratefully acknowledged.

For the revision of the English manuscript I would like to thank John Shepherd.

I am grateful to all my friends for being around. Special mention is given to the “juoksu ryhmä” (Gerbrand Bijmolt and Sjoerd Wanrooij) for the endless hours running through the Finnish woods (“…does anybody know where we are?”); it was always great fun. Thank you guys!

Finally, I would like to specially thank my beloved wife Katja for her support, motivation, and enthusiasm. I am indebted to her for showing me so much patience and understanding in the course of this dissertation process. I also would like to thank my parents, Christel and Sigmund, and my sister Susan, for everything they have done for me.

Tampere, December 2007

Philipp Beierer

CONTENTS

NOMENCLATURE

Roman Symbols

A	Characteristic area, for example flow cross-section	[m^2]
A_1	Flow area, restriction	[m^2]
A_2	Flow area, downstream restriction	[m^2]
A_S	Heat transfer surface area	[m^2]
a	Speed of sound	[m/s]
a_i	Acceleration in *i*-direction	[m/s^2]
$a_{0...7}$	Fit coefficients of state equations	
B	Bulk modulus	[Pa]
C_D	Flow coefficient	[]
C_f	Fanning pipe wall friction coefficient, total	[]
$C_{f,s}$	Fanning pipe wall friction coefficient, steady	[]
C_H	Hydraulic capacity	[m^4 s^2/kg]
C_p	Pipe flow, minor losses coefficient	[]
C_{pr}	Pressure recovery coefficient	[]
$C_{pr,t}$	Theoretical pressure recovery coefficient	[]
c_p	Specific heat at constant pressure	[J/(kg K)]
c_v	Specific heat at constant volume	[J/(kg K)]
$\vec{c}$	Velocity vector	[m/s]
D	Diameter	[m]
D_{dif}	Diffusion tensor	[kg/(m s^3)]
d_{exp}	Flow split, expansion diameter	[mm]
d_p	Diameter, high pressure connection pipe	[mm]
E	Young's modulus of elasticity	[MPa]
e_0	Specific total energy	[J/kg]
e	Specific internal energy	[J/kg]
F	Force	[N]
F_{Ac}	Acceleration force	[N]
F_{NP}	Force acting on needle-pin-plunger mass	[N]
F_p	Pressure force acting on plunger-top wall	[N]
F_i	Flux column vector	[]

F_t	Unsteady friction factor	[]
f	Oscillation frequency	[Hz]
f_s	Sampling frequency	[Hz]
f_P	High pressure pump excitation frequency	[Hz]
G	Primitive of arbitrary function	
g	Arbitrary function	
h_0	Specific total enthalpy	[m^2/s^2]
h	Specific enthalpy	[m^2/s^2]
$h_{ref,\ liq}$	Reference specific enthalpy, liquid	[m^2/s^2]
h_{vap}	Specific vaporization enthalpy	[m^2/s^2]
i	Unit vector in x-direction	[]
j	Unit vector in y-direction	[]
K_d	Damping coefficient	[]
K_s	Static transfer coefficient	[]
k	Unit vector in z-direction or index in frequency domain	[]
L	Length	[m]
L_H	Hydraulic inductivity	[kg/m^4]
l_{char}	Flow split, characteristic length	[mm]
l_p	Length, high pressure connection pipe	[mm]
M_{const}	Friction multiplier, steady state	[]
M_{trans}	Friction multiplier, transient	[]
m	Mass	[kg]
m_{CFL}	Time step multiplier (smaller or equal 1)	[]
$mflx$	Boundary mass flux into volume	[kg/s]
N	Number of samples	[]
Nu	Nusselt number	[]
n	Index in Time domain	[]
P	Mechanical power	[W]
Pe	Peclet number	[]
Pr	Prandtl number	[]
P_V	Boundary work	[W]
p	Pressure	[Pa], [bar]
$\hat{p}$	Pressure amplitude	[Pa]
pDE	Pressure at downstream end of 2nd high pressure line	[bar]

p_e	External pressure	[Pa]
p_{max}	Maximum positive pressure amplitude	[bar]
p_{mean}	Mean pressure	[bar]
$p_{min,1}$	Absolute value of first negative pressure amplitude	[bar]
$p_{min,2}$	Absolute value of second negative pressure amplitude	[bar]
pII	Pressure at the injector inlet	[bar]
p_i	Internal pressure	[Pa]
pRa	Pressure at the upstream end of the rail	[bar]
p_{ref}	Reference pressure	[Pa]
$p_{ref,sat}$	Reference saturation pressure	[Pa]
p_{set}	Set pressure	[bar]
Q	Heat flux	[J/s], [W]
q_E	Replacement character: heat conduction fluid-boundary	[W/m^2]
q_i	Heat flux density	[W/m^2]
R	Specific gas constant	[J/(kg K)]
Re	Reynolds number	[]
r_M	Replacement character: diffusion terms in momentum equation	[Pa]
r	Radius	[m]
r_E	Replacement character: diffusion terms in energy equation	[W/m^2]
r_i	Inner pipe radius	[m]
r_o	Outer pipe radius	[m]
S	Replacement character: heat flux through the wall and work done due to a change of volume	[J/s], [W]
s	Replacement character: heat flux through the wall and work done due to a change of volume per unit volume	[W/m^3]
T	Temperature	[K]
T_f	Temperature fluid	[K]
T_{inj}	Injection period	[ms]
T_{ref}	Reference temperature	[K]
T_w	Temperature wall	[K]
t	Time	[s]
t_{inj}	Injection duration	[µs]
U	Solution column vector	[]
u	Velocity component in x-direction	[m/s]

V	Volume	[m^3]
VdZ	Volume downstream Z-nozzle	[mm^3]
VuA	Volume upstream A-nozzle	[mm^3]
VuZ	Volume upstream Z-nozzle	[mm^3]
V_{ref}	Reference volume	[m^3]
$\dot{V}$	Flow rate	[m^3/s]
$\hat{\dot{V}}$	Flow rate amplitude	[m^3/s]
v	Velocity component in *y*-direction	[m/s]
v'	Specific volume liquid (mixture phase)	[m^3/kg]
v''	Specific volume vapour (mixture phase)	[m^3/kg]
w	Velocity component in *z*-direction	[m/s]
x	Cartesian coordinate	[m]
y	Cartesian coordinate	[m]
Z	Characteristic impedance	[Pa s/m^3]
Z_I	Characteristic inlet impedance	[Pa s/m^3]
Z_E	Characteristic exit impedance	[Pa s/m^3]
z	Cartesian coordinate	[m]

Greek Symbols

α	Heat transfer coefficient	[$W/(m^2K)$]
ε_t	Tangential strain	[]
λ	Second viscosity coefficient	[N s/m^2]
λ_T	Conductibility of temperature	[m^2/s]
λ_f	Moody/Darcy wall friction factor	[]
μ	Molecular or dynamic viscosity	[N s/m^2]
ν	Poisson ratio	[]
ρ	Fluid density	[kg/m^3]
ρ_{ref}	Reference fluid density	[kg/m^3]
σ_r	Radial stress	[Pa]
σ_t	Tangential stress	[Pa]
T	Transfer matrix	[]

τ_{ij}	Components of shear stress tensor (acts on a plane normal to *i* axis, directed parallel to *j* axis)	[N/m^2]
Φ	General variable	
$\overline{\Phi}$	General variable, mean value	
Φ'	General variable, fluctuating value	
ω	Angular frequency	[rad/s]
ω_e	Angular frequency of the damped oscillation	[rad/s]

Mathematical Symbols

$\frac{D}{Dt}$	Substantial derivative
d	Differential, for example dx
$\frac{\partial}{\partial \Phi}$	Partial derivative
Δ	Difference
e	Basis of natural logarithm
i	Imaginary unit
∇	Nabla operator

Abbreviations

AC	Alternating current
CAD	Computer-aided design
CR	Common rail
CFD	Computational fluid dynamics
CFL	Courant-Friedrichs-Lewy condition
CV	Control volume
DFT	Discrete Fourier transform
ECU	Electronic control unit
FEM	Finite element method
FFT	Fast Fourier transform
FDM	Finite difference method
FVM	Finite volume method
FSI	Fluid structure interaction
MOC	Method of characteristics

PDE	Partial differential equation
RANS	Reynolds-averaged Navier-Stokes
RLC	Resistor, inductor, capacitor
RMS	Root mean square
TLM	Transmission line method

1. INTRODUCTION

Fluid mechanics is defined as the science that analyses the kinematic and dynamic behaviour of fluids. Generally, the description of the underlying physics follows the nature of the flow. Besides aspects like, for example, internal – external flow, forced – free convection, laminar – turbulent, and inviscid – viscous flow, it is common practice to differentiate between compressible and incompressible fluid flow problems. The term *compressible flow* is normally used for flows that involve gases; incompressible fluids, on the other hand, represent the physical behaviour of liquids. It is emphasised at this point that these classifications reflect traditional understanding in fluid dynamics [51, 99]. Modern diesel fuel injection systems, which are characterized by small time constants, do not fit, for example, in the last category as the fluid density varies noticeably due to large pressure gradients. Therefore, it is possible to divide the theory into further side branches, each serving a particular problem in fluid mechanics.

The description and analysis of highly unsteady phenomena in liquid flow is a typical representative of such a specialised field. In classical hydraulics it is referred to as *Transient Fluid Flow* or simply *Fluid Transients* [101]. The theory applies where it is important to describe the instantaneous state of a fluid as a function of spatial coordinates and time. It can be noted that here the term fluid is used, as in the presence of cavitation or degassing effects the liquid may undergo a partial phase change.

This thesis deals with the analysis of fluid transients in a high pressure hydraulic system using state of the art measurement and simulation methods.

1.1. Background

Fluid transients represent an important role in the respective fields of fluid power and hydraulics. Most commonly, the observed phenomenon can be sub-divided according to the source of excitation. On the one hand, pressure and flow variations are introduced by the unsteady displacement of the fluid inside of pumps and motors. Depending on the design, the disturbances vary in intensity. For example, gear pumps are characterised by a considerably smaller non-uniformity grade than piston pumps [56]. However, the choice of a specific pump or motor design is not exclusively based on the dynamic behaviour in steady state conditions,

but also on other aspects. Efficiency, noise emissions, reliability, operating range and adjustability are just some of the characteristics that need consideration [56]. Accordingly, research in this field aims to optimise the various designs [27, 37, 48, 49].

On the other hand, flow transients may also be caused by fast switching valves, actuators, and load conditions. The system reaction that follows the sudden closing of a flow path is commonly known as the water hammer phenomenon. Because of the fluid inertia the liquid column upstream of the valve does not come to rest at once. Starting at the first layer of fluid next to the closed valve, the inertial kinetic energy is transformed to a local pressure gain. This conversion subsequently travels at the speed of sound upstream, where it is eventually reflected at, for example, a channel expansion or contraction. Due to the energy imbalance the wave continues to travel up and down between valve and upstream reflection point until dissipative effects bring the system to a steady state again [65, 72]. The destructive character of such pressure surges is particularly problematic in the field of water supply and power generation. Due to considerable flow rates and pipe cross-sections a pressure pulse might be sufficient to cause pipe rupture [3]. Smaller hydraulic applications may not directly face a system break as the flow forces on the boundaries are usually smaller. Although it is feasible that the long term integrity of the structure is shortened by the pressure pulses, such systems face more stringent problems on the control side. Digital hydraulics, for example, relies on the fast and accurate opening and closing of on/off valves. Potential overlaps of different valves

Figure 1, Cutting process – harvester head [75].

that are caused by different time characteristics can trigger pressure waves that compromise the robustness and reliability of the system [63, 64]. Concerning actuators that experience sudden load variations, examples can be found the same as before in a variety of applications. In the field of mobile hydraulics, forest machines, for example, are subjected to abrupt changes of working load. As is depicted in Figure 1, the cutting process of the log terminates with a rapid drop of the required feed and drive force of the harvester head chain saw.

Finally, fast switching actuators can be found, for example, in the hydraulic circuit of camless valve train systems for internal combustion engines. Due to the fast valve motion, pressure transients can only be avoided through additional measures [69].

1.2. Motivation for the work

Traditional methods for analysing theoretically fluid transients in hydraulic systems are not ideal for studting oscillatory effects in high pressure applications, that is, at pressure levels of 1000 bar and more. Firstly, the present industry and mobile hydraulic components operate at pressure levels of up to approximately 450 bar [90]. The analysis tools to study such systems are naturally adapted to the corresponding conditions. As the expectable pressure amplitude of the oscillation is rather small, it is possible to utilise a simplified description of the fluid compressibility. High pressure applications, in contrast, may undergo significant pressure variations in the range of +/- 300 bar. It is therefore understandable that, for example, the former simplification is not valid. Indeed, it is shown in this dissertation that the fluid itself has to be treated as a dynamic component that interacts with the system.

Similarly, high pressure systems are more prone to the impact of internal flow features than their low pressure counterparts. The inertial effects may become more dominant as, for example, the pressure drop over flow restrictions appears more severe. The same is true for elements of sudden contraction or expansion. Not only is the energy aspect of interest in such cases, but also the direction of vector quantities.

Although it has been indicated in the above section that current pressure levels do not exceed 500 bar, the trend in hydraulic research and development is to go beyond that level. The advantages are manifold:

- Fast actuation times also under increased load (external)

- High system responsiveness, that is, the system acts more stiffly than at lower pressure levels (internal)
- Shift of system natural frequency to higher values
- Application specific advantages

As is stated in the last aspect, the main reason for moving to higher pressure levels is based on the expectable benefits for the particular application at hand. Speaking for diesel fuel injection systems, the shift to higher injection pressures is a logical consequence in the pursuit of more efficient combustion. Until the mid-1980s diesel fuel injection systems for light vehicles operated at pressures of 300 to 400 bar. Today, modern common rail (CR) applications utilise maximum injection pressures of 1500 bar and more [93]. Together with advances in electronics, the combustion specialist is able to shape the actual combustion process. A minimum of three injections per cycle, that is, pilot, main and post injection, are standard for direct injection diesel engines to ensure maximum fuel efficiency and performance along with minimum emissions [26, 39, 40, 81]. In view of the high pressure level (1500 bar and more) and short valve activation times that are in the range of some hundreds of microseconds to one to two milliseconds, it is understandable that slight variations in, for example, the set pressure alter the injected fuel rate and combustion process considerably.

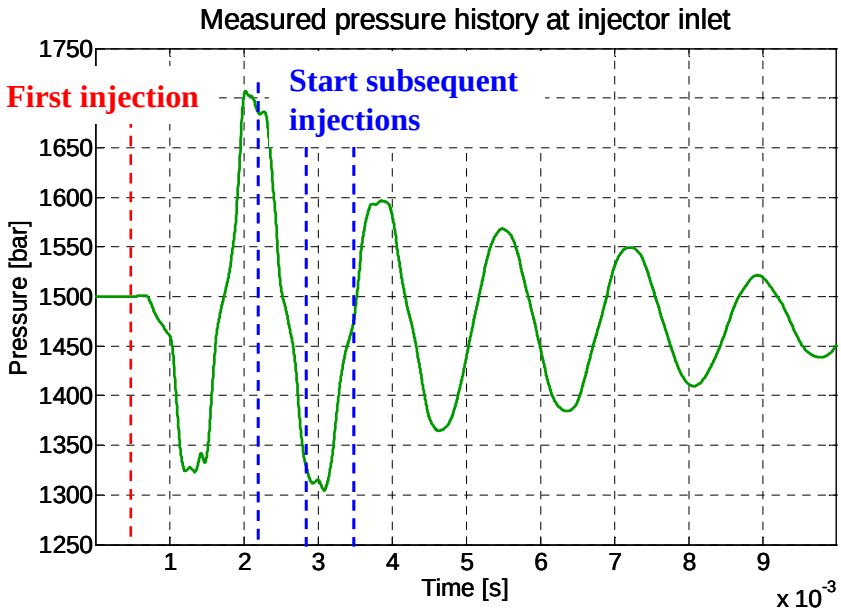

Figure 2. Pressure history at injector inlet for single injection CR system.

Figure 2 exemplifies a time history plot of a measured pressure signal at the injector inlet. It is noticeable that the first injection triggers a large pressure oscillation. With subsequent

injections following at specific dwell times after the previous injector activation, it is likely that such oscillations alter the combustion process in a disadvantageous way. In principle, a high pressure diesel fuel injector represents a fast acting on/off valve. The corresponding schematic is presented in Figure 3.

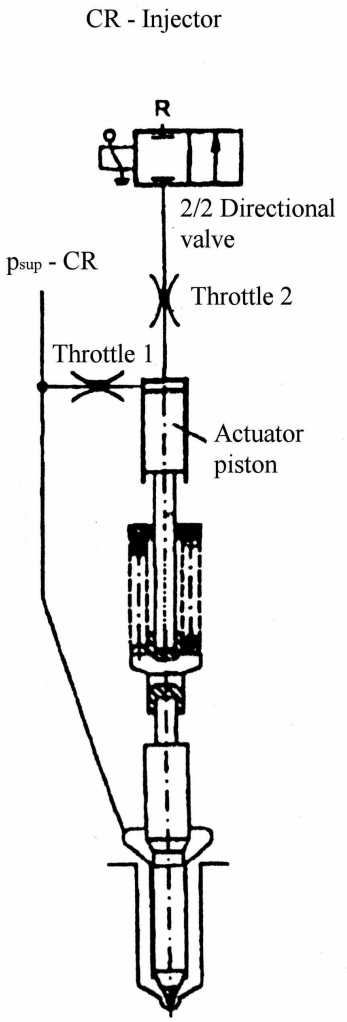

Figure 3. Schematic of a high pressure CR injector [40].

The nozzle holes of the fuel injector define at full needle lift the main restriction between high pressure supply and cylinder chamber. Physically, the restriction acts like an orifice, that is, it limits the flow rate for a given pressure gradient to a finite value. Equation (1) is commonly used to describe the turbulent flow through an orifice [72]. Because of the aforementioned similarity the same equation is used in this context for illustrative purposes.

$$Q = C_D \cdot A \cdot \sqrt{\frac{2 \cdot \Delta p}{\rho}} \tag{1}$$

Accordingly, variations of the instantaneous pressure head over the injector have a direct impact on the fuel amount delivered through the valve. Work by Bianchi et al. [19] and Pontoppidan et al. [76] support this theory. The former group has studied the correlation between injection amount and dwell time in a high pressure CR system. They conclude that the variations of measured injection amount are linked to the pressure oscillations upstream of the fuel injector. Pontoppidan et al. [76] include in their CR study the connection between instantaneous rail pressures and spray picture. As pressure waves are transmitted throughout the high pressure circuit, the wave that is emitted from one injector may also affect the injection at a neighbouring injector. This might become particularly important when new combustion strategies are applied, that is, when the time between activation of two consecutive acting injectors is reduced [26].

In the light of the previous section it is desirable to minimise pressure oscillations in a CR system as much as possible. Most of the methods that are used in traditional low and medium pressure hydraulics are not suitable for high pressure applications. A hydraulic damper, for example, utilises an enclosed air chamber for pressure wave attenuation. Elastic hoses are often used to remove peak values from the system. Both measures can not be used for CR fuel injection systems due to the high pressure level. Active damping systems represent a solution only at first glance. Although it is possible to conceive the utilisation of actuators that are built on, for example, fast piezo technology, it is also likely that the required hardware and reliability requirements would make the method in general unattractive. Another aspect that needs to be considered for this particular application is the small amount of available space. Usually, the engine compartment area is very limited, so that potential solutions have to fit into existing locations.

1.3. Earlier research on fluid transients in high pressure fuel injection systems

Publications in the field of diesel fuel injection are manifold. Until the mid-1990s, most of the work concentrated on the analysis and modelling of injection systems that operate at pressures less than 500 bar [23, 52, 61, 70, 71, 77, 100]. Typically, the core of the system has been based on a mechanically governed in-line or distributor pump. The injectors were still passive actuators, that is, without any electrical control [11].

With the shift to higher injection pressures, interest has moved towards injector designs. Favennec et al. [41], Bianchi et al. [18], and Hu et al. [53] discuss in their work different aspects concerning the modelling of a high pressure diesel fuel injector. Explicit aspects of the hydraulic circuit are not discussed.

In [42], Favennec et al. include the results of their earlier work [41] in studying a complete high pressure CR circuit. The results of Coppo et al. [33] are of a similar nature, that is, they present a numerical model for a complete CR system. Both research groups compare their simulation results to some measurement data. As their emphasis is placed on model features, the evaluation of hydraulic properties is not studied. The masters' theses of Ahlin [2] and Gullaksen [47] follow the previous groups. Although more detailed in their description, the hydraulic properties of the circuits remain unchanged. Catania et al. [30] present results analogous to the preceding authors, but concentrate on a circuit that is based on a high pressure distributor pump.

Only a few publications deal with the actual impact of the hydraulic circuit properties on the fluid transients in a high pressure CR system. D. van Bebber [94] discusses various aspects of the hydraulic circuit for a V8 engine application. His analysis and conclusions are based exclusively on simulations. Indeed, van Bebber lays emphasis on the modelling of such systems by means of stochastic methods. Accordingly, the model itself is not based on physical grounds. The latest publication of Catania et al. [28] deals with fluid transients in a CR system. The authors utilise numerical simulation, based on the mathematical description of the underlying physics, and experimental measurement. The objective of their study is to develop a completely new injection system that is basically only partly related to classical injection systems. Finally, studies of fluid transient in a conventional high pressure CR system are presented in this writer's own publications [13, 15, 16].

1.4. Objectives of the thesis

This work is intended to provide a detailed view of the mechanisms of fluid transients in a high pressure hydraulic system. The object of study is a commercial CR diesel fuel injection system for light vehicle applications (Figure 4).

The objectives of the thesis concern the following aspects:

- the correlation between fluid transients and design of a commercial CR system

- the acquisition of experimental measurement data for analysis of the hydraulic system characteristics and as a basis for a numerical simulation model
- the development and use of numerical modelling to enhance the range of analysed parameters and to obtain a better understanding of the hydraulic circuit
- the advantage of numerical modelling for analysing the effect of various parameters on the system characteristics and the possibility to evaluate new concepts for system improvement

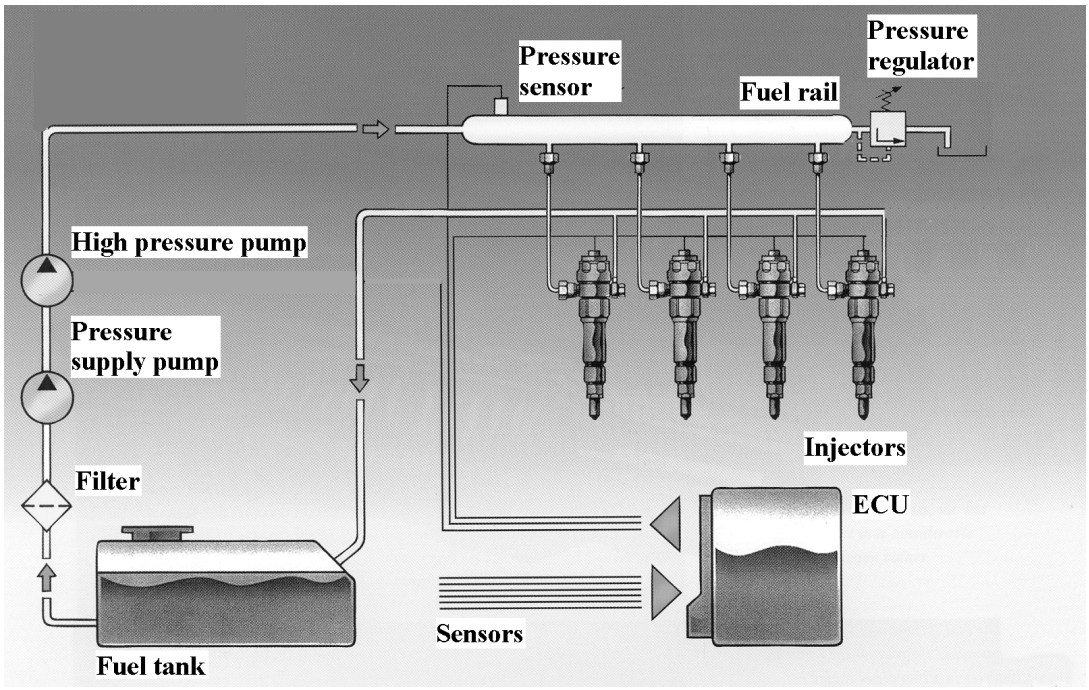

Figure 4. Schematic of a high pressure CR system (based on [88]).

The rail or accumulator design follows the purpose of providing at all times for all injectors the required amount of fuel at a constant pressure. The task of the connection lines is primarily to ensure the supply of fuel from rail to injector. With respect to the dynamic characteristics of the complete system, the connection lines play an important role. The hydraulic behaviour of the connection pipes depends strongly on their geometrical properties. In this thesis, the impact of this correlation is analysed by extensive measurements and numerical simulations. Typical input parameters include injection pressure, injection duration, dwell time, connection pipe length, and connection pipe diameter.

Modelling of fluid flow incorporates the use of simplifications and assumptions due to the strong coupling and non-linearity of the governing equations. Accordingly, various aspects are discussed that are important for simulating fluid transients in high pressure environments. Since traditionally such problems are solved in one-dimension for efficiency reasons, this thesis also addresses issues where it is meaningful to analyse the three-dimensional flow field.

A simulation model can significantly enhance the understanding of a physical system. As for the CR fuel injection circuit, it is literally impossible to measure experimentally all the desired properties at all locations. The injector consists of several channels, volumes and restrictions, with the largest characteristic dimensions in the range of approximately three millimetres or less. Positioning a sensor in such an environment ultimately alters the flow field, so that no meaningful conclusions can be drawn for the original system. Correspondingly, the numerical analysis of the validated model is extended to investigate further properties of the CR circuit. This includes the study of flow field properties and parameters at various locations, the rail properties, elasticity of the high pressure piping, and the impact of the injector dynamics on the findings.

In respect of the damping of unwanted pressure oscillations, the thesis concentrates on two methods: the Helmholtz resonator and in-line attenuator. Both measures are passive in nature, cheap, and relatively simple to implement. Their expected effectiveness is discussed and finally evaluated by comparing the simulated results.

Thus, the objectives of this thesis are:

- to study the impact of connection pipe geometrical properties on the pressure wave characteristics in a CR system as a function of injection parameters by means of experimental measurements and numerical simulation
- to study the impact of connection pipe geometrical properties on the fuel delivery variation by means of experimental measurements and numerical simulation
- to develop a numerical simulation model in the GT-Fuel[1] environment that is suitable to accurately describe the underlying physics in a high pressure CR fuel injection system

[1] GT-Fuel is a commercial code of Gamma Technologies Inc.

- to extend the validated simulation model to analyse parameters that are not possible to measure experimentally or that are part of a single component which exists only as a whole
- to develop potential solutions to minimise unwanted oscillations in a CR system and which are also suitable for other high pressure hydraulic applications

1.5. Restrictions

The emphasis of this thesis is on the analysis of the hydraulic circuit of a commercial high pressure CR system. The injector is part of the hydraulic circuit and greatly affects the overall behaviour of the entire system. Nevertheless, this component is seen in this study solely as a fast acting on/off valve. The injector characteristics are considered for the analysis. It is not the aim of this thesis to improve the performance of the injector. In this sense, the simulation model is based on an approach that is *as detailed as possible but only as complex as necessary*.

The experimental measurements are conducted on a hydraulic test bench that has been specifically designed for this analysis. No own data is available that documents the actual impact of pressure transients on the running combustion engine, that is, the link from injected fuel amount to combustion product is not presented in this work. Secondly, the primary goal of this study is to analyse the hydraulic characteristics of the injection system in an isolated environment. The potential effects that are caused by the vibrations of a running engine are reported to be negligible [2, 11].

Only a narrow fluid temperature range is studied in the thesis. The selected set value was chosen as it represents a typical temperature level at engine operating conditions [33, 41]. The main findings of this thesis can be approximated to other temperature levels or other fluids that behave similarly at the studied measurement point.

The evaluation of the measured injected fuel amount as a function of pressure oscillations in the high pressure CR circuit is intended to provide reasonably accurate results. In the experiment fuel is injected into a closed container. After exiting the injector nozzle holes, the fuel spray breaks up into small droplets, which after some time attach to the container walls. Although the actual weight measurement is conducted with some time delay after a series of injections, it can not be excluded that some fuel mist remains inside the container during the

mass measurement. By considering that the total quantities of injected fuel per injection are in the range of one to forty milligrams, it is possible that the real values vary slightly from the ones that have been actually measured.

1.6. Structure of the thesis

This thesis consists of five main chapters and five appendices. The contents of the chapters are briefly discussed below.

Chapter 1 starts with background information about the nature of fluid transients in hydraulic systems. Based on that, the motivation for the thesis is formulated. There follows a short summary of other work in this area. Sub-chapters with thesis objectives and restrictions define the scope of this work.

Chapter 2 discusses modelling issues that are important when analysing fluid transient. Firstly, a review of different techniques is presented. Secondly, the basic set of equations necessary to model fluid flow are presented. From this stage, the final equations that are used in the utilised codes are derived. The text provides, where applicable, differences in the implementation to other, popular methods in fluid transient. This chapter ends with a short discussion of two alternative methods that are often used in traditional hydraulics to obtain estimations about the expected frequency.

Chapter 3 is divided into three main sub-chapters. Chapter 3.1 deals with the experimental measurements. Firstly, the test bench is introduced. This is followed by a description of the various measurements and their analysis. Chapter 3.2 discusses the numerical modelling of the system in analogy to chapter 3.1. After introducing the main features of the utilised simulation code, the model is verified by the measurements. The second section ends with an extension of the parameter study of chapter 3.1. Chapter 3.3 builds on 3.1 and discusses properties that are not readily available by measurements. This includes geometrical circuit variations, the study of particular components, analysis of variables that are inaccessible by measurements, and concepts to minimise unwanted pressure oscillations in the system.

A summary of the thesis and discussion is presented in Chapter 4.

Chapter 5 concludes the thesis with the main findings and several topics suitable for future research.

Five appendices are included in the thesis. Appendix A and B concern numerical data of the CR test bench and the one-dimensional simulation model, respectively. Appendix C gives a short overview of the pre-processor settings of the three-dimensional simulation model and some results that are less important for the overall understanding. Appendix D describes the main settings and models for the simplified injector study. Finally, Appendix E presents briefly the theoretical background for the discussion of oscillation attenuation by additional damping devices.

2. THEORY OF FLUID TRANSIENTS MODELLING

2.1. Simulation methods

Basically, the fluid type defines the final set of equations that are used to compute the flow field at hand. In common fluid flow theory it is in many situations convenient to link the fluid flow variables via the ideal gas law to the three thermodynamic state variables: pressure *p*, volume *V*, and temperature *T*. Calculations that are based on liquid flows, in contrast, normally neglect any compressibility effects, as the density variation as a function of pressure is negligible in many cases [99].

Certainly, special applications have also driven the development of solution methods that differ from the above mentioned general understanding of fluid mechanics. The discipline of fluid transients, or more precisely the science of pressure wave transmission through liquids, is a typical example of such a specialised field. The foundation of this theory was laid at the beginning of the 20th century with the work of Joukowsky and Allievi [4]. From the middle of the last century, research has picked up at an accelerated pace, mainly due to the increase of problems that are based on the potentially destructive character of pressure surges [3, 101]. Stecki and Davis [86] show that at first glance the individual contributions in this field are manifold; however, they conclude that ultimately the studied methods are essentially the same.

At present, mainly two different approaches are utilised to describe the unsteady motion of fluid transients in hydraulic systems: frequency and time domain methods. The following two sub-chapters briefly introduce the main aspects of both techniques.

2.1.1 Frequency domain methods

Frequency domain methods are used primarily to study the response of a component or system over a wide range of frequencies. Relatively low computational effort and the ability to cope with complex fluids and geometry are known to be their biggest advantage. In contrast, frequency domain methods are not readily suitable for including non-linear effects such as, for example, significant boundary displacement, convective inertial terms or large amplitudes. Another difficulty is often the appropriate description of the system boundary conditions [20, 74].

The basic idea of the frequency domain method is based on the work of A. F. D'Souza and R. Oldenburger [34]. In their first publication the researchers show that it is possible to describe the dynamic characteristics of a pipe flow through transfer functions, which relate the pressure and velocity variables at two cross-sections with each other. Essentially, this concept can be described by the following matrix relation:

$$\begin{pmatrix} p_i \\ Q_i \end{pmatrix} = \begin{bmatrix} \mathrm{T}_{11} & \mathrm{T}_{12} \\ \mathrm{T}_{21} & \mathrm{T}_{22} \end{bmatrix} \cdot \begin{pmatrix} p_{i+1} \\ Q_{i+1} \end{pmatrix} \tag{2}$$

The individual terms T_{ij} of the transfer matrix T represent functions in the frequency domain that describe the dynamic behaviour of the component. According to equation (2) values for the pressure and volumetric flow at one position (*index i*) are available by multiplying the transfer matrix with the corresponding values at a second position (*index i+1*).

The ratio of pressure amplitude to flow rate amplitude is commonly described as characteristic impedance Z [9]. Later work in this field has concentrated on the analysis of this parameter for various components. K. A. Edge and D. N. Johnston [36, 58, 59], for example, evaluate the characteristic impedance for relief valves, accumulators, restrictors, and control valves. In 2006, D. N. Johnston presents some results concerning the dynamic behaviour of non-uniform passageways that are based on a novel implementation of the frequency domain method into a finite volume formulation [57].

Along with the comments at the beginning of this sub-chapter, it can be said that frequency domain methods are more suitable for modelling dynamic characteristics at steady state conditions, that is, excitations that are based on, for example, a sinusoidal pattern. As the analysis method of this thesis is based on a time domain method, no further explanations about frequency methods are given at this point.

2.1.2 Time domain methods

Time domain methods are in some respects more complex than frequency domain methods, as it is necessary to deal to a greater extent with PDE's. In the course of the last century several approaches have been developed that are built on the basic governing equations but they differ in their implementation and the assumptions utilised. The *arithmetic water hammer* is a very basic concept that excludes any friction and thermodynamic effects. Similarly, the *graphical water hammer* is based on the continuity and the inviscid momentum equation.

Viscosity effects, however, can be incorporated through some lumped correction parameter. Both methods have been the first choice in the first half of the last century and are replaced nowadays by more complex approaches that take advantage of modern digital computers [101].

Taylor et al. [89] give a brief description of commonly employed methods that are widely used today. The *lumped parameter method* follows the concept of dividing the length of a pipe into several sections. Watton et al. [97] define for each section the dynamic line properties in the form of characteristic series impedance and shunt admittance. The latter two properties are then combined to form the general wave equation. In their conclusion the authors find that the accuracy of this method is strongly affected by the number of pipe sections. Therefore, this method is recommended only for simulations where the pipe dynamics have only a modest impact on the overall system behaviour [89, 97].

The theory for modelling electrical circuits serves as the basis for the *transmission line method (TLM)*. The characteristics of hydraulic elements are described by inductive and capacitive means [96]. It is at first glance very appealing to perform a knowledge transfer from electrical to hydraulic science due to the many similarities. Nevertheless, it has to be kept in mind that this method can not represent unambiguous hydraulic phenomena like, for example, cavitation effects [82].

Modal approximation methods are based on a description of the flow model through a finite number of rational polynomials in the Laplace domain. The system variables, on the other hand, are expressed in the form of a state space representation in the time domain [62]. In its original form the model is not capable of representing non-linearities and variable fluid properties [67, 89].

The *method of characteristics (MOC)* is certainly one of the most popular approaches for modelling fluid transients in hydraulic systems. Besides Wylie et al. [101], the contributions of W. Zielke [102] and F. T. Brown [22] are seen as significant contributions to this method. The main idea of the MOC is to decompose the original PDE for continuity and momentum into four ordinary differential equations. The latter are linked in pairs; one set represents the wave propagation in the positive direction, the other set in the negative direction. This method in its original form requires the definition of fixed time steps, as the computational domain is

defined by a regular time-distance grid. Correspondingly, the fluid properties are required to behave with time invariant. Variable sonic speeds can only be incorporated by applying some linear interpolation, as presented by Mueller [74]. On the other hand, the latter approximation is also known as a source of model inaccuracy [44, 89]. Towards the end of last century, the MOC was extended to model also the interaction between fluid and structure (FSI). For example, Wiggert et al. [98] and Tijsseling et al. [92] show that the method of characteristics can be used exclusively or in combination with the finite element method (FEM) for FSI analysis. The latter approach is also referred to as the hybrid MOC-FEM method [98].

More recently, *finite element (FEM)* and *finite difference methods (FDM)* have been used to model fluid transients in hydraulic systems [84, 89]. Taylor et al. [89] have used FEM to analyse the highly non-linear interaction between the fluid and flexible hoses. The researchers concluded that this method is particular suitable for including time variant fluid properties and non-linearities. On the other hand, they indicate that the approach may generate unphysical oscillations caused by the natural frequency of the model.

In this thesis, methods that belong to the previous listing are referred to as *classical methods* for modelling fluid transients in hydraulic systems. As is shown in the next chapter in detail, the utilised method of this study is based on the *finite volume method (FVM)*. Generally, numerical schemes are either implicit or explicit. The former method is commonly used in commercial CFD codes, as it accelerates the solution progress in many fluid flow problems. In case of problems dealing with fluid transients, this advantage can not be put forward, since an inadequate selection of the time step deteriorates the solution quality [101]. Explicit schemes, on the other hand, are based on the direct computation of the dependent variables. While this is advantageous for modelling, for example, pressure transients in a hydraulic system, the computation time for common problems in fluid dynamics increases significantly [55]. During this study, two commercial codes were used, with implicit and explicit implementation of the governing equations, respectively.

2.2. Mathematical description of flow physics

The first principle of modelling fluid flow and fluid transients in particular is that the fluid can be treated as a continuum. This condition is true as long as the characteristic time and length scales of the problem are significantly larger than the corresponding values that characterise the molecular constitution of the fluid. For liquids the limit for the smallest dimensions is in

the range of approximately 0.5 µm [51]. The diameter of the nozzle holes of the studied high pressure injector is about 150 µm. Even smaller, approximately 2 µm [35], is the clearance between the injector needle and its guidance.

The continuum condition assumes a continuous distribution of the physical properties. Accordingly, it is possible to represent the fluid domain by small control volumes (CV) in which the fluid variables can be written as averaged values (Figure 5).

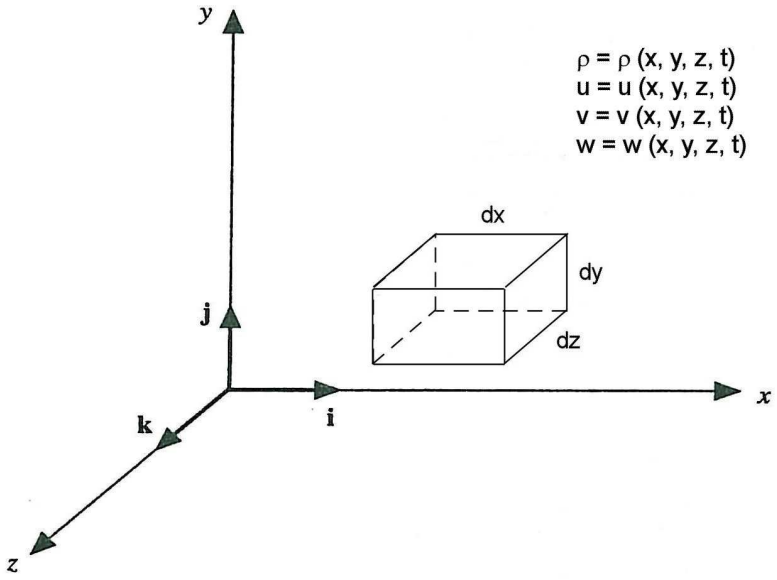

Figure 5. Model of infinitesimal small control volume fixed in space.

2.2.1 Basic governing equations

The physical description of fluid flow is composed of the conservation of mass, momentum, and energy. The equations, which are also known as *complete Navier-Stokes* equations [5], define the basis for the simulation tools that are used in this thesis. It can be noted that the presentation and discussion rest mainly on the conservative differential form.

The *continuity equation* states that the total mass in a CV is neither destroyed nor created. The corresponding mathematical implementation follows:

$$\frac{\partial \rho}{\partial t} + \frac{\partial(\rho \cdot u)}{\partial x} + \frac{\partial(\rho \cdot v)}{\partial y} + \frac{\partial(\rho \cdot w)}{\partial z} = 0 \qquad (3)$$

In short term notation using the Nabla operator:

$$\frac{\partial \rho}{\partial t} + \nabla(\rho \cdot \vec{c}) = 0 \qquad (4)$$

The first term in equation (3) and (4), respectively, describes the time rate of increase of mass inside a CV. The second term denotes the net mass flow out of the element. Figure 6 visualises the convective part by showing mass fluxes over the faces of the CV.

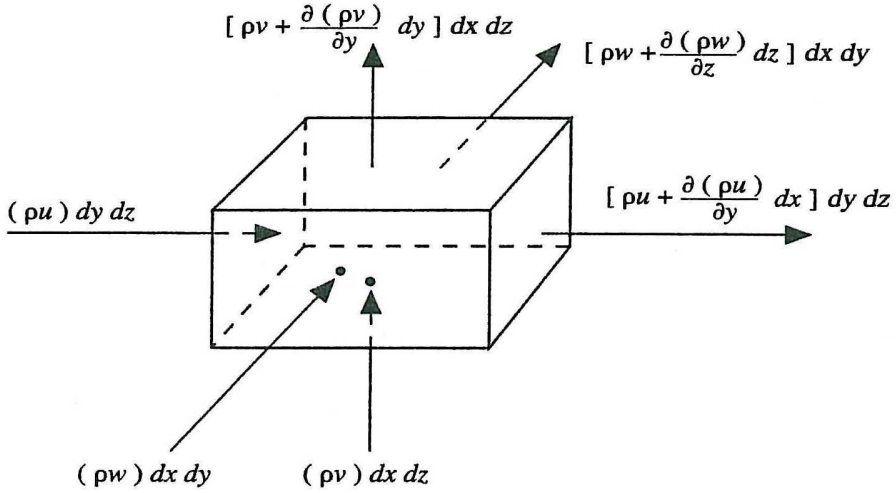

Figure 6. Mass fluxes through CV [5].

The *momentum equation* is built on Newton's second law. Generally, it is possible to divide between body and surface forces. Body forces are based on gravitational forces, but may also include electric and magnetic forces. None of these are relevant in the present study and are accordingly not presented here. Surface forces act, as the name indicates, on the surfaces of the CV. They are defined by pressure forces and normal and parallel acting stress forces.

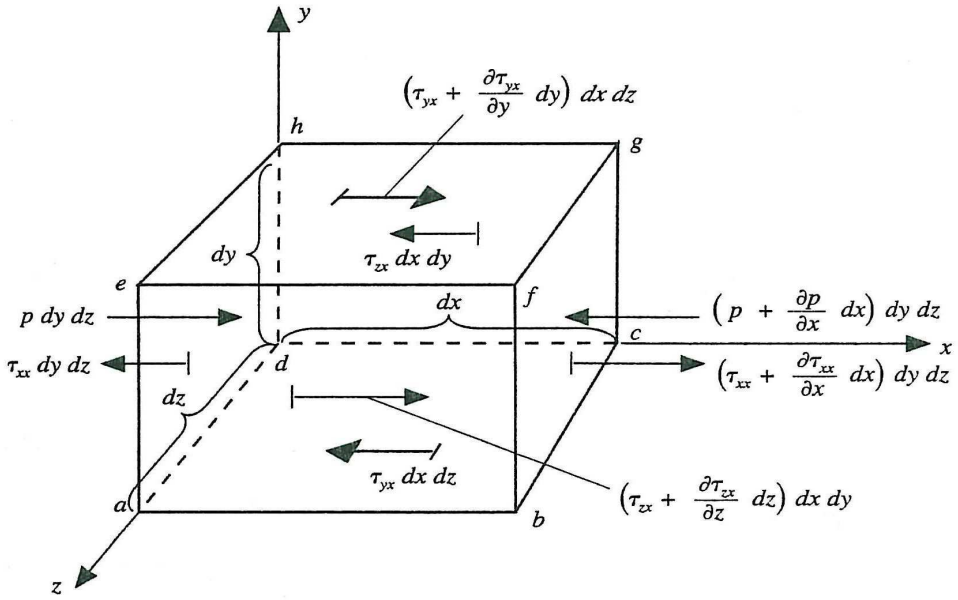

Figure 7. Forces in *x*-direction acting on CV [5].

Figure 7 shows as an example the surface forces that act in the *x*-direction on a CV. The corresponding mathematical formulation per unit volume for all three dimensions is:

$$\frac{\partial(\rho \cdot u)}{\partial t} + \nabla(\rho \cdot u \cdot \vec{c}) = -\frac{\partial p}{\partial x} + \frac{\partial \tau_{xx}}{\partial x} + \frac{\partial \tau_{yx}}{\partial y} + \frac{\partial \tau_{zx}}{\partial z} \tag{5}$$

$$\frac{\partial(\rho \cdot v)}{\partial t} + \nabla(\rho \cdot v \cdot \vec{c}) = -\frac{\partial p}{\partial y} + \frac{\partial \tau_{xy}}{\partial x} + \frac{\partial \tau_{yy}}{\partial y} + \frac{\partial \tau_{zy}}{\partial z} \tag{6}$$

$$\frac{\partial(\rho \cdot w)}{\partial t} + \nabla(\rho \cdot w \cdot \vec{c}) = -\frac{\partial p}{\partial z} + \frac{\partial \tau_{xz}}{\partial x} + \frac{\partial \tau_{yz}}{\partial y} + \frac{\partial \tau_{zz}}{\partial z} \tag{7}$$

The left hand side of equations (5) to (7) correspond to the initial term mass times acceleration. For the *x*-direction it can be written, for example as:

$$\frac{1}{V} \cdot (m \cdot a_x) = \frac{1}{V} \cdot \left(\rho \cdot V \cdot \frac{Du}{Dt} \right) \tag{8}$$

The total or substantial derivative [21] represents the shift from Lagrangian, fixed to fluid mass, to Eulerian, fixed to spatial coordinates, notation [51]:

$$\rho \cdot \frac{Du}{Dt} = \rho \cdot \frac{\partial u}{\partial t} + \rho \cdot \vec{c} \cdot \nabla u \tag{9}$$

Combining equation (9) with the continuity equation, it follows that:

$$\frac{1}{V} \cdot (m \cdot a_x) = \frac{\partial(\rho \cdot u)}{\partial t} + \nabla(\rho \cdot u \cdot \vec{c}) \tag{10}$$

As a convention, tensile stresses always act in the positive normal direction [95]. Accordingly, the pressure gradient is subtracted in equations (5) to (7). For Newtonian fluids the stress terms are proportional to the velocity gradient. In 1845, Stokes derived the following [5]:

$$\tau_{xx} = \lambda \cdot (\nabla \vec{c}) + 2 \cdot \mu \cdot \frac{\partial u}{\partial x} \tag{11}$$

$$\tau_{yy} = \lambda \cdot (\nabla \vec{c}) + 2 \cdot \mu \cdot \frac{\partial v}{\partial y} \tag{12}$$

$$\tau_{zz} = \lambda \cdot (\nabla \vec{c}) + 2 \cdot \mu \cdot \frac{\partial w}{\partial z} \tag{13}$$

$$\tau_{xy} = \tau_{yx} = \mu \cdot \left(\frac{\partial v}{\partial x} + \frac{\partial u}{\partial y} \right) \tag{14}$$

$$\tau_{xz} = \tau_{zx} = \mu \cdot \left(\frac{\partial u}{\partial z} + \frac{\partial w}{\partial x} \right) \tag{15}$$

$$\tau_{yz} = \tau_{zy} = \mu \cdot \left(\frac{\partial w}{\partial y} + \frac{\partial v}{\partial z} \right) \tag{16}$$

In respect of the tensile stresses τ_{xx}, τ_{yy}, and τ_{zz} (equations (11) to (13)), the first term on the right side of the equal sign represents a multiplication of the second viscosity coefficient λ with the divergence of the velocity vector. The Stokes Hypothesis states [83]:

$$\lambda = -\frac{2}{3} \cdot \mu \tag{17}$$

If the fluid density in a flow field remains constant, the terms with λ drop out as a result of the mass conservation. In the present analysis the fluid density as a function of pressure and temperature can not be neglected, that is, it is essential to include fluid compressibility and thermal expansibility. Therefore, equations (5) to (17) represent the basic set for representing the momentum conservation. By using the Einstein summation convention [21] the short term form follows as:

$$\frac{\partial(\rho \cdot c_j)}{\partial t} + \nabla(\rho \cdot c_j \cdot c_k) = -\frac{\partial p}{\partial x_j} + \frac{\partial}{\partial x_j}\left(\lambda \cdot \frac{\partial c_k}{\partial x_k}\right) + \frac{\partial}{\partial x_i}\left[\mu \cdot \left(\frac{\partial c_i}{\partial x_j} + \frac{\partial c_j}{\partial x_i}\right)\right] \tag{18}$$

Conservation of energy is based on the first law of thermodynamics [31]. For a fluid element of constant mass that moves through the domain, the rate of change of energy inside the element equals the work done on the element and the total heat flux into it:

$$\Delta m \cdot \frac{D}{Dt}\left(e + \frac{1}{2} \cdot \vec{c}^{\,2}\right) = P + Q \tag{19}$$

The sum on the left hand side of equation (19) represents the total energy e_0 of the fluid element, that is, the internal energy due to molecular motion and the kinetic energy of the moving mass. On the right hand side, P equals the forces acting on the fluid element times the element velocity. By neglecting again any body forces, P becomes:

$$P = \left(-\left(\frac{\partial(u \cdot p)}{\partial x} + \frac{\partial(v \cdot p)}{\partial y} + \frac{\partial(w \cdot p)}{\partial z}\right) + D_{dif}\right) \cdot dxdydz \tag{20}$$

D_{dif} represents the diffusion tensor and includes the lateral and normal shear stress components:

$$D_{dif} = \begin{pmatrix} \frac{\partial(u \cdot \tau_{xx})}{\partial x} + \frac{\partial(u \cdot \tau_{yx})}{\partial y} + \frac{\partial(u \cdot \tau_{zx})}{\partial z} \\ + \frac{\partial(v \cdot \tau_{xy})}{\partial x} + \frac{\partial(v \cdot \tau_{yy})}{\partial y} + \frac{\partial(v \cdot \tau_{zy})}{\partial z} \\ + \frac{\partial(w \cdot \tau_{xz})}{\partial x} + \frac{\partial(w \cdot \tau_{yz})}{\partial y} + \frac{\partial(w \cdot \tau_{zz})}{\partial z} \end{pmatrix} \tag{21}$$

The heat flux into the fluid element is indicated by Q. By neglecting volumetric heating due to absorption or emission of radiation, the term Q is solely defined by heat conduction through the element faces:

$$Q = -\left(\frac{\partial q_x}{\partial x} + \frac{\partial q_y}{\partial y} + \frac{\partial q_z}{\partial z} \right) \cdot dxdydz \tag{22}$$

Equations (19) to (22) are in Lagrangian form. Usually, for open systems that are fixed in space the energy equation is represented in terms of total enthalpy h_0. The latter is defined by [31]:

$$h_0 = e_0 + \frac{p}{\rho} \tag{23}$$

The substantial derivative of the second summand of equation (23) is added on both sides of equation (19). On the right hand side the new term can be combined with the divergence term of equation (20) to form:

$$\Delta m \cdot \frac{D}{Dt}\left(\frac{p}{\rho} \right) - \left(\frac{\partial (u \cdot p)}{\partial x} + \frac{\partial (v \cdot p)}{\partial y} + \frac{\partial (w \cdot p)}{\partial z} \right) \cdot dxdydz = \frac{\partial p}{\partial t} \cdot dxdydz \tag{24}$$

Accordingly, the enthalpy equation in Eulerian format per unit CV is:

$$\frac{\partial (\rho \cdot h_0)}{\partial t} + \nabla (\rho \cdot h_0 \cdot \vec{c}) = -\left(\frac{\partial q_x}{\partial x} + \frac{\partial q_y}{\partial y} + \frac{\partial q_z}{\partial z} \right) + \frac{\partial p}{\partial t} + D_{dif} \tag{25}$$

Equation (4), (18), and (25) represent the basis for analysing the transient fluid flow in the high pressure CR system. Depending on the utilised simulation code, further assumptions and extensions apply.

2.2.2 Implementation of the governing equations

Two simulation codes were used in this study. The core of the modelling was made in the GT-Fuel environment, version 6.2, of Gamma Technologies Inc. This code solves the governing equations in one dimension. Alternatively, ANSYS-CFX 10.0 of ANSYS Inc. was used for simulating locally the three-dimensional flow field. The results of the latter analysis were utilised to obtain a better understanding of the flow physics at particular locations inside the hydraulic circuit. That knowledge was then used to enhance the one-dimensional GT-Fuel model in order to obtain better closure with the measurements.

Both codes are based on a time-marching solution procedure. However, GT-Fuel employs an explicit, and ANSYS-CFX an implicit technique [7, 43].

One-Dimensional Analysis

In an explicit time marching algorithm the unknowns are exclusively computed from known properties. The governing equations (4), (5) to (7), and (19) accordingly can be rearranged to the form:

$$\frac{\partial U}{\partial t} = -\frac{\partial F_x}{\partial x} - \frac{\partial F_y}{\partial y} - \frac{\partial F_z}{\partial z} \tag{26}$$

With:

$$U = \begin{Bmatrix} \rho \\ \rho \cdot u \\ \rho \cdot v \\ \rho \cdot w \\ \rho \cdot e_0 \end{Bmatrix} \tag{27}$$

$$F_x = \begin{Bmatrix} \rho \cdot u \\ \rho \cdot u^2 + p - \tau_{xx} \\ \rho \cdot u \cdot v - \tau_{xy} \\ \rho \cdot u \cdot w - \tau_{xz} \\ \rho \cdot e_0 \cdot u + p \cdot u + q_x - u \cdot \tau_{xx} - v \cdot \tau_{xy} - w \cdot \tau_{xz} \end{Bmatrix} \tag{28}$$

$$F_y = \begin{Bmatrix} \rho \cdot v \\ \rho \cdot v \cdot u - \tau_{yx} \\ \rho \cdot v^2 + p - \tau_{yy} \\ \rho \cdot v \cdot w - \tau_{yz} \\ \rho \cdot e_0 \cdot v + p \cdot v + q_y - u \cdot \tau_{yx} - v \cdot \tau_{yy} - w \cdot \tau_{yz} \end{Bmatrix} \tag{29}$$

$$F_z = \begin{Bmatrix} \rho \cdot w \\ \rho \cdot w \cdot u - \tau_{zx} \\ \rho \cdot w \cdot v - \tau_{zy} \\ \rho \cdot w^2 + p - \tau_{zz} \\ \rho \cdot e_0 \cdot w + p \cdot w + q_z - u \cdot \tau_{zx} - v \cdot \tau_{zy} - w \cdot \tau_{zz} \end{Bmatrix} \tag{30}$$

U represents the solution vector. The flux terms are labelled F_x, F_y, and F_z, respectively. By looking, for example, exclusively at the x-component of the momentum equation, it follows that:

$$\frac{\partial(\rho \cdot u)}{\partial t} = -\frac{\partial\left(\rho \cdot u^2 + p - \tau_{xx}\right)}{\partial x} - \frac{\partial\left(\rho \cdot v \cdot u - \tau_{yx}\right)}{\partial y} - \frac{\partial\left(\rho \cdot w \cdot u - \tau_{zx}\right)}{\partial z} \tag{31}$$

It should be noted that equation (31) is identical to equation (5). As GT-Fuel solves the flow variables only in one dimension, the terms that are related to more than one dimension drop

out. As a first step, all the terms are omitted that are related to the velocity components *v* and *w*. For example the momentum equation in the *x*-direction can be rewritten to the form:

$$\frac{\partial(\rho \cdot u)}{\partial t} = -\frac{\partial(\rho \cdot u^2 + p)}{\partial x} + \frac{\partial(\tau_{xx})}{\partial x} + \frac{\partial(\tau_{yx})}{\partial y} + \frac{\partial(\tau_{zx})}{\partial z} \tag{32}$$

A similar expression can be obtained for the one-dimensional energy equation:

$$\frac{\partial(\rho \cdot e_0)}{\partial t} = -\frac{\partial(\rho \cdot e_0 \cdot u + p \cdot u)}{\partial x} + \frac{\partial(u \cdot \tau_{xx})}{\partial x} + \frac{\partial(u \cdot \tau_{yx})}{\partial y} + \frac{\partial(u \cdot \tau_{zx})}{\partial z} - \frac{\partial q_x}{\partial x} - \frac{\partial q_y}{\partial y} - \frac{\partial q_z}{\partial z} \tag{33}$$

The terms in equation (32) and (33) that describe the shear stresses and heat transfer refer to more than one dimension. Accordingly, a substitution is required to describe the friction and heat transfer effects in a purely one-dimensional flow. Equations (27) to (30) may be simplified to:

$$U = \begin{Bmatrix} \rho \\ \rho \cdot u \\ \rho \cdot e_0 \end{Bmatrix} \tag{34}$$

$$F_i = \begin{Bmatrix} \rho \cdot u \\ \rho \cdot u^2 + p - r_M \\ \rho \cdot e_0 \cdot u + p \cdot u + q_E - r_E \end{Bmatrix} \tag{35}$$

In equation (35) the terms with the shear and normal stresses τ_{ij} are replaced by the terms r_M and r_E, respectively. When analysing fluid transients in hydraulic circuits, it is common practice to assume constant flow properties over the cross-section of the channel. For example, for the fluid pressure this assumption holds in this study because the expected wave length of the pressure oscillation is significantly larger than the diameter of the pipe connections. Secondly, the flow theory inside channels and pipes is well established [99]. For Hagen-Poiseuille flows the steady state losses can be computed by:

$$\frac{\Delta p}{\rho} = \sum_i \left(\lambda_{f,i} \cdot \frac{L_i}{D_i} \cdot \frac{u_i^2}{2} \right) + \sum_k \left(C_{p,k} \cdot \frac{u_k^2}{2} \right) \tag{36}$$

Traditionally, the coefficient λ_f depends on the type of flow. For laminar flow, λ_f equals:

$$\lambda_f = \frac{64}{Re} \tag{37}$$

Turbulent flows are more complex. Therefore, no exact solution exists for λ_f, but several approximations. For hydraulic smooth surfaces the Blasius equation has been shown to be valid for Reynolds numbers smaller than 10^5 [99]:

$$\lambda_f = \frac{0.3164}{Re^{0.25}} \tag{38}$$

Alternatively, in the case of fully rough surfaces, Nikuradse defines [83]:

$$\frac{1}{\sqrt{\lambda_f}} = 2 \cdot \log \frac{D}{2 \cdot k_{tech}} + 1.74 \tag{39}$$

It has to be pointed out that GT-Fuel calculates internally with a friction factor that is based on the definition of Fanning [87]. The latter derivation is based on the hydraulic radius. For a circular duct the relation between the Moody/Darcy friction factor λ_f and the Fanning factor is given by:

$$\lambda_f = 4 \cdot C_{f,s} \tag{40}$$

Equations (37) to (39) are certainly not adequate to represent the physics of oscillatory flows. Indeed, for highly transient flows the instantaneous velocity profile differs considerably from the steady state profile [12, 24, 45, 83]. Due to the high inertia at the centre of the pipe, the flow particles can not adapt instantly to the new conditions at the upstream and downstream end. This is not the case for fluid particles near the wall. There, the flow is mainly driven by viscous forces. A change of, for example, the pressure gradient is followed accordingly faster than at the centre. Based on this consideration, it is clear that the frequency of the oscillation plays a major role.

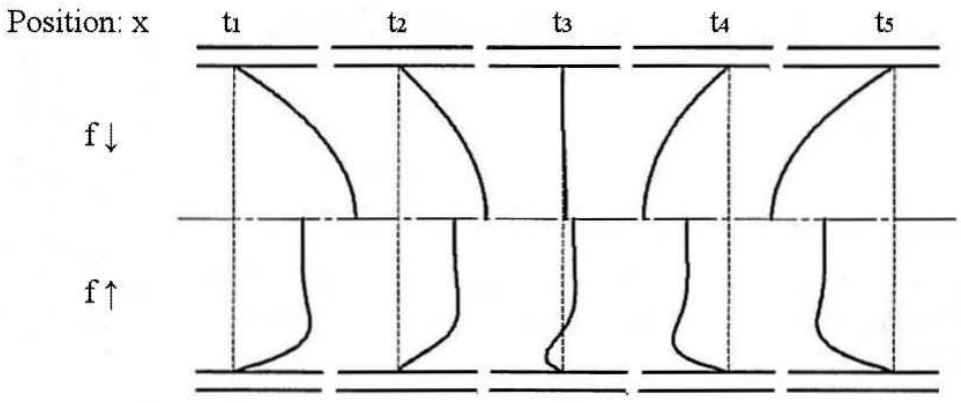

Figure 8. Pipe velocity profile at one location during different times for low (top) and high frequency oscillations (bottom); (figure based on [74]).

As is depicted schematically in Figure 8, the offset between near wall and centre flow increases for higher frequencies - the flow field is characterised by a large velocity gradient in

the vicinity of the wall. The latter aspect explains the rise of friction losses at high frequencies [74]. Axworthy et al. [8] give a short summary about the historical development of transient friction models for one-dimensional pipe flows. Essentially, two approaches are commonly used at present. On the one hand, unsteady effects are accounted for by weighted time histories of past flow conditions (for example, W. Zielke [102]). On the other hand, Brunone et al. [25] show that it is also possible to relate frequency dependent friction effects to instantaneous fluid acceleration. The unsteady friction model in GT-Fuel is based on the latter approach, that is, the friction coefficient in one CV is based on a steady state contribution, plus a factor that depends on the instantaneous temporal and convective acceleration of the fluid flow [8, 43]:

$$C_f = C_{f,s} \cdot M_{const} \cdot \left(1 + M_{trans} \cdot F_t\right) \tag{41}$$

The appearance of equation (41) indicates that this model is not fully analytical, but includes some empirical terms. Although the equation allows fine tuning via the two friction multipliers M_{const} and M_{trans}, the simulation model following later utilises for both factors a value of 1. Going back to equation (36), the second summand on the right hand side accounts for steady state losses due to abrupt changes in the flow path. This includes, for example, bends, tapers or irregular cross-sections. The loss coefficient C_p is computed by [85]:

$$C_p = \frac{\Delta p}{1/2 \cdot \rho \cdot u^2} \tag{42}$$

For modelling fluid transients in pipes and channels GT-Fuel employs a one-dimensional finite volume approach. This means, with respect to the previously used term ‘CV’, that the finite volume has a finite axial length and a diameter that corresponds to the geometrical diameter of, for example, the pipe. Within such a finite volume the fluid properties are assumed to be constant. Along the circumference of the volume no fluid particles are allowed to enter or escape; secondly, the no-slip condition applies at the wall boundary. Mass flux can enter or leave a finite volume via fluid-fluid interfaces. Heat can be exchanged with the surrounding via conduction to the wall boundaries and through forced convection. Free convection, on the other hand, is assumed to be negligible. For the studied CR system, as well as for similar high transient problems, the Peclet number is expected to be large. The latter dimensionless parameter is defined by the ratio of inertia to heat conduction [51]:

$$Pe = \frac{\vec{c} \cdot L}{\lambda_T} \tag{43}$$

Accordingly, the parameter q_E in equation (35) defines exclusively the heat conduction to the wall boundary. The parameter r_E in the same equation represents the viscous diffusion term (see equation 21). In comparison to the other terms this contribution is seen as negligible, and therefore omitted in the final energy equation. In contrast, the boundaries of the finite volume or CV, respectively, are not fixed, but may vary as a function of time. The energy equation (25) therefore needs to be extended by a term that represents work done due to a change of volume. Generally, this is defined by [31]:

$$P_V = \int p \cdot dV \tag{44}$$

Figure 9 illustrates the main concept of the code for modelling fluid transients. Known as the staggered grid approach [5, 95], the vector variables are stored at the faces of the CV. Scalar variables, on the other hand, are assigned to the centre of the finite volume.

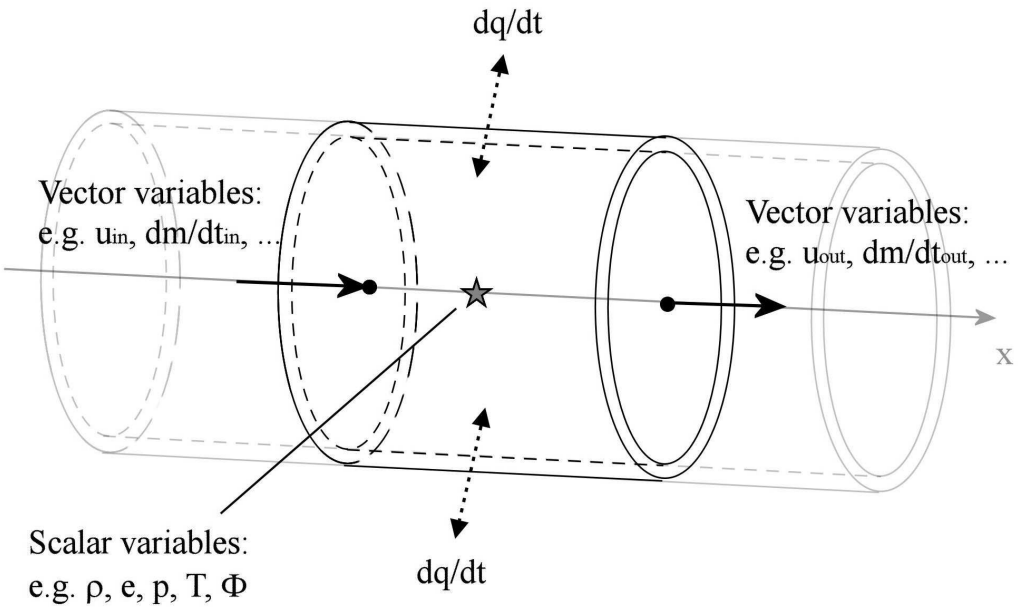

Figure 9. CV with scalar and vector variables.

By considering the above mentioned assumptions and extensions, the set of equations is integrated over each CV of length *dx*. The *continuity equation* is rewritten as:

$$\frac{dm}{dt} = \sum_{boundaries} mflx \tag{45}$$

In the above equation the mass flux is defined as the product of density, velocity at the CV face, and flow cross-section:

$$mflx = \rho \cdot u \cdot A \tag{46}$$

In its principle form, the *momentum equation* states that the net force on a fluid element equals its mass times the acceleration of the element. Mathematically, this is written as [51]:

$$\rho \cdot V \cdot \frac{Du}{Dt} = \sum F \tag{47}$$

The volume V of a CV is commonly defined through the product of characteristic area A times the axial extension dx. Secondly, it is more convenient to represent the force relative to CV length dx:

$$\rho \cdot A \cdot \frac{Du}{Dt} = \frac{\sum F}{dx} \tag{48}$$

The left hand side of equation (48) contains the substantial derivation of the fluid velocity. In Eulerian notation, and after moving the convective term to the right hand side, it follows that:

$$\frac{\partial(\rho \cdot A \cdot u)}{\partial t} = \frac{\sum F}{dx} - \frac{\partial}{\partial x}\left(\rho \cdot A \cdot u^2\right) \tag{49}$$

From equation (49) it can be seen that only one velocity component, u, is present. In accordance with the definition of the differential of a function with one unknown, it is possible to replace the partial derivatives through ordinary differentials [21]. Its total contribution may, further, be substituted by the sum of fluxes through all the boundaries. Together with equation (46), it can be written:

$$\frac{d(mflx)}{dt} = \frac{\sum F + \sum_{boundaries}(mflx \cdot u)}{dx} \tag{50}$$

The first summand in the numerator on the right hand side of equation (43) symbolizes the external forces acting on the fluid element. These are the differential pressure force over the CV and the friction losses; it should be noted that the friction term includes a factor of 4, since in the momentum equation the Moody/Darcy factor is required (see also equation (40)). In analogy to equation (34) and (35), respectively, the final momentum equation becomes:

$$\frac{d(mflx)}{dt} = \frac{dp \cdot A + \sum_{boundaries}(mflx \cdot u) - \frac{\rho \cdot u \cdot |u|}{2} \cdot A \cdot \left(4 \cdot C_f \cdot \frac{dx}{D} + C_p\right)}{dx} \tag{51}$$

It should be emphasised that in equation (51) *dp* represents the pressure difference over the length *dx* of the CV. Secondly, it is essential to consider the flow direction in the computation of the flow momentum [101]. The particular implementation of the velocity component in the loss term ensures, therefore, the preservation of the sign of the flow direction.

Based on equation (25) and the previously mentioned adaptations, the *enthalpy equation* is redefined as:

$$\frac{\partial(\rho \cdot h_0)}{\partial t} + \nabla(\rho \cdot h_0 \cdot \vec{c}) = \frac{\partial p}{\partial t} + s \tag{52}$$

The second summand on the right hand side, *s*, denotes the sum of heat flux through the wall and the work done due to a change of volume per unit volume. For simplicity, both contributions are added at the end of the derivation to the final energy equation. With equation (23) the enthalpy equation is split up to form:

$$\frac{\partial(\rho \cdot e_0)}{\partial t} + \nabla(\rho \cdot e_0 \cdot \vec{c}) + \frac{\partial\left(\rho \cdot p \middle/ \rho\right)}{\partial t} + \nabla\left(\rho \cdot \frac{p}{\rho} \cdot \vec{c}\right) = \frac{\partial p}{\partial t} + s \tag{53}$$

The local derivative of pressure drops out, and after some rearrangement equation (53) yields to:

$$\frac{\partial(\rho \cdot e_0)}{\partial t} = -\nabla(\rho \cdot e_0 \cdot \vec{c}) - \nabla\left(\rho \cdot \frac{p}{\rho} \cdot \vec{c}\right) + s \tag{54}$$

Indeed, the two divergence terms can be combined again to form a product that includes the total enthalpy. Secondly, by considering the fact that only one dimension is solved, equation (54) simplifies further:

$$\frac{d(\rho \cdot e_0)}{dt} = -\frac{d}{dx}\left(\rho \cdot u \cdot \left(e_0 + \frac{p}{\rho}\right)\right) + s \tag{55}$$

Equation (55) is integrated over the CV length *dx*, that is, the volume *V* of the CV, which leads to:

$$\frac{d(m \cdot e_0)}{dt} = -\Delta\left(\rho \cdot A \cdot u \cdot \left(e_0 + \frac{p}{\rho}\right)\right) + S \tag{56}$$

In respect of the placeholder *S*, the heat flux term *Q* (equation (22)) is rewritten for one-dimensional flow as [31]:

$$Q = \alpha \cdot A_S \cdot (T_f - T_w) \tag{57}$$

The instantaneous heat transfer coefficient α is based on the Chilton-Colburn analogy that relates heat to mass transfer [32]:

$$Nu = \frac{\lambda_f}{8} \cdot Re \cdot Pr^{1/3} \tag{58}$$

In this equation *Nu* is defined as the dimensionless Nusselt number, which can be written as:

$$Nu = \frac{\alpha \cdot Re \cdot Pr}{u \cdot \rho \cdot c_p} \tag{59}$$

In the denominator there appears a new term c_p, which represents the specific heat of the fluid at constant pressure. *Pr* symbolizes the Prandtl number that correlates the momentum flux to the heat flux. By combining the last two equations and replacing the Moody/Darcy friction factor by the Fanning factor (see equation (40)), it follows:

$$\alpha = \frac{1}{2} \cdot C_f \cdot \rho \cdot u \cdot c_p \cdot \mathrm{Pr}^{-2/3} \tag{60}$$

Equations (44) and (57) are substituted into equation (56). As before, the difference is replaced by the sum of fluxes over the boundaries, which leads to the final version of the utilised energy equation:

$$\frac{d(m \cdot e_0)}{dt} = p \cdot \frac{dV}{dt} + \sum_{boundaries} (mflx \cdot h_0) - \alpha \cdot A_S \cdot (T_f - T_w) \tag{61}$$

The subsequent equations for mass (45), momentum (51), and energy conservation (61) represent the basic set of equations that are used in GT-Fuel for modelling fluid transients:

$$\frac{dm}{dt} = \sum_{boundaries} mflx \tag{45}$$

$$\frac{d(mflx)}{dt} = \frac{dp \cdot A + \sum_{boundaries} (mflx \cdot u) - \frac{\rho \cdot u \cdot |u|}{2} \cdot A \cdot \left(4 \cdot C_f \cdot \frac{dx}{D} + C_p \right)}{dx} \tag{51}$$

$$\frac{d(m \cdot e_0)}{dt} = p \cdot \frac{dV}{dt} + \sum_{boundaries} (mflx \cdot h_0) - \alpha \cdot A_S \cdot (T_f - T_w) \tag{61}$$

The primary solution variables are density, total inner energy, and mass flux. Secondary variables include, for example, pressure, velocity, fluid temperature, and total specific enthalpy. With the velocity explicitly given through equation (46), the system of equations is characterised by five unknowns. Based on the assumption of thermodynamic equilibrium [95], it is possible to connect the four thermodynamic variables ρ, p, T, and e to two

additional state equations. For problems involving gas flows, the closing equations are commonly provided by the ideal gas law and a caloric equation of state:

$$p = \rho \cdot R \cdot T \tag{62}$$

$$e = c_v \cdot T \tag{63}$$

For liquids, on the other hand, no analytical general valid complement to equation (62) is available. At present, empirical equations are used that are fitted to experimental data [50, 79]. In GT-Fuel the density is related to pressure and temperature by the following equation [43]:

$$\rho(p,T) = a_0 + \frac{\left[p + a_1 \cdot T + a_2\right]^{(a_3+1)}}{a_3 + 1} + p \cdot \left[a_4 \cdot T^{a_5} + a_6\right] + a_7 \cdot \sqrt{T} \tag{64}$$

The parameters a_0 to a_7 represent fit coefficients that are exclusive to a particular fluid. The caloric relationship is expressed by an approximate function for the specific enthalpy [43]:

$$h = \left(h_{ref}\right)_{liq} + a_1 \cdot \left(T - T_{ref}\right) + a_2 \cdot \left(T - T_{ref}\right)^2 + a_3 \cdot \left(T - T_{ref}\right)^3 \tag{65}$$

In the above equation, $h_{ref,liq}$ is the reference enthalpy, which is defined as the difference of the vapour enthalpy and heat of vaporization at the reference temperature T_{ref} = 298 K. As this enthalpy equation is valid for a reference pressure p_{ref} = 1 bar, other pressure values are interpolated using the expression [43]:

$$h(p) = h(p_{ref}) + \frac{\partial h}{\partial p}(p - p_{ref}) + \frac{\partial^2 h}{\partial p^2}(p - p_{ref})^2 \tag{66}$$

During one time step, the solver iterates through (64) to (66) until each equation is satisfied. The obtained values are used in the subsequent time step to compute new values for the primary variables. Unless the final simulation time is reached, a new cycle is started again and the computation sequence is repeated. For clarity, it is stressed that the derivation to this point is intended to describe the development of the individual terms from the general Navier-Stokes equations to the ones that are used in the simulation code. In this sense, implementation aspects that concern the actual coding process are not considered during the derivation presented here.

The time step selection holds an important role in the solution process. Due to the strong coupling of the governing equations and the initially described solution procedure, explicit solvers are only conditionally stable.

The stability criterion is defined by the Courant-Friedrichs-Lewy condition (CFL), which is written in the utilised code as [43]:

$$\frac{\Delta t}{\Delta x} \cdot \left(|u| + a \right) \leq 0.8 \cdot m_{CFL} \tag{67}$$

Equation (67) implies that information, that is, pressure or a flux, can not propagate across a CV of length Δx during the time Δt. During the solution process, the solver may adapt the time step to the instantaneous fluid conditions to ensure efficient but still stable progress. The general selection of the time step is dependent on the smallest CV extension in the complete circuit. Accordingly, a compromise has to be found between solution accuracy and computation efficiency.

Further equations that are important in this context and which extend the previously described governing and state equations are given by a formulation for phase change of the fluid and a correction equation for sudden expansions in the flow path after restrictions. The former approach is implemented in the code to account for cavitation effects in the system. Concerning the studied CR fuel injection system, it is likely to observe this phenomenon in the nozzle holes of the fuel injector due to the large gradients and strong curvature of the flow path at the nozzle hole inlets [14, 46, 80]. In respect of a CV, GT-Fuel treats the fluid as a homogeneous continuum, which is in thermodynamic equilibrium. If the static pressure drops below the vapour pressure during a time interval, the liquid transforms into a mixture that is composed of liquid and vapour. Each phase employs its own state equation - equations (64) to (66) for the liquid, and, for example, equations (62) and (63) for the vapour. The quantity of cavitation in a CV is calculated as the ratio of vapour volume to total volume of the cell. As the fluid temperature in a CV is not fixed but varies as a function of system state, the instantaneous vapour pressure needs to be adapted. This is done in the code by using the Clausius-Clapeyron equation, which states [31]:

$$\frac{dp}{dT} = \frac{\Delta h_{vap}}{T \cdot \left(v'' - v' \right)} \tag{68}$$

As the volume of the vapour phase is assumed to be considerably larger than the liquid phase, the specific volume of the latter quantity is omitted:

$$\frac{dp}{dT} = \frac{\Delta h_{vap}}{T \cdot v''} \tag{69}$$

The vaporization enthalpy in the denominator of the above equation includes both the heat of vaporization at the reference temperature T_{ref} = 298 K and the differences in enthalpies for the

liquid and vapour phase. By providing, in addition, the vapour pressure at T_{ref}, it is possible to calculate a new saturation pressure:

$$p_{sat} - p_{sat,ref} = \int_{T_{ref}}^{T} \frac{dp}{dT} dT \tag{70}$$

In internal flow problems the fluid path may undergo several restrictions and expansions. The latter ones require particular attention, as energy transformation depends strongly on the local geometry. If the difference between the restriction area (A_1) and the flow cross-section downstream of the restriction (A_2) is large, that is, the ratio *A1* to A_2 is small, the kinetic energy of the fluid particles in the restriction is converted into heat during deceleration. On the other hand, for ratios close to 1 not all kinetic energy is dissipated but partly used to recover the static pressure; the downstream pressure at A_2 is lower than upstream of the restriction but higher than at the exit of the restriction. Borda and Carnot have described this phenomenon in the mathematical form [87, 99]:

$$C_p = \left(1 - \frac{A_1}{A_2}\right)^2 \tag{71}$$

C_p in equation (71) describes a loss coefficient and can be put straight in a loss equation, as, for example, equation (36). In GT-Fuel, however, expansions are calculated separately from restrictions. This is necessary if the flow is divided into more than one path downstream of the restriction. Accordingly, the code employs a recovery coefficient for each expansion in order to account explicitly for the local characteristics. The recovery coefficient is defined by:

$$C_{pr} = C_{pr,t} - C_p \tag{72}$$

The factor $C_{pr,t}$ symbolizes the theoretical recovery coefficient, which is formulated as [73]:

$$C_{pr,t} = 1 - \left(\frac{A_1}{A_2}\right)^2 \tag{73}$$

By putting equation (71) and (73) into (72), there follows the recovery coefficient for mild expansions:

$$C_{pr} = 2 \cdot \frac{A_1}{A_2} \cdot \left(1 - \frac{A_1}{A_2}\right) \tag{74}$$

The presented FVM differs from the MOC, a typical representative of a classical approach for modelling fluid transients, by a number of explicit features. Firstly, classical methods commonly assume a mild fluid compressibility. By applying the momentum equation to

describe the propagation of pressure waves in liquids, the propagation velocity and the fluid properties density and pressure are connected by [51]:

$$a^2 = \frac{\rho_1}{\rho_0} \cdot \left(\frac{p_1 - p_0}{\rho_1 - \rho_0} \right) \tag{75}$$

In equation (75) index 1 denotes the state after the pressure wave and index 0 the state before the fluid particles are affected by the surge. Mild compressibility means, in this context, that the first quotient on the right hand side, the density ratio, equals approximately 1. However, in high pressure applications this assumption ceases to be valid. In the studied CR fuel injection system the maximum pressure amplitude transiently reaches values beyond 1800 bar. The minimum pressure, on the other hand, is given by the atmosphere downstream of the nozzle holes. Similarly, the pressure in the fuel return line between pilot stage and pump unit is in the range of a few bar. Based on these numbers, the density variation of the liquid may be as large as 10 %. Despite the fact that the impact of the density ratio on the speed of sound is reduced, as the latter number appears squared in equation (75), it must be pointed out that even a minor variation of the fluid density is likely to have a significant impact on the local propagation of pressure waves. Secondly, the MOC utilises in its traditional form a constant bulk modulus to describe the fluid compressibility. The latter is connected to the speed of sound by [9, 101]:

$$a = \sqrt{\frac{B}{\rho}} \tag{76}$$

If the bulk modulus is assumed to be constant, the code is not capable of representing the non-linear nature of a travelling shock wave; a compression wave tends to steepen, while a rarefaction wave ultimately flattens [51]. The most apparent difference of classical methods for modelling fluid transients from the presented FVM is the fact that the former ones commonly neglect any thermodynamic effects. As before, this assumption is not adequate when modelling high pressure applications. For example, Catania et al. [29] show that the impact of energy transfer due to the fluid compressibility is not negligible. Pressure waves are always associated with a change of enthalpy. The state equation of the fluid defines, on the other hand, the fluid properties at a particular thermodynamic state. Fluid compression and rarefaction is therefore connected to a change of pressure and temperature. As is shown in the discussion of the simulation results which follows later, also the latter variable undergoes substantial variations. In view of that, it is more appropriate for applications with large pressure variations to utilize basic thermodynamic and fluid dynamics relations rather than

characteristic numbers like, for example, the speed of sound or the bulk modulus that are based on assumptions and restrictions, respectively.

Three-Dimensional Analysis

The three-dimensional analysis that is conducted in ANSYS-CFX 10.0 is based on the implicit solution of the unknown variables. Different to the explicit formulation, the implicit solver simultaneously computes during one time step the unknowns at all grid points. A computer code of this solver type requires a large memory, since one of the key tasks during the computation is to manipulate large matrices. Then again, implicit formulations are often, as for example, ANSYS-CFX 10.0, unconditionally stable. This means that the time step of a transient solution is not fixed to the Courant criterion (see equation (59)), but can be chosen arbitrarily. The latter aspect is particular interesting if the total simulation time is relatively large and if fluid transients are not of interest. However, for studying the propagation of pressure waves, the CFL condition applies, as otherwise the wave front smears out and the results have no physical ground [12]. Because of the involvement of large matrices, implicit methods are generally less efficient than explicit formulations when modelling fluid transients.

The fundamental governing equations for solving the fluid field in three dimensions are presented in chapter 2.2.1 through the equations (4), (18), and (25). These equations are, in principle, enough for modelling the single-phase flow of the studied problem - whether the flow is laminar or turbulent. However, because of the small time scale of turbulence effects, it is much more economical to actually model the turbulence phenomena. A very popular, and in the engineering community widely adopted method, is based on the Reynolds-averaged Navier-Stokes (RANS) approach [51, 99]. The RANS method is based on the idea of describing any turbulent flow by a mean contribution and a part that fluctuates around the mean value. For any scalar or vector, such as, for example, the velocity vector, the mathematical implementation follows the general form of equation (77):

$$\Phi = \overline{\Phi} + \Phi' \tag{77}$$

The second summand of the above equation is added to the basic governing equations, which are rearranged to separate the terms with mean values from the ones with fluctuating contribution. The latter ones are finally modelled by one of the manifold turbulence models [7]. It needs to be pointed out that the utilised turbulence model may have a significant effect on the studied variables [17]. But as highlighted in more detail in chapter 3.2.3, the current

three-dimensional investigation is not intended to provide highly accurate results, but an approximate picture of the local flow field. Consequently, the ANSYS-CFX CFD calculations utilise the fairly universal k-ε two-equation turbulence model [7, 51, 99].

Since ANSYS-CFX 10.0, the same as GT-Fuel, is based on the FVM, the complete Navier-Stokes equations are integrated over each control volume [7]. The thus obtained volume integrals are subsequently approximated by discrete functions. Generally, several schemes are suitable for the latter operation; first or higher order schemes and central difference approximations are just a few typical methods that are provided, for example, in the utilised CFD code [5, 7, 95]. Despite the choice of different schemes, it is worth mentioning that each method is more or less suitable only for a specific class of flow problem. Besides the efficiency aspects, the underlying physics and mesh topology need to be considered during pre-processing. First order schemes are known to be computationally efficient, but at the same time they promote *numerical diffusion* if the mesh is not aligned with the main flow direction. Figure 10 illustrates the latter terminology in a graphical way.

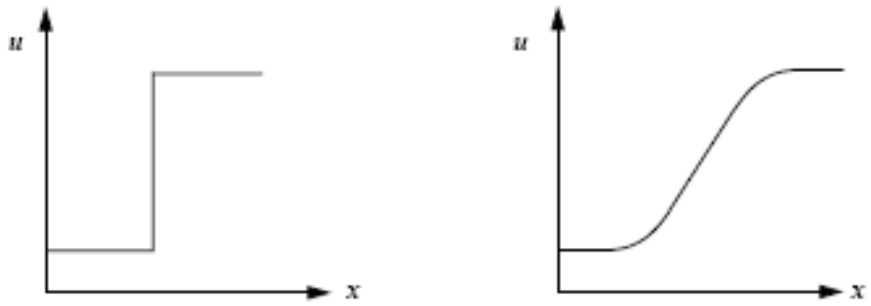

Figure 10. Numerical diffusion (right) of step profile (left) by 1st order discretization of mesh not aligned with main flow direction [7].

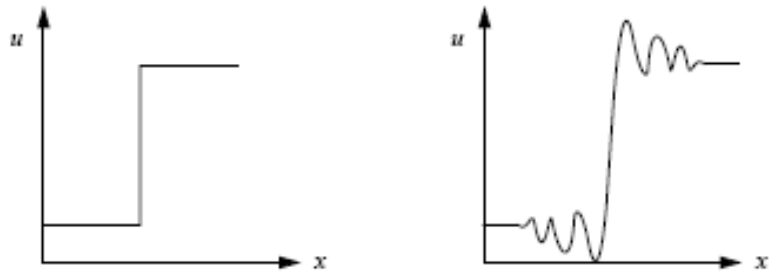

Figure 11. Numerical dispersion (right) of step profile (left) by even-order discretization scheme [7].

Schemes that are based on even-order accuracy minimize the aforementioned drawback, but support the appearance of non-physical variable oscillation in the presence of strong shock waves (Figure 11). Also identified as *numerical dispersion* [7], the phenomenon diminishes when first order accurate methods are used [12].

Analogous to the previously addressed basic nature of three-dimensional computations, the CFD model assumes isothermal flow. Secondly, the fluid density is defined as a function of pressure alone. The barotropic relationship is given by:

$$\rho = \rho_{ref} \cdot e^{\frac{p - p_{ref}}{B}} \tag{78}$$

It has to be emphasised at this point that the three-dimensional analysis is not intended to study the pressure wave transmission through the domain. In fact, only the large scale interaction of the flow field with the boundaries is of interest. Fluid compressibility is taken into account, as it is necessary to include effects such as fluid squeezing. In this respect, equation (78) is in contradiction to the arguments of the previous section about the modelling of the one-dimensional flow field, but adequate to incorporate the main characteristics of the flow problem at hand.

2.3. Approximate methods for estimating characteristic frequencies

Besides the comprehensive analysis of a hydraulic system it is often desirable in the engineering world to obtain an approximate and quick overall picture of some selected variables. In this sense, the expected frequency response of the system to some excitation is one of the most interesting parameters. Here, two simple methods are presented that are often used to gain a first estimate of the expectable main frequencies. A discussion of the performance of each method follows, together with a review of the detailed simulation and measurement results in the next chapter.

2.3.1 Estimation based on natural frequency of hydraulic line

The first method is based on the idea that the frequency response to an arbitrary excitation follows the natural frequency of the studied hydraulic line. For the investigated CR system the hydraulic line is represented as the volume of the pipe between rail and injector plus the main flow path inside the injector down to the needle seat (see, for example, page 21, Figure 4).

The natural frequency of a hydraulic line can be derived by means of the hydraulic impedance, which is defined as the ratio of pressure to flow amplitude [9]:

$$Z = \frac{\hat{p}}{\hat{\dot{V}}} \tag{79}$$

By using the general approach for solving the wave equation and assuming a harmonic excitation, the time-space distribution of pressure and flow is described through:

$$\Phi(x,t) = \left(\Phi_1 \cdot e^{\left(-i \cdot \frac{\omega}{a} \cdot x\right)} + \Phi_2 \cdot e^{\left(i \cdot \frac{\omega}{a} \cdot x\right)} \right) \cdot e^{i \cdot \omega \cdot t} \tag{80}$$

Flow and pressure are connected through the momentum equation. If the convective acceleration and any friction effects are neglected, it follows for one-dimensional flow from equation (18):

$$\frac{\partial \dot{V}}{\partial t} = -\frac{A}{\rho} \cdot \frac{\partial p}{\partial x} \tag{81}$$

After partial differentiation of equation (80) and combination with (81) it can be shown that, after some rearrangement, the local distribution of the flow and pressure amplitude is described by [9]:

$$\hat{\dot{V}}_x = \hat{\dot{V}}_{x=0} \cdot \cos\left(\frac{\omega}{a} \cdot x\right) - i \cdot \frac{\hat{p}_{x=0}}{Z} \cdot \sin\left(\frac{\omega}{a} \cdot x\right) \tag{82}$$

$$\hat{p}_x = \hat{p}_{x=0} \cdot \cos\left(\frac{\omega}{a} \cdot x\right) - i \cdot Z \cdot \hat{\dot{V}}_{x=0} \cdot \sin\left(\frac{\omega}{a} \cdot x\right) \tag{83}$$

Equations (82) and (83) are universally valid in conjunction with the above assumptions and restrictions. The most critical part is the proper implementation of the boundary conditions. With respect to the CR system, it is assumed that the connection line has an open end at the rail and a closed termination at the needle seat. If the coordinate of the hydraulic line is denoted with 0 at the rail connection, the inlet impedance becomes:

$$Z_I = \frac{\hat{p}_{x=0}}{\hat{\dot{V}}_{x=0}} \tag{84}$$

On the other hand, the principle of the rail volume is to provide a constant pressure to all injectors at all times. It is therefore reasonable to assume that the numerator in equation (84) and the inlet impedance, respectively, are 0. For the exit impedance it can be written:

$$Z_E = i \cdot Z \cdot \tan\left(\frac{\omega}{a} \cdot L\right) \tag{85}$$

From equation (85) it can be seen that the exit impedance has maxima for the tangent argument being an odd integer of half π:

$$\frac{\omega}{a} \cdot L = n \cdot \frac{\pi}{2} \tag{86}$$

And:

$$n = 1,3,5,\ldots \tag{87}$$

Rearranging equation (86) and replacing the angular frequency ω with f, the natural frequencies are:

$$f = n \cdot \frac{a}{4 \cdot L} \tag{88}$$

Equation (85) implies that only small flow variations at the line exit, that is, at the needle seat, are sufficient to cause significant pressure oscillations at the same location.

2.3.2 Estimation based on theory of electromagnetic oscillations in AC circuits

Due to the similarities between oscillating AC and hydraulic circuits it is appealing to describe the phenomenon of fluid transients through the science of electrical engineering. The hydraulic capacity is related to the bulk modulus; it is defined by the ratio of volume decrease over increase in pressure [9]:

$$C_H = -\frac{dV}{dp} \tag{89}$$

Or:

$$C_H = \frac{V_{ref}}{B} \tag{90}$$

The hydraulic inductance is based on Newton's second law. Because of the fluid inertia a pressure difference is required to lead to a change in volumetric flow:

$$\Delta p = \frac{L \cdot \rho}{A} \cdot \frac{d\dot{V}}{dt} \tag{91}$$

The first quotient of equation (91) is named in analogy to the science of electrical engineering as hydraulic inductance [9]:

$$L_H = \frac{L \cdot \rho}{A} \tag{92}$$

In an electrical RLC circuit the natural angular frequency is defined as the inverse of the square root of the inductance and capacitance product [60]. Correspondingly, for a hydraulic circuit it follows in the same way:

$$\omega = \frac{1}{\sqrt{L_H \cdot C_H}} \tag{93}$$

And with f instead of the angular frequency ω:

$$f = \frac{1}{2 \cdot \pi} \cdot \frac{1}{\sqrt{L_H \cdot C_H}} \tag{94}$$

Besides the restriction to only linear variations around the set point, the approach presented here also neglects phenomena that can be related to viscous friction and thermodynamic effects.

In respect of the high pressure CR circuit it is assumed that each main flow section can be represented by a discrete parameter set consisting of a hydraulic inductance and capacitance. As discussed thoroughly in the next chapter, Figure 12 shows the simplified schematic layout of the CR test bench that has been used in this sub-chapter.

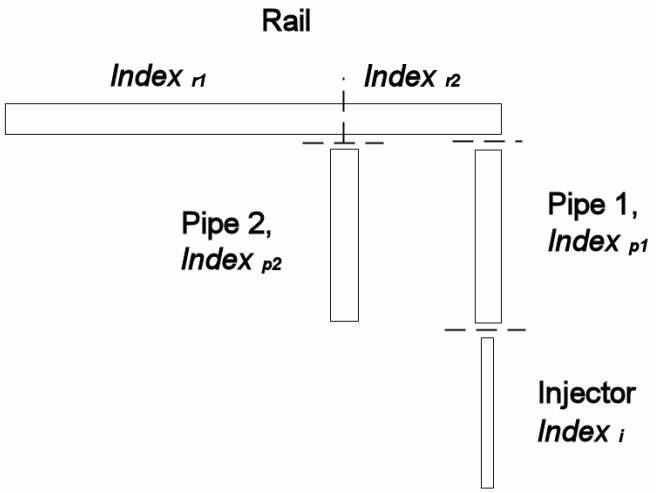

Figure 12. Simplified schematic hydraulic line layout of CR test.

From the above figure it can be seen that even a very simplified representation of the circuit leads to a dynamic system of higher order (two degrees of freedom for each line section). For obtaining a rough picture about the dynamic characteristics it is often sufficient to know only the base natural frequency. Accordingly, the aim is to simplify the above circuit so that it can be represented by a single set of effective capacitance and inductance.

Before combining individual sections of the hydraulic circuit with each other, the following discussion clarifies in which way the capacitances and inductances are added together. If, for example, a set of two identical pipes (length L, cross-section area A, volume V) in series with

one end open and the other end closed is replaced by an equivalent single line (see Figure 13, left), the effective inductance and capacitance of the single line is:

$$L_{H,serial,1} = \frac{2 \cdot L \cdot \rho}{A} \tag{95}$$

$$C_{H,serial,1} = \frac{2 \cdot V}{B} \tag{96}$$

The individual inductances and capacitances of the single pipes can be combined using either the rules for serial or parallel connections of LC networks [60]. By employing first the rules for serial connections it can be seen that the effective inductance and capacitance of the two pipes equals:

$$L_{H,serial,eff} = \frac{2 \cdot L \cdot \rho}{A} \tag{97}$$

$$C_{H,serial,eff} = \frac{V}{2 \cdot B} \tag{98}$$

While equation (97) aligns with the result of equation (95), it can be seen that the serial connection of the individual capacitances (equation (98)) does not comply with the result for the equivalent single pipe (equation 96)). Indeed, the same result is obtained only if the capacitances are combined in accordance with the rules for parallel LC circuits. The same strategy is also applied for pipes that are connected parallel to each other. In the latter case, it can be shown that both the individual inductances and capacitances are added together with the rules for parallel LC networks (see Figure 13, right).

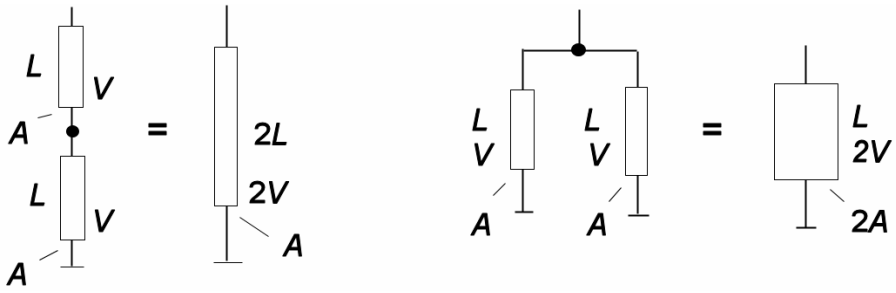

Figure 13. Combination of pipes, series (left) and parallel (right).

The above rules for serial and parallel pipe sections are applied for the analysis of the complete CR circuit. As a result, the hydraulic network is replaced by a single equivalent inductance and capacitance, respectively:

$$C_{eq} = C_{r1} + C_{p2} + C_i + C_{p1} + C_{r2} \tag{99}$$

$$L_{eq} = L_{r1} + \frac{L_{p2} \cdot \left(L_{r2} + L_{p1} + L_i\right)}{L_{r2} + L_{p1} + L_i + L_{p2}} \tag{100}$$

It is stressed at this point that this approach includes significant simplifications that may compromise the quality of the prediction. The subsequent discussion will evaluate to what degree such an approach can be useful for evaluating a hydraulic CR circuit (see, for example, Table 3, page 114).

3. ANALYSIS OF THE HYDRAULIC CIRCUIT

3.1. Experimental measurements

The analysis of the hydraulic circuit of the CR system is based to a great extent on the results of experimental measurements. This ensures not only extensive validation of the subsequently presented simulation model but also a sound foundation for the thesis statements. The centre of this study is defined by a commercial high pressure CR diesel fuel injection system for light vehicle applications. The same or similar systems can be found in present passenger cars with diesel engine propulsion.

3.1.1 CR test bench

In order to study the fundamental phenomena of the hydraulic CR circuit the system was installed on a hydraulic test bench (Figure 14). Special care has been paid to ensure maximum flexibility in respect of the system setup; the bench allows easy and quick modification of the main hydraulic components. The principle design of the bench follows the modular layout of the CR system. Each component was mounted onto a separate frame and the connection points between the frames were kept to a minimum. In this way unwanted mechanical vibrations from, for example, the power unit were isolated to a great extent to a particular part of the hydraulic test bench.

The main components of the high pressure CR system are presented schematically in Figure 4 on page 21 and in the photograph of the actual test bench (Figure 14). The tank of the system, not shown in the photograph, is positioned above the other components in order to minimize any possibility of air entrainment during operation. Passing through a filter, a gear-type supply pump delivers fuel to the high pressure pump; the latter is a three-piston radial displacement design. Both pumps are driven by a standard three-phase AC electrical motor. To ensure constant rotational speed at all load conditions, the motor is controlled by an inverter. From the high pressure pump the pressurised fuel arrives at the rail through a high pressure connection pipe. Generally, the rail serves in CR systems as a storage or accumulator. As has been indicated earlier, the main purpose of this component is to provide a source of constant pressure during operation for all injectors. This also includes the minimization of unwanted oscillations in the system. The upstream end of the rail is sealed by a pressure sensor. Information on this usually resistive-type transducer is passed to the

electronic control unit (ECU), which controls a pressure regulator valve at the downstream end of the rail. Depending on engine load and other parameters, the rail pressure is automatically adjusted in the final application to the target injection pressure. The latter value is pre-defined through operation maps that are stored in the ECU [11, 35]. The characteristic frequency of the pressure regulator valve is reported to be about 1 kHz [2, 11]. Depending on the number of cylinders, the rail is equipped with several ports for connecting the accumulator volume with the fuel injectors. These latter can be categorised by the type of their design - piezo or solenoid controlled.

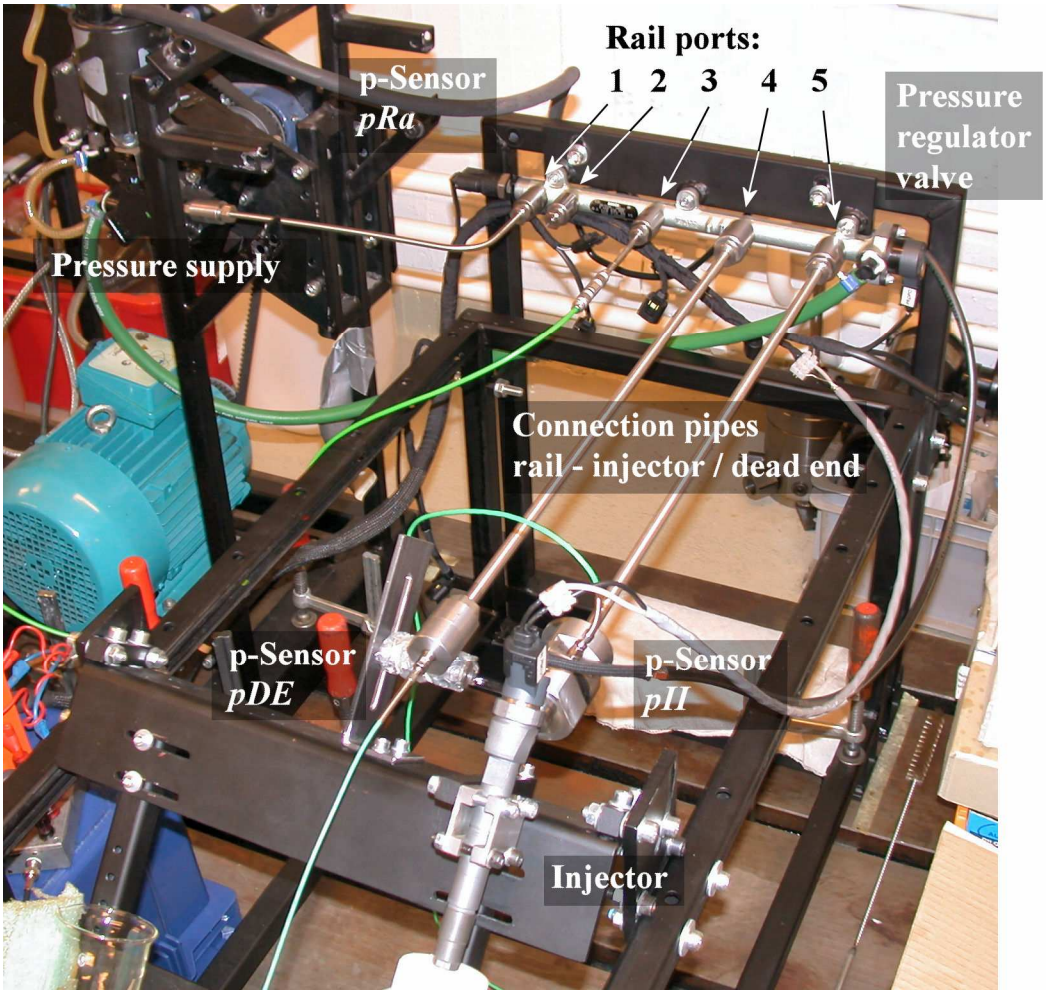

Figure 14. Test bench of the CR fuel injection system.

Not all rail ports are connected to fuel injectors in the present analysis. As presented in Figure 14, port one of the rail is used to connect the supply line to the accumulator. Port two is plugged. Through port three the instantaneous fluid temperature inside of the rail is recorded. Two high pressure lines are fitted to ports four and five of the rail. Both pipes are based on the same geometrical properties. The difference between the last two ports is that the high pressure pipe of the former port is equipped with a pressure sensor at the downstream end,

while a solenoid injector is mounted onto the latter high pressure line. Throughout this study the connection pipes between rail and injector or dead end, respectively, are of the main interest. In total, 9 geometrical variations of this pipe are considered during the experimental investigation. Figure 15 provides a schematic view of the utilised CR injector. This type of solenoid controlled injector is a typical representative of a needle lift steered injector [10]. Different to pressure steered injectors, needle lift controlled types are characterised by a constant pressurisation of the internal flow channels. The working sequence of a solenoid injector starts by switching on the current flow through the coil of the pilot stage. As a result, the pilot stage anchor and the attached ball valve are lifted. With a new flow passage open, pressurised fluid can escape via the A-nozzle. Because the Z-nozzle diameter is smaller than the A-nozzle diameter, the total net mass flow has a negative sign - the intermediate chamber

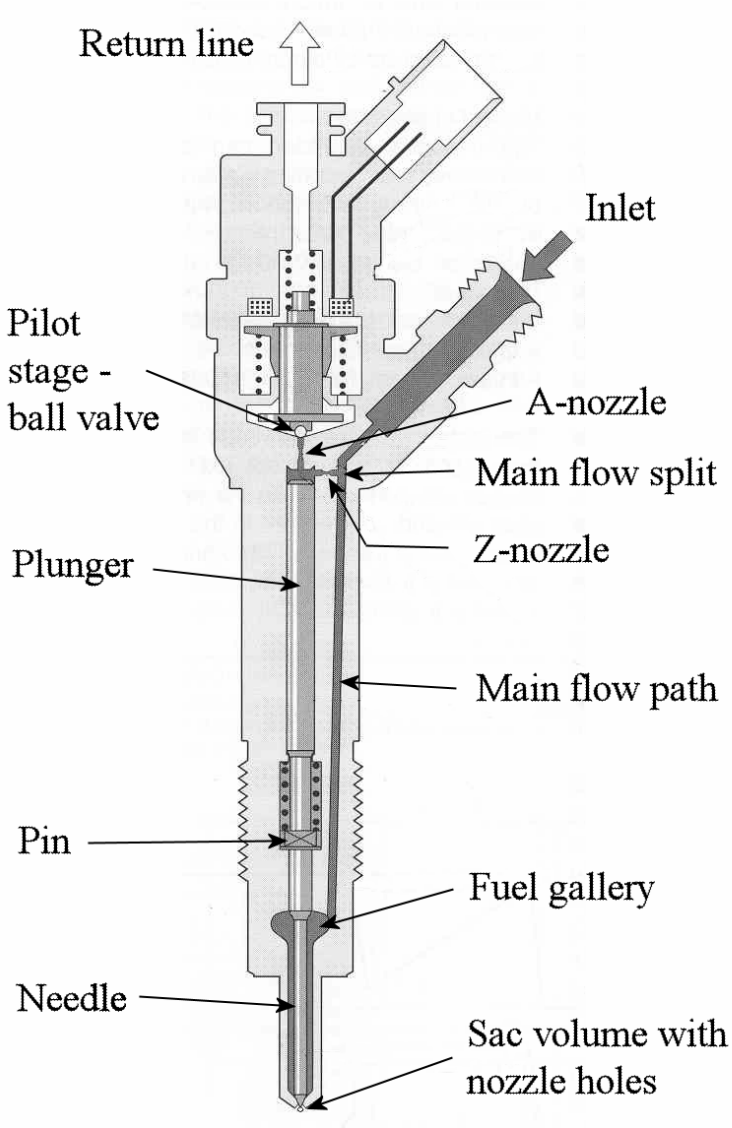

Figure 15. Schematic of solenoid injector [11].

is emptied quicker than it is filled-up again. This leads ultimately to a drop of static pressure above the plunger. At the same time, pressurised fluid acts on the needle ring areas in the fuel gallery and at the needle seat. As soon as the pressure force above the plunger is smaller than the fluid force from below, the unit of plunger, pin, and needle move upwards to open the main flow path through the injector. The injection is terminated again by releasing the solenoid current. The pilot ball valve closes and the pressure above the plunger increases to its initial value. As the plunger top side area is larger than the equivalent area of the needle, the needle moves back into its seat [11].

For the duration of the experimental measurements, Shell oil S-9365 was used as the pressure medium. This fluid is specially designed for calibrating fuel injection systems. It complies, amongst others, with the ISO 4113 and SAE J967D standards. The main properties are comparable to light diesel oils that are sold at European gas stations for end-consumers.

Altogether, six parameters were recorded per single measurement run. Firstly, the fluid temperature inside the rail was monitored by using a K-type thermocouple. Sensor calibration and all measurements were conducted within the range of 308 to 312 K. This temperature bandwidth describes the complete range from first to last measurement. As a general rule each measurement point was repeated multiple times. During such a repetition the temperature variation was less than 2 K. Secondly, four electrical signals were monitored. Data integrity was ensured by selecting a resolution of 16-bit and a sampling frequency of 250 kHz for each signal. One out of the four signals describes the injector current. As the test bench was controlled by a custom-made ECU [66], this signal served mainly for monitoring purposes.

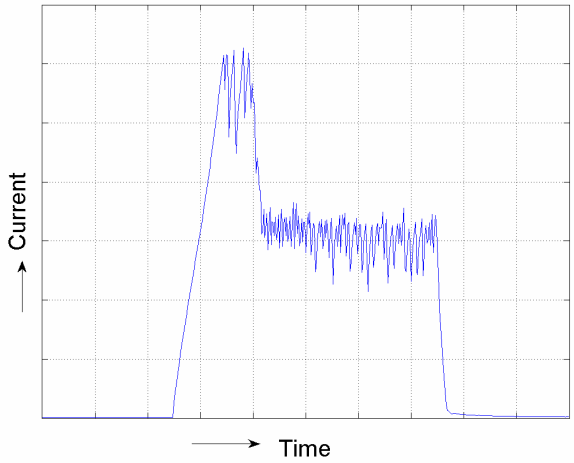

Figure 16. Typical injector current profile, single injection.

Figure 16 shows a typical plot of the injector current profile for a single injection event. Initially, the current is boosted to ensure rapid acceleration of the solenoid anchor and pilot ball valve, respectively. In the second stage only a hold current is applied, which finally drops at the end of the injection process. The other three electrical signals represent data from pressure transducers. One signal refers to the accumulator pressure *pRa*. It was measured by the build-in CR system rail pressure sensor. The second pressure transducer was mounted to the inlet of the injector. On first view it might seem more logical to place the transducer closer to the needle seat of the injector instead, as the oscillations originate from there. Then again, this task is exceptionally difficult due to the small dimensions inside of the injector and the high operating pressure. Secondly, and more importantly, a boring for the pressure sensor right next to the needle is likely to alter the flow field and the characteristics of the injector. The placement of the sensor at the injector inlet is therefore seen as a compromise between technical feasibility and data integrity. Throughout the thesis the data array of the injector inlet transducer is defined as *pII*. It should be noted that the connector for the injector inlet sensor increases the total distance between rail and injector. This means that the subsequently utilised parameter l_p for the pipe length defines the axial extension of the high pressure pipes alone. The downstream end of the high pressure line at port four represents a dead end for the pressurised fluid. Data from the sensor that has been attached to this line is denoted accordingly as *pDE*. The main purpose of this sensor was to study the transmission of pressure waves through the CR system. To be exact, *pDE* is the instantaneous pressure at the inlet of an imaginary injector that is affected through the injection at the adjacent port. Both the injector inlet pressure *pII* and the pressure at the dead end *pDE* were gauged by piezo-resistive high pressure transducers from Kistler, which were specially designed for measurements of fuel injection systems. In order to reduce random fluctuations, each measurement point was repeated a minimum of n = 20 times. A time span of 20 seconds or more was used between two consecutive measurement runs to allow the system to settle again to its original state. Figure 17 shows an example for a connection pipe length l_p = 400 mm, a diameter d_p = 2.4 mm, injection set pressure p_{set} = 1250 bar, and injection duration t_{inj} = 800 µs (single injection), the individual pressure histories at the injector inlet plus a curve that represents the average of, in this case, 20 data sets. Generally, the aforementioned injection duration is defined by the solenoid triggering times, as this parameter is controlled by the ECU. If not otherwise specified, all measured signals were filtered using a 4^{th} order Butterworth lowpass filter with a normalised cut-off frequency of 10 kHz [91].

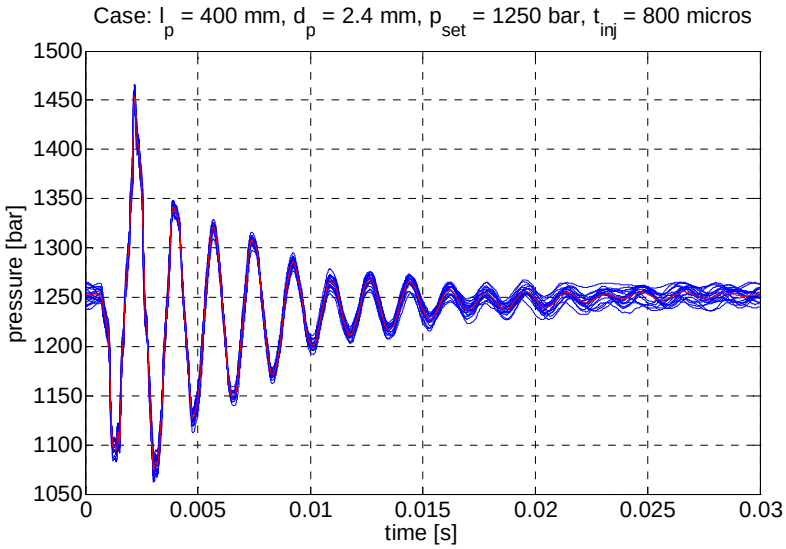

Figure 17. Example: repeatability of *pII*; 20 repetitions - original (blue) and average (red).

Figure 18 presents at an arbitrary set point (l_p = 200 mm, d_p = 1.6 mm, p_{set} = 1500 bar, and t_{inj} = 1000 µs) a comparison of the three pressure histories *pII*, *pDE*, and *pRa*. The dashed vertical lines indicate the start and end of the single injection event.

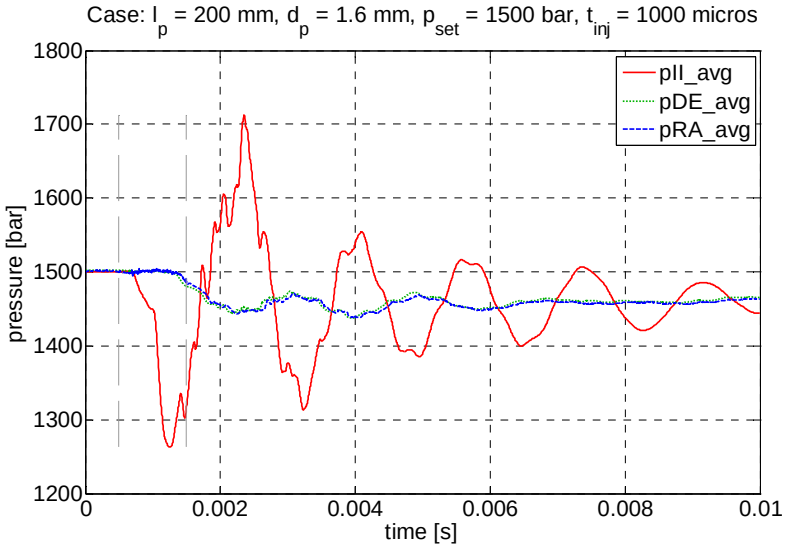

Figure 18. Comparison *pII*, *pDE*, and *pRa* at example set point

Based on this example figure, it is obvious that the pressure oscillation at the injector inlet is the most critical one. The pressures *pDE* and *pRa* also show some fluctuation, but at a significantly reduced intensity. Indeed, for the given case, that is, if the injection pressure is high and the injection duration long, the foremost impact on the latter pressure values is generally given by the drop of mean pressure below the initial set pressure. As a consequence, if not otherwise specified, the discussion of the subsequent following result presentation focuses mainly on the pressure history at the injector inlet. The last and sixth parameter that

was recorded during the measurements was the amount of injected mass. Analogous to the particular geometrical and flow field characteristics inside of the injector, the emerging diesel spray that exits the injector nozzle holes is commonly very complex. Accordingly, the instantaneous measurement of the injected mass is not trivial. In fact, at present only a few tools and methods are available (for example [1, 68]). Time-accurate knowledge of the injected fuel amount is, however, not mandatory for the analysis of the hydraulic CR circuit. Consequently, mass measurement was based on the weight variation of a closed container volume into which the fuel was injected; the measurements themselves were conducted by using a high precision laboratory scale. To minimise the impact of random fluctuations, the injected mass per injection is calculated as the average of total mass over the number n of repetitions. For the analysis of double injections, the explicit injection duration t_{inj} for both events was chosen to be identical. As a result, the mass of the second injection can be calculated as the difference of total mass minus the mass quantity for a single injection event. If the subsequent analysis refers to injected volume instead of injected mass, the volume is calculated as the ratio of weighed mass over the fluid density, which is based on data from the state equation of GT-Fuel.

3.1.2 Pressure signal prior to injection

In order to evaluate the system characteristics prior to an injection, the presentation of the measurement results starts with an analysis of the frequency content of the rail pressure signal at steady state conditions. For this analysis, and all frequency studies that follow in subsequent chapters, a discrete Fourier transform (DFT) was used to extract the main frequencies from the data set at hand.

The continuous Fourier transform for non-periodic functions is defined by [21]:

$$G(\omega) = \int_{-\infty}^{\infty} g(t) \cdot e^{-i \cdot \omega \cdot t} dt \tag{101}$$

With the angular frequency related to the frequency:

$$\omega = 2 \cdot \pi \cdot f \tag{102}$$

The integral in the above equation is approximated in the DFT by a sum of equally spaced rectangles. By defining the total number of rectangles with N and the time step size with Δt, it follows that [6, 54]:

$$G(k) = \sum_{n=0}^{N-1} g(n \cdot \Delta t) \cdot e^{-2 \cdot \pi \cdot i \cdot \frac{k \cdot n}{N}} \tag{103}$$

With the domain defined as:

$$k = 0 \ldots N - 1 \tag{104}$$

The variables n and k are indices in the time and frequency domain, respectively. The link between the frequency and the discrete frequency index is given by:

$$f = k \cdot \frac{f_s}{N} \tag{105}$$

In practice, the mean value of the original data was subtracted from the real values to form a data array that varies around zero. To enhance the frequency resolution, the data was extended in a second step with zeros. Finally, the FFT-algorithm of Matlab[1] was employed to compute the main frequencies of the source data.

The sampling frequency f_s was set to 250 kHz for all measurements. By combining this number with the explicit duration of 1 s for this particular investigation, N = 250000 samples were recorded for each set point. The latter figure has been increased by zero padding, which leads to a total sample number of 262144 or 2^{18}, respectively. Based on equation (105), the frequency resolution becomes 6 rad/s, or about 1 Hz. During this and all other measurements, the electrical motor was driven at a constant speed of 600 rpm. As the high pressure pump is designed as a three-piston radial displacement pump, it is to be expected that one or more of the main excitation frequencies are based on the pump characteristics.

Equation (106) defines the excitation frequency due to pump rotation:

$$f_P = \frac{600 rpm}{60 \frac{s}{\min}} \cdot 3 = 30 Hz \tag{106}$$

[1] The MathWorks, Inc., version 7.2.0.232 (R2006a)

Figure 19 to Figure 24 confirm that at steady state conditions, that is, before the actual injection, the main oscillation frequency is based on the irregular fluid displacement in the three-piston high pressure pump.

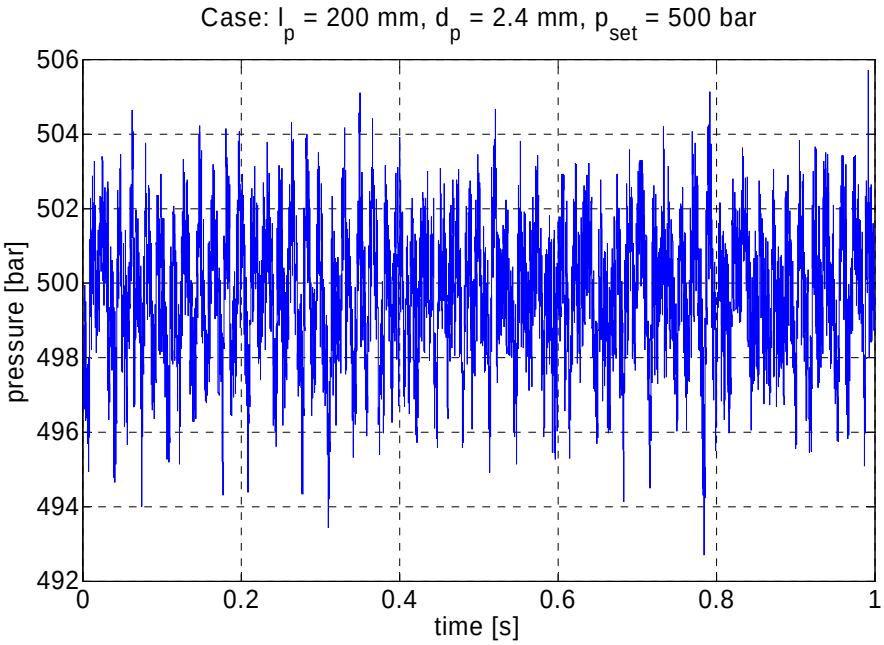

Figure 19. Pressure signal *pRa*, p_{set} = 500 bar.

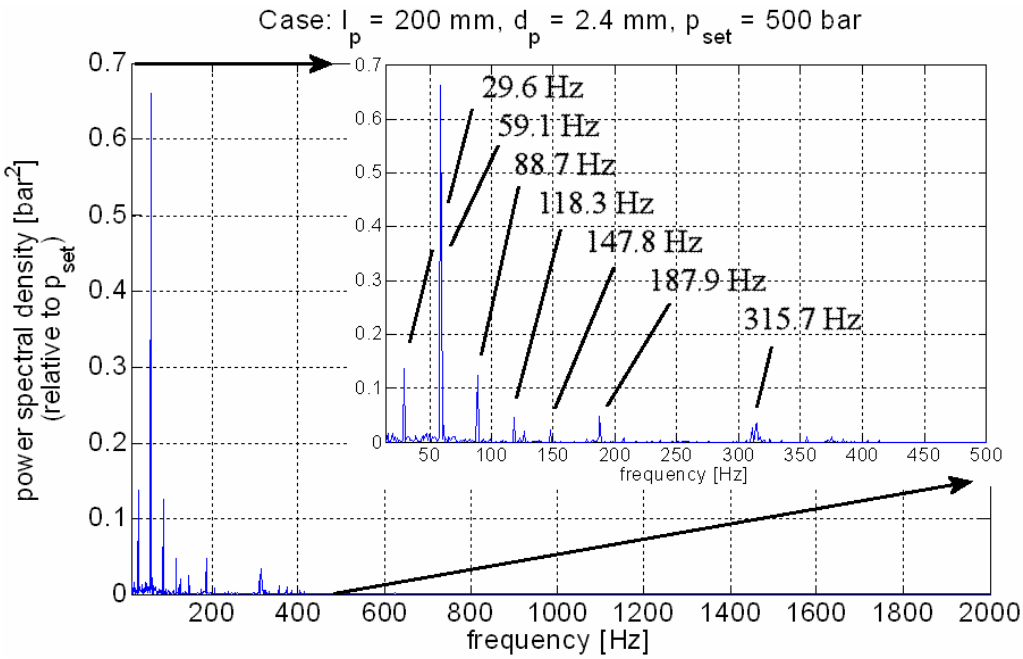

Figure 20. Power spectral density, *pRa*, p_{set} = 500 bar.

Figure 19 presents for a setup of l_p = 200 mm, d_p = 2.4 mm, and p_{set} = 500 bar the signal of the rail pressure transducer *pRa*. It should be noted that this curve is not based on averaged data, but on an arbitrarily selected curve of the measurement series.

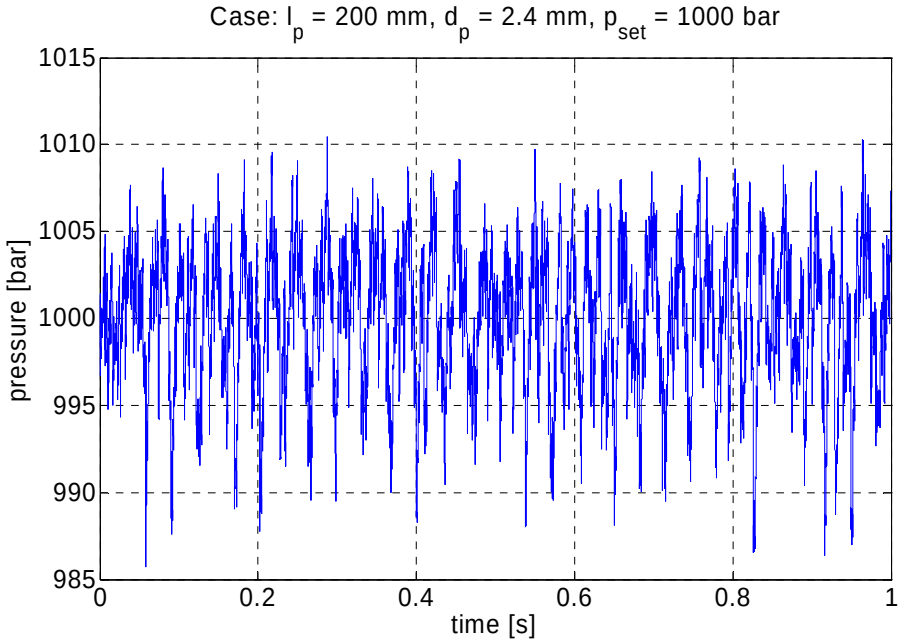

Figure 21. Pressure signal *pRa*, p_{set} = 1000 bar.

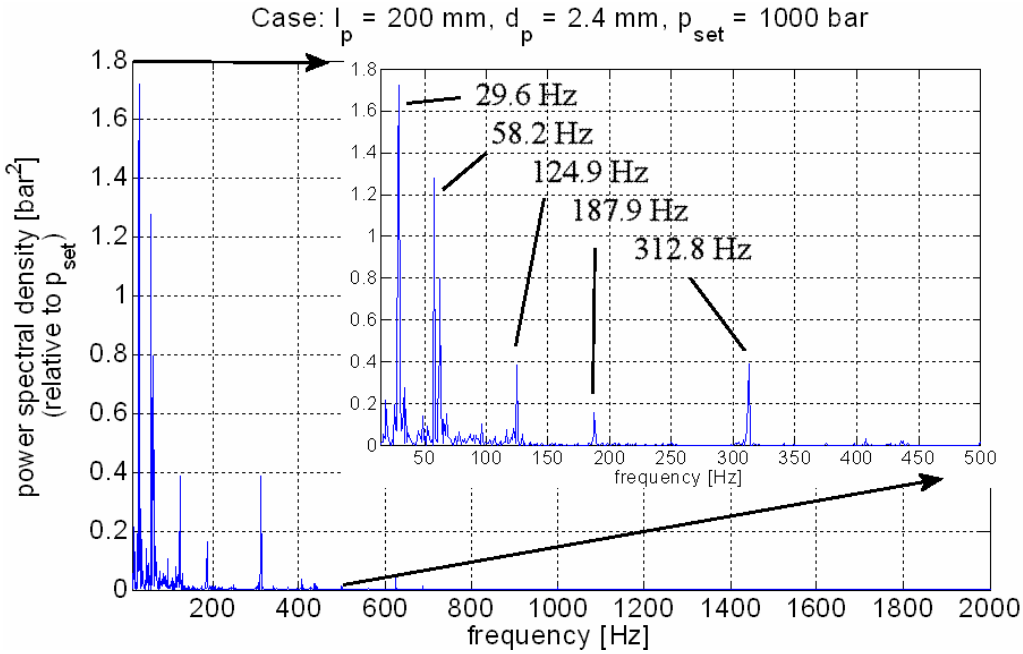

Figure 22. Power spectral density, *pRa*, p_{set} = 1000 bar.

The plots in Figure 21 and Figure 23 are analogous to Figure 19, but differ in the utilised set pressure, p_{set}.

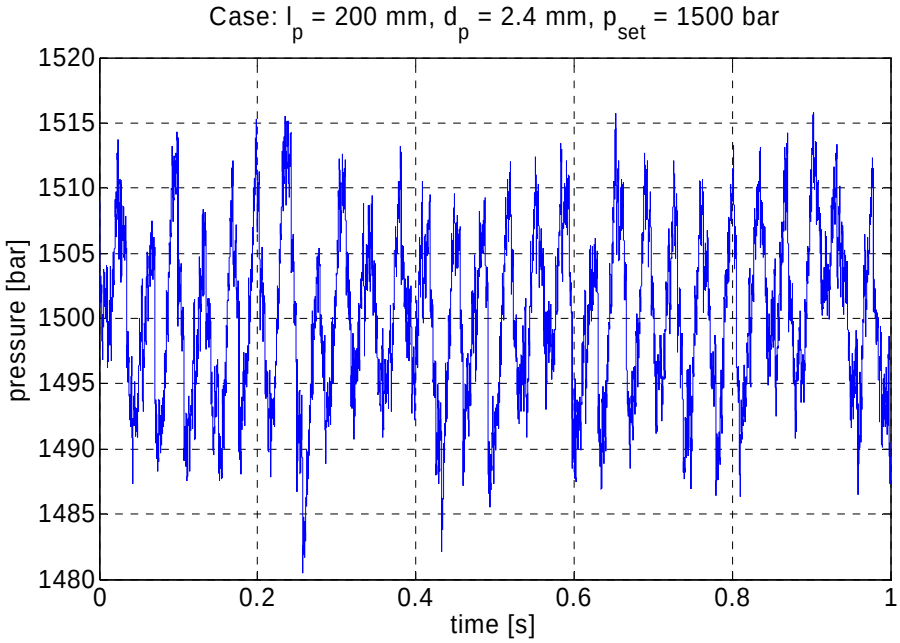

Figure 23. Pressure signal *pRa*, p_{set} = 1500 bar.

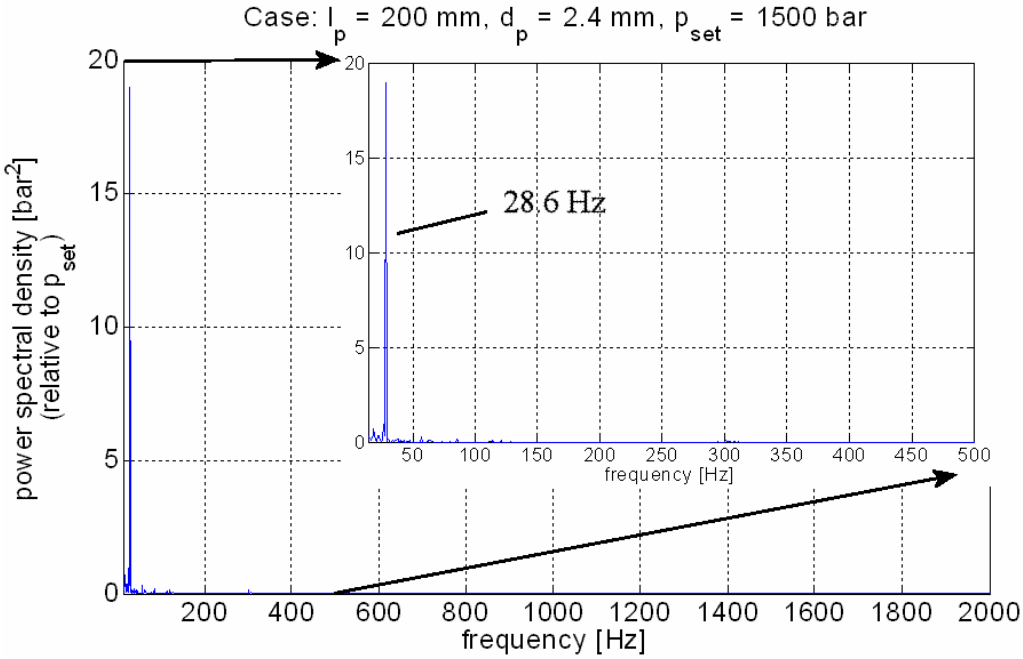

Figure 24. Power spectral density, *pRa*, p_{set} = 1500 bar.

Firstly, the analysis of the raw data confirms that the main oscillation at steady state is driven by the high pressure pump. Figure 20, Figure 22, and Figure 24 show that the main frequency consists of the pump excitation frequency f_P or an integer multiple of it. Secondly, it is interesting to note that the number of significant frequencies diminishes when the set pressure is increased. As, for example, Figure 24 indicates, only the base frequency appears in the *pRa* signal at p_{set} = 1500 bar. One explanation for this might be found in the dynamic behaviour of

the individual components involved. It seems that at lower pressure levels the system response is amplified, which leads to the appearance of several harmonics. For high injection pressures, on the other hand, the harmonics are literally filtered out, which indicates that the components oscillate less, or that the corresponding natural frequencies have shifted, respectively. Overall, the steady state frequencies are confined to oscillations lower than 500 Hz. No proof has been found to indicate the appearance of earlier mentioned pressure regulator valve frequency at about 1000 Hz. Consequently, it is concluded that for this measurement setup the pressure regulator valve characteristics are of minor importance.

3.1.3 Impact of injector mounting point on measured variables

As has been explained in chapter 3.1.1, only one injector was mounted onto the high pressure rail. If not otherwise specified, the test bench setup corresponds to specifications that have been made previously. The downstream end of the high pressure line at port 4 was sealed by a pressure transducer (*pDE*); the fuel injector was attached at the end of the equivalent pipe at port 5 (see, for example page 56, Figure 14). Ideally, it is expected that any other mounting point of the injector to the rail leads to the same findings. This condition is, indeed, elementary for the proper function of the high pressure rail concept.

The present study investigates the validity of this general assumption by comparing the pressure histories of *pII* and *pDE* as a function of injector rail mounting port, injection pressure p_{set}, and duration of the single injection t_{inj}. As an alternative to the default setup, the dead end and the injector pipe connections were switched, that is, the injector was mounted onto the end of port 4 and the pressure sensor *pDE* at the downstream side of port five. Only single injection events were considered. The injection pressure was varied between 750, 1000, and 1250 bar; the injection duration was set to 600 µs or 800 µs. The geometry of the connection pipes was defined by l_p = 400 mm and d_p = 2.4 mm.

The results that are presented in Figure 25 to Figure 28 verify that it is irrelevant for the pressure history at the injector inlet or the dead end to which port the injector is actually connected. Secondly, neither the injection pressure nor the injection duration has an impact on the pressure oscillation that is potentially related to the injector location. Therefore, it is concluded that it is possible to analyse the hydraulic circuit of a high pressure CR system by connecting only a single injector.

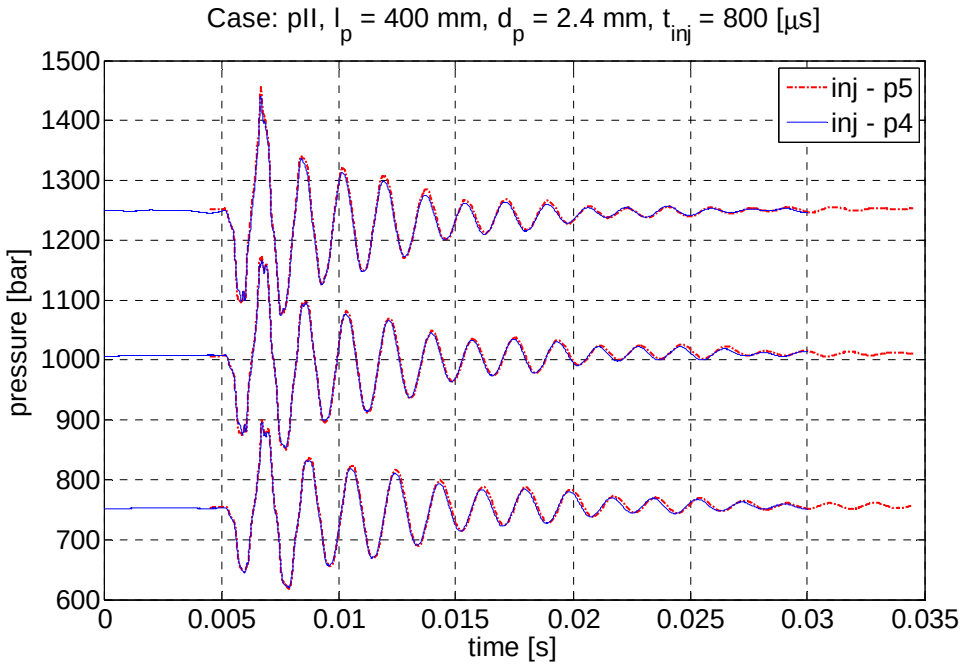

Figure 25. Comparison injector mounting port 5 vs. 4, t_{inj} = 800 µs, signal: *pII*

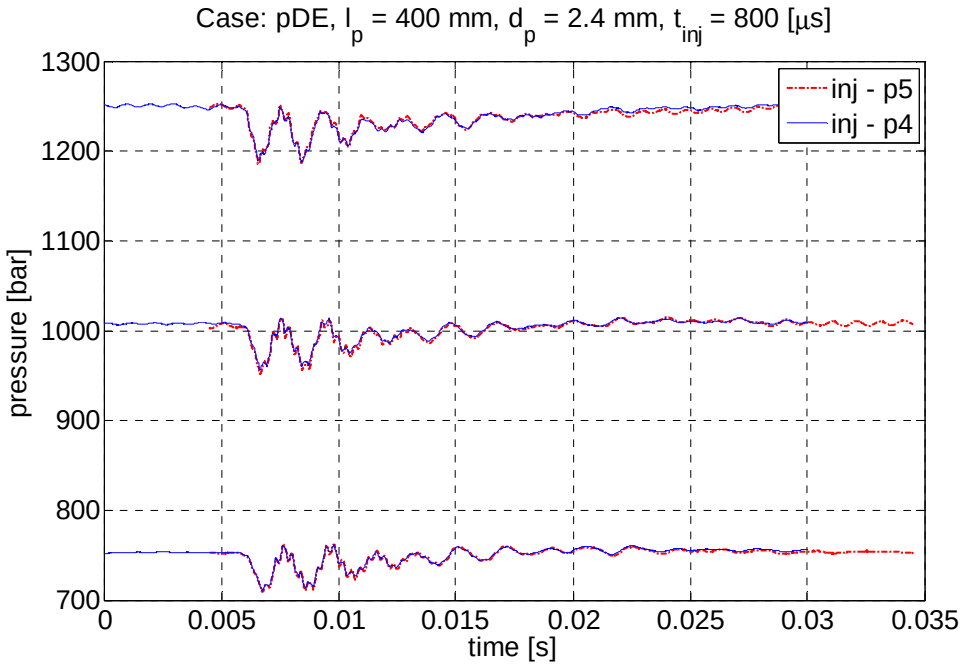

Figure 26. Comparison injector mounting port 5 vs. 4, t_{inj} = 800 µs, signal: *pDE*

In analogy to Figure 18 on page 60, the two sets in Figure 25, Figure 26 and Figure 27, and Figure 28 underline the statement made earlier that the pressure fluctuation of *pDE* is, in general, much lower than the one of *pII*. Both Figure 26 and Figure 28 indicate that the pressure deteriorates for large p_{set}. The main discrepancy is, in fact, caused by the drop in system pressure, which gradually recovers to its initial state after a few milliseconds.

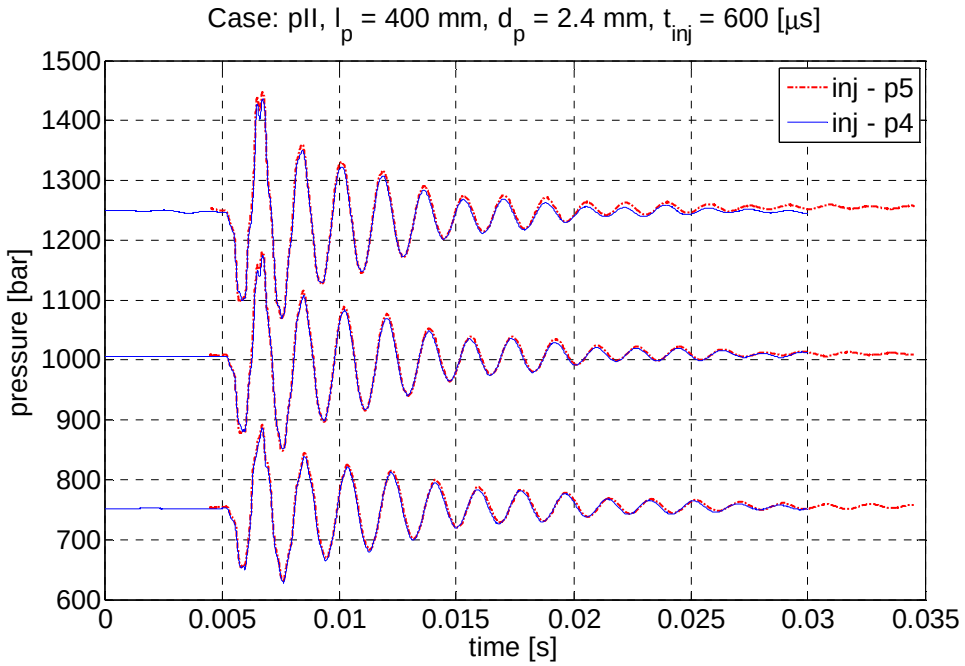

Figure 27. Comparison injector mounting port 5 vs. 4, t_{inj} = 600 µs, signal: *pII*

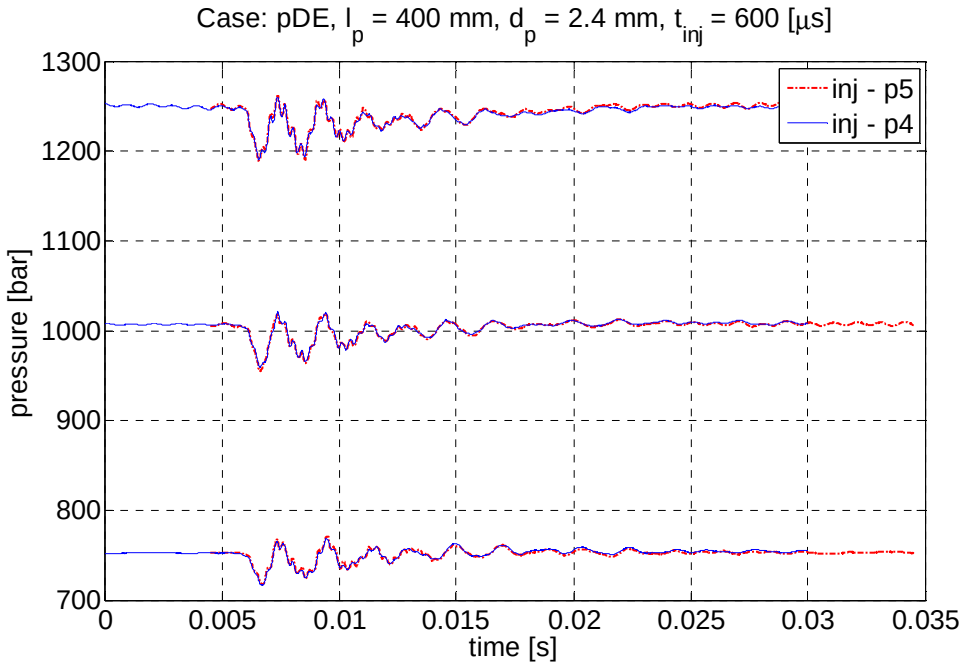

Figure 28. Comparison injector mounting port 5 vs. 4, t_{inj} = 600 µs, signal: *pDE*

3.1.4 Parameter study for single injection event

The connection pipe between rail and fuel injector is seen as a crucial part of a CR system. Most ideally the connection behaves neutrally in respect of the injection process, that is, it simply delivers fuel from the high pressure reservoir to the consumer. Yet, reality shows that the geometrical characteristics of the connection pipe are, in fact, part of the overall dynamic

behaviour of the system. As a rule of thumb, manufacturers of CR systems claim that the connection pipes should be kept as short as possible in order to minimise any unwanted effects [11]. For the same reason, it is argued that the pipes to each injector should have identical lengths [35]. Recent research results from Catania et al. [28] show, however, that it might be actually advantageous to use different pipe configurations. As they investigate a new CR concept, the researchers emphasise that it is actually crucial to consider the alternating dynamics of the connection pipes for achieving optimum performance. Finally, it might in some cases not be possible to use very short connection pipes; on the one hand, the engine head and rail layout enforce a minimum pipe length. On the other hand, the dimensions of the complete engine may require particular solutions for linking the fuel accumulator with the injectors. Although this study is carried out on a CR system for small high speed diesel engines, it is very likely that analogous correlations can be found also for larger engines, for example, medium speed engine types, due to their similarity.

In the present investigation, 9 different connection pipe geometries were studied for the high pressure line between rail and injector and dead end, respectively. Each pipe configuration was measured at 5 injection pressures and 4 injection times. Only single injections were considered at this time. As summarised in Table 1, the measurement setup consisted of a total of 180 configurations.

Table 1. Summary of experimental connection pipe parameter study.

Injection pressure p_{set} [bar]		500, 750, 1000, 1250, 1500		
Injection duration t_{inj} [µs]		400, 600, 800, 1000 (only single injection)		
Temperature range [K]		308 to 312		
Fluid		Shell calibration oil S-9365		
Type No. connection line rail to injector / dead end		length l_p [mm]		
		200	400	600
diameter d_p [mm]	1.6	7301353	7301354	7301359600
	2.4	7301343	7301344	7301349600
	3.2	7301233	7301234	7301239600

In line with the previous chapters, the main focus of this study is on the pressure history at the injector inlet, *pII*; the impact on *pDE* is discussed only briefly. Secondly, the amount of injected mass per injection as a function of connection pipe properties is presented.

Pressure history at the downstream end of the pipe parallel to the injector - *pDE*

Figure 29 and Figure 30 present for the intermediate connection pipe diameter (d_p = 2.4 mm) the data *pDE* at maximum injection pressure and as a function of connection line length. Pressure histories for smaller p_{set} are omitted at this point, as the maximum pressure setup represents the most extreme case.

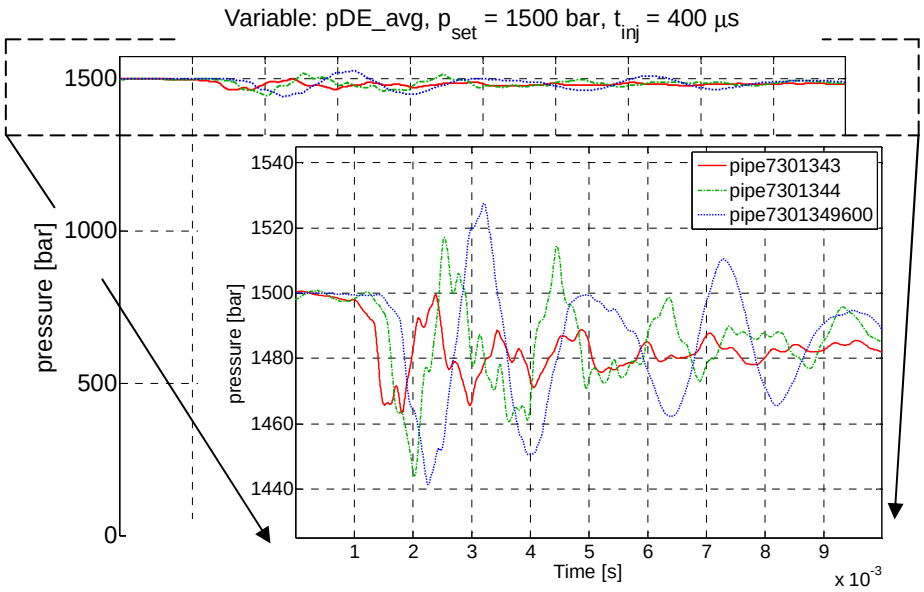

Figure 29. Comparison of *pDE* as f(l_p), d_p = 2.4 mm, t_{inj} = 400 µs.

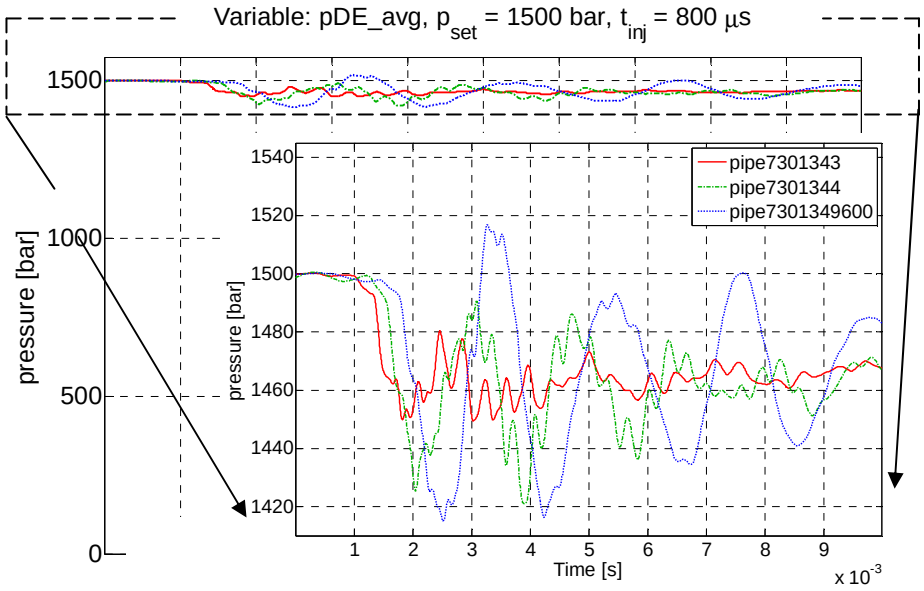

Figure 30. Comparison of *pDE* as f(l_p), d_p = 2.4 mm, t_{inj} = 800 µs.

It can be seen from these plots that the oscillation amplitude increases significantly for long pipes. In the case of short t_{inj}, the difference between the setup with l_p = 400 mm and l_p = 600 mm are minor (Figure 29). On the other hand, a long injection time tends to reverse this phenomenon by showing a closer relation between the cases l_p = 200 mm and l_p = 400 mm (Figure 30).

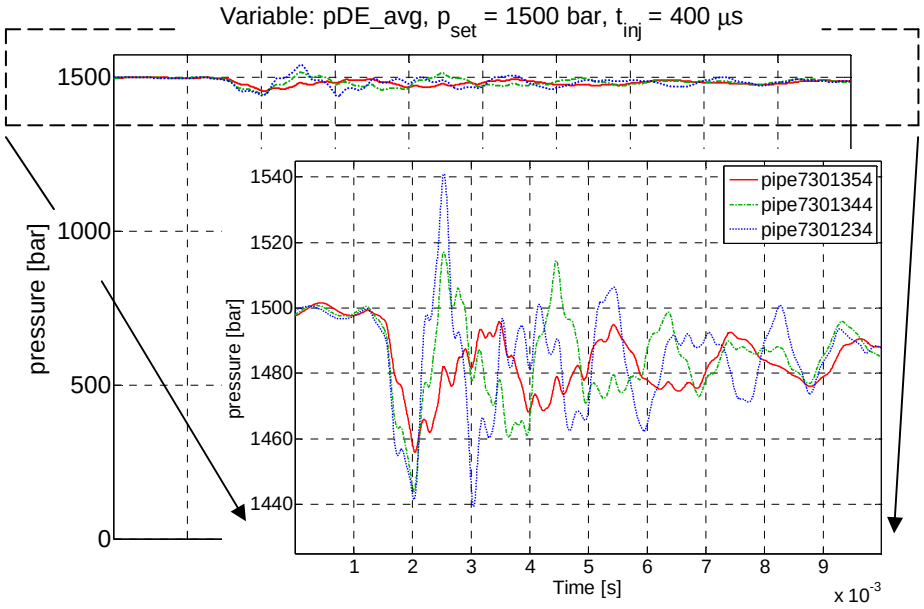

Figure 31. Comparison of *pDE* as f(d_p), l_p = 400 mm, t_{inj} = 400 µs.

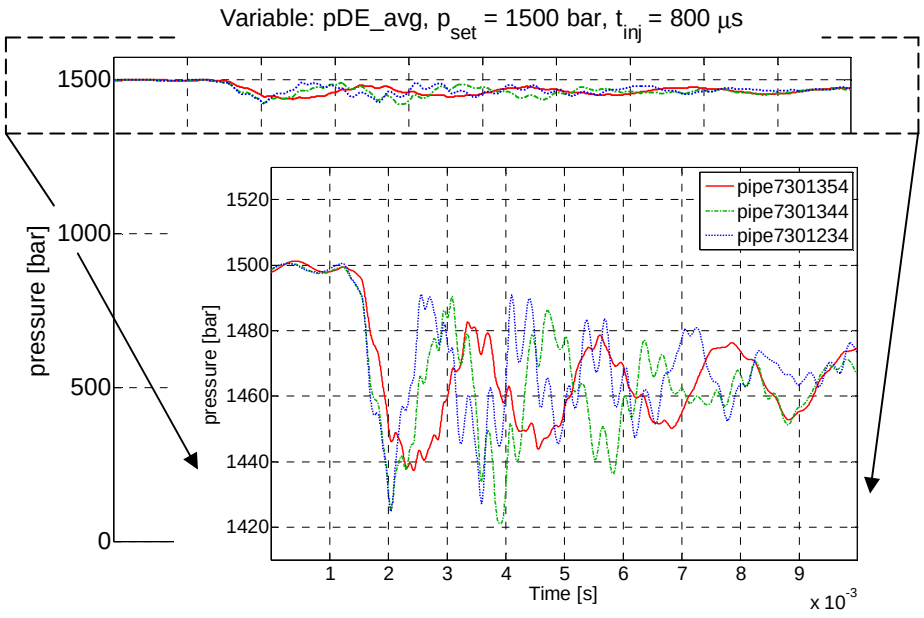

Figure 32. Comparison of *pDE* as f(d_p), l_p = 400 mm, t_{inj} = 800 µs.

Figure 31 and Figure 32 are similar to the previous two graphs, but compare the impact of the pipe diameter d_p on *pDE*. The results indicate that for long injection times the difference in

oscillation amplitude is small only. Then again, if an injection duration t_{inj} = 400 µs is used, Figure 31 shows a noticeable increase in oscillation amplitude for large d_p.

Pressure history at injector inlet - *pII*

Altogether, the pressure history at the injector inlet (*pII*) shows similar trends to the data of the adjacent port (*pDE*). On closer examination, however, the differences are apparent. Firstly, the study of *pII* verifies that the oscillation amplitudes at the injector inlet are considerably larger than at the neighbouring port (*pDE*). On the other hand, if the injection time is very short, Figure 33 reveals that the connection pipe length has no effect on the extreme values of the oscillation. For p_{set} = 500, 1000, and 1500 bar all three curves indicate similar maxima and minima. The situation changes if the injection time is increased to 600 µs (Figure 34) or longer (Figure 35, Figure 36). As a rule, the case with l_p = 600 mm (pipe7301349600) shows the largest amplitudes, followed by l_p = 400 mm (pipe7301344) and l_p = 200 mm (pipe7301343). It is interesting to note that the shortest connection pipe causes the largest variation of amplitudes as a function of injection duration. This is particularly true for a large injection pressure, such as, for example, p_{set} = 1500 bar. All four figures support the general conception about the frequency of the individual oscillations. The characteristic time constant of the oscillation is directly related to the connection pipe length - the shorter the pipe, the higher is the oscillation frequency.

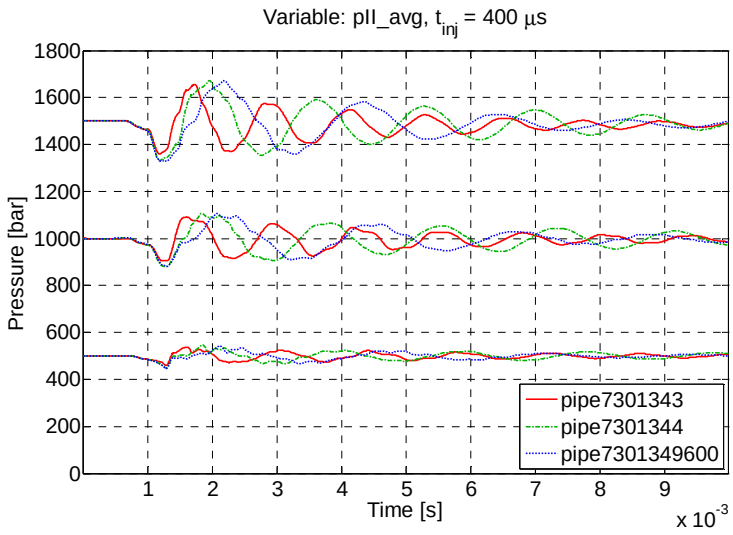

Figure 33. Comparison of *pII* as f(p_{set}, l_p), d_p = 2.4 mm, t_{inj} = 400 µs.

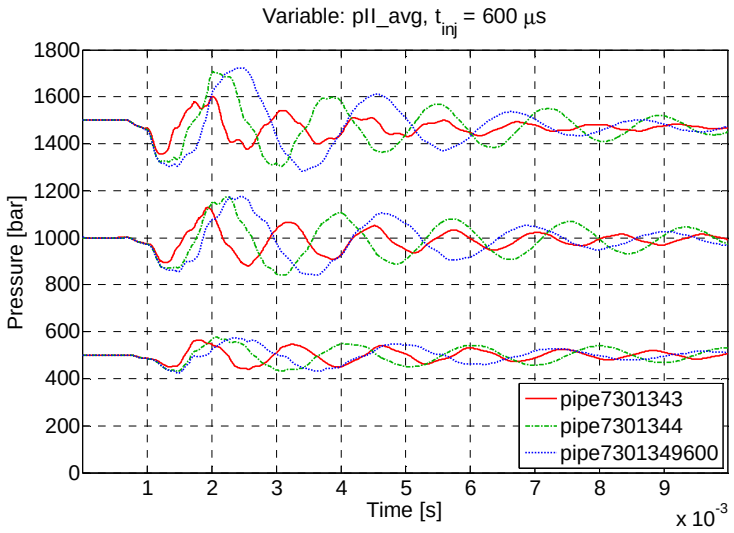

Figure 34. Comparison of *pII* as f(p_{set}, l_p), d_p = 2.4 mm, t_{inj} = 600 µs.

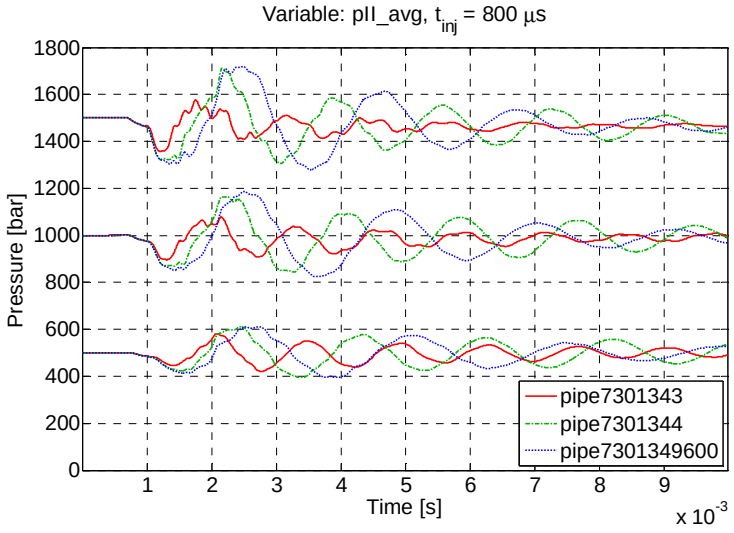

Figure 35. Comparison of *pII* as f(p_{set}, l_p), d_p = 2.4 mm, t_{inj} = 800 µs.

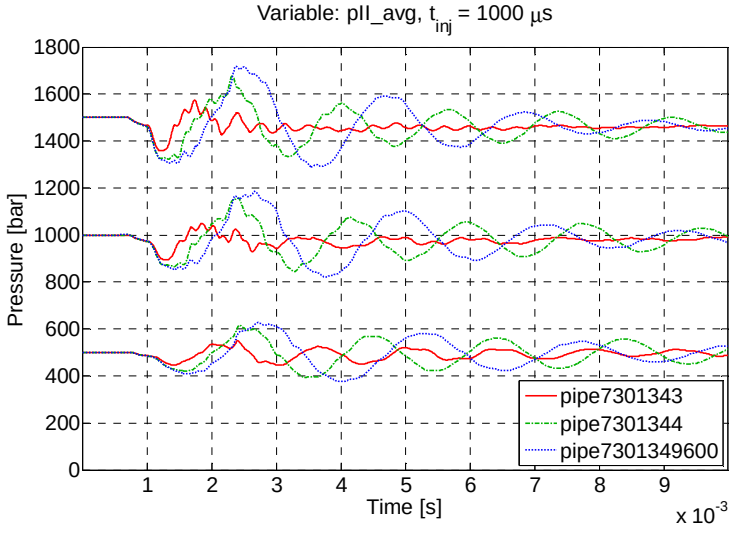

Figure 36. Comparison of *pII* as f(p_{set}, l_p), d_p = 2.4 mm, t_{inj} = 1000 µs.

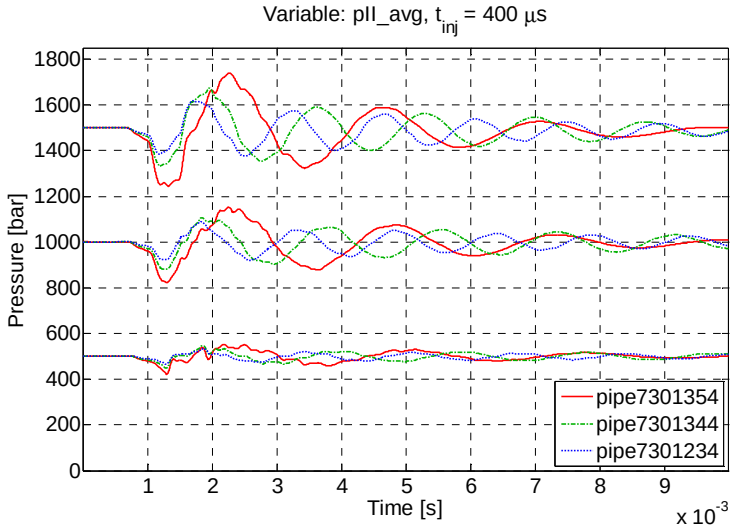

Figure 37. Comparison of *pII* as f(p_{set}, d_p), l_p = 400 mm, t_{inj} = 400 µs.

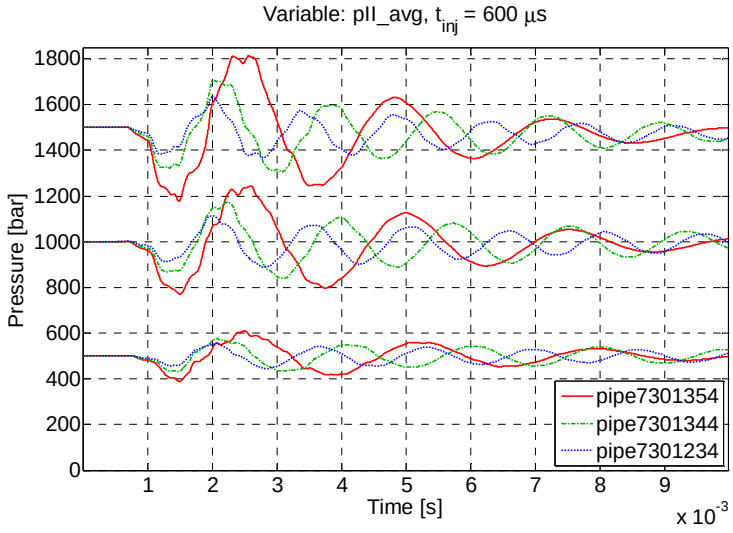

Figure 38. Comparison of *pII* as f(p_{set}, d_p), l_p = 400 mm, t_{inj} = 600 µs.

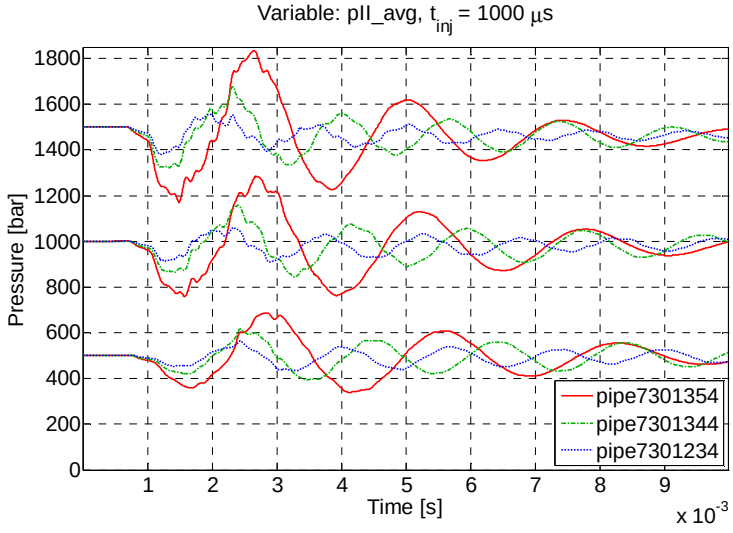

Figure 39. Comparison of *pII* as f(p_{set}, d_p), l_p = 400 mm, t_{inj} = 1000 µs.

Figure 37 to Figure 39 represent examples of the impact of the connection pipe diameter on the pressure variation at the injector inlet. It is worth mentioning at this point that only results are presented for the case l_p = 400 mm. The findings for the other two lengths (l_p = 200 mm, l_p = 600 mm) are, however, similar. In the graphs above it is most apparent that a small line diameter leads ultimately to a significant increase of oscillation amplitude. As before, this is especially true in the case of high injection pressures. The impact of the injection duration follows the previous trend, that is, the amplitudes at t_{inj} = 400 µs appear smaller than for longer injection times. With respect to the oscillation frequencies, Figure 37 to Figure 39 indicate that the time constant decreases along with an enlargement of the line diameter.

The following FFT plots in Figure 40 to Figure 43 exemplify for some selected measurement points the general valid correlation between frequency content of the oscillation versus the studied parameter. As in the previous statement, Figure 40 verifies that the frequency drops for increasing connection pipe length; in the given case about 460 Hz is found for the longest pipe (pipe7301349600), 558 Hz for l_p = 400 mm (pipe7301344), and around 780 Hz for the setup with the shortest pipe (pipe7301343). Overall, this trend is to be expected, since a single pulse requires more time in a long pipe to travel from the injector upstream to the rail and back than in its short counterpart. Figure 41, on the other hand, comes as a surprise. Although only the connection pipe diameter is variable, the graph shows a clear variation of the oscillation frequency. Indeed, all measurements of this study support a general trend, which claims higher frequencies for larger connection pipe flow cross-sections. In the case presented, the approximate frequencies are 380 Hz (pipe7301354), 553 Hz (pipe7301354), and 654 Hz (pipe7301354).

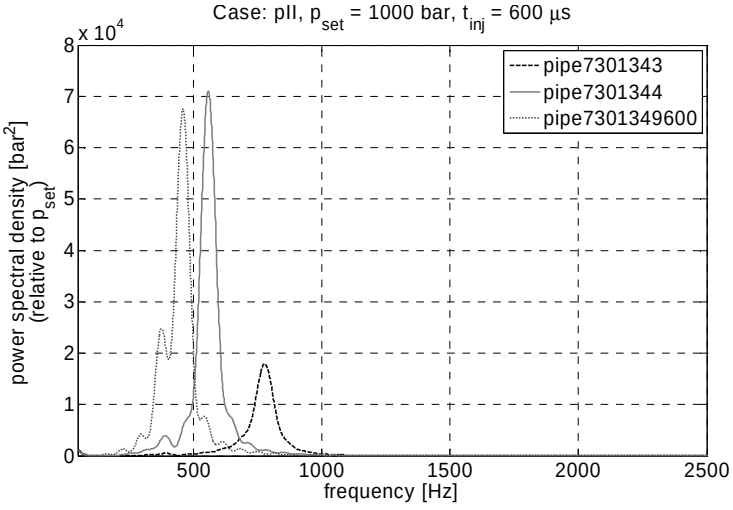

Figure 40. Example: comparison of frequency content of *pII* as f(l_p).

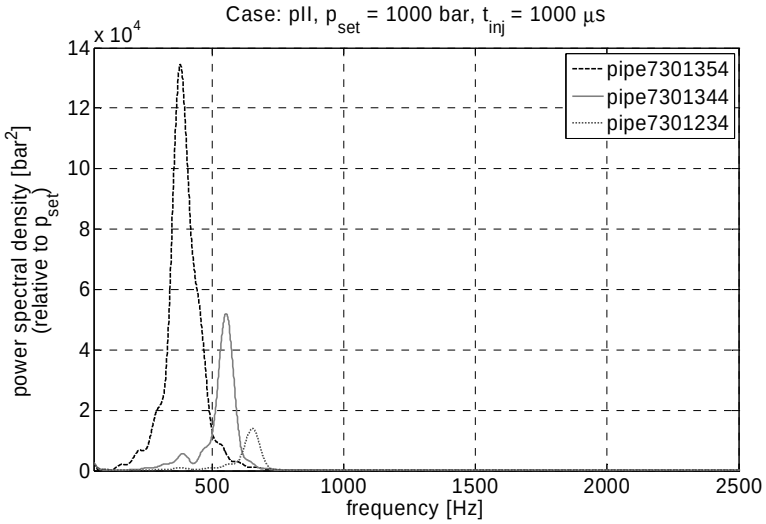

Figure 41. Example: comparison of frequency content of *pII* as f(d_p).

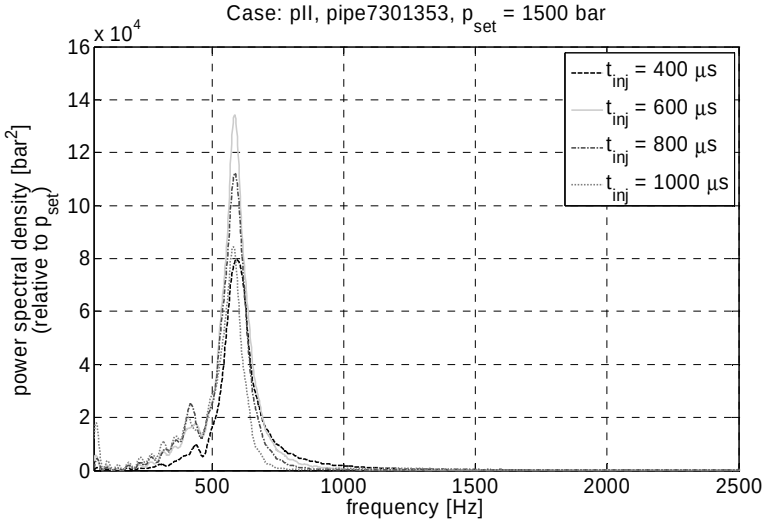

Figure 42. Example: comparison of frequency content of *pII* as f(t_{inj}).

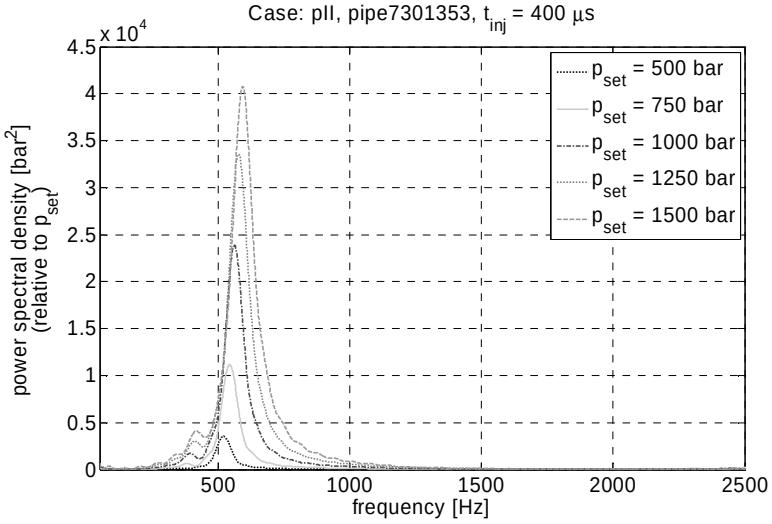

Figure 43. Example: comparison of frequency content of *pII* as f(p_{set}).

Figure 42 compares the impact of the injection duration on the frequency. The graph shows as an example that t_{inj} has no effect on the characteristic time constant of the oscillation. For the presented setup the power spectra reach a maximum at about 590 Hz. Finally, Figure 43 presents the variation of frequency as a function of injection pressure. Similar to the study of the connection pipe length, the plot confirms the expectation. The higher the injection pressure p_{set}, the higher is the oscillation frequency. This is due to the fact that the fluid density increases along with the pressure, which ultimately leads to a faster propagation of disturbances through the medium. The numerical frequency values for the setup in Figure 43 rise from 521 Hz for p_{set} = 500 bar to 544 Hz (750 bar), 563 Hz (1000 bar), 577 Hz (1250 bar), and 593 Hz for the highest measured injection pressure (1500 bar).

In the studied CR system the high pressure pump delivers fuel continuously to the rail. The excess fluid is returned to the low pressure circuit via the ECU controlled pressure regulator valve (see, for example, page 56, Figure 14). This ensures in theory that the pressure in the system is kept constant. In practice, the ideal can not be fully reached because of the fast transients and the physical behaviour of the finite fluid volume. By suddenly applying, for example, a pressure gradient on a fluid column that is initially at rest, the individual fluid particles are accelerated to equalize the newly introduced external force. This adaptation to the new condition does not happen instantly, but requires some time. Indeed, this inertial effect goes hand in hand with the fluid compressibility, that is, the density of the fluid is not constant, but varies as a function of external forces or static pressure. A fluid can therefore be seen as a dynamic system, which does not behave ideally in the dynamic sense, but introduces some additional oscillatory behaviour to the global system. Due to the finite size of the CR accumulator, the mean system pressure inevitably drops if the injector needle is opened. The following study analyses this phenomenon as a function of previously defined parameters.

A new output parameter is introduced, which is defined as the difference between set and mean pressure value:

$$\Delta p_{mean} = p_{set} - p_{mean} \tag{107}$$

The second parameter in equation (107), p_{mean}, is taken as the average of *pII* from injection start until t = 10 ms. Figure 44 below exemplifies the mean pressure drop for two different measurement configurations.

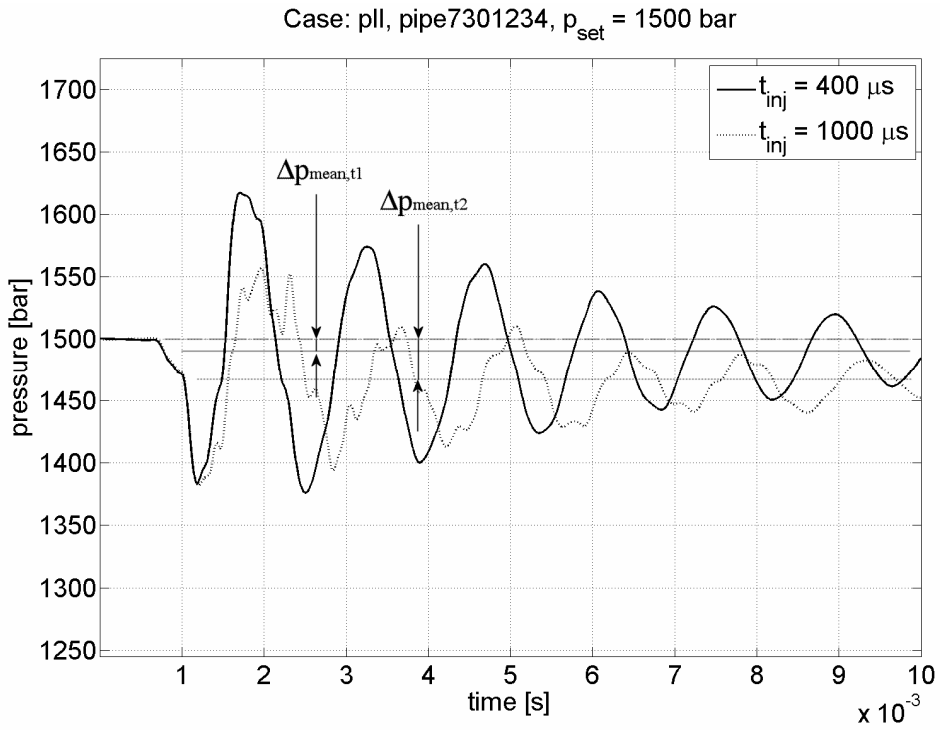

Figure 44. Example of mean pressure drop after injection.

It should be emphasised at this point that the absolute values of the mean pressure drop are not of importance, but rather its variation as a function of the other input parameters. By doing so, it becomes possible to study the principle behaviour of the system at hand. In the final engine application the pump speed is not fixed to 600 rpm, but varies with engine speed. In fact, higher rotational speeds are likely, which reduces the absolute drop of the system mean pressure level. The data presentation in Figure 45 to Figure 48 shows explicit values of Δp_{mean}. Figure 45 plots the results as a function of the set pressure and injection duration for a particular pipe configuration; Figure 46 to Figure 48 present the data for each measurement point as a function of the volume between rail port and injector inlet. The latter volume is defined as the distance between rail and injector, that is, pipe length l_p plus length of the *pII* sensor connector times the flow cross-section of the connection line. The case for t_{inj} = 800 μs is omitted here, as the findings fit well between the results for the slightly shorter (Figure 47) and longer injection time setup (Figure 48). Firstly, the results in Figure 46 to Figure 48 confirm that an increase of injection pressure generally causes a greater drop of the mean system pressure level after injection. The correlation between these two parameters is illustrated in a different way in Figure 45 for the case l_p = 400 mm and d_p = 2.4 mm. The graph indicates that the pressure drop and the set pressure are not linked linearly to each other. In fact, Δp_{mean} tends to increase disproportionately much for higher injection pressures. The same result, although less obvious, can be obtained by comparing in Figure 46 to Figure 48

for each pipe setup the relative change of the individual values (dots on vertical lines). In respect of the injection time, it can be summarised that a long needle opening time unavoidably causes a large drop of the system pressure. Interestingly, the impact of the injection duration on Δp_{mean} seems to be emphasised for short injection durations and high injection pressures. If, for example, the pipe configuration with the smallest volume is chosen together with an injection pressure of 1250 bar, Figure 46 indicates that Δp_{mean} equals about 10 bar at t_{inj} = 400 µs. The same setup at t_{inj} = 600 µs (Figure 47) and t_{inj} = 1000 µs (Figure 48) equals 19 bar and 31 bar, respectively. In other words, an injection time increase from 400 µs to 600 µs leads approximately to the same variation of Δp_{mean} as for a change from 600 µs to 1000 µs. The right half of Figure 45 underlines this finding by showing the lines for injection times longer than 400 µs somewhat separated from the case with the shortest injector activation time. The situation looks slightly different for low injection pressures. The results indicate that the Δp_{mean} variations are small for short injection periods, but increase gradually for longer injection times (see, for example, Figure 46 to Figure 48, p_{set} = 500 bar, t_{inj} = 600 µs to 1000 µs). Again, Figure 45 supports this statement by showing in the left half of the graph a slightly higher dot-density at short injection times. Concerning the impact of the geometrical properties pipe length and diameter on Δp_{mean}, the results predict only a minor correlation between the parameters. Eventually, it can be concluded that an increase of l_p leads to a small reduction of the mean pressure drop; similarly, a larger pipe diameter supports a slight decrease of Δp_{mean} if the injection pressure is set to a high level.

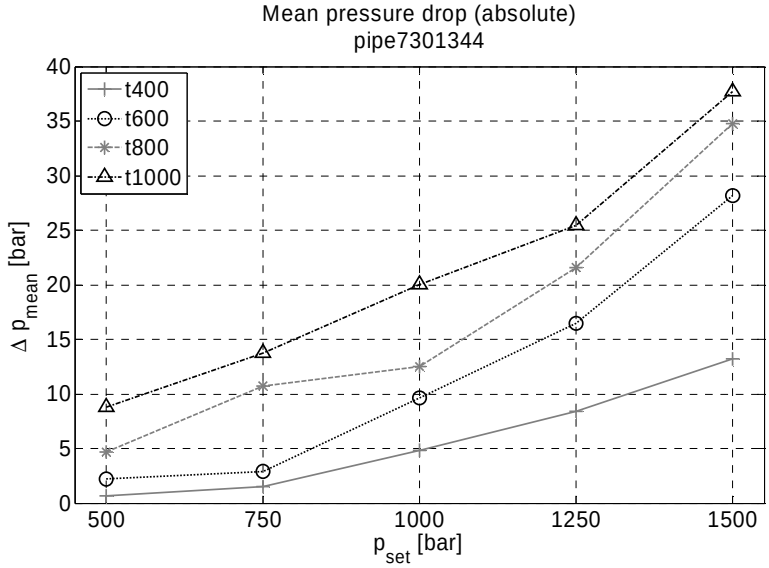

Figure 45. Example: Δp_{mean} as f(p_{set}, t_{inj}), l_p = 400 mm, d_p = 2.4 mm

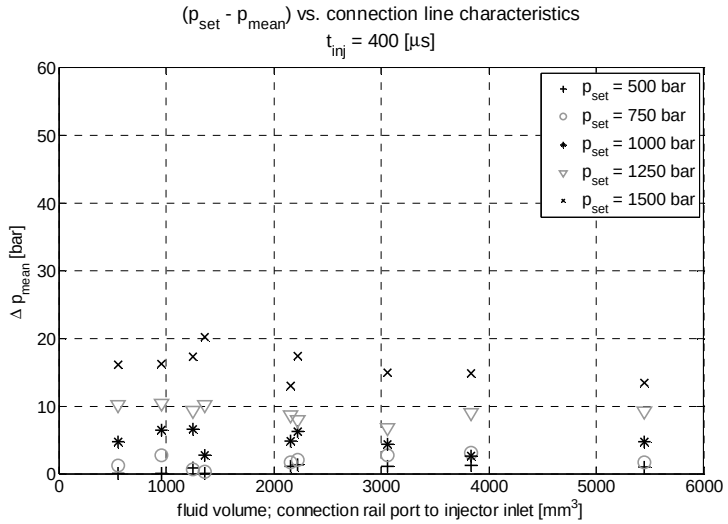

Figure 46. Δp_{mean} as f(pipe geometry, p_{set}), t_{inj} = 400 µs.

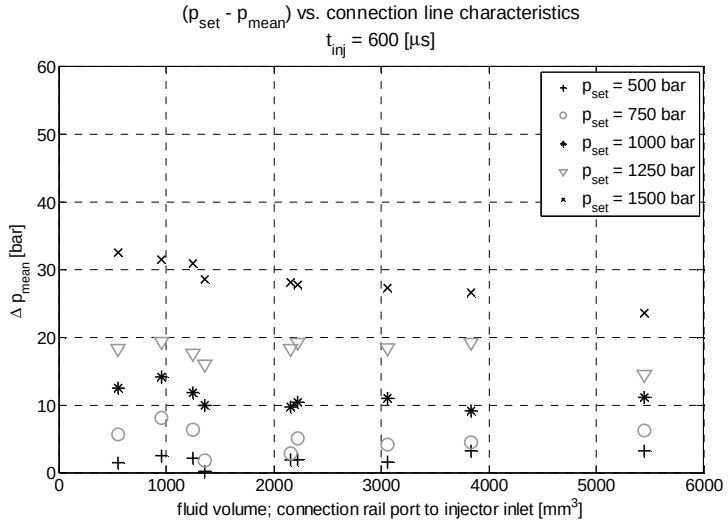

Figure 47. Δp_{mean} as f(pipe geometry, p_{set}), t_{inj} = 600 µs.

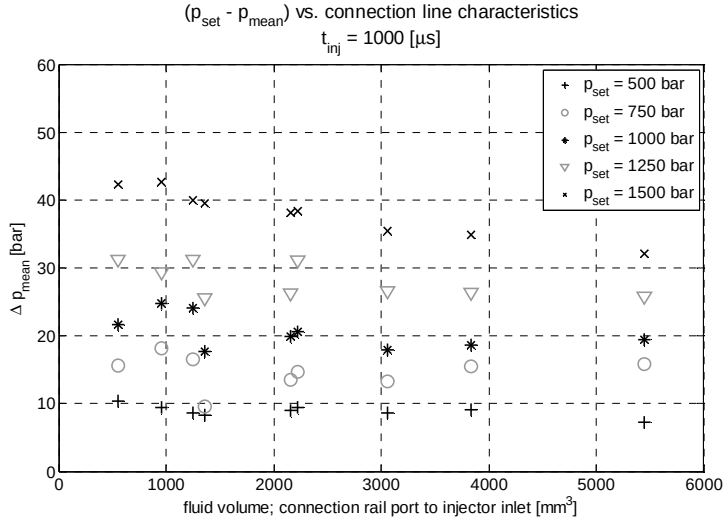

Figure 48. Δp_{mean} as f(pipe geometry, p_{set}), t_{inj} = 1000 µs.

Injected mass per injection

In Figure 49 to Figure 51 some typical results are presented that illustrate the effect of the input parameters on the mass of the injected volume per injection. In the introduction on page 18, equation (1) indicates the impact of the injection pressure on the mass per injection.

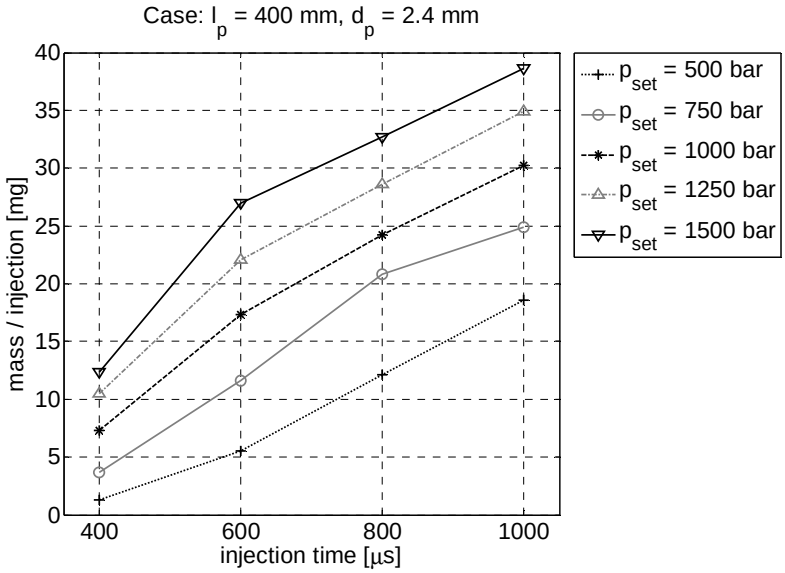

Figure 49. Example: plot of injected mass / injection as f(t_{inj}, p_{set}).

Accordingly, the appearance of Figure 49 is not surprising - the higher p_{set}, the bigger in general is the amount of fuel that exits the injector nozzle holes. It is in this context interesting to note that the slopes of the curves appear to be partially linear with respect to the injection duration. The vertical line at t_{inj} = 600 µs seems to separate the graph into two main regions. With the exception of the case p_{set} = 750 bar and t_{inj} = 800 µs, it can be seen that the curves of constant set pressure tend to be parallel for injection times longer than 600 µs. Two reasons might explain this phenomenon. On the one hand, it is likely that the fluid undergoes a partial or full phase transformation inside of the nozzle holes. The appearance of a choked flow condition can explain that the volumetric flow is independent of the pressure gradient over the injector. As cavitation onset does not occur instantly, but requires some time [80], it is conceivable that for very short injection times the flow conditions inside of the nozzle holes differ from setups with t_{inj} longer than 600 µs. Secondly, the injector needle might not be fully open during short injections. In practice, probably both phenomena appear in a combined manner, that is, partial needle opening and choked flow due to cavitation act together and lead to the finding that is presented in Figure 49. It should be mentioned at this point that the kink for p_{set} = 750 bar and t_{inj} = 800 µs is not affected by the connection pipe properties. Also the

remaining eight geometry studies (not presented here) show the same behaviour. Finally, it must be pointed out that the current number of 180 configuration points is probably not sufficient to reveal all details of the system. Further insight is therefore expected from the simulation model presented later.

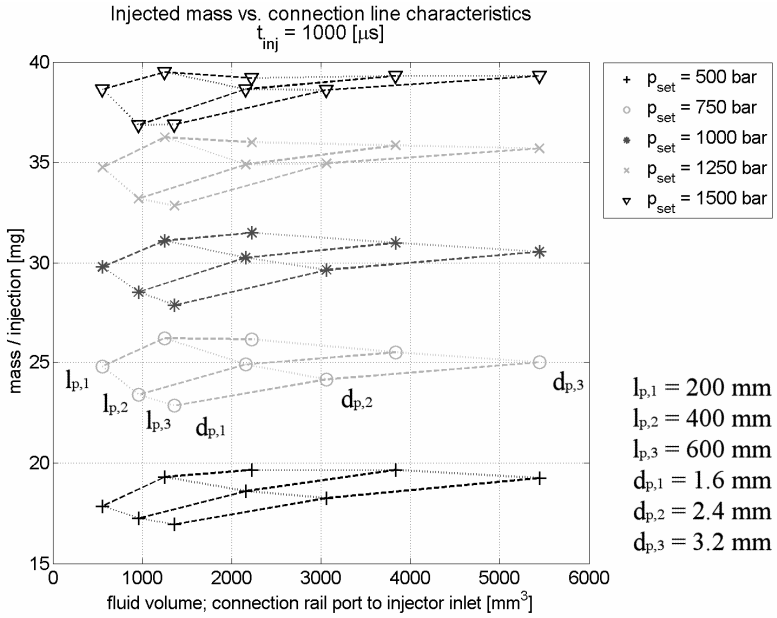

Figure 50. Mass / injection as f(pipe geometry, p_{set}) at t_{inj} = 1000 µs.

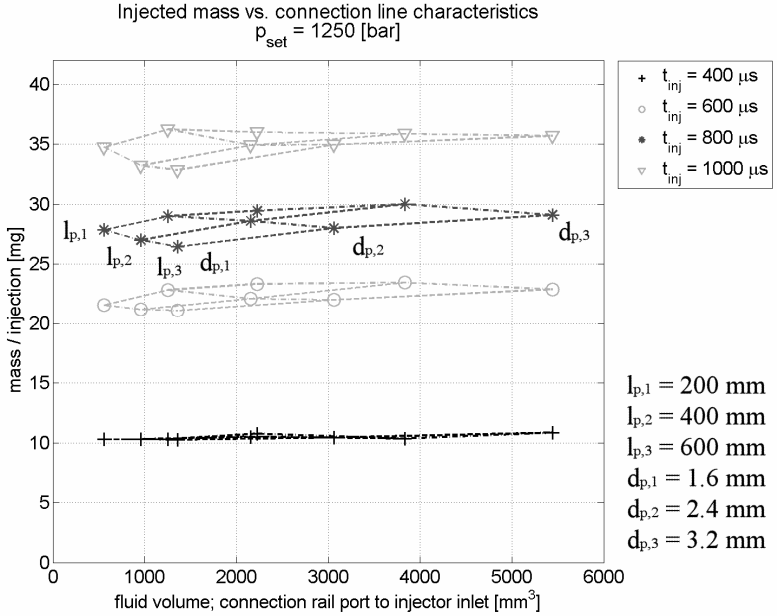

Figure 51. Mass / injection as f(pipe geometry, t_{inj}) at p_{set} = 1250 bar.

Figure 50 also refers to the injection pressure, but displays the impact of the pipe dimensions on the mass in a more clear way. Again, it has to be noted that the abscissa is defined by the total volume between rail port and injector inlet. For the case of a long injection time, the plot

indicates that a long connection pipe l_p supports a reduction of the injected mass per injection. This phenomenon is emphasised for small pipe diameters. In respect of the latter variable, it can be said that large diameters lead to higher injection rates than connections with a small value for d_p, particularly if long pipes are used. Figure 51 is equivalent to the previous plot, except that emphasis is set on the injection time. The figure shows a summary of measurement results at an injection pressure of 1250 bar. Firstly, it is confirmed that long injection times cause a high amount of injected fuel per injection. Figure 51 reveals, further, that the impact of the geometry on mass injected diminishes for short injection times. The latter finding is not fixed to a particular set pressure, but holds also for other setups (not shown here).

3.1.5 Analysis of double injection event

A measurement series that is based on a double injection strategy has been conducted to analyse the dynamic behaviour of the CR system and its impact on the injection rate per injection. All measurements were carried out on a setup with fixed geometrical properties, that is, l_p = 400 mm and d_p = 2.4 mm (same configuration as in Figure 14 on page 56). The injection pressure was kept constant at p_{set} = 1000 bar. In order to be able to make a statement concerning the injected fuel amount, both injection times were set to t_{inj} = 600 µs. The only variable in this study was defined by the injection period T_{inj}. Altogether, five configurations were considered: T_{inj} = 1.4 ms, 1.875 ms, 2.35 ms, 2.775 ms, and 3.2 ms.

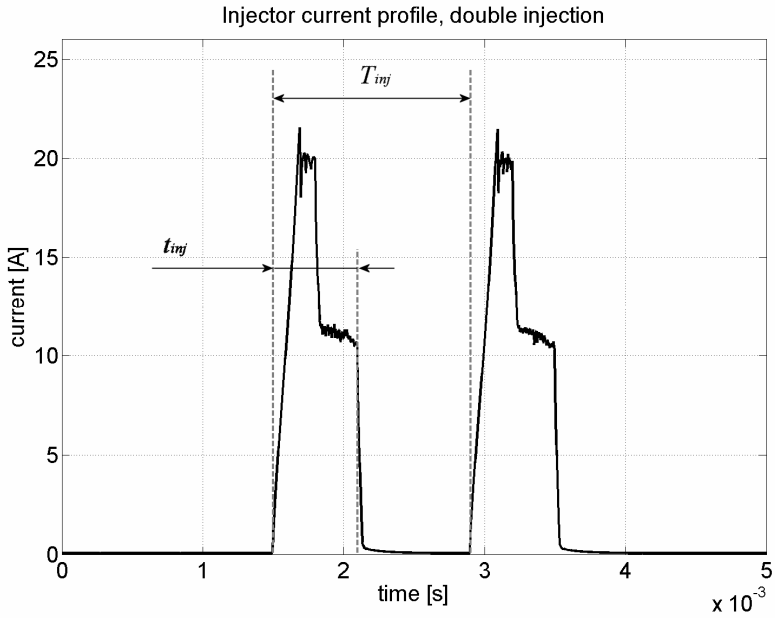

Figure 52. Definition of double injection event, injector current profile.

Figure 52 shows as an example the corresponding injector current profile with a definition for T_{inj} and t_{inj}. It is emphasised that each measurement point of this study represents an average of 30 individual runs. Generally, the selection of the injection period T_{inj} is dictated by the combustion process. For the given study T_{inj} is selected to represent extreme cases. In this sense, the setups that are based on T_{inj} = 1.4 ms and 3.2 ms trigger the second injection at the arrival of the first and second positive peak at the injector inlet. T_{inj} = 2.35 ms, on the other hand, defines the case with the second injection starting at the first negative amplitude of *pII*. Figure 53 illustrates the corresponding history of the pressure signals at the injector inlet. In comparison to the single injection case, it appears that a second injection that is in phase with the maximum peak considerably increases the resulting oscillation of *pII*. For an injection that starts together with a negative peak, the situation is slightly different. Although the intensity of the oscillation increases somewhat, its absolute change remains smaller than for the two previous cases. This is particularly true with respect to the minimum system pressure after injection.

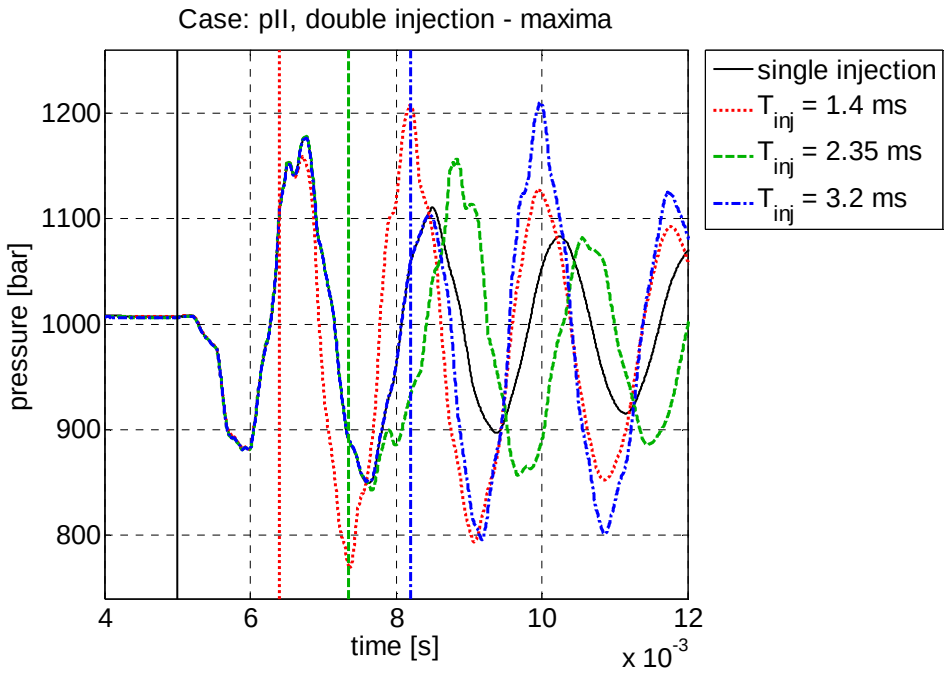

Figure 53. Pressure history *pII*, double injection - maxima (pipe7301344).

The setups with T_{inj} = 1.875 ms and 2.775 ms open the injector needle for the second injection at the first negative and second positive flank of the oscillation, respectively. In both situations the injection pressure is approximately on the same level as for the first injection. For the T_{inj} = 1.875 ms case the second injection is in-line with the incoming wave, while for T_{inj} = 2.775 ms the needle opening timing is in contrast to the pressure surge. As a result of

these timings, Figure 54 clearly shows how in the former case the subsequent oscillation of the pressure at the injector inlet is significantly amplified. In the latter case, however, the plot shows that the waves from the first and second injection eliminate each other to a great extent; the final variation of *pII* appears to be equal or slightly smaller than for the single injection event.

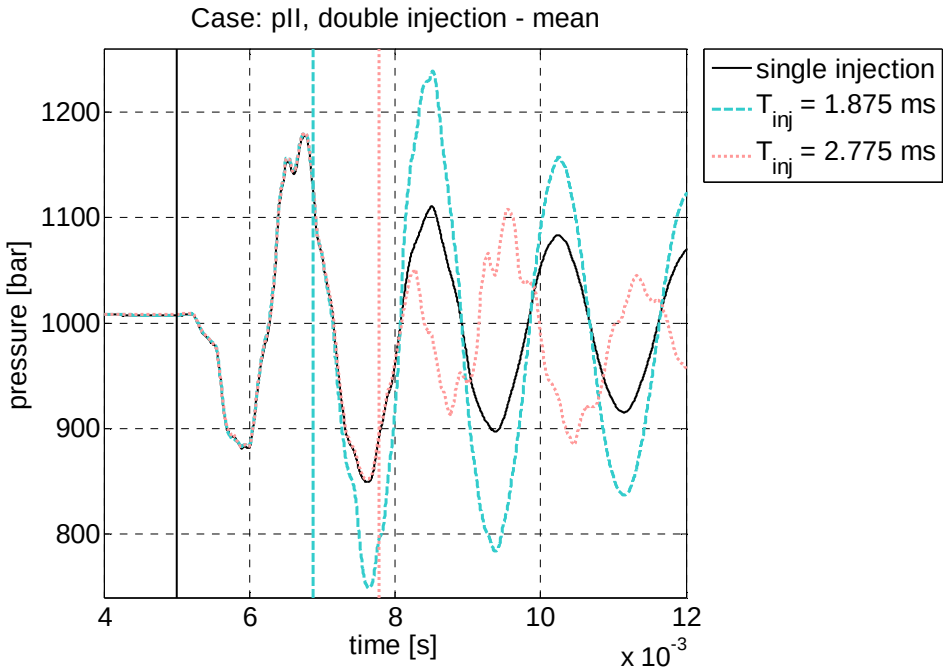

Figure 54. Pressure history *pII*, double injection - mean (pipe7301344).

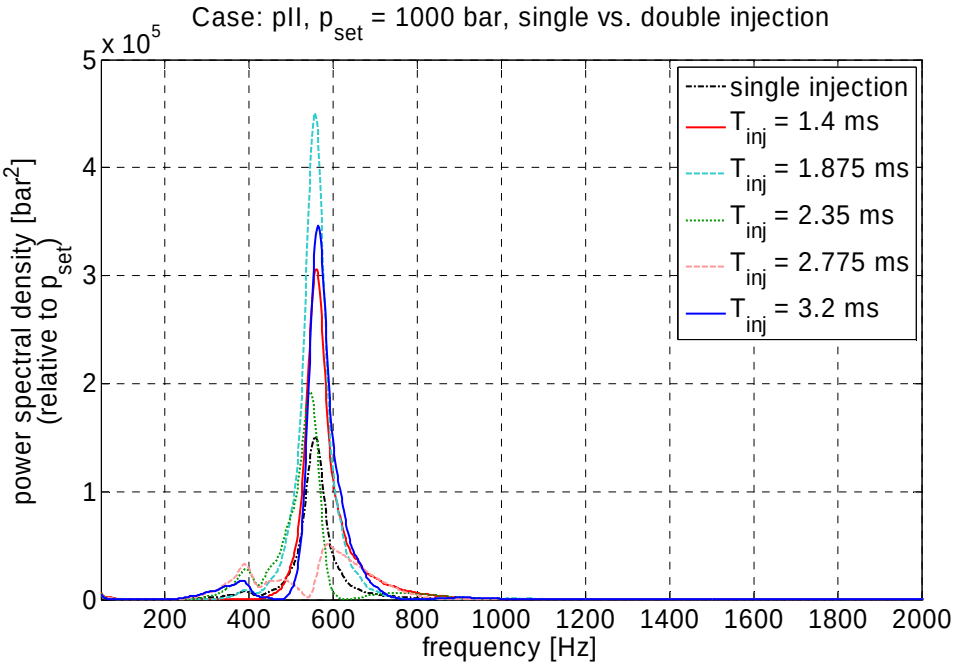

Figure 55. Comparison single vs. double injection, frequency content of *pII*-history.

Figure 55 presents the frequency analysis of the pressure signal at *pII*. It is interesting to notice that the second injection has practically no effect on the main oscillation frequency. For all cases, including the single injection measurement, the main frequency is found at about 560 Hz (resolution $\Delta f \approx 1.9$ Hz). The case for T_{inj} = 2.775 ms represents an exception to this trend due to the alteration of the underlying pressure signal. For the latter case the main frequency is computed to reach 589 Hz. Finally, Figure 56 shows the impact of the injection timing on the amount of injected mass during the second injection.

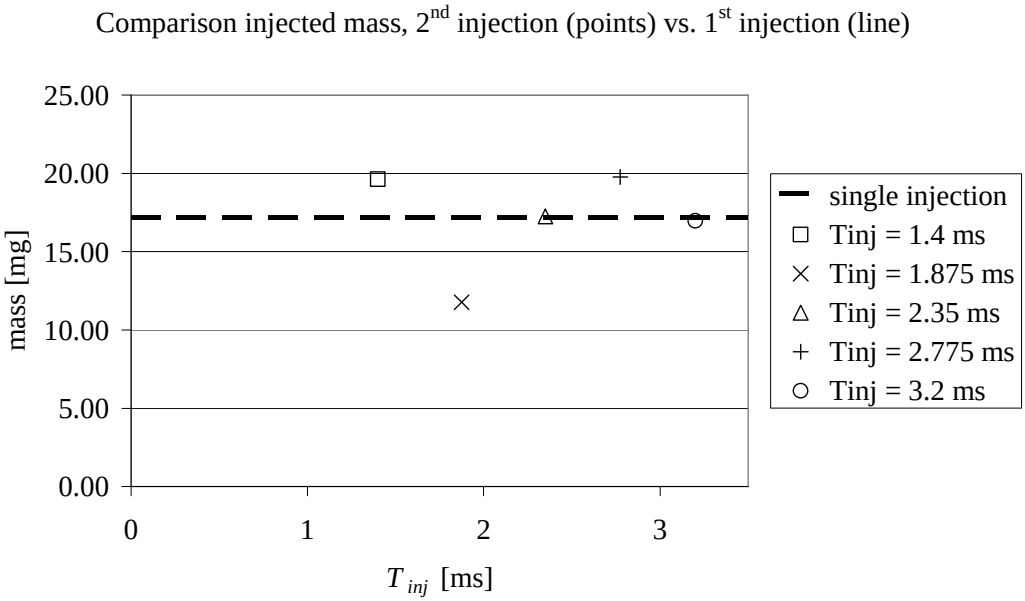

Figure 56. Case: pipe7301344, individual masses - double injection (t_{inj} = 600 μs).

From the figure above, it can be seen that a second injection at the first positive oscillation peak (T_{inj} = 1.4 ms), in comparison to the first injection, leads to an increase of the injected mass. In contrast, for an injection at the first negative (T_{inj} = 2.35 ms), or second positive peak (T_{inj} = 3.2 ms), the result indicates that both injections are characterised by the same injection amount. The finding for the latter injection period, T_{inj} = 3.2 ms, is especially worth emphasising, as this result is not anticipated based on the previously presented pressure history (Figure 53). The mark for T_{inj} = 1.875 ms shows that the injection rate drops considerably for the second injection; in comparison to the single injection event, the injection rate varies by more than 30 %. If the injection period is set to 2.775 ms, the absolute mass of the second injection is, as for the T_{inj} = 1.4 ms case, about 16 % higher than anticipated under ideal conditions.

3.2. Numerical modelling of the hydraulic CR system analogous to experimental measurements

Numerical modelling can be used to widen efficiently the number of studied parameters and to obtain a better understanding of the physics at hand. In any case, it is fundamental that the simulation model is capable of representing the main features of the problem. This study is mainly based on simulations in the GT-Fuel environment. The fundamental equations for modelling fluid transients have been developed in chapter 2. Subsequently, several extension and additions are introduced, which allow the code to accurately represent the hydraulic circuit of the CR system.

3.2.1 Introduction to the simulation environment

The main components for modelling fluid flow in GT-Fuel are defined by *Pipe*, *Orifice*, and *Flow split* objects. Firstly, the flow cross-section of a *Pipe* object is not restricted to a round inlet and outlet; any other shape that can be implemented through the two parameters area and wetted perimeter is possible. Generally, the total length of a single pipe is divided into small segments or CV's of length Δx; the latter parameter is commonly identified as the discretization length of a CV. If wall flexibility is neglected, the governing equations are defined by the equations for modelling the fluid field (see chapter 2). Essentially, this assumption was applied throughout this study. Chapter 3.3.3 represents an exception to this rule as it also contains simulation results that are based on an FSI computation; in order to include wall flexibility, it is necessary to calculate the respective stress components in radial and tangential direction [43]:

$$\sigma_r(r) = p_i \cdot \frac{r_i^2}{r_o^2 - r_i^2} \cdot \left(1 - \frac{r_o^2}{r^2}\right) - p_o \cdot \frac{r_o^2}{r_o^2 - r_i^2} \cdot \left(1 - \frac{r_i^2}{r^2}\right) \tag{108}$$

$$\sigma_t(r) = p_i \cdot \frac{r_i^2}{r_o^2 - r_i^2} \cdot \left(1 + \frac{r_o^2}{r^2}\right) - p_o \cdot \frac{r_o^2}{r_o^2 - r_i^2} \cdot \left(1 + \frac{r_i^2}{r^2}\right) \tag{109}$$

The radial deformation of the wall is derived in a second step through rearranging the subsequent definition for tangential strain [43]:

$$\varepsilon_t = \frac{\Delta r}{r} = \frac{1}{E} \cdot \left(\sigma_t - \nu \cdot \sigma_r\right) \tag{110}$$

Orifice objects are universally used in the code to represent explicit flow restrictions. The main input parameters incorporate orifice diameter and forward and reverse discharge

coefficient, respectively. All parameters can be written as a function of other variables like, for example, time or displacement. As shown in chapter 3.2.2 and 3.2.3, this study was taking extensive advantage of this capability to achieve closure to the measured system.

Thirdly, *Flow split* objects represent a single CV with one or more openings. The volume of the CV defines the main parameter of this entity. The code allows, similar to pipe objects, the implementation of regular and irregular shapes. The latter aspect becomes particularly important when the fluid inertia is significant. To account correctly for such phenomena, the *Flow split* object requires two additional parameters for each opening - expansion diameter d_{exp} and characteristic length l_{char} of the port. The first variable describes the diameter to which the flow may expand after entering this entity. The characteristic length, on the other hand, stands for the distance a fluid particle may travel inside of a flow split until it reaches an opposite located wall or a fluid boundary of another opening. In fact, by defining the spatial orientation of the port relative to the local coordinate system, the flow field in flow splits is calculated locally in three dimensions. Figure 57 presents the main parameters of this object in a graphical way for a two-dimensional case.

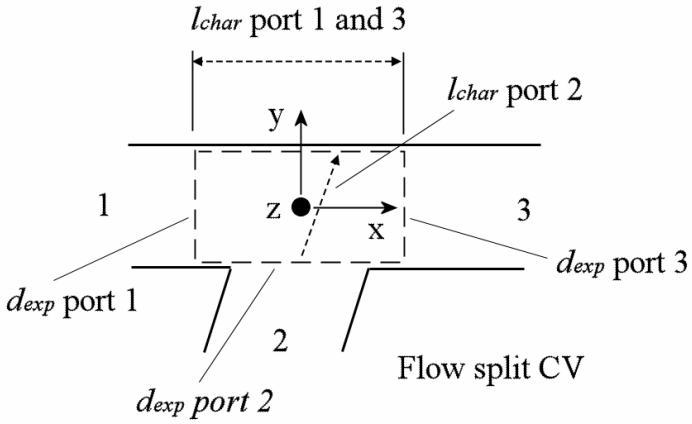

Figure 57. Example flow split, planar case.

The consideration of rigid body dynamics is a crucial part in accurately modelling valve characteristics. Besides the simple *Mass* object, the main components are *Spring*, *Damper*, and *Contact* entities. Gravitational forces are negligible in this study. Accordingly, mass motion in one dimension is defined solely by Newton's second law. Interaction with the flow field is implemented via *MechFlowConn* objects, which translate, for example, the linear displacement of a *Mass* entity to a volume and pressure variation, and vice versa. The change of an adjacent volume is given by the product of characteristic area A times displacement Δx:

$$\Delta V = A \cdot \Delta x \tag{111}$$

Conversely, the hydrostatic force on the mass is calculated from the pressure inside the adjacent volume, *p*, times the same characteristic area *A*:

$$F_p = p \cdot A \tag{112}$$

Additionally, it is possible to sense mass acceleration and velocity. The latter parameter has been used in this study to account correctly for leakage flow, which is described in the form of a Couette-Poiseuille flow [43, 99].

3.2.2 Implementation of CR system into the simulation environment

Figure 58 shows the layout of the CR system in the GT-Fuel environment analogous to the measurement setup (see chapter 3.1.1). The upper part of Figure 58 represents the main components of the hydraulic circuit, that is, the pressure supply, rail, two connection pipes, and a block for the injector. Firstly, the high pressure pump has been replaced in the simulation model by a constant pressure source. In alignment with the measurement results, it is assumed that it is not important to consider the small flow and pressure perturbations that are emitted by the pump. Similarly, the model employs a pressure source that is mounted directly to the rail. The connection line between pump and rail is therefore incorporated in the constant pressure supply. It has to be pointed out that the terminology *constant pressure supply* in fact includes a variation of the pressure head during injection. Based on the findings of the experimental measurements, the supply pressure in the model is reduced during a simulation run to account for the mean pressure drop as a result of the needle opening. If other, not measured configurations are used in the model, the drop of the supply pressure is interpolated from experimental data. As depicted in the upper part of Figure 58, the rail consists of several *Pipe* and *Flow split* objects. The latter entities symbolize the various ports of the rail. The *Pipe* objects are used to represent the sections between the ports. The wall of the rail is assumed to be perfectly rigid in this model. The same is true for the connection pipes that are linked to rail ports 4 and 5. As with the experimental measurements, the numerical analysis of the circuit investigates extensively the impact of the connection pipe properties on the hydraulic system dynamics. Downstream of the connection pipe at port 5 is shown a single block, which symbolises the solenoid injector.

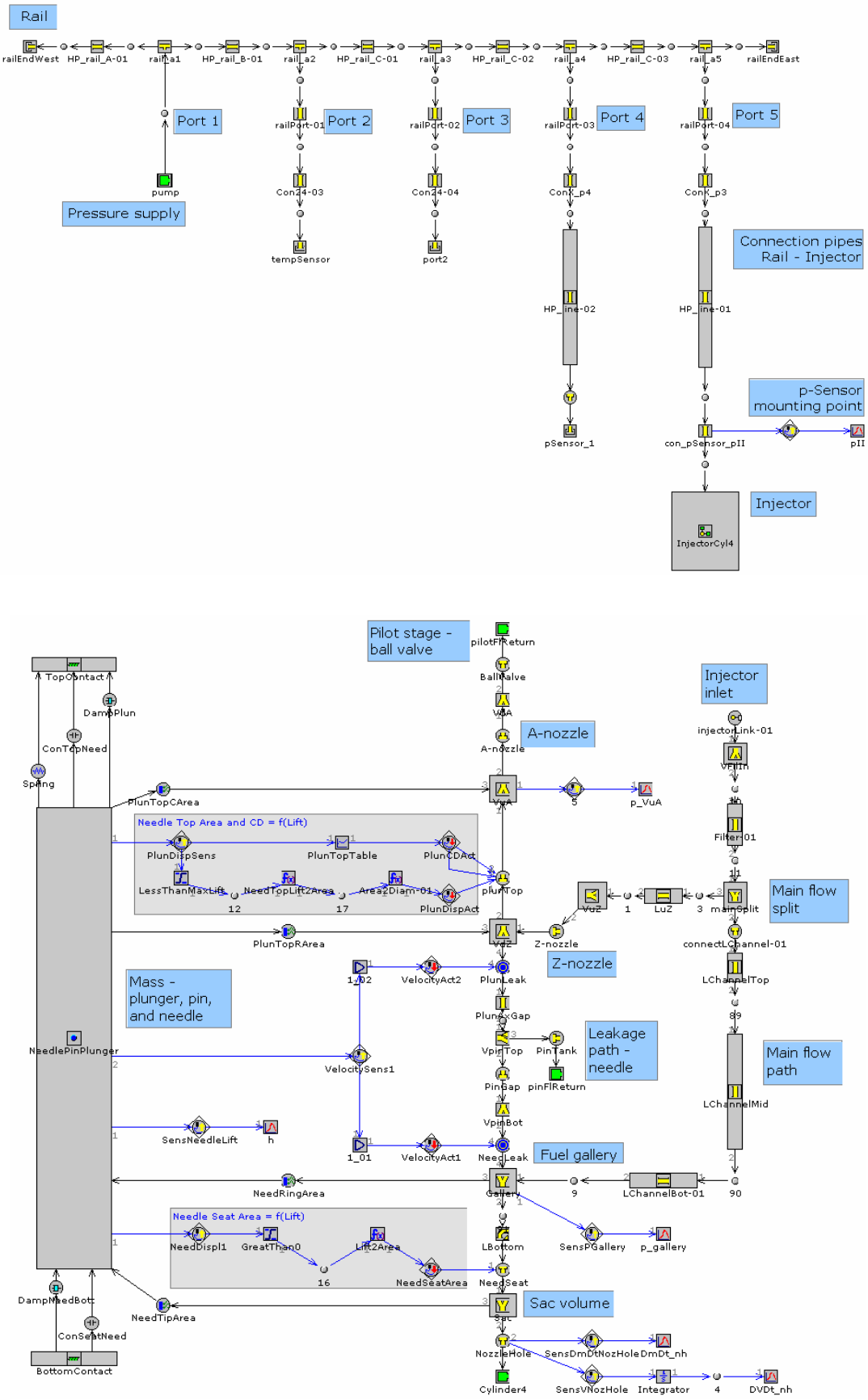

Figure 58. GT-Fuel model of CR system; main circuit (top) and detailed injector model (bottom).

Generally, the fuel injector itself is not of main interest in this study (see Figure 15 for a schematic picture of the injector and Figure 58, bottom). Primarily, it is seen as a fast acting valve that excites the hydraulic circuit. The injector was consequently modelled only in as much detail as necessary. For example, the solenoid stage is simplified by representing the activation of the pilot stage ball valve through a look-up table. Secondly, the individual masses of needle, pin, and plunger are replaced by a single mass object. On the other hand, as shown in chapter 3.3.2, the injector dynamics are a fundamental part of the overall system characteristics. Therefore, accurate representation of the internal flow paths, volumes and restrictions is crucial for meaningful predictions. Most of the utilised dimensions are based on measurements of a disassembled and modified fuel injector by means of a laboratory microscope and high precision scale. Alternatively, the three-dimensional flow field was calculated in ANSYS-CFX to obtain a better understanding of the flow physics under transient conditions. The latter approach was employed to estimate the discharge coefficients (forward and backward) of the plunger-top restriction. As shown in the bottom half of Figure 58, the mechanical part of the injector is presented on the left hand side. This includes the mass and links to the upper and lower boundaries, that is, the stiffness, damping, and contact interfaces to the upper stop and needle seat, respectively. On the right hand side are the hydraulic entities. Analogous to Figure 15, the flow path is divided at the main flow split into two branches. One is directed to the pilot stage and one guided downstream via the fuel gallery to the needle seat. A further path is used between fuel gallery and pilot stage to account for fluid leakage. At the centre-left the interfaces between mechanical and fluid objects are drawn. The greyed out boxes represent definitions that are more complex like, for example, the plunger top restriction and the needle seat orifice.

The numerical simulation model omits any effects that are based on the pressure regulator valve. Firstly, the results of the experimental measurements confirm that the dynamic characteristics of the pressure regulator valve have no effect on the observed findings (see, for example, chapter 3.1.2). Secondly, mass conservation has been ensured in the numerical circuit because the high pressure pump with fixed displacement is modelled by a pressure boundary condition. The pressure source was not constant. As has been indicated previously, the drop of the mean pressure level due to the injection is considered during the simulations. Finally, the utilised fluid in the simulation model was assumed to behave the same under pressure and temperature variations as the fluid in the experiment. Although both oils comply with the ISO-4113 standard small, differences can not be excluded.

3.2.3 Three-dimensional modelling of injector pilot stage flow field

The behaviour of the injector is very sensitive to the geometrical characteristics of the internal flow channels. Besides obvious parameters like, for example, the diameter of the A- and Z-nozzle, it has been found that the restriction above the plunger plays a fundamental role. Figure 59 illustrates this correlation graphically. When the pilot stage solenoid is energised, the ball valve opens and the plunger starts to move upwards. As a result of the displacement the flow area between volume *VdZ* and *VuA* decreases, which also reduces the speed at which the pressure in *VdZ* drops. At some point in time the mass comes to a halt because of force equilibrium - the pressure force above and below the plunger and needle cancel each other out. The characteristics of this particular orifice are rather complex and can not be represented by constant parameters. Indeed, it is likely that the main flow field between *VuZ* and *VuA* undergoes various transitions of streamlined to highly chaotic flow, depending on the gap between plunger top and upper wall.

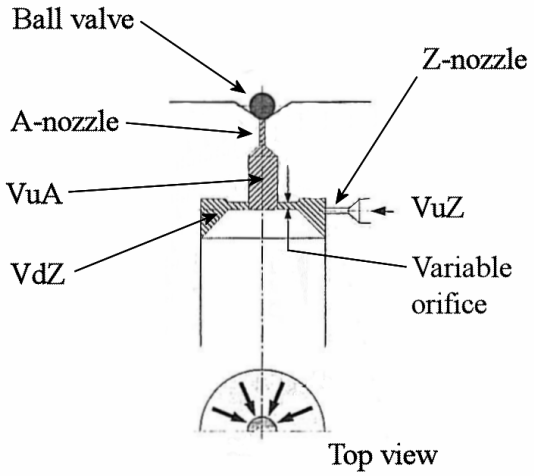

Figure 59. Detailed view of injector pilot stage.

In order to get a better understanding of the flow field at this location, a three-dimensional simulation model was developed in the ANSYS-CFX environment. It is emphasised here that highly accurate results were not expected from this simulation, but rather some insight into the flow physics at hand. This knowledge was then used in a subsequent step to adjust the forward and backward discharge coefficients of the plunger-top orifice as a function of plunger lift (see, for example, the previous chapter and Table B 3 in Appendix B).

The main equations for solving the three-dimensional flow field are developed in chapter 2. Only one pressure level, p_{set} = 1000 bar, was considered in this study. Secondly, a full cycle

of plunger movement was not calculated, but only its opening until the equilibrium state was reached. The computational domain corresponds to the schematic drawing in Figure 59. Because of symmetry, only 180° of the geometry were modelled. Special attention is required for the boundary conditions of the model. Both the inlet at the volume upstream of the Z-nozzle, *VuZ*, and the exit downstream of the A-nozzle were implemented as *Openings*. This means that the flow direction was not imposed by the boundary definition but was allowed to adjust as a function of the local flow field. The latter aspect might be particularly important for the former inlet boundary, as it can not be completely excluded that the flow reverses for some short time. The main parameter for the *Opening* boundary condition is static pressure, which varies in both cases with time. As no pressure measurements were available for these two locations, the corresponding profiles were based on approximations from GT-Fuel runs. In this context, it becomes clear that this process is iterative in nature, that is, a GT-Fuel model is run, and the results are next used in an ANSYS-CFX computation, which is again used to improve the GT-Fuel model. Altogether, two repetitions were used to achieve good correlation between the models. The motion of the plunger wall boundary is the third unknown condition of the model. As has been indicated before, the position of the plunger is the result of the forces acting on the mass.

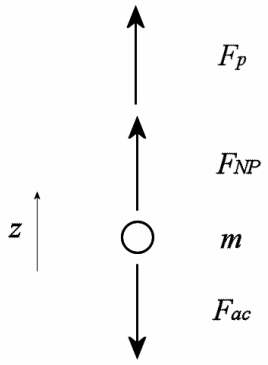

Figure 60. Simplified force balance of needle-pin-plunger mass.

Figure 60 presents schematically the main force vectors, that is, net or acceleration force F_{ac}, pressure force F_p (*VdZ*), and external plunger force F_{NP}. Gravitational and damping forces were not considered as their contribution was regarded as negligible. The force equilibrium is written as:

$$\sum F_z = F_p + F_{NP} - m \cdot a_z = 0 \tag{113}$$

The acceleration factor in equation (113) can be written in the form of known parameters at the previous time step. The time rate of change in the plunger's linear momentum is

proportional to the net force acting on the plunger. In differential form, the equation for the motion of the plunger is:

$$\frac{\partial(m \cdot w)}{\partial t} = F_P + F_{NP} \tag{114}$$

The variable m represents the plunger mass and w the velocity in z-direction. Subsequently, equation (114) is discretised and rearranged to provide an expression for the position of the plunger. The time derivative of the plunger velocity is:

$$\frac{\partial(w)}{\partial t} = \frac{w_t - w_{t-1}}{\Delta t} \tag{115}$$

In equation (115) the index t stands for the current and t-1 for the previous time step. The new velocity can be defined through the change in position over time:

$$w_t = \frac{z_t - z_{t-1}}{\Delta t} \tag{116}$$

In the last step equation (116) is put into (115) and (114), respectively. After some rearrangement the new position of the plunger is calculated as:

$$z_t = z_{t-1} + \Delta t \cdot w_{t-1} + \frac{(\Delta t)^2}{m} \cdot \left(F_p + F_{NP}\right) \tag{117}$$

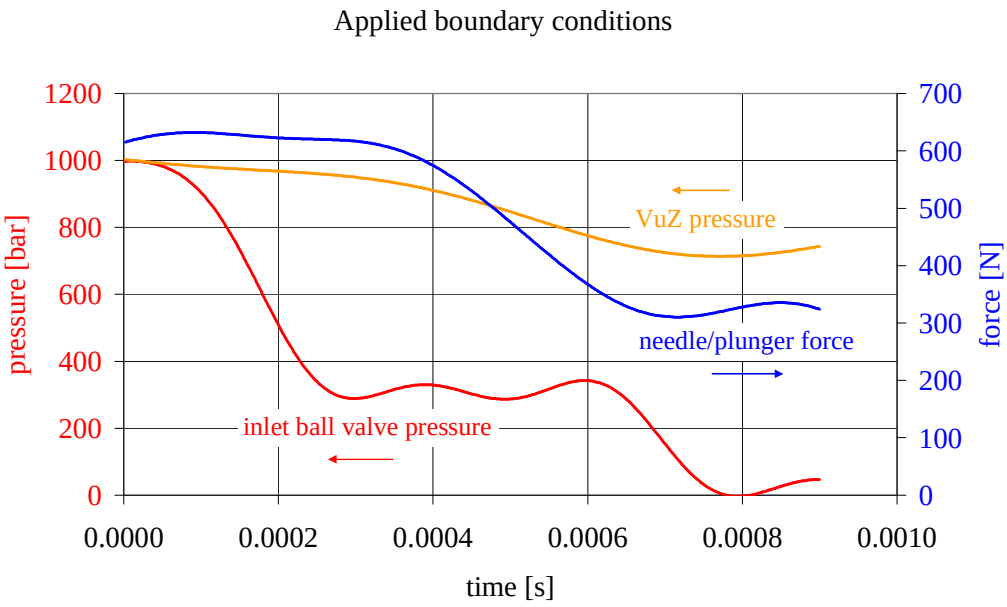

Figure 61. Boundary conditions for pilot stage 3D simulation.

The pressure force F_p was calculated by the code as part of the solution. On the other hand, the needle-pin-plunger force F_{NP} needs to be entered by an array. In this case the profile was based on the result of a previously performed GT-Fuel simulation. Figure 61 shows

graphically the input data for all three boundaries - static pressure curve in volume *VuZ* and upstream of the ball valve and external force on the plunger-top wall.

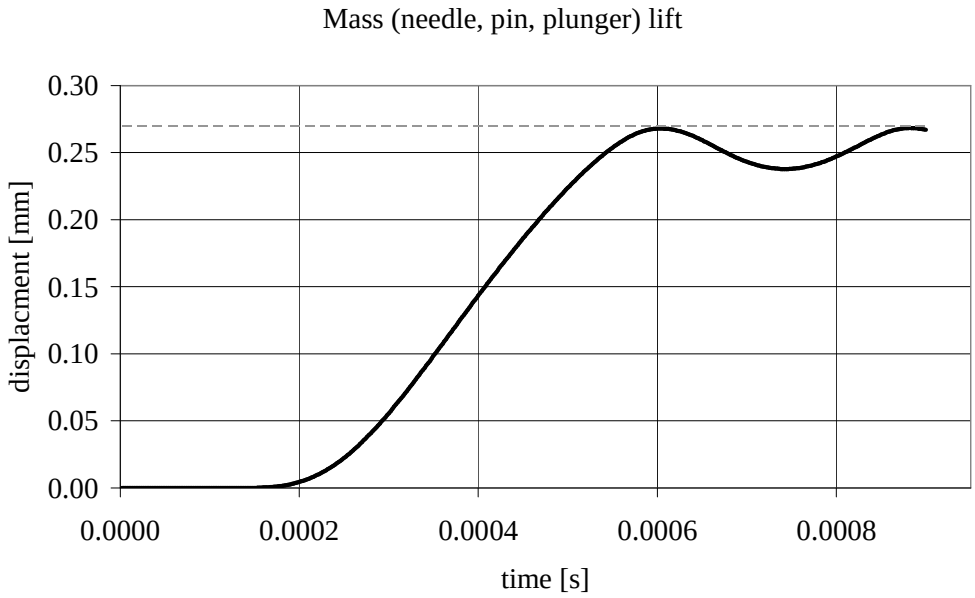

Figure 62. Pilot stage, computed lift by 3D model

Figure 62 presents the result of the calculated plunger-top displacement for the first 900 μs. The graph indicates that the full plunger stroke takes roughly 400 μs. Because of force imbalance the mass motion is reversed at about t = 730 μs. It is emphasised that the plunger actually never touches the upper wall (indicated by the horizontal dashed line in Figure 62).

Figure 63 and Figure 64 show for various time steps the computed stream lines though the domain (coloured by the velocity) and the static pressure at the plunger-top wall. At a very early stage, t = 100 μs, the pressure gradients are small and the velocities low. Later, the plunger-top wall starts to move upwards (t = 260 μs). The incoming jet passes across *VdZ* and leaves through the exit after completing a full recirculation. At t = 420 μs stream lines appear differently. Now the main path is redirected to pass straight through *VuA* to the A-nozzle. The t = 580 μs plot shows that the plunger has reached almost the uppermost position. The fluid gets squeezed and the pressure inside *VdZ* increases considerably. At t = 740 μs the plunger reverses its motion, which immediately releases the pressure in the plunger-top chamber. Finally, t = 900 μs shows again the same state as for the t = 580 μs plot.

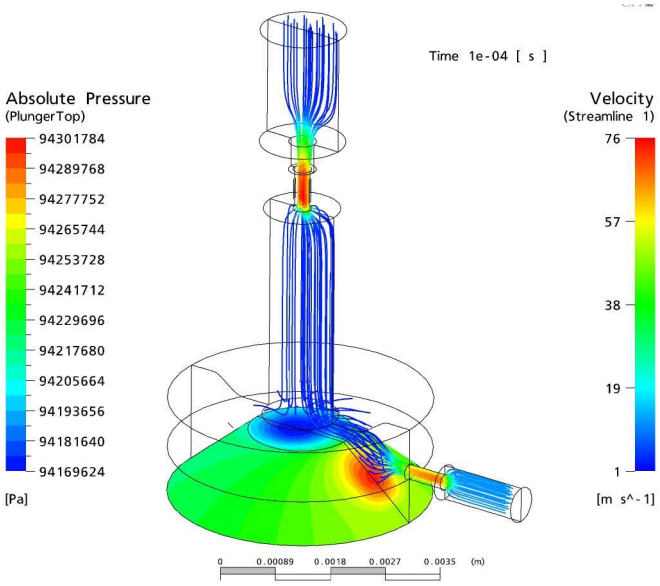

Time t = 100 μs

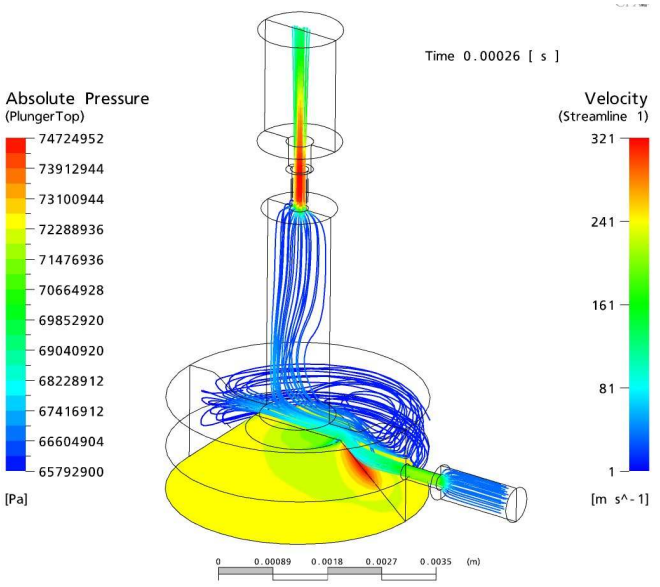

Time t = 260 μs

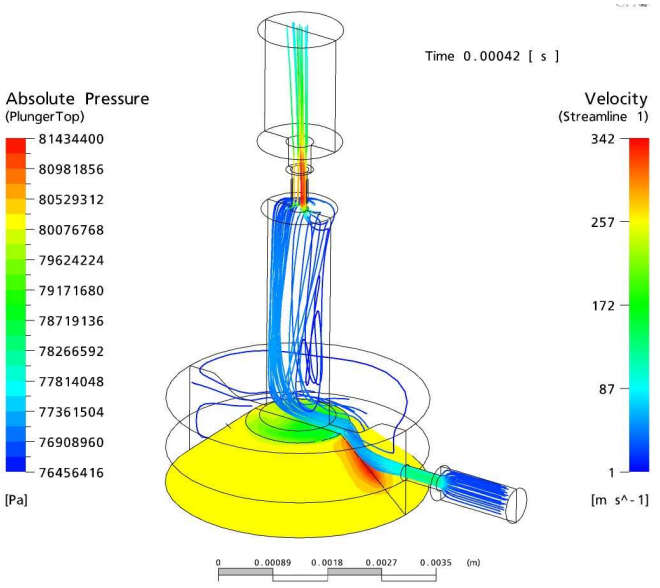

Time t = 420 μs

Figure 63. Pilot stage, stream lines (180°) and pressure contour (360°) - a.

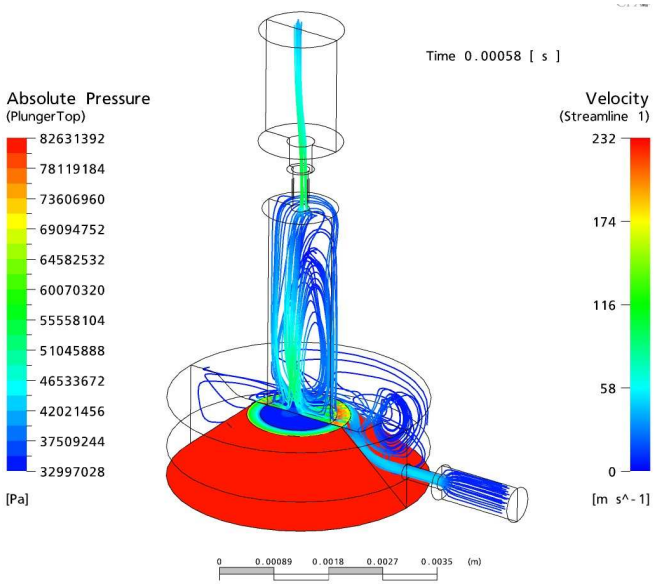

Time t = 580 µs

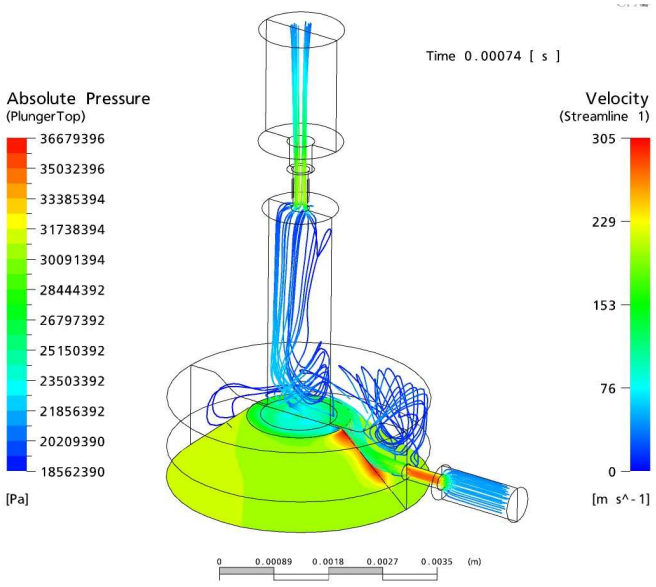

Time t = 740 µs

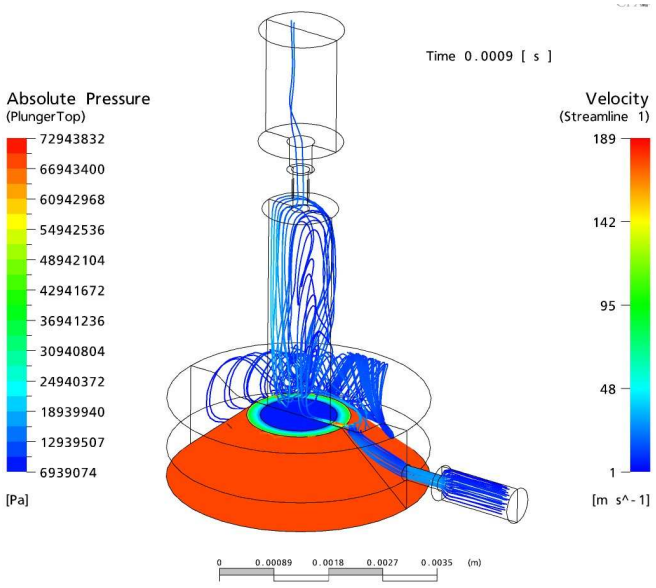

Time t = 900 µs

Figure 64. Pilot stage, stream lines (180°) and pressure contour (360°) - b.

3.2.4 Verification of simulation model by measurements

A numerical simulation model is always an attempt to represent a physical system through mathematical equations. The quality of such a model depends on the level that the theoretical approach accounts for explicit details. Evaluation of a model simply by theoretical reasoning is generally very problematic, as it is exceptionally difficult to estimate in advance the impact of, for example, a general assumption or a specific mathematical algorithm on the solution. Consequently, it is essential for any numerical study that the model is verified by actual experimental measurements.

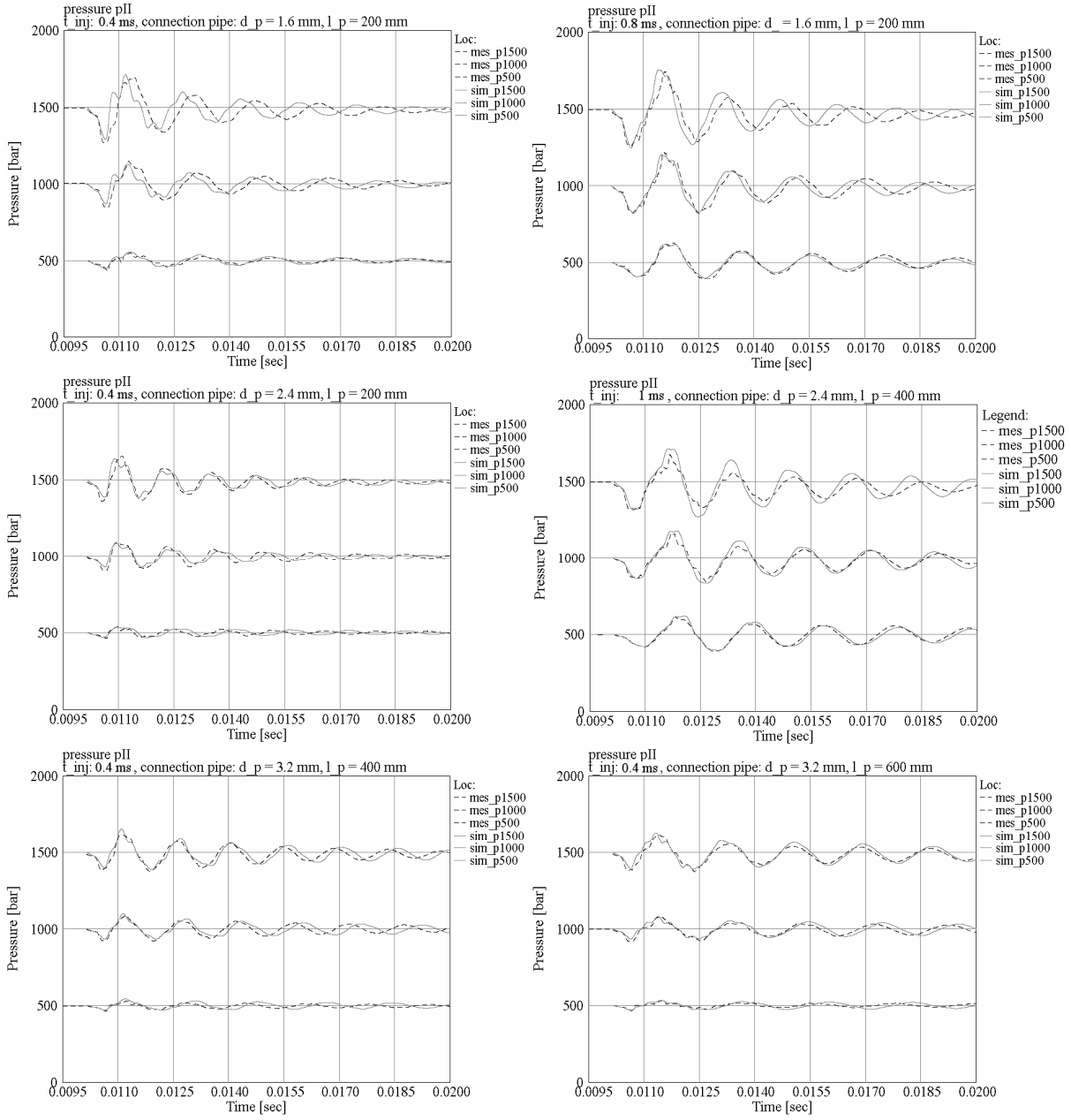

Figure 65. Pressure *pII* at injector inlet; comparison of measured (‘mes_’, dashed) to simulated (‘sim_’, solid) curves at various system configurations.

As presented in chapter 3.1, the CR system was analysed thoroughly by experimental measurements. The GT-Fuel model verification concentrates, therefore, not on a single operation point, but considers the whole range of analysed parameters. Figure 65, for example, compares the measured to simulated pressure history at the injector inlet, *pII*, for various connection pipe geometries l_p and d_p, injection pressures p_{set}, and injection times t_{inj} (only single injections). Overall, the simulated curves match well with the signal that has been recorded on the hydraulic test bench. On closer examination, it can be noted that the model predicts, for example, for a setup with d_p = 2.4 mm, l_p = 400 mm, and t_{inj} = 1000 µs (Figure 65, centre-right plot) slightly too large amplitudes between t = 11 ms and 17 ms, if a large injection pressure is chosen. For a configuration with short connection pipe (l_p = 200 mm) and a small diameter (d_p = 1.6 mm), the two uppermost plots in Figure 65 reveal that, for different injection times t_{inj}, the shape of the initial pressure peak differs between model and measurement. The two plots at the centre-left and bottom-left are in some respect similar. For both configurations (centre-left: d_p = 2.4 mm, l_p = 200 mm, t_{inj} = 400 µs; bottom-left: d_p = 3.2 mm, l_p = 400 mm, t_{inj} = 400 µs) a direct comparison shows that the oscillation frequency of the simulated curve slightly lags behind the measured curve.

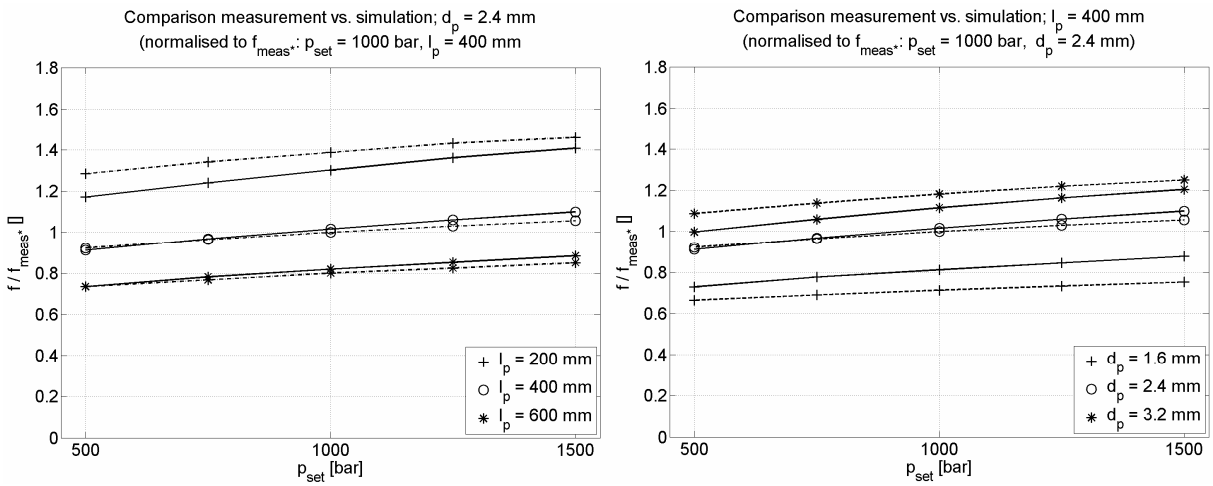

Figure 66. Comparison frequency *pII* – measurement (dashed) vs. simulation (solid); normalised to meas.: p_{set} = 1000 bar, l_p = 400 mm, d_p = 2.4 mm - l_p (left), d_p (right).

Figure 66 presents for both measured and simulated data the oscillation frequency at the injector inlet in the form of an explicit and normalised output parameter. It is stressed at this point that the injection duration parameter is not included in this presentation, since it has no effect on the oscillation frequency (see, for example, page 76, Figure 42 and chapter 3.2.5). In analogy to the centre-left plot of Figure 65, the graph on the left hand side of Figure 66 shows

that for a short connection pipe, l_p = 200 mm, the values for the simulated *pII* frequency are generally lower than the measured numbers. The difference appears bigger in the case of a low injection pressure. On the right side of Figure 66, the results indicate that for a setup with l_p = 400 mm and an injection pressure of p_{set} = 1000 bar, the simulated frequency values are higher than the measured ones if the system uses connection pipes with a small diameter (d_p = 1.6 mm). Conversely, for large diameters (d_p = 3.2 mm) the same plot shows that now the simulated oscillations are somewhat slower than the measured pressure variations. The latter observation is also presented in the bottom-left graph of Figure 65 in the form of a direct *pII*-curve comparison for the injection pressures p_{set} = 500 bar, 1000 bar, and 1500 bar.

Figure 67 compares for the most extreme geometry combinations that have been measured in this study the injected volumes of the measurement with the data of the simulation. It should be noted that the results correspond to differences between both approaches that are normalised by the corresponding injection volume of the measurement.

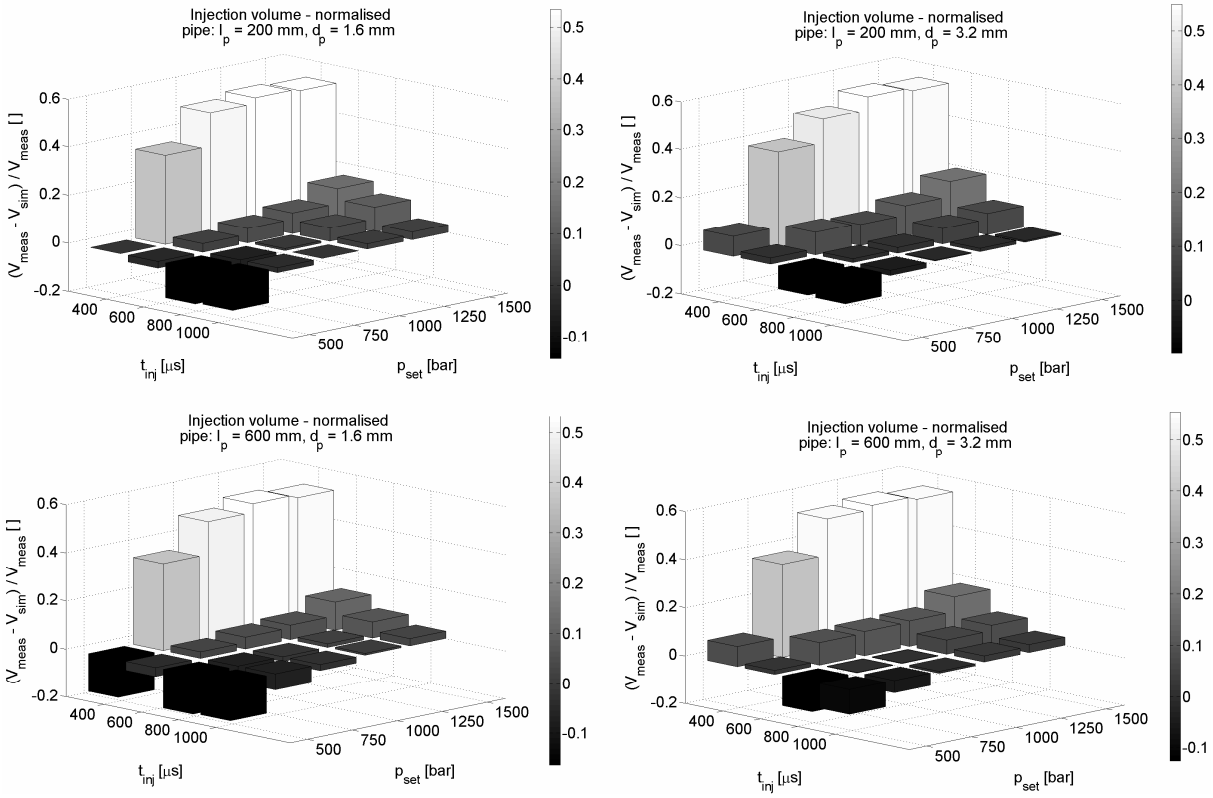

Figure 67. Comparison injected volume - measurement vs. simulation; normalised to measurement.

Most apparent in the figure above is the large relative discrepancy of the injected volumes for the setups with the shortest injection duration (t_{inj} = 400 µs) and injection pressures higher than 500 bar. Then again, by considering the total amount of the injected quantities during one injection, the discrepancy appears in a different perspective. For example, for the bottom-right graph of Figure 67, that is, a setup with l_p = 600 mm, d_p = 3.2 mm, and t_{inj} = 400 µs, the experimentally weighed mass increases as a function of pressure from about 1.2 mg to 13.45 mg per injection. As the total amounts are rather small, it is conceivable that some error is introduced by the limited accuracy of the measurement hardware and procedure (see, for example, chapter 3.1.1). Secondly, it has to be emphasised that this comparison assumes identical fluid properties. In fact, it is to be expected that some discrepancy exists, which is large enough to have an effect on the total quantities. The injector model itself might certainly also have some weakness at that particular injection time, which causes generally too small injection quantities when compared to the measurement. This weakness, however, is not detectable from a direct comparison of pressure histories at the injector inlet; for example, the bottom–right graph of Figure 65 shows, the pressure curves may match rather well despite the large relative difference of the injected masses (see the corresponding plot at bottom-right, Figure 67).

3.2.5 Numerical parameter study for single injection event

The numerical parameter study is based, just as the experimental investigation in chapter 3.1.4, on the analysis of the impact of the connection pipe geometry between rail and injector and dead end on the system characteristics. Because the analysis of a specific system configuration in the virtual domain is much more time efficient than the measurements on the real test bench, the numerical investigation widens and refines the range of studied parameters. Accordingly, in the numerical study the connection pipe was defined from l_p = 100 mm to 600 mm in steps of 100 mm. The diameter variation was refined into steps of 0.4 mm; the range reached the same as for the measurements from d_p = 1.6 mm to 3.2 mm. The values for the injection pressure remained identical. The duration of a single injection was chosen from t_{inj} = 400 µs to 1000 µs in steps of 100 µs. Altogether, the number of parameters were increased from 180 measurement points to 1050 simulation configurations. Table 2 summarises the main settings in tabular format.

Table 2. Summary of numerical connection pipe parameter study.

Injection pressure p_{set} [bar]	500, 750, 1000, 1250, 1500
Injection duration t_{inj} [µs]	400, 500, 600, 700, 800, 900, 1000 (only single injection)
Connection pipe length l_p [mm]	100, 200, 300, 400, 500, 600
Connection pipe diameter d_p [mm]	1.6, 2.0, 2.4, 2.8, 3.2
Temperature [K]	310.5
Fluid	GT-Fuel, ISO 4113 oil

The main focus of the pressure oscillation study is set on the signal at the injector inlet. Due to the vast amount of configurations it is not meaningful to compare the individual cases directly. Indeed, output parameters are defined that make it easier to evaluate the various setups.

Analysis of initial pressure peaks at *pII*

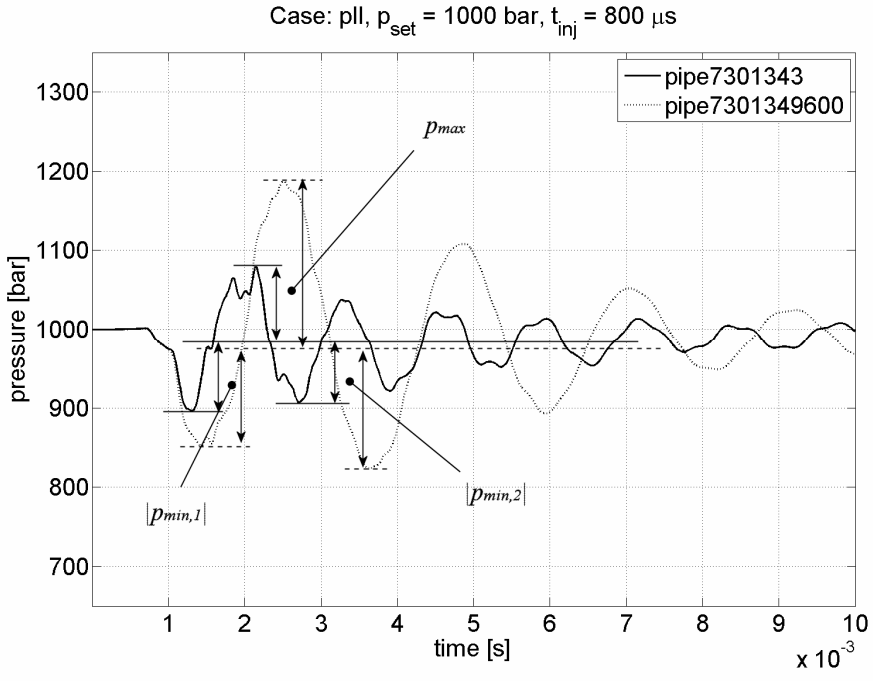

Figure 68. Analysis pressure oscillation, *pII*; definition of output parameters.

Since in the case of multiple injections the subsequent needle openings follow shortly after each other, the initial oscillation characteristics are particularly important. Three parameters were defined for this purpose. Firstly, the maximum positive pressure amplitude at *pII* is denoted as p_{max}. Regarding the minimum pressure at the same location, the attention is set on

both the absolute values of the first and second negative amplitude $p_{min,1}$ and $p_{min,2}$, respectively. All three parameters were evaluated with respect to the mean pressure level at *pII*. The latter value was based, as has been mentioned earlier, on measurement data. Figure 68 illustrates the definition of the parameters in a graphical way. The plot shows that the absolute value of $p_{min,2}$ may be smaller or bigger than $p_{min,1}$, depending on the configuration of the system. If not otherwise specified, the results are generally presented over the fluid volume between rail port and injector inlet (see, for example, also measurements, chapter 3.1.4).

In Figure 69 some typical graphs are plotted for the maximum pressure amplitude p_{max}. The injection time t_{inj} is chosen as the main variable. Firstly, the figure underlines that the maximum pressure at *pII* commonly increases for long injection times. A comparison of, for example, the upper-left plot with the bottom-right plot shows that the impact of the injection time appears to be emphasised in the case of a low injection pressure; for a large p_{set} the relative gap between the t_{inj} = 400 µs and 1000 µs values tends to become smaller. Although the cases for t_{inj} = 800 µs and 900 µs are omitted in this presentation, it can be seen that the

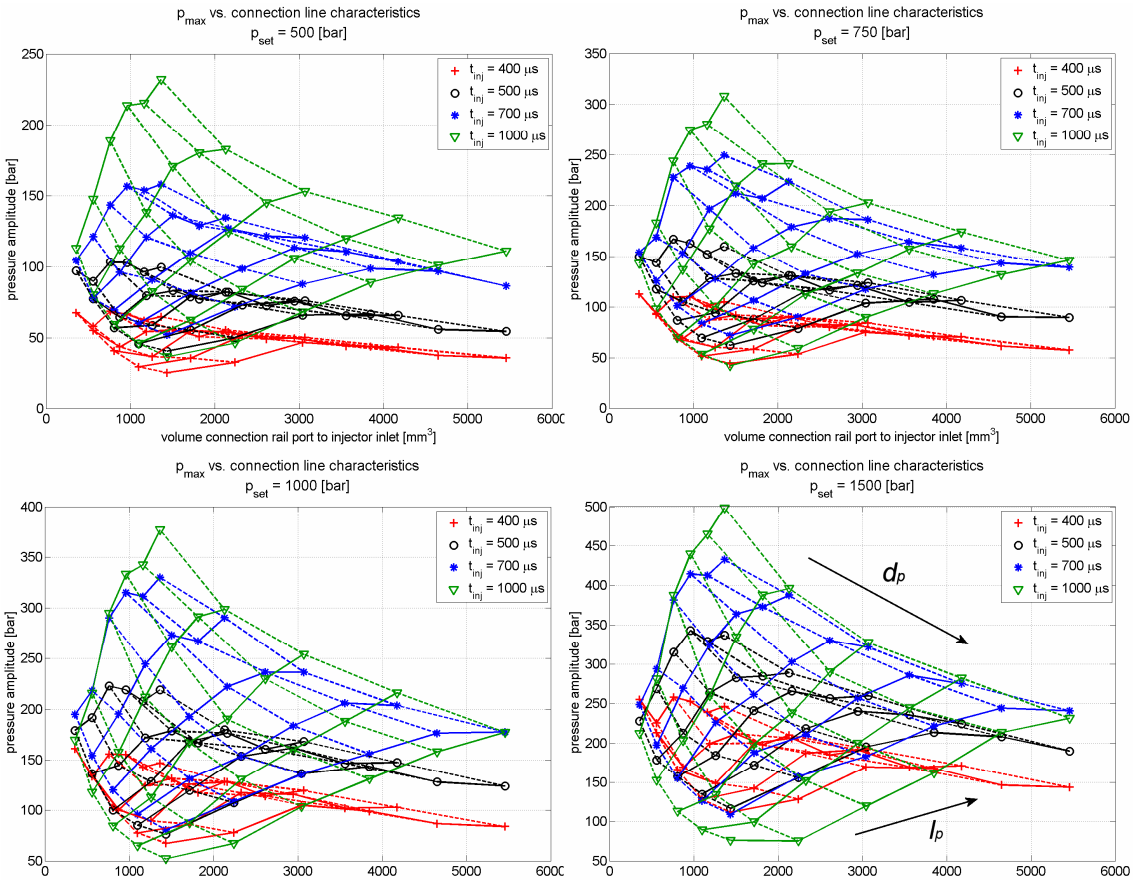

Figure 69. p_{max} as f(p_{set}, t_{inj}, l_p, d_p) - main variable: t_{inj}.

p_{max} values show a tendency to align for t_{inj} longer than 700 µs. This phenomenon is promoted particularly in the case of long connection pipes that are characterised through a large diameter (see also arrow-pair in the bottom-right plot of Figure 69). Altogether, the connection pipe geometry can be identified as a parameter that affects the weight of t_{inj} on p_{max}. In the case of a small connection pipe length, the graphs indicate that the impact of the injection time is only minor. Indeed, for l_p = 100 mm the final value for p_{max} is affected primarily by the injection pressure. At p_{set} = 1500 bar the bottom-right graph shows that the smallest maximum amplitude values are reached for the longest injection time; conversely, for a setup with an injection pressure of 500 bar, the minimum p_{max} values are computed for t_{inj} = 400 µs. In Figure 70 the maximum pressure amplitude is presented with the injection pressure as the main variable. For clarity, the plots show only the data for p_{set} = 500 bar, 1000 bar, and 1500 bar; the p_{max} values for the other two pressure cases, however, fit well between the presented ones. Generally, the figure supports the expectation, that is, the higher the injection pressure, the higher the maximum pressure amplitude at *pII*. On closer examination it is possible to notice that the maximum pressure amplitude does not increase linearly with the injection pressure; the difference between the values for p_{set} = 1500 bar to p_{set} = 1000 bar seems to be slightly smaller than the change from p_{set} = 1000 bar to p_{set} = 500 bar. Concerning the impact of the connection pipe geometry, the findings in Figure 69 and Figure 70 show that the maximum amplitude increases for long connection pipes. A large diameter, on the other hand, helps to reduce the value of p_{max}. Both l_p and d_p affect the output parameter in a non-linear way and are, furthermore, also dependent on the injection duration. In the case of very short injection times (Figure 70, t_{inj} = 400 µs), it appears that the geometry impact reduces to a minor role, that is, the graph shows some correlation between geometry and p_{max} only for pipe lengths shorter than 200 mm (see, for example, case p_{set} = 500 bar in the uppermost-left graph, Figure 70). Certainly, the effect increases for larger injection pressures, but the differences remain significantly smaller than for setups with injection durations of 500 µs or longer. As a rule, it can be stated that the rate of change of p_{max} as a function of l_p increases if a small connection line diameter is chosen. On the other hand, the relative impact of d_p reduces for long connection pipes. Overall, p_{max} tends to a minimum the shorter the length and the bigger the diameter of the pipes are.

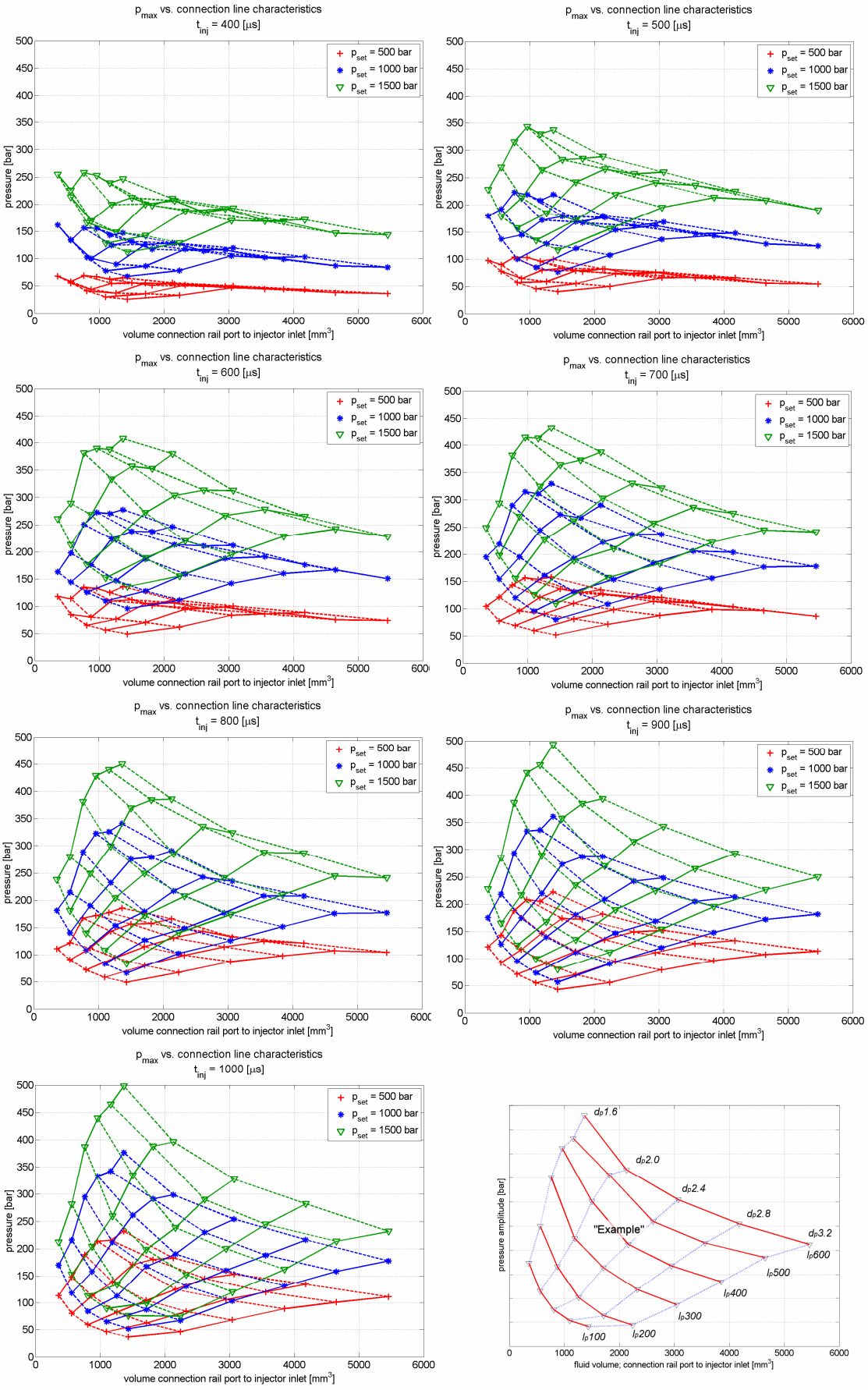

Figure 70. p_{max} as f(p_{set}, t_{inj}, l_p, d_p) - main variable: p_{set}.

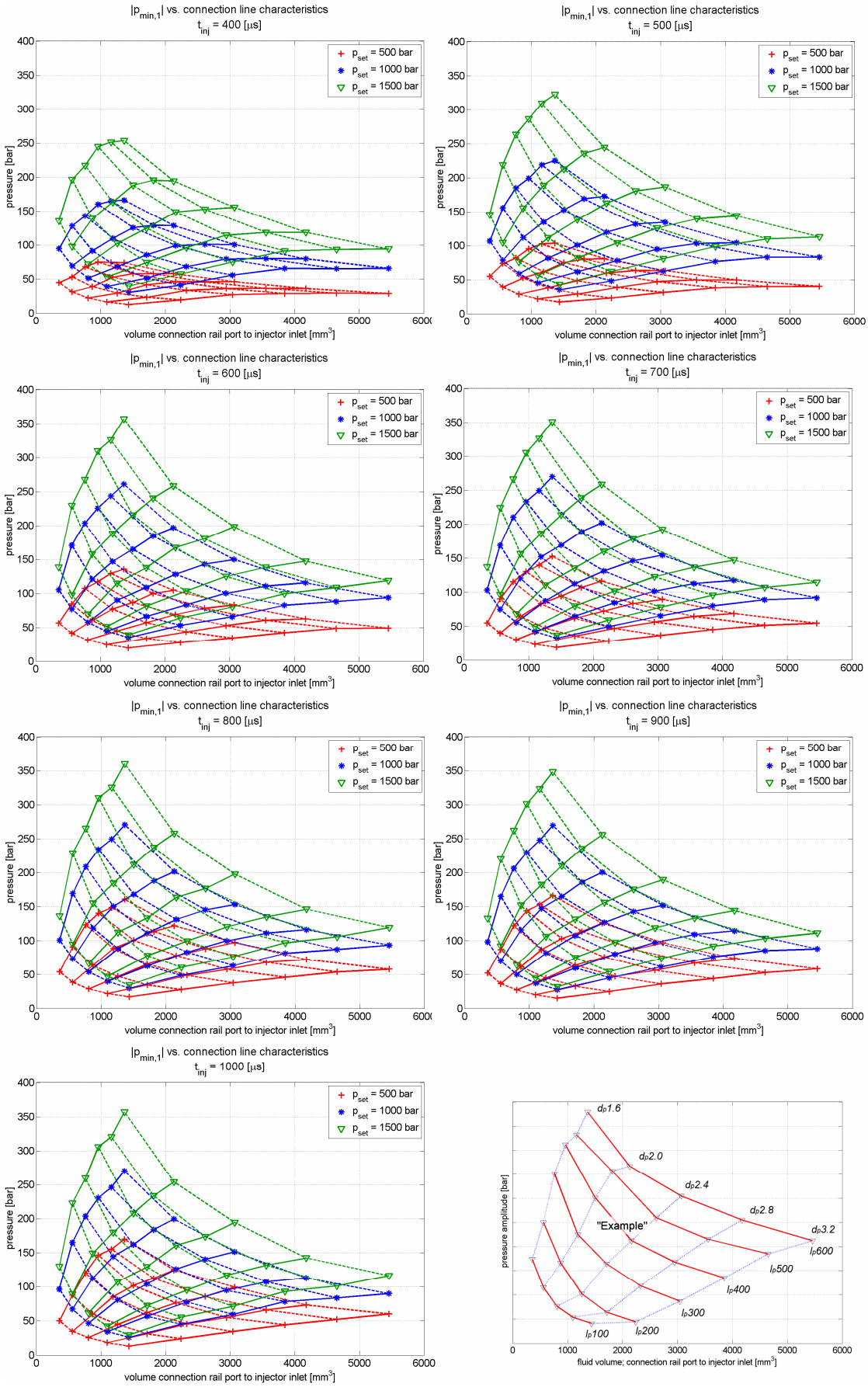

Figure 71. $p_{min,1}$ as f(p_{set}, t_{inj}, l_p, d_p) - main variable: p_{set}.

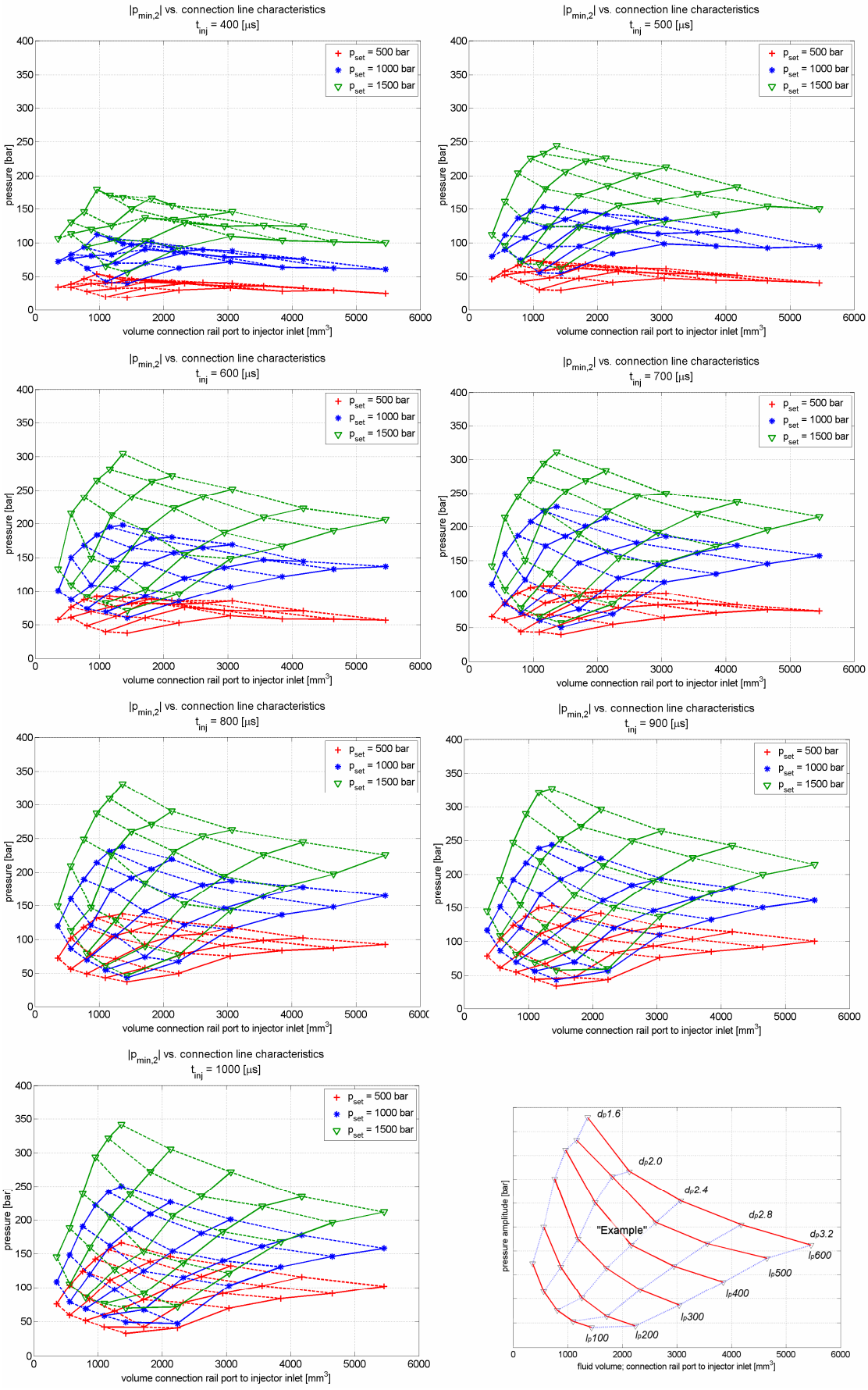

Figure 72. $p_{min,2}$ as f(p_{set}, t_{inj}, l_p, d_p) - main variable: p_{set}.

Figure 71 and Figure 72 depict the absolute value of the first and second pressure undershoot amplitude, respectively. Both figures show the injection pressure as the main variable. In general, the variables $p_{min,1}$ and $p_{min,2}$ behave similarly to p_{max}. Firstly, the absolute value of both amplitudes increases with increasing injection pressure. The variation is particularly strong in the case of a setup with a small connection line diameter. With respect to the geometry the plots support the earlier result through predicting an amplitude increase for long pipes and a reduction of the same parameter for large line diameters. Again, the correlation of $p_{min,1}$ and $p_{min,2}$ to the geometry is not linear, but shows the same trends as for the maximum positive pressure amplitude (Figure 70). If the values for $p_{min,1}$ and $p_{min,2}$ are compared to each other, it emerges that for large injection pressures and small connection pipe diameters the amplitudes of the second pressure undershoot are normally smaller than the first pressure minimum. In all other cases, the plots in Figure 71 and Figure 72 show the opposite tendency.

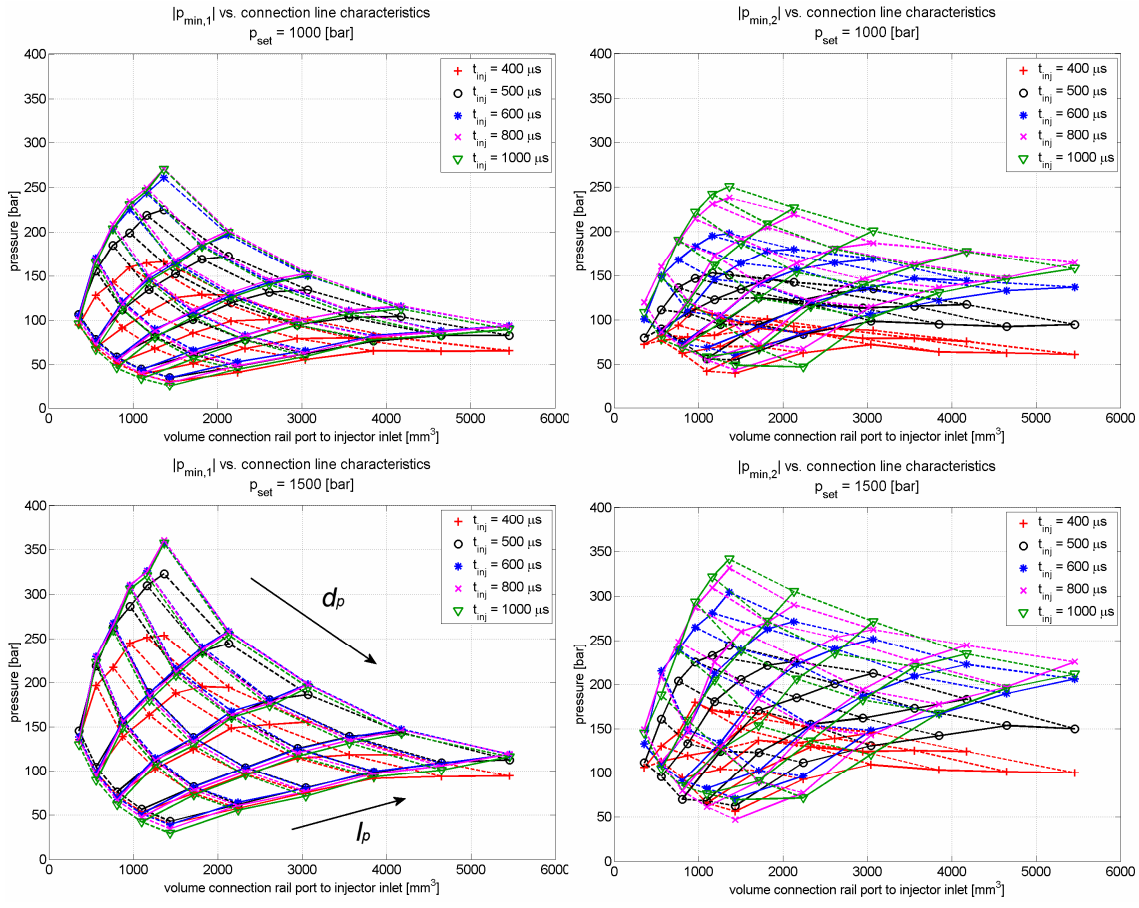

Figure 73. $p_{min,1}$ (left) and $p_{min,2}$ (right) as f(p_{set}, t_{inj}, l_p, d_p) - main variable: t_{inj}.

The differences between both negative amplitudes become more evident when plotting the absolute values of the respective amplitudes $p_{min,1}$ and $p_{min,2}$ with the injection time t_{inj} as the main variable. As exemplified for two injection pressures on the left hand side of Figure 73,

the first pressure undershoot becomes independent of the injection duration for injection times longer than 500 µs. The graphs on the right hand side of Figure 73 depict for the same configuration the values for $p_{min,2}$. In the latter case the amplitudes clearly show some dependency on the injection duration. Usually, the longer the injection duration, the larger becomes the amplitude. The same as for p_{max}, the variation of $p_{min,2}$ as a function of t_{inj} is stronger at the lower end of the injection time range. As a general remark, it is emphasised at this point that in the case of an injection time of 400 µs, the findings are somewhat different from the overall trends. This result underlines the special state of the injector at this operating point as has been already indicated during the discussion of the measurement results in chapter 3.1.4.

Comparison of oscillation frequencies

The frequency of the pressure oscillation at the injector inlet is, like the amplitudes of the initial pressure variation, an important parameter in the fuel injection process, as it defines the timing of the peak values. The same as for the previous FFT analyses of the measurement data (see, for example, chapter 3.1.2), the present investigation is based on a DFT of the simulated pressure signal at the injector inlet, *pII*.

Firstly, Figure 74 and Figure 75 present the calculated main frequencies for two arbitrary system configurations as a function of injection duration and injection pressure.

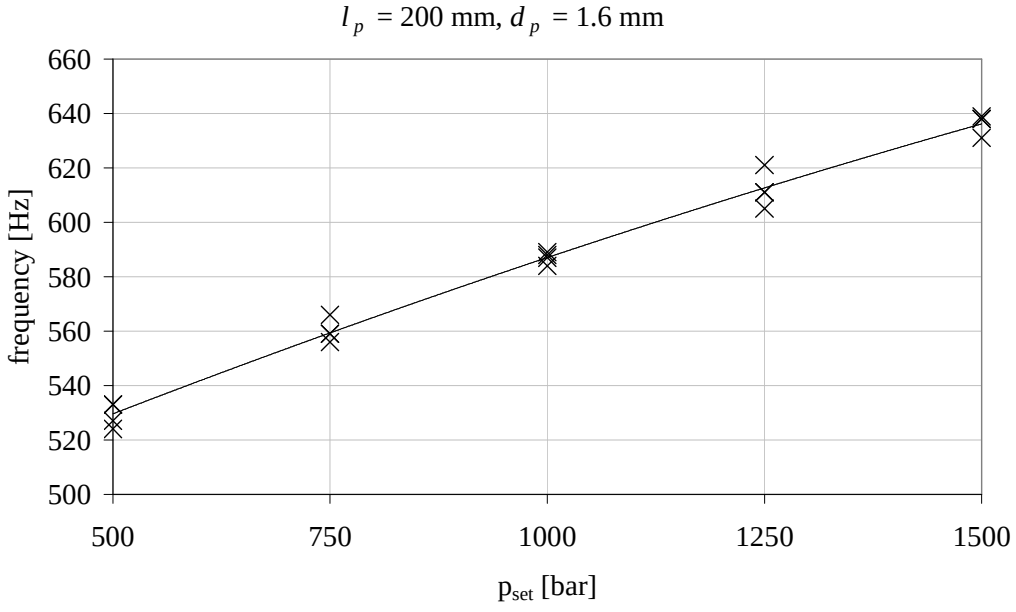

Figure 74. Main frequencies of *pII* signal as f(t_{inj}, p_{set}); l_p = 200 mm, d_p = 1.6 mm.

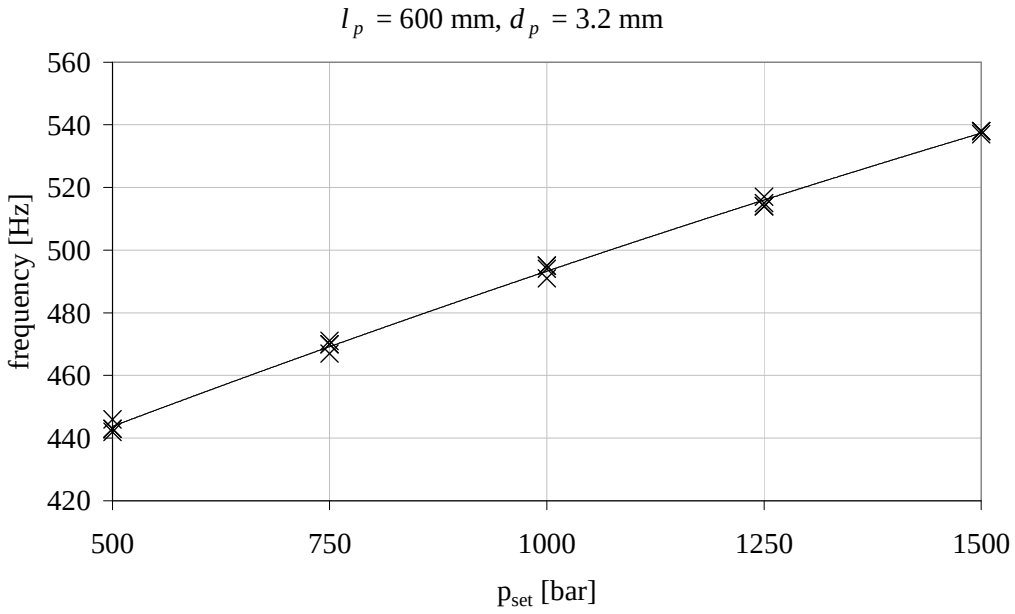

Figure 75. Main frequencies of *pII* signal as f(t_{inj}, p_{set}); l_p = 300 mm, d_p = 3.2 mm

Both plots confirm the results from the measurement (see, for example, page 76, Figure 41), that is, the oscillation frequency is not a function of the injection duration t_{inj}. On the other hand, the graphs clearly show that the characteristic time of the oscillation decreases, along with a shift to higher injection pressures. It is worth mentioning that the frequency does not increase linearly as a function of set pressure. The trend lines indicate that the slope of the curve gets smaller for large pressure values. In general, the oscillation frequency is related to the speed of sound at which information is passed through the system. The latter parameter is not constant, but depends on the static pressure. By plotting for a fluid the speed of sound over pressure, the result is a downwards bended curve [79]. Accordingly, the shape of the curves above has been expected.

As a result of Figure 74 and Figure 75, the parameter for the injection duration, t_{inj}, is excluded in the following discussion of the oscillation frequency. All presented values for f correspond, therefore, to a single value, which represents the average of all injection times at a particular system setup (l_p, d_p, p_{set}).

Figure 76 presents in a single graph the variation of the oscillation frequency for various connection pipe lengths, diameters, and injection pressures. The explicit frequency value is plotted as before over the volume between rail port and injector inlet. Analogous to the previous two figures, Figure 76 underlines that the oscillation frequency increases for

increasing injection pressure. In this context it is interesting to notice that the rate of the variation depends on the geometry of the connection line. A small line diameter (d_p = 1.6 mm) tends to reduce the impact of the injection pressure on *f*. This is particularly true when a long connection pipe is used. For large diameters, on the other hand, the plot identifies larger steps between the explicit frequency values (see, for example, l_p = 100 mm, *f* variation between p_{set} = 500 bar and p_{set} = 1500 bar at d_p = 1.6 m and 3.2 mm).

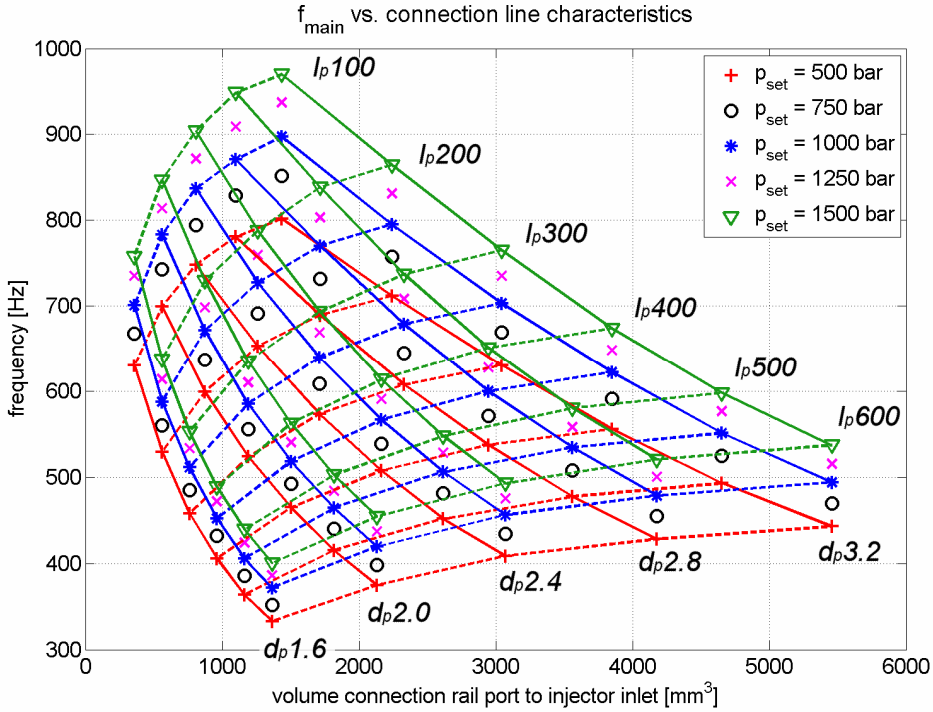

Figure 76. Main frequencies (averaged) as f(line geometry, p_{set}).

Concerning the correlation of geometry and oscillation frequency, Figure 76 firstly confirms that *f* drops along with an increase of the distance between rail and injector. As has been explained in the discussion of the measurement results, this finding is not surprising, but expected. The same cannot be said when studying the values of *f* for different line diameters. Analogous to the measurements, the simulation model predicts a rise of the oscillation frequency as a function of the flow cross-section. The latter phenomenon is especially emphasised for short connection lines. For the opposite case, that is, for long connection pipes, the impact of d_p reduces if large diameters are selected. In fact, it appears that the frequency tends to aim for a finite value.

An interesting observation can be made by plotting the frequencies along constant pipe diameters and lengths. In Figure 77 the frequency at a particular pressure, $p_{set,i}$, is normalised

to the value that corresponds to a setup with a pipe length of l_p = 100 mm. By applying this procedure to all injection pressures and line diameters, it can be seen that, firstly, the injection pressure has no effect on the frequency variation due to a change in pipe length - at various pressures the ratio of f_{l1} to f_{l2} is nearly constant, that is, the graph shows horizontal lines for constant line lengths and variations in p_{set}. Secondly, the plot reveals that the variation of the oscillation frequency as a function of rail to injector distance is stronger at the lower end of the length range. The slightly more packed lines in the centre of Figure 77 (around 0.6) show that the impact of the connection length becomes smaller if long pipe lengths are chosen.

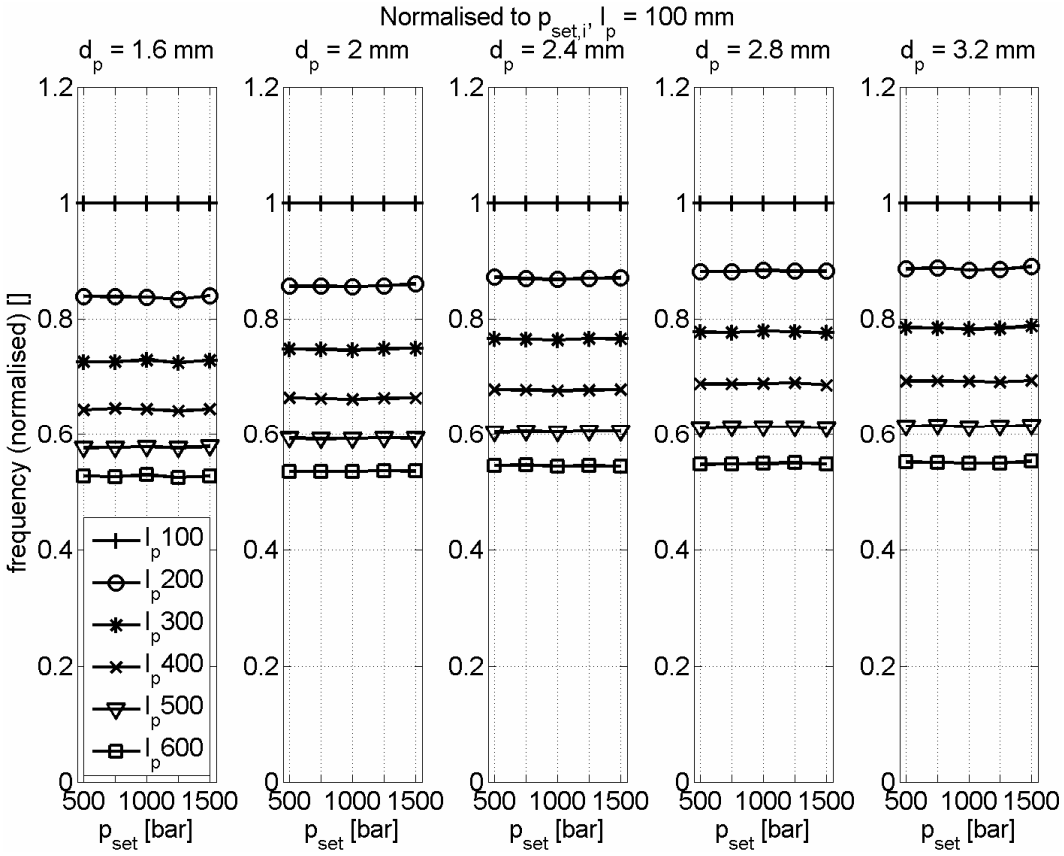

Figure 77. Impact of l_p on oscillation frequency, normalised.

Figure 78 is equivalent to Figure 77 in the way that it depicts the correlation between the changes of oscillation frequency due to an increase or decrease, respectively, of the connection line diameter. It should be noted that only three out of the six investigated lengths are presented in this plot. All data points are normalised to the case with d_p = 3.2 mm at the respective injection pressure. The figure shows that the impact of the flow cross-section on f is not depending on the injection pressure; again, the graphs are characterized through fairly horizontal lines for constant diameter and variable pressure. As before, the effect of d_p is not

linear. Indeed, it can be seen that change of frequency as a function of line diameter increases considerably for variations of the flow cross-section at the lower scale of the studied range.

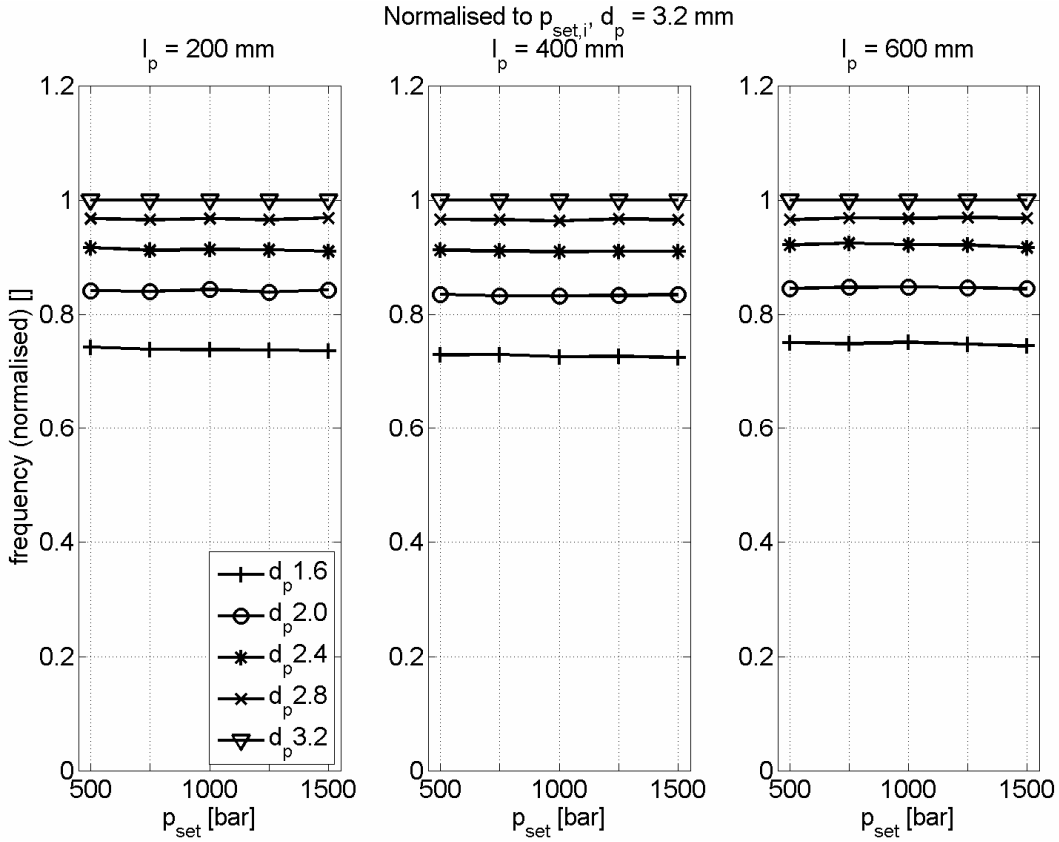

Figure 78. Impact of d_p on oscillation frequency, normalised.

By recapitulating the main findings of this sub-chapter the question emerges as to whether it would be possible to obtain similar findings through applying a more simplified method from, for example, chapter 2.3. Firstly, the method based on the natural frequency of the hydraulic line is in its present form clearly not adequate to describe the system. Since the formulation (equation (88)) relates the oscillation frequency to the line length, but not to its diameter, it is not possible to account for a frequency variation as a function of the latter parameter. Alternatively, the method derived from electromagnetic oscillations in AC circuits seems more advanced due to the consideration of the flow cross-section in the hydraulic capacitance (equation (90)) and inductance term (equation (92)). On closer examination, however, it can be shown that the line diameter cancels out if it is put into the final equation for the oscillation frequency (equation (94)). Accordingly, this approach, in principle, also relates the frequency only to the distance between rail and injector.

Table 3. Example: comparison of simplified (AC circuit) vs. GT-Fuel model.

Setup	p_{set} = 1000 bar, l_p = 400 mm (fluid properties based on GT-Fuel data)		
Oscillation frequency [Hz]	d_p = 1.6 mm	d_p = 2.4 mm	d_p = 3.2 mm
Simplified model (AC circuit)	135.9	182.5	217
GT-Fuel model	450	566	622

Table 3 compares for an arbitrary chosen setup the computed oscillation frequencies of the simplified model to the data from the GT-Fuel simulation as a function of line diameter. Firstly, it is apparent that the simplified model underpredicts significantly the main oscillation frequencies. Consequently, it has to be concluded that this approach is not appropriate to gain useful information about the system. The idea of representing the circuit by a single set of equivalent capacitance and inductance is therefore not adequate. It does not help much in this context that the general trend between frequency and diameter is predicted correctly. As can be seen in equation (99) and equation (100) (see page 52), the latter phenomenon is the result of the individual section terms being nested in the equivalent C_H and L_H terms.

Attenuation of pressure oscillations

The damping of the oscillation after system excitation is, in comparison to the pressure amplitudes and the oscillation frequency, only of minor importance. In the case of a multiple injection strategy, the needle lift profile is characterised by a very fast sequence of individual injections. Typical dwell times between two subsequent needle lifts are in the range of some hundred microseconds to a few milliseconds [11]. The oscillation decay, on the other hand, requires approximately 8 to 20 ms (see, for example, page 60, Figure 18), which means that a subsequent injection is already triggered before the system damping fully affects the previous oscillation. Certainly, the situation changes when alternative injection strategies are considered [11, 26]. If the time between two subsequent injections is large enough, the damping of the oscillation might become a more important factor.

Two methods are employed in this study in order to evaluate the decay of the oscillation. Firstly, it is assumed that the pressure variation that is triggered by a single injection behaves mathematically the same as a dynamic system of second order, which reacts upon a step input signal.

For the latter case, the system response can be described by:

$$f(system) = K_S \cdot e^{-\frac{\omega_e \cdot K_d}{\sqrt{1-K_d^2}} \cdot t} \cdot \left(cos(\omega_e \cdot t) + \frac{K_d}{\sqrt{1-K_d^2}} \cdot sin(\omega_e \cdot t) \right) \quad (118)$$

This equation was fitted to the simulated pressure curve *pII* through employing the *lsqcurvefit* algorithm of the Matlab optimization toolbox. The latter method, which is based on a least-squares approach, produces through iteration some numeric values for the static transmission coefficient K_s, the damped natural frequency ω_e, and the equivalent damping coefficient K_d. Figure 79 presents a typical plot with the original data and the guess curves before and after applying the optimization routine.

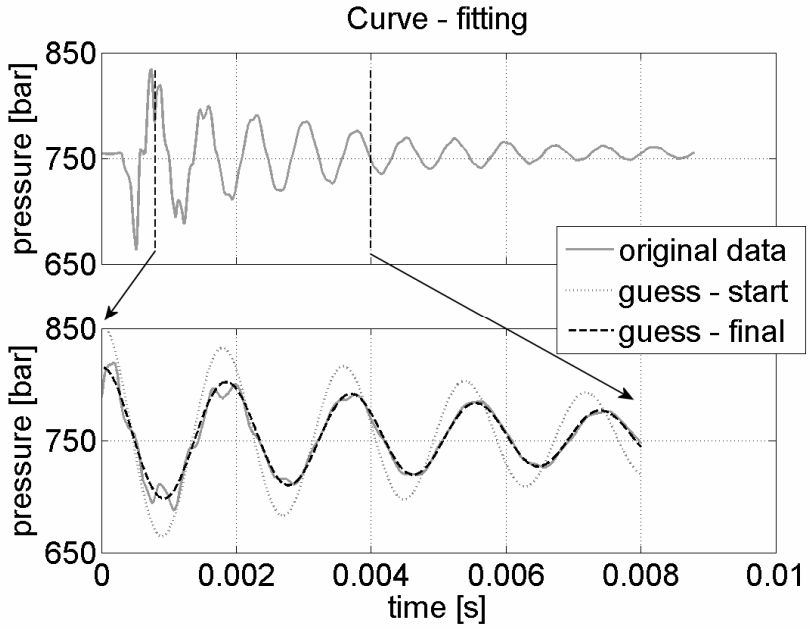

Figure 79. Method 1: example of curve fitting procedure.

It must be pointed out that the final value for K_d depends, to some degree, on the initial settings of the guess function. Generally, the analysis range starts at the first positive peak. In this way, any transient effects during the initial stage that can be attributed to the injector needle operation are greatly minimised. By considering all simulations, it can be summarised that the damping coefficient is smaller than 0.15. In fact, because of the small total level of K_d, it can not be excluded that slight uncertainties in the setup definition of the optimization routine might have a considerable impact on the final result.

Due to the limited accuracy of the former method, a second approach is introduced, which qualitatively evaluates the damping of a single configuration through comparing it directly to other setups. The idea of this method is based on the evaluation of the peak to peak variation for both the positive and negative amplitudes. As each of the peak values can be plotted along a common variable that represents a counter for the oscillation period, it is possible to show visually the rate of the oscillation decay.

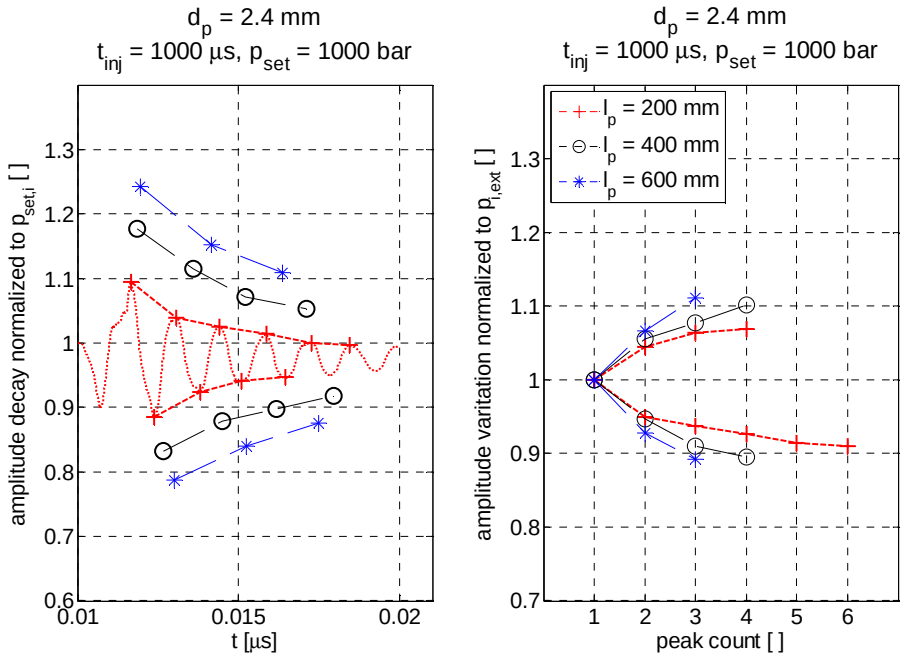

Figure 80. Method 2: example peak to peak variation.

Figure 80 depicts this approach in a graphical way for a setup with t_{inj} = 1000 µs, p_{set} = 1000 bar, d_p = 2.4 mm, and three connection pipe lengths. Firstly, each pressure history at *pII* is normalised by the corresponding mean pressure level (Figure 80, left). Except for the l_p = 200 mm case, only some representative extreme values are plotted. In a second step, the negative peaks are normalised by their respective largest value, and the positive peaks through the smallest number. Each array is subsequently plotted in a new graph (Figure 80, right). To decouple the frequency from the damping rate, the time axis is replaced by a simple peak count. The branch with the concave side pointing downwards corresponds to the negative peaks, the opposite swing to the positive ones. The bigger the gap between two data sets, the larger the attenuation of the oscillation. In the present example it can be said that the configuration with the longest connection line is characterised through a higher damping rate than the l_p = 400 mm and 200 mm case. It has to be noted that, because of the normalisation

step, the second method is not suitable to compare setups with different injection pressure to each other.

In Figure 81 some selected results for the oscillation damping are presented that are based on the first method. The main comparison variable is the injection pressure p_{set}. The individual plots show consistently that a high injection pressure results in a stronger oscillation damping. As has been indicated before, the total variation of the values is rather small. Accordingly, the findings should be understood as a trend that describes the differences on a detailed level.

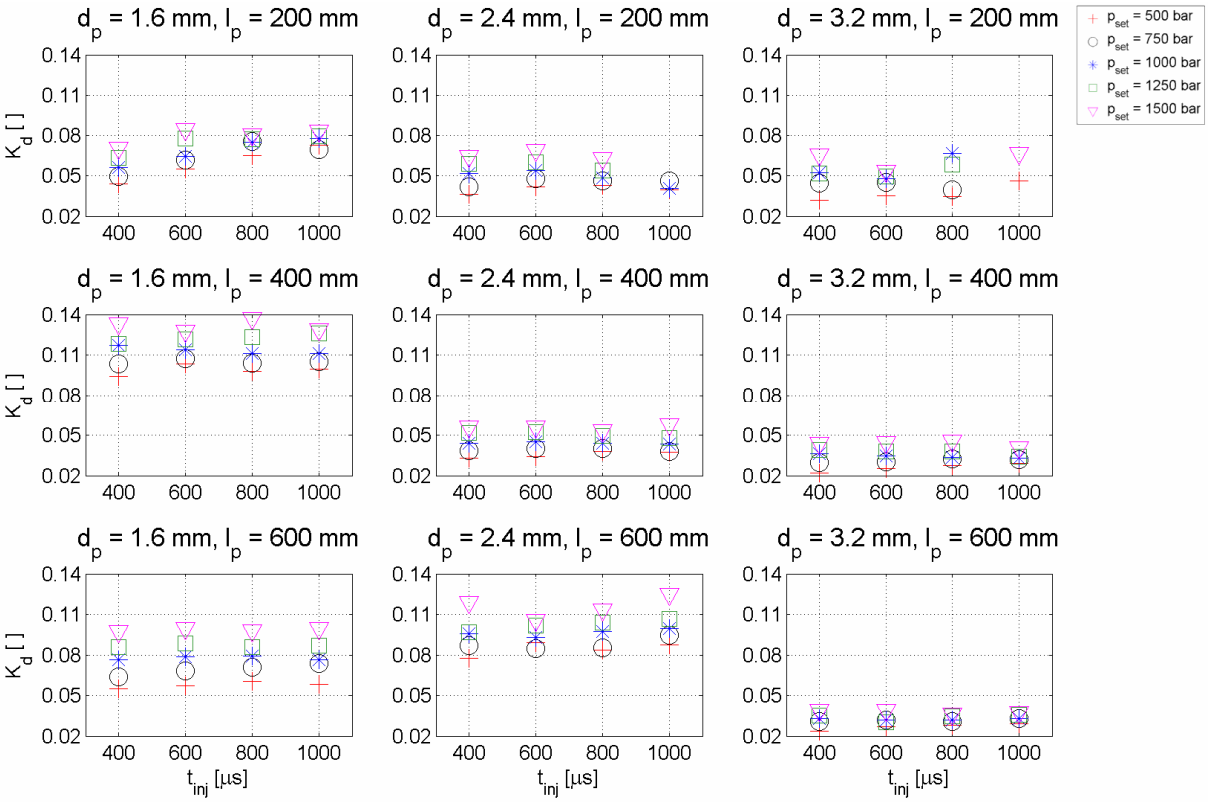

Figure 81. Method 1: oscillation decay; main variable: p_{set}.

Figure 82 exemplifies for two pipe configurations and an injection pressure of p_{set} = 1000 bar the impact of the injection duration on the decay of the oscillation. Generally, the curves are very similar, that is, the effect of t_{inj} on the normalised amplitude variation is only minor. It is eventually possible to detect a slightly stronger oscillation damping for long injection times.

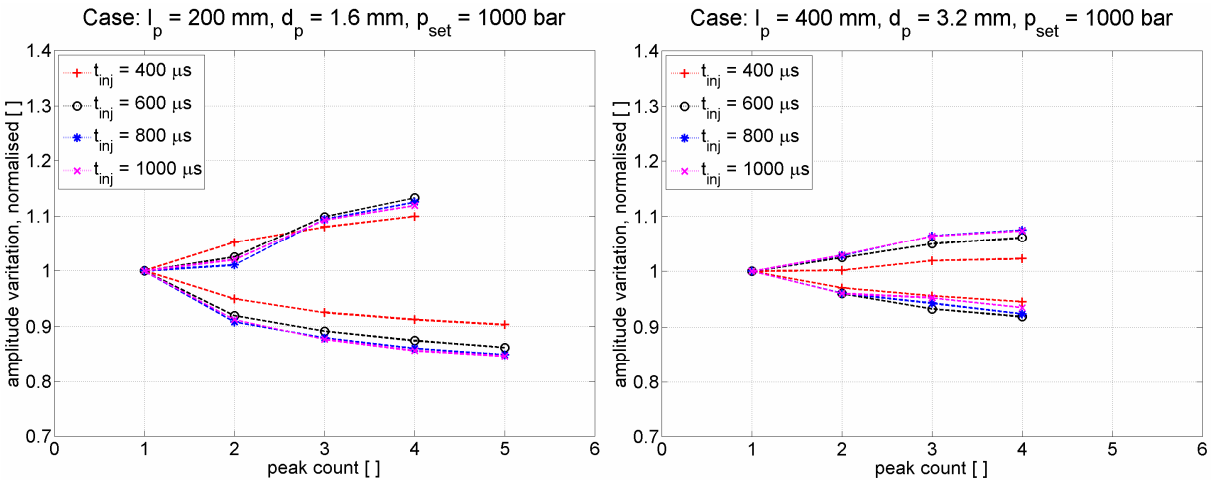

Figure 82. Method 2: oscillation decay (example graphs); main variable: t_{inj}.

Concerning the correlation between d_p and the attenuation of the oscillation, it can be said that a trend appears that supports an increase of damping for small connection line diameters. Figure 83 provides two examples of this statement. The first method aligns with this finding, as in Figure 81 the lowest values for K_d are generally computed for setups with the largest flow cross-section.

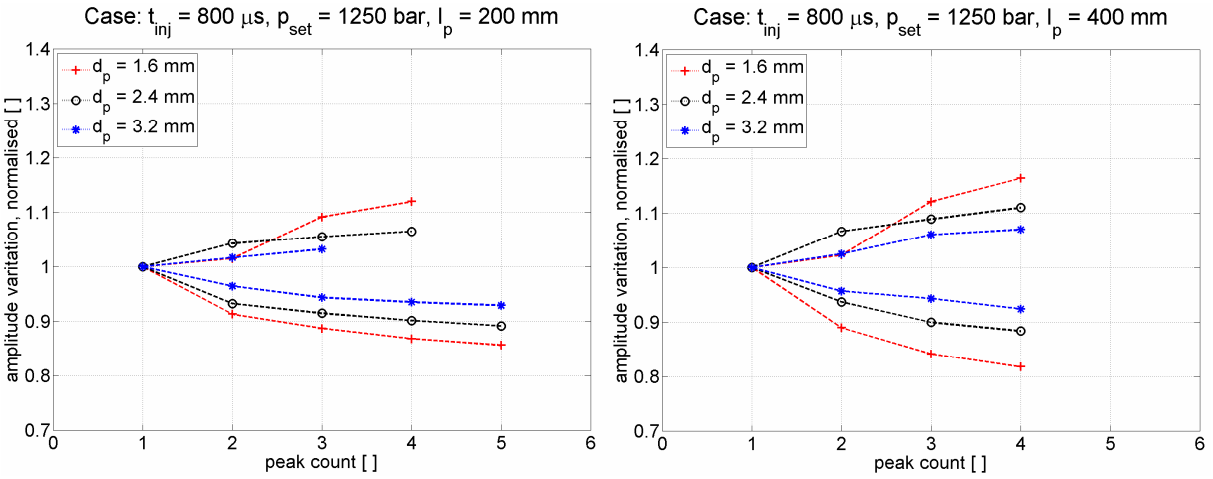

Figure 83. Method 2: oscillation decay (example graphs); main variable: d_p.

If, temporarily, wave interfering phenomena are excluded, the oscillation is damped only due to viscous friction effects. A pipe with a small diameter has a smaller wetted surface than a line with a big diameter, since the area is proportional to the diameter. On first inspection, this argument supports the idea that an oscillation is maintained longer in a small pipe due to less area and friction forces. However, if identical mass flows are assumed for both the small and big pipe, the flow velocity in the small line must be higher, and with it the velocity gradients near the wall. The latter fact may explain why, overall, the damping in the small pipe configuration is higher. The initial assumption concerning the damping due to interference

effects is probably not fully correct for the final CR system, as it is likely that differences in expansion and contraction ratios cause a stronger or weaker transmission of pulsations.

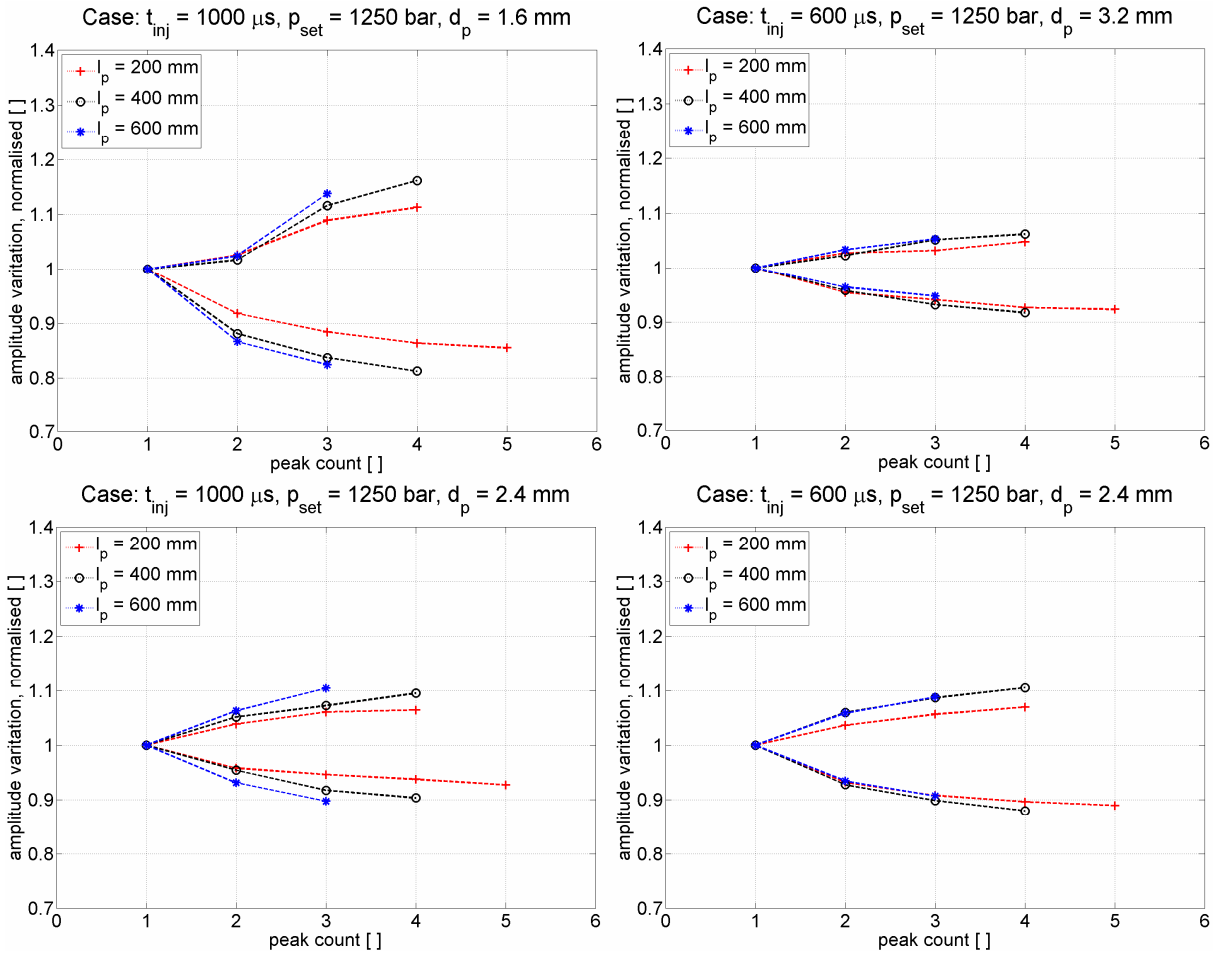

Figure 84. Method 2: oscillation decay (example graphs); main variable: l_p.

Method 1 suggests that the impact of the connection line length on the damping depends strongly on the diameter of the pipe. For d_p = 1.6 mm, Figure 81 shows the highest damping coefficients for the intermediate pipe length; if the diameter equals 2.4 mm, the situation changes and the strongest damping appears for the longest pipe setup. It has to be pointed out that it is not possible to detect the same behaviour by the second method. As the upper-left graph of Figure 84 exemplifies for a configuration with d_p = 1.6 mm, the curves for l_p = 400 mm and 600 mm are very similar. In fact, it is possible to say that both cases promote a somewhat higher damping than the system with the shortest pipe length. If a diameter of 2.4 mm is chosen, the results of method 2 align with the findings of the first method if the injection duration is long (Figure 84, bottom-left). For shorter t_{inj}, the differences in oscillation attenuation diminish (Figure 84, bottom-right and Figure 80). Finally, for the

largest flow cross-section, it is not possible to see any differences in oscillation damping as a function of the distance between rail and injector.

Injection rate as function of system configuration

The plots in Figure 85 are the numerical equivalent to the measurement results in Figure 50 and Figure 51. On the left hand side is presented the impact of the injection pressure on the total amount of injected mass at three different durations of the single injection. As for the measurement, the simulation results clearly show an increase of the injected mass for high set pressures. It is apparent that the injected mass is also affected through the connection line geometry between rail and injector. If the injection time is long (Figure 85, bottom-left), the total amount of injected fuel is less for a long connection pipe configuration than for a short line setup - this is especially true for small line diameters. On the other hand, if the length is kept constant, the graph illustrates that, generally, a larger flow cross-section also leads to a higher flow rate through the nozzle holes. The plots on the right half of Figure 85 use the injection duration as the main variable. Firstly, the results confirm the expectation, that is, long injection times lead to high injection rates. Secondly, the plots for p_{set} = 500 bar, 1000 bar and 1500 bar illustrate clearly that the impact of the line geometry on the injection rate diminishes for injection times equal or less than t_{inj} = 600 µs. While for a setup with long injection time the mass values appear evenly spread as a function of line geometry, the plots indicate that in the case of short needle openings the data points are located within a narrow band.

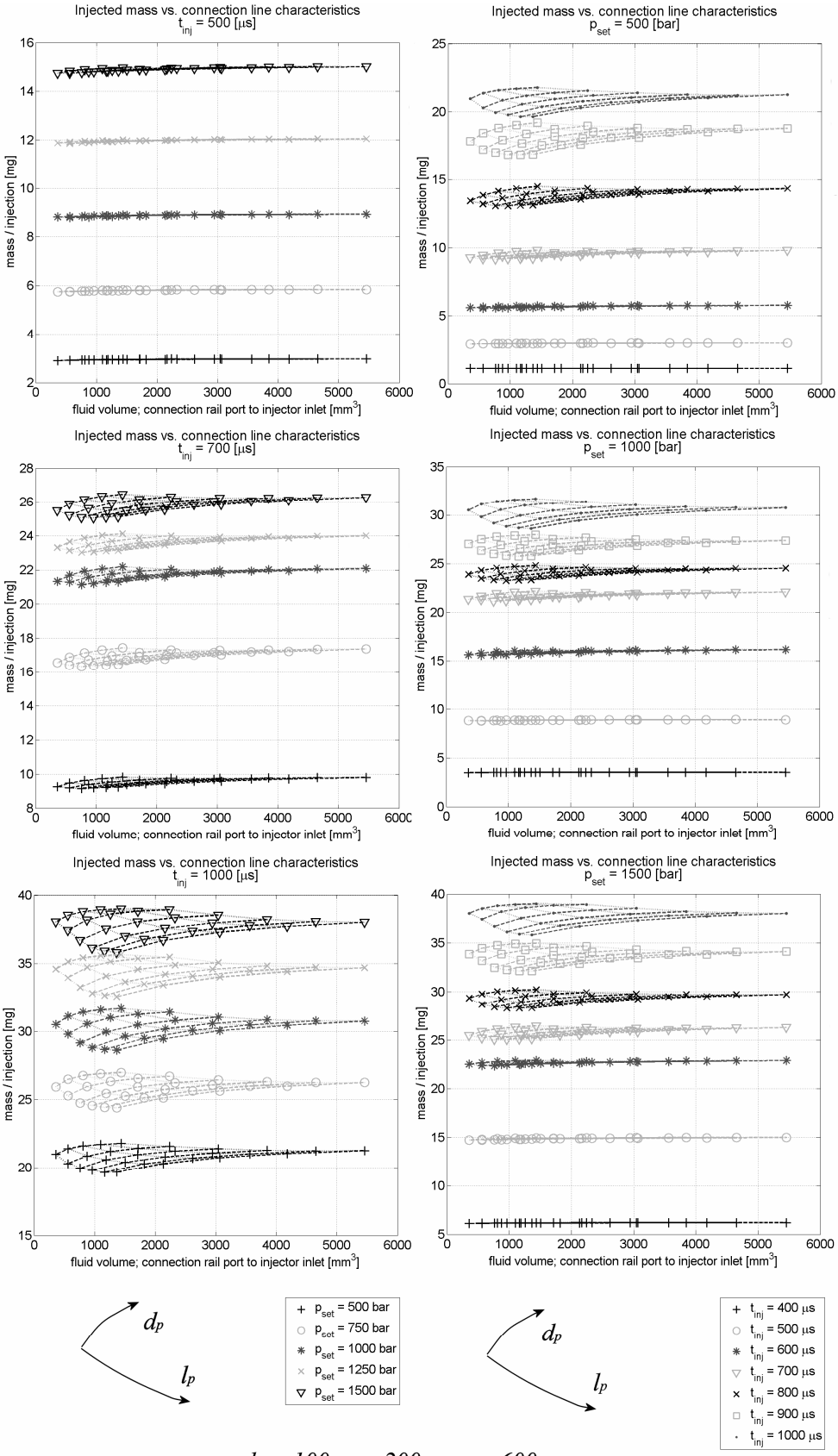

l_p = 100 mm, 200 mm, ... 600 mm
d_p = 1.6 mm, 2.0 mm, ... 3.2 mm

Figure 85. Mass / injection as f(pipe geometry, p_{set}), left and mass / injection as f(pipe geometry, t_{inj}), right.

3.2.6 Numerical study of double injection event

The numerical study of double injection events are based on the same assumptions as the experimental analysis in chapter 3.1.5. All simulations were conducted for an injection pressure of p_{set} = 1000 bar and an injection time of t_{inj} = 600 µs for both injection events. If not otherwise specified, the system was defined by connection pipes with l_p = 400 mm and d_p = 2.4 mm. The step size of the injection period T_{inj} was refined to allow for a more detailed representation of the phenomena. Table 4 summarises the studied injection periods[1].

Table 4. Definition of injection period T_{inj}.

Configuration	**1**	2	**3**	4	**5**	6	**7**	8	**9**
T_{inj} [ms]	1.4	1.637	1.875	2.112	2.35	2.562	2.775	2.987	3.2

The presentation of the results starts in Figure 86 with a comparison of the measured and simulated pressure signal at the injector inlet, *pII* (see also measurement results, Figure 53 and Figure 54). As can be seen, the simulation model (solid lines) agrees well with the recorded signals (dashed lines) for almost all injection periods. The largest discrepancy between measurement and simulation is found for the setup with T_{inj} = 2.775 ms (Figure 86, bottom). In this configuration the second needle opening is timed so that the newly introduced pressure wave is in the opposite phase to the one from the first injection. For times longer than about 14 ms the numerical model generally predicts too large amplitudes. On the other hand, the shape of especially the first three peaks corresponds fairly well with the experimental curve. It is therefore concluded that the utilised model is suitable to predict the pressure history at the injector inlet also for other configurations.

Because of the good fit between measured and simulated *pII*-curves, no further plots are presented that explicitly discuss the impact of the second injection event on the oscillation frequency. Further information about the latter parameter can be found in chapter 3.1.5, for example, Figure 55.

[1] Configurations in **Bold** are also studied by experimental measurement (see chapter 3.1.5)

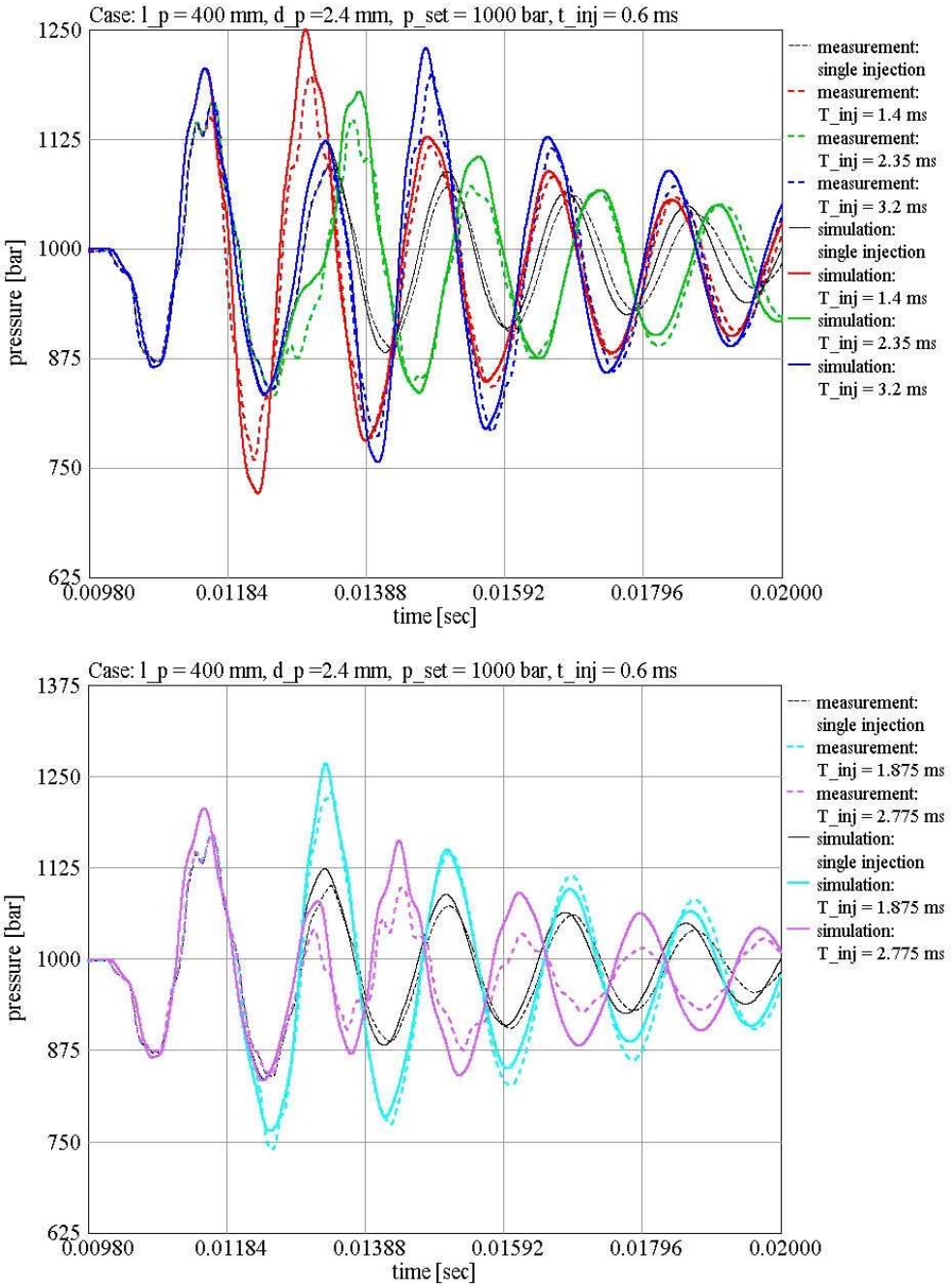

Figure 86. Double injection - pressure *pII*; measurement (dashed) vs. simulation (solid).

Figure 87 compares the amount of the injected mass of the second injection (dot) to the first injection (horizontal line) for both the measurement and the simulation series. Overall, it can be said that the simulation model captures the correlation between the parameters well. In analogy to the measurement results, the simulation model predicts for the shortest injection period a slightly higher mass flow rate during the second injection event. For configurations that trigger the second needle opening between the maximum and the second minimum peak, the injected mass for the second needle stroke reaches a minimum. Despite the slight

discrepancy of *pII* at T_{inj} = 2.775 ms, the prediction of the injected mass for the second injection at that particular operation point fits well with the overall trend

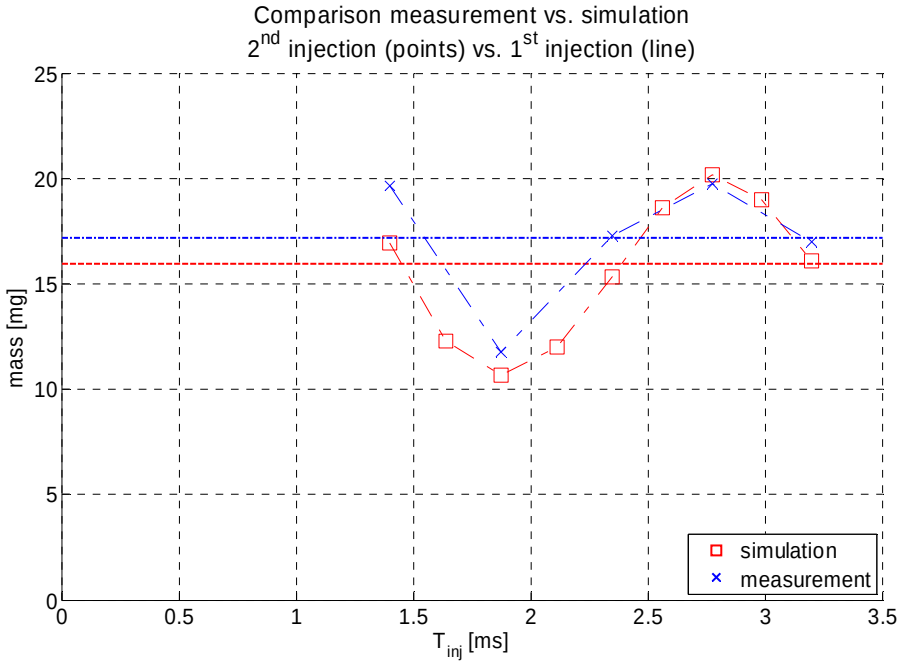

Figure 87. Double injection - mass per injection; measurement (dashed) vs. simulation (solid) (l_p = 400 mm, d_p = 2.4 mm, p_{set} = 1000 bar, t_{inj} = 600 µs).

Figure 88 and Figure 89 exemplify the impact of the connection line geometry on the mass flow rate of the second injection as a function of the injection period. Generally, a geometry modification causes the characteristic curve to shift either to the left or right. If, for example, the pipe flow cross-section is reduced, the smallest amount of fuel for the second injector activation is injected at a later point in time. In this particular case T_{inj} is increased from 1.875 ms to about 2.35 ms (Figure 88, case d_p = 2.4 mm and 1.6 mm). This trend seems plausible, since a smaller line diameter also leads to a lower oscillation frequency (see, for example, Figure 76), which in turn slows down the individual pressure peaks in the system. An increase of the flow cross-section consequently causes a shift of the original curve to the left. It is, however, interesting to notice that the gap between the d_p = 2.4 mm and the 3.2 mm case is considerably smaller than the difference between the d_p = 2.4 mm and 1.6 mm pair (Figure 88). Figure 89 presents the same parameters, except that the line diameter is replaced by the connection pipe length. Overall, the trend is very similar to the former plot. If a longer pipe between the rail and injector is chosen, the smallest mass flow rate of the second injection happens at a larger time period. A shorter pipe leads, conversely, to the appearance of the minimum at a small T_{inj}. Indeed, the graph of the l_p = 200 mm, d_p = 2.4 mm setup in Figure 89

shows clearly that the next extreme values follow more shortly after each other when the distance between rail and injector is small. Again, this trend aligns well with the findings for the oscillation frequency (Figure 76).

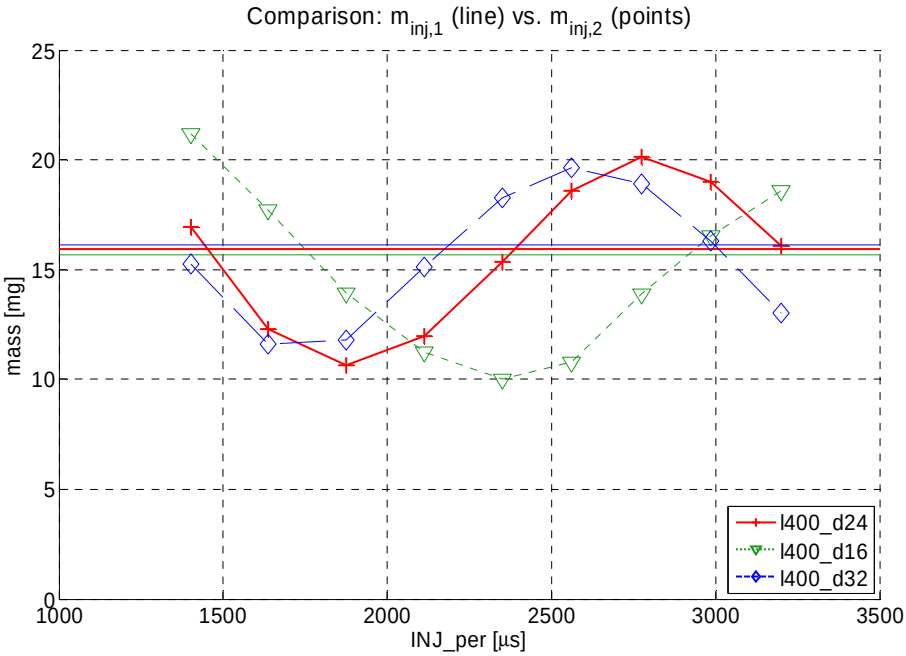

Figure 88. Double injection - mass per injection; main variable: d_p (l_p = 400 mm, p_{set} = 1000 bar, t_{inj} = 600 µs).

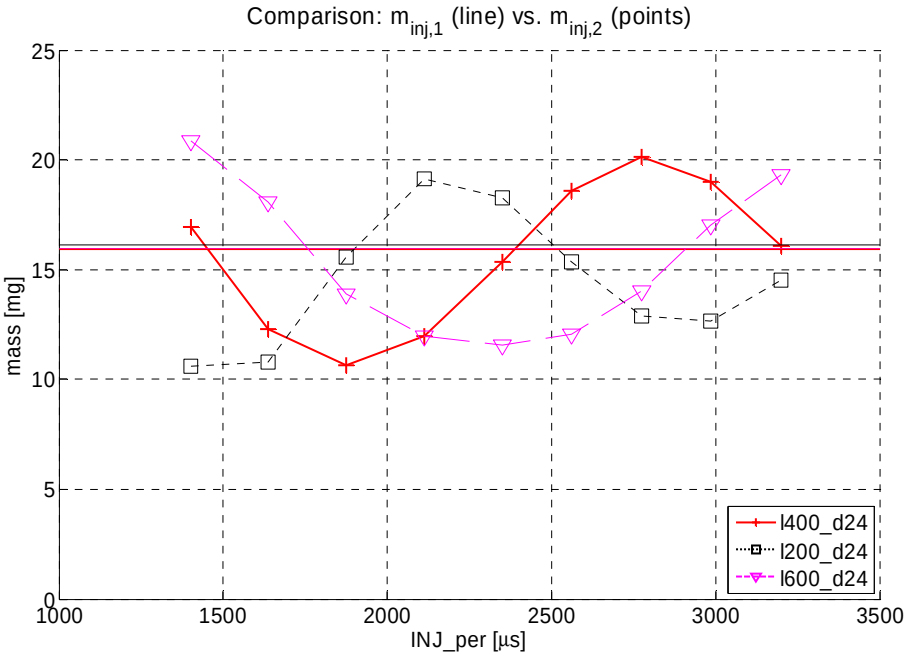

Figure 89. Double injection - mass per injection; main variable: l_p (d_p = 2.4 mm, p_{set} = 1000 bar, t_{inj} = 600 µs).

Based on the definition in Table 4, Figure 90 presents the simulated pressure histories at the injector inlet for a double injection with the default setup. In the top-left graph the second injection is triggered between the first positive peak and the p_{set} crossing. It can be seen that such a configuration causes a significant increase of the subsequent negative and positive peaks. If the injector is activated for the second time between the p_{set} crossing ($t \approx 11.84$ ms) and the second negative peak, the picture alters considerably. As the top-right graph shows, the amplitudes decrease greatly for larger injection periods. The bottom-left plot presents the setups with the second injection starting between the second negative peak and $t = 12.775$ ms; the curves clearly show that the oscillation of the first injection is in opposite phase to the wave that is triggered by the second needle opening. Particularly for $T_{inj} = 2.775$ ms, it is possible to observe a considerable disturbance of the original wave pattern. Finally, the bottom-right graph illustrates the cases with an injection period between the second p_{set} crossing and the second positive peak. With the oscillation phases still in opposite direction,

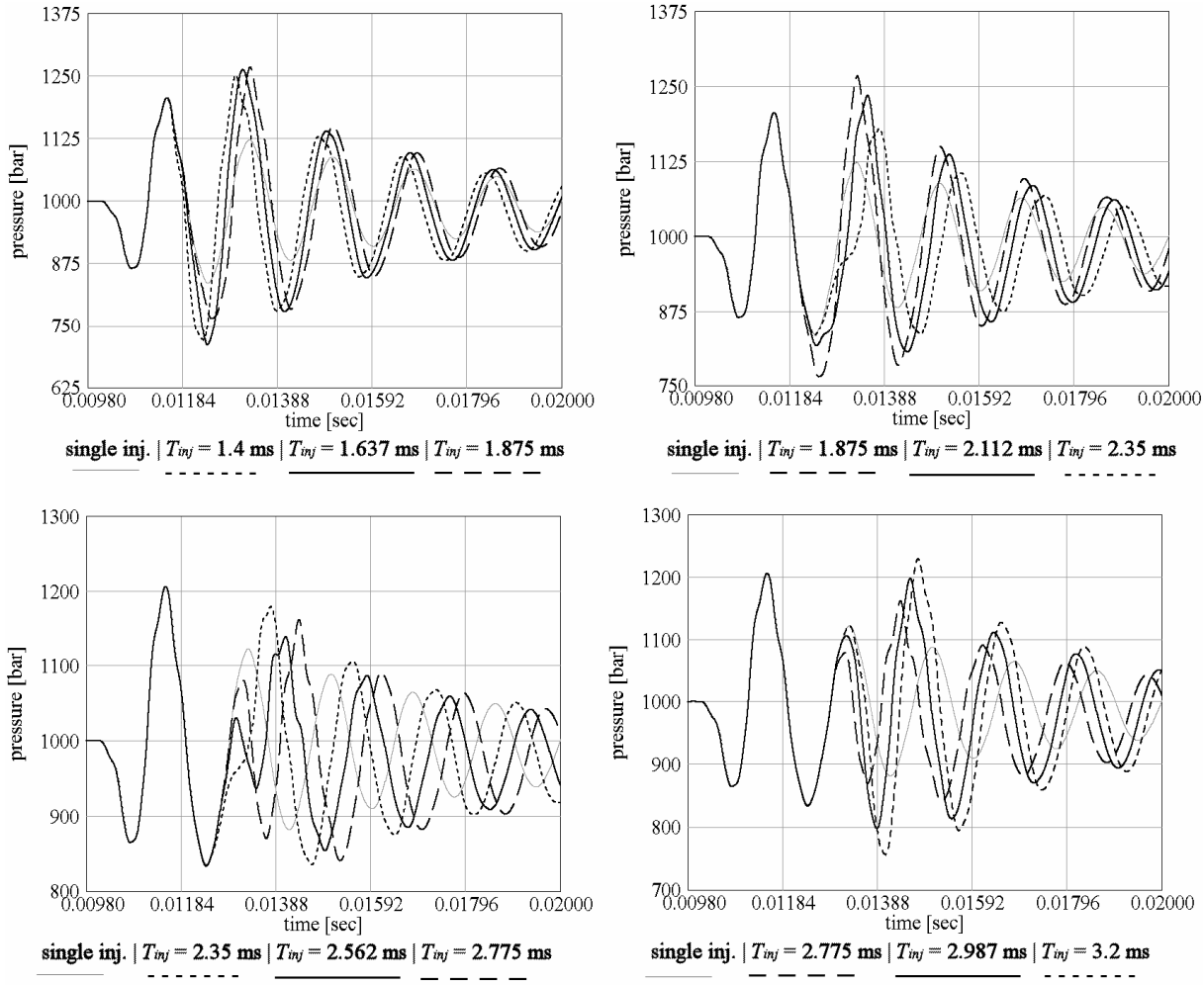

Figure 90. Double injection - pressure *pII*

($l_p = 400$ mm, $d_p = 2.4$ mm, $p_{set} = 1000$ bar, $t_{inj} = 600$ µs)

the profile of the second positive peak now tends to align to a common shape. On the other hand, the plot reveals that the subsequent peaks remain strongly affected by the injection period. For example, the simulation with T_{inj} = 3.2 ms predicts a significant increase of the following minimum and maximum peaks.

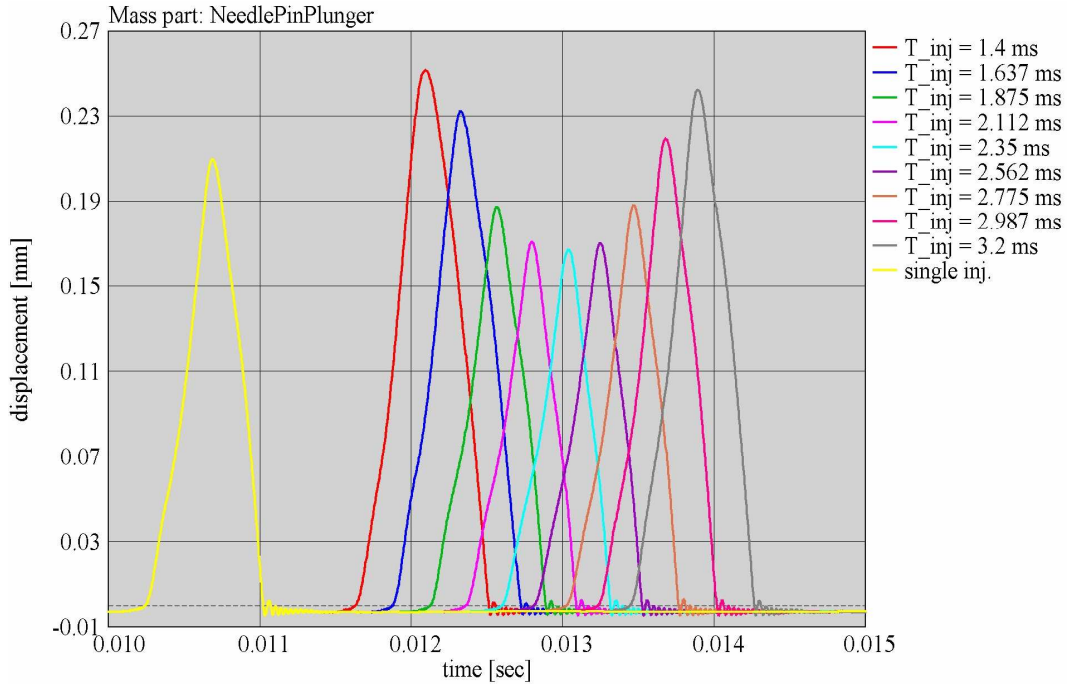

Figure 91. Double injection - plunger displacement

(l_p = 400 mm, d_p = 2.4 mm, p_{set} = 1000 bar, t_{inj} = 600 µs).

Figure 91 presents, for example, for the configuration l_p = 400 mm, d_p = 2.4 mm, p_{set} = 1000 bar, and t_{inj} = 600 µs the displacement of the needle-pin-plunger mass as a function of various injection periods. Firstly, all needle lifts are characterised by a triangular shape of the displacement curve. Because of the short injection time the mass actually never reaches its full stroke close to 0.27 mm. Secondly, the plot reveals that the maximum needle-pin-plunger displacement is strongly affected by the forces acting above the plunger and below the needle. This force equilibrium causes the injector to open during the second injection to a greater or smaller extent, respectively. It is in this context worth mentioning that the smallest lift for the second injection is predicted for an injection period of 2.35 ms. The case with the smallest mass flow rate (T_{inj} = 1.875 ms), on the other hand, is characterised by a somewhat larger lift. Consequently, it can be concluded that the actual mass flow rate during the second injection is a combination of the actual needle-pin-plunger mass displacement and the instantaneous pressure head.

3.3. Numerical analysis of hydraulic circuit and component properties

The present chapter represents an extension to the previous chapter 3.2. By using the same model as before, chapter 3.3 focuses on the discussion of parameters that are not easily accessible through measurements. Secondly, this chapter underlines the benefits of numerical simulation models for analysis purposes. On the one hand, the model is used to investigate the impact of, for example, wall elasticity and injector characteristics on the findings. Finally, this chapter closes with a discussion and evaluation of alternative designs of the CR circuit.

3.3.1 Analysis of variables that are not readily available by measurements

Figure 92 presents a comparison of the static pressure at the injector inlet and at the fuel gallery (see, for example, Figure 15). It should be noted that at this point only one example circuit is presented, that is, the results correspond to the setup with l_p = 200 mm, d_p = 2.4 mm, t_{inj} = 600 µs (single injection), and the three injection pressures p_{set} = 500 bar, 1000 bar, 1500 bar.

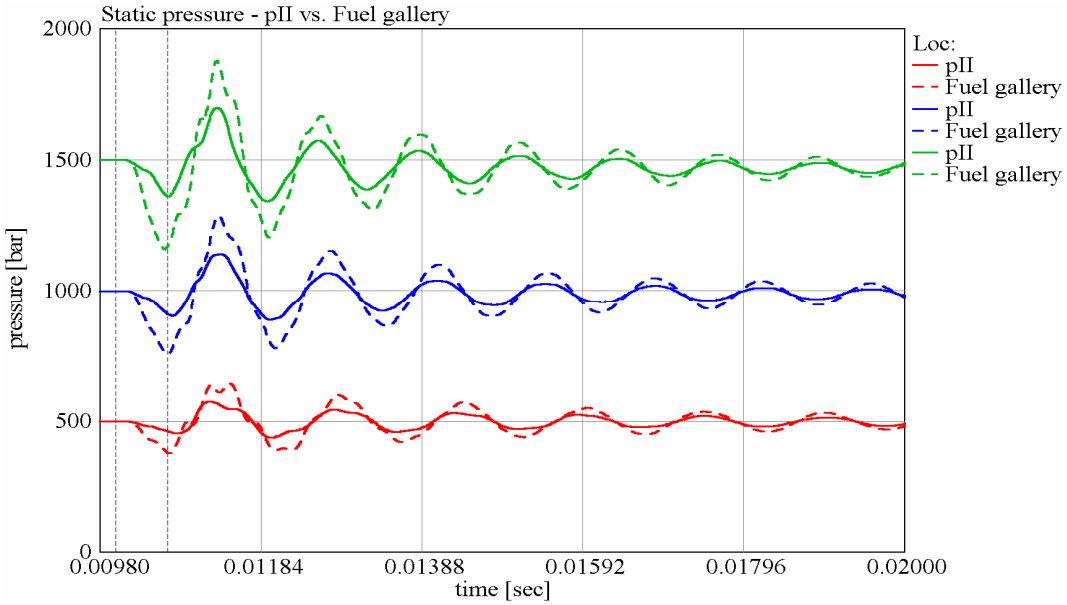

Figure 92. Comparison static pressure, *pII* vs. fuel gallery (l_p = 200 mm, d_p = 2.4 mm, and t_{inj} = 600 µs).

The figure above confirms that it is possible to base the circuit analysis on the pressure signal at the injector inlet. Firstly, the pressure oscillations inside the fuel gallery and at the injector inlet are in phase. Hence, statements that are based on the frequency can be used to describe the dynamics of the injector. Secondly, the amplitudes inside the fuel gallery are considerably larger than at the injector inlet. For evaluation purposes this condition is fundamental, as it

shows that the oscillation at *pII* is mainly driven by the flow field at the needle seat. If the situation were vice versa, that is, the injector inlet oscillation exceeded the fuel gallery pressure variation, it would be more problematic to evaluate the injector characteristics only by the *pII* data.

During the discussion of the theoretical background it has been emphasised that it is important to include energy conservation in the basic set of equations for modelling fluid transients. As an example, Figure 93 demonstrates for a system with l_p = 200 mm, d_p = 2.4 mm, p_{set} = 1250 bar, and t_{inj} = 600 µs the variation of the instantaneous fluid temperature inside the fuel gallery and at the centre of the high pressure connection pipe between rail and injector. In alignment with the pressure profile, the temperature variation is stronger inside the former object. The pressure oscillation at the centre of the connection pipe is affected by the rail volume and therefore somewhat smaller. By assuming hypothetically a constant pressure of 1250 bar, the fluid density varies due to the temperature change alone by a maximum of approximately 3 kg/m^3 (see, for example, Appendix A, Figure A 1). In the real case the fluid density is defined through the instant values of the thermodynamic variables pressure and temperature. Consequently, the correlation is more complex and the previous assumption is not valid. By considering the fast transients in the system it is, on the other hand, obvious that it is essential to remain as close as possible to the underlying physics, that is, to consider instantaneous phenomena for modelling the complete system.

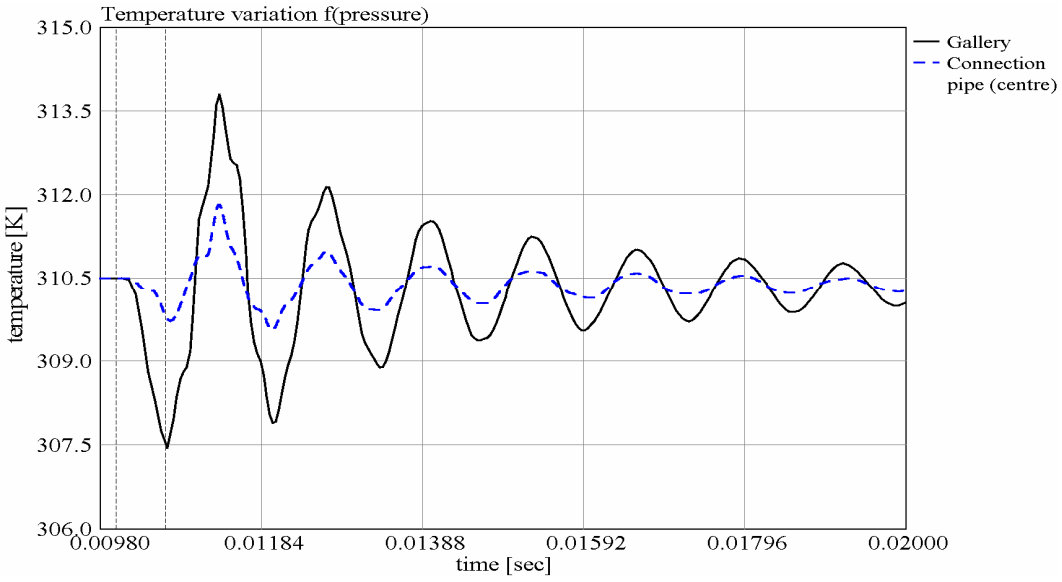

Figure 93. Variation of fluid temperature due to pressure oscillation (l_p = 200 mm, d_p = 2.4 mm, p_{set} = 1250 bar, t_{inj} = 600 µs).

In the previous section it has been stated that the pressure at the connection pipe centre is affected by the volume of the rail, which explains the lower pressure amplitude. Theoretically, a second reason might be also present: in the case of a standing wave in the connection pipe, it is conceivable that a wave node exists at the location of data recording. However, for the present setup this is true, as the pressure history along the connection pipe clearly shows a gradual change of the pressure amplitudes between connection pipe inlet and outlet (Figure 94, variable *x* starts at rail).

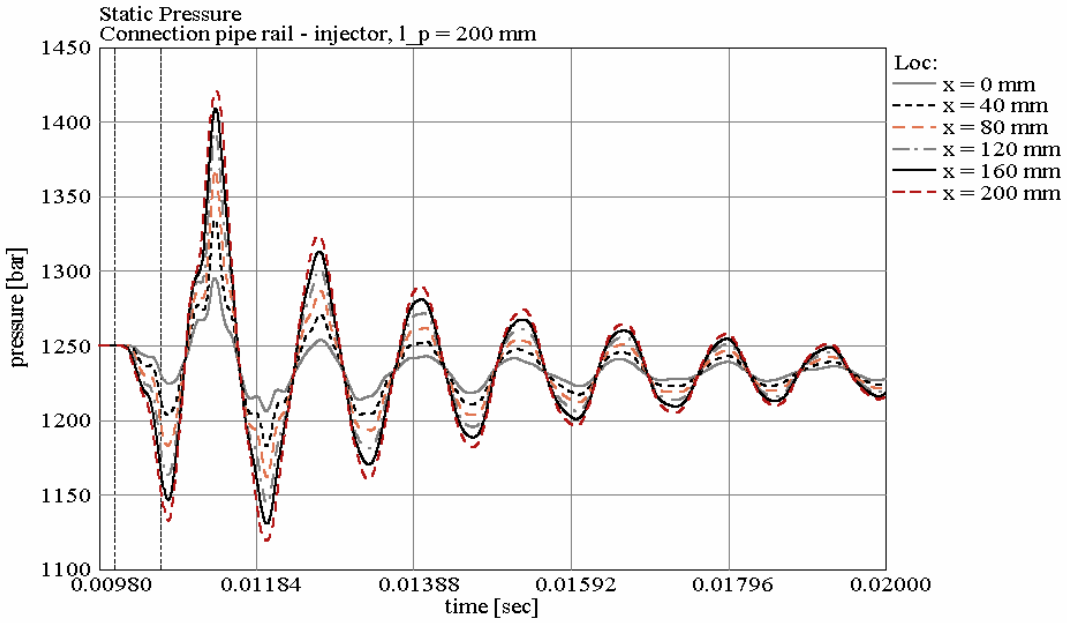

Figure 94. Pressure history connection pipe rail - injector, intervals: Δx = 40 mm (l_p = 200 mm, d_p = 2.4 mm, p_{set} = 1250 bar, t_{inj} = 600 µs).

Figure 95 shows for a configuration of p_{set} = 1500 bar and t_{inj} = 600 µs the calculated speed of sound, *a*, at the centre of the connection pipe between rail and injector. Firstly, it can be seen that the speed of sound is not constant, but may change at this particular location by up to 6 % (Figure 95, top). The plot reveals that the instantaneous value of this variable depends strongly on the setup of the system. This, on the other hand, is not surprising as *a* is directly linked to the fluid density and the thermodynamic variables *p* and *T*, respectively.

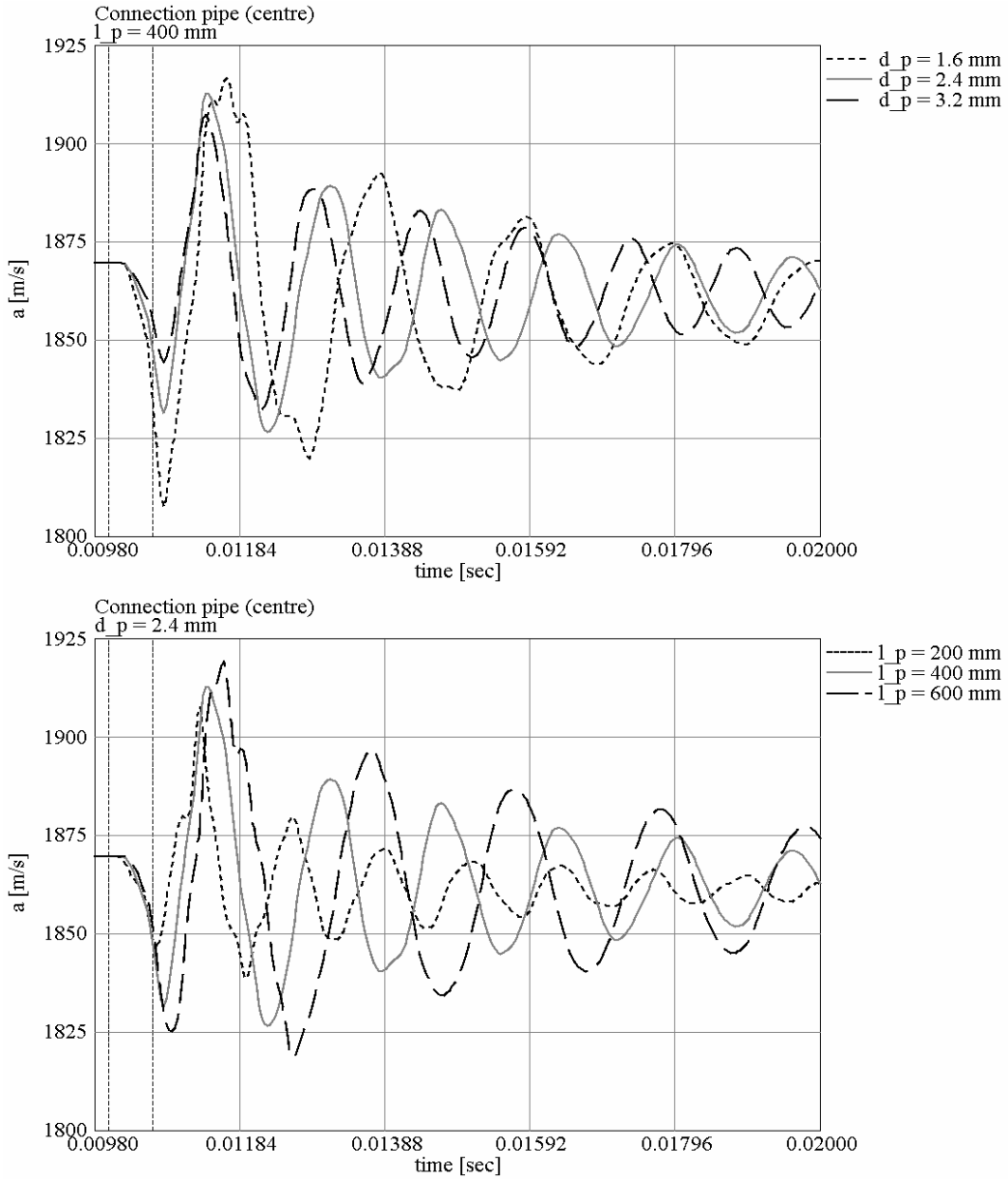

Figure 95. Sonic speed at centre of connection pipe (rail to injector),

(p_{set} = 1500 bar, t_{inj} = 600 µs)

General fluid flow problems can be classified by the Reynolds number *Re*; the flow is either laminar or turbulent. In contrast, when analysing fluid transients, this division ceases to be useful. As in the case of the CR fuel injection system, the flow is not steady but highly transient. This means that common limit values to describe, for example, the transition from laminar to turbulent flow are not suitable.

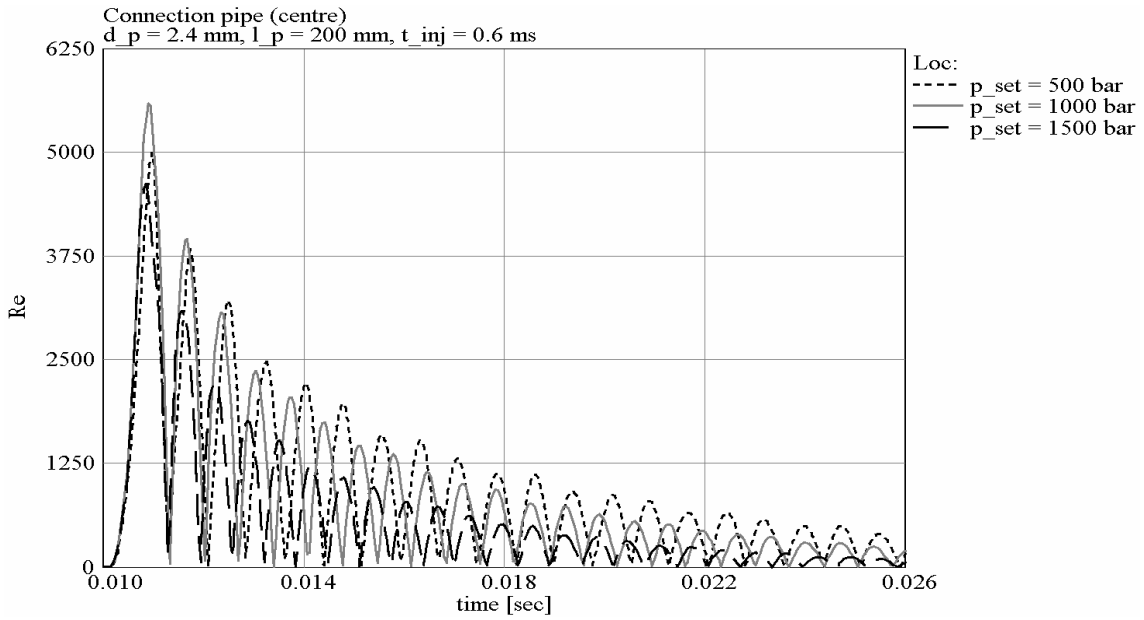

Figure 96. Example: Re number at centre of connection pipe (rail to injector).

Figure 96 presents as an example for a setup with l_p = 200 mm, d_p = 2.4 mm, and t_{inj} = 600 µs the computed *Re* number at the pipe centre between rail and injector for three injection pressures. It is evident from this plot that it is very unlikely that the flow field inside of the system is fully developed at any point in time.

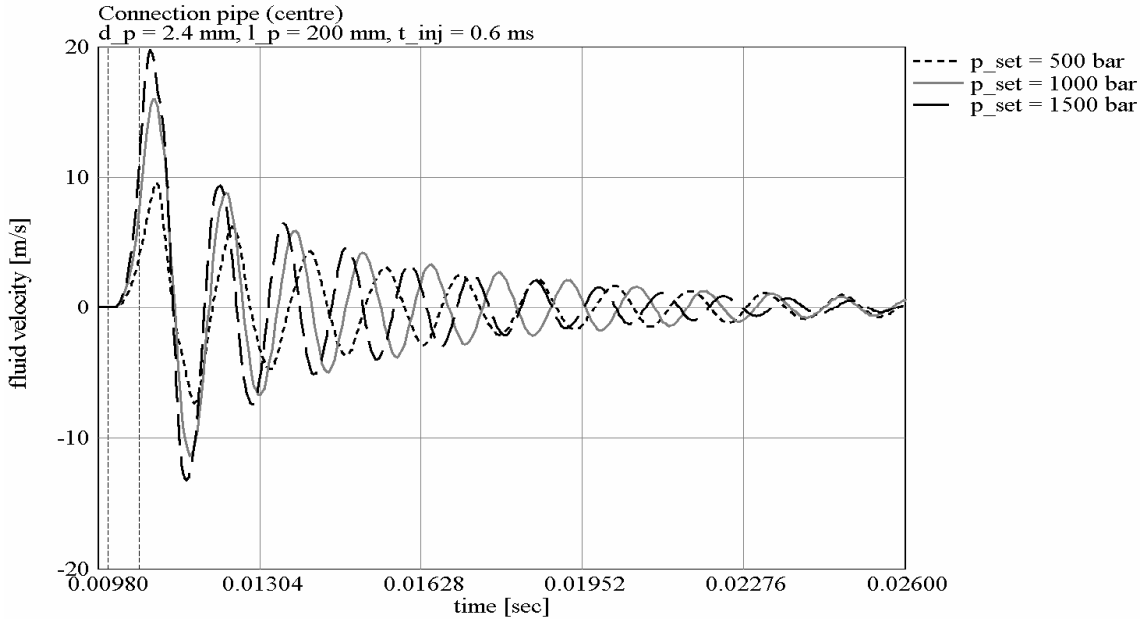

Figure 97. Example: fluid velocity at centre of connection pipe (rail to injector).

Figure 97 corresponds to Figure 96, as it shows for the same configurations the fluid velocity at the centre CV of the connection pipe to the injector. The plot clearly shows that the single injection triggers a strong flow oscillation inside of the connection line. Initially, the fluid is

accelerated to the exit of the injector. After valve closure and due to the fluid inertia, the pressure at the needle seat surpasses the supply pressure, which causes the fluid to decelerate and actually flow in the reverse direction (Figure 97, negative amplitudes). This highly transient oscillation continues until dissipative effects dampen the system to reach the initial equilibrium state.

One of the main advantages of a numerical simulation model is the opportunity to analyse parameters that are not possible or very difficult to access by experimental measurements. In this sense, the model can be used to gain insight into very local parts of the problem, which in turn helps to obtain a better understanding of the complete system. This possibility has been found to be very useful during the analysis of the CR system. Figure 98 exemplifies the pressure histories at various locations inside of the injector together with the displacement of the needle-pin-plunger mass for a setup with l_p = 200 mm, d_p = 1.6 mm, p_{set} = 1000 bar, and t_{inj} = 1000 µs (see Figure 15 and Figure 59 for a schematic injector view).

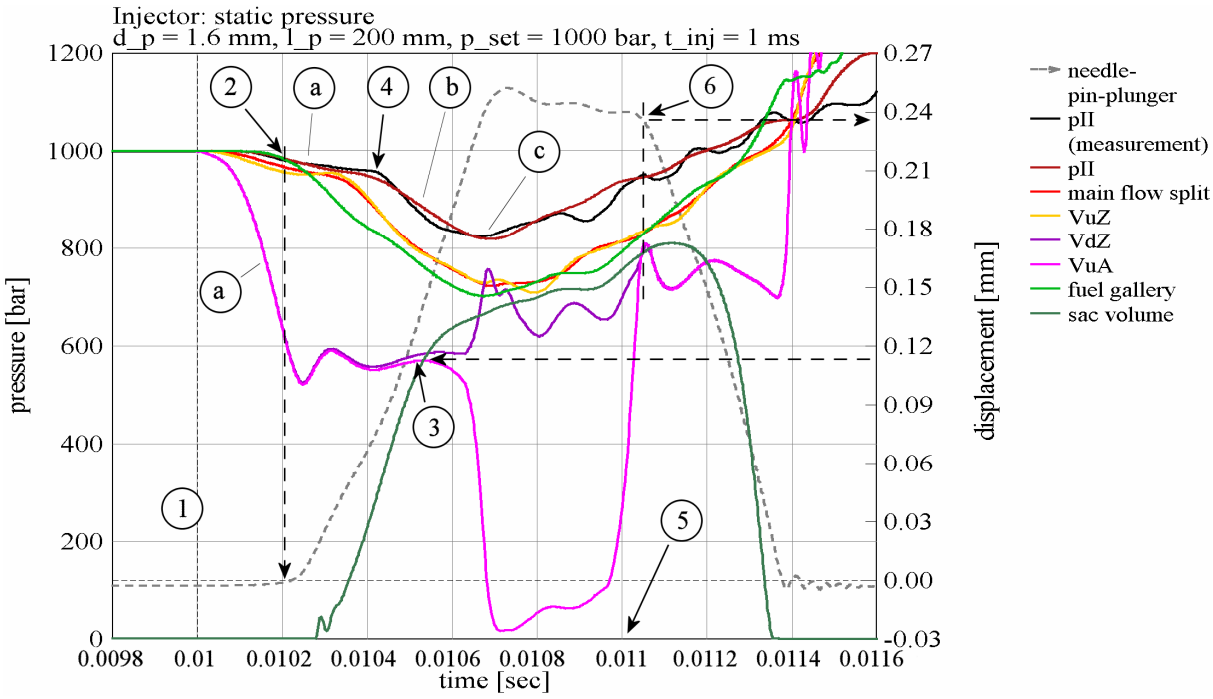

Figure 98. Example: pressure field inside injector.

In the figure above “1” denotes the start of the pilot stage activation, that is, the time when the pilot stage ball valve begins to move. As the fluid escapes, the pressure firstly drops inside the volumes upstream the A-nozzle, *VuA*, and downstream the Z-nozzle, *VdA*. Shortly afterwards follow the static pressures values of the other locations that are recorded in this example. However, the plot shows that in the latter case the corresponding slopes are considerably

smaller than for *VuA* and *VdZ*, since the Z-nozzle effectively disconnects the pilot stage from the main injector circuit. During this study it has been found that, generally, the appearance of the initial pressure drop (Figure 98, “a”) is mainly dependent on the activation profile of the pilot stage, that is, the effective flow area out of the injector as a function of time. At point “2” the pressure above the plunger has decreased so much that the pressure force in the fuel gallery and at the needle shoulder (not shown in the above figure) overcomes the downwards directed closing force; the needle-pin-plunger mass starts to move upwards. Interestingly, the graph shows that subsequent to the needle opening, the pressure above the plunger does not decrease further, but remains on a relatively stable level. As a direct consequence of the mass movement, it is possible to detect an accelerated decrease of static pressure in the fuel gallery and more upstream in the main flow split and *VuZ*. At the same time, fuel passes the needle seat, which explains the pressure rise in the sac volume, and it escapes via the nozzle holes. The kink at “4” indicates that the pressure drop due to the injection has now also reached the volumes above the plunger. For a needle-pin-plunger mass displacement of about 120 µm (“3”) the two volumes *VuA* and *VdZ* start to separate. With a variable flow restriction in place between the former two volumes, the fluid in *VdZ* is compressed, which can be seen in Figure 98 by the slight increase of the static pressure. *VuA*, on the other hand, becomes decoupled from the fuel supply. Consequently, the pressure in the same volume drops close to the pressure in the fuel return line. Opposite to the slopes that are denoted by “a”, the rate of pressure decrease during phase “b” is essentially defined by the instantaneous flow cross-section at the needle seat. The same is true for the minimum pressure level ($p_{min,1}$) at “c”. It is worth mentioning that the pressure at “c” does not remain for a long period, but increases right away again (see measured and simulated signal *pII* at $t \approx 0.0107$ s), despite the fact that in this case the full lift is reached. Finally, at about “5” the pilot stage ball valve begins to close the flow path to the fuel return line. The pressure in *VuA* recovers as a result to the same level as in volume *VdZ* (“6”). In fact, point “6” shows clearly that the flow restriction between *VuA* and *VdZ* is fully effective at a lift of approximately 240 µm or more.

Figure 99 displays the impact of the injection parameters p_{set} and t_{inj} on displacement of the needle-pin-plunger mass. Overall, it can be said that a high injection pressure supports a fast actuation of the injector valve. Because the overall duration of the injection, t_{inj}, is constant, the slopes of the curves get smaller for low p_{set}. In this context, it is apparent that an injection time of 400 µs is too short to reach the full stroke. At t_{inj} = 600 µs only the highest injection

pressures cause a mass displacement close to the full stroke (Figure 99, bottom-left). For injection times longer than 600 µs the needle-pin-plunger mass usually reaches the full stroke; an exception to this rule is observable for the lowest injection pressure at t_{inj} = 800 µs. It is interesting to note that the closing slope for the t_{inj} = 800 µs, p_{set} = 750 bar case differs somewhat from the other setups. This discrepancy may, in fact, explain the kink in the mass rate per injection over injection time curve that is observable in both the simulation and measurement results (see, for example, page 81, Figure 49 and Figure 100, below). The configuration based on t_{inj} = 1000 µs, p_{set} = 500 bar (bottom-right) does not seem on first view to align with this theory, since a similar needle closing pattern does not lead to an outstanding result for the mass rate per injection (see, for example, page 81, Figure 49). Then again, it should be noted that the rising slope of the latter case is also noticeably smaller than the other curves, which might compensate for the effect of the special valve closing pattern.

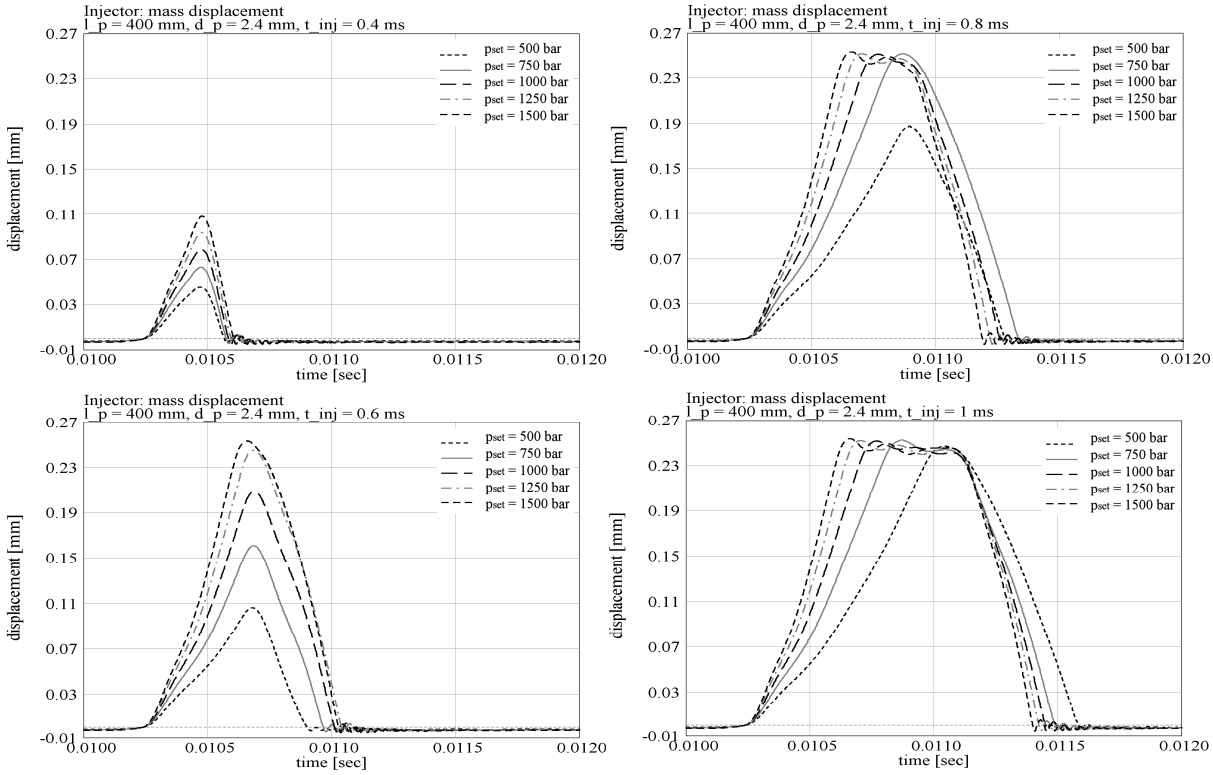

Figure 99. Displacement needle-pin-plunger mass as f(t_{inj}, p_{set}).

Figure 100 presents in analogy to the measurement results the simulated mass per injection as a function of p_{set} and t_{inj} for the case of l_p = 400 mm and d_p = 2.4 mm. Together with the plots in the figure above, it is now possible to identify more clearly the reasons for the particular appearance of the graph. As an example, the bottom left plot in Figure 99 reveals that all except the mass per injection value for p_{set} = 1500 bar correspond to a needle lift that is

smaller than the maximum displacement. Indeed, it can be seen that all values below or left of the inclined and shaded bar represent data for partial needle lifts. The kink at t_{inj} = 800 µs, p_{set} = 750 bar and the aforementioned setup with t_{inj} = 1000 µs, p_{set} = 500 bar characterise configurations at which the needle just reaches its maximum displacement before it is pushed back into the needle seat.

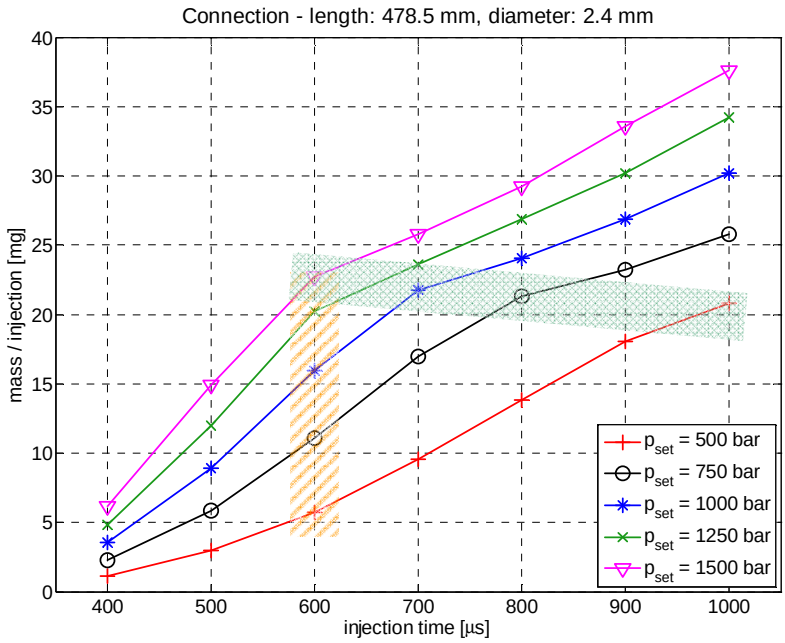

Figure 100. Example: injected mass / injection as f(p_{set}, t_{inj})

In analogy to the presentation in chapter 3.2.6, Figure 91, it can be summarised that the actual needle position is very sensitive to the injection parameters. This result is seen as an important finding for understanding of the working characteristics of such injectors. The variety of displacement curves underline that it is probably not adequate to simplify the injector model further by employing, for example, some look-up table for the needle lift (see also chapter 3.3.2 for an analysis of the injector characteristics).

Figure 101 shows, as an example, that in the configuration of p_{set} = 1250 bar and t_{inj} = 800 µs the connection line geometry has basically no effect on the lift of the needle-pin-plunger mass. For both a variable connection pipe length (Figure 101, left) and diameter (Figure 101, right) the calculated curves are almost identical. Only slight differences are detectable for the valve closing slope. Together with the findings for the mass flow rate as a function of the connection pipe geometry (chapter 3.1.4 and 3.2.5), it can be concluded that it is more likely

that the differences in the instantaneous total pressure at the needle seat are responsible for the observed injection rate diversity.

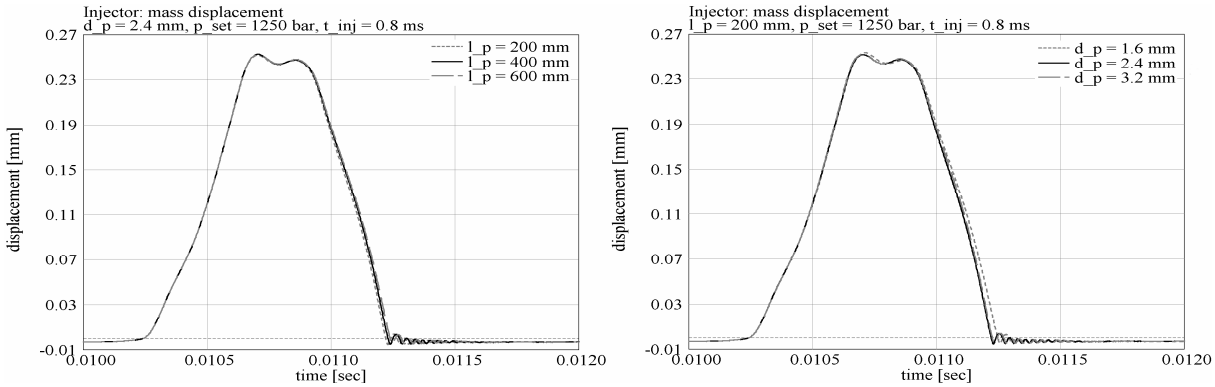

Figure 101. Displacement needle-pin-plunger mass as f(l_p, d_p).

3.3.2 Impact of injector model on predictions

The dynamic characteristics of the hydraulic CR circuit consist, in general, of various components. One possibility is to classify the individual contributions by their source. On the one hand, a component is passive, that is, the properties are not changing. Any pipe element belongs, for example, in this category. On the other hand, a component might also change its state during operation. The fuel injector is a typical representative of the latter group. In order to evaluate the impact of the injector on the overall characteristics of the circuit, some additional simulation runs were carried out. For each new simulation setup the injector model was modified. The results are subsequently compared to the default model (see page 90, Figure 58).

Altogether, 4 additional simulation models were used in this particular study. As the default setup is already fairly complex the new models have been based on a simplification of the existing system. In this way it is also possible to identify the needed degree of model detail to obtain acceptable correlation with the real system. By starting with the default injector model (Figure 58) all new models omitted any effects that were based on rigid body dynamics. Secondly, the pilot stage was completely removed; instead, the injection process was controlled by defining a look-up table for the effective diameter of the needle-seat orifice (see Appendix D for a presentation of the explicit injector models). Table 5 provides a summary of the most important differences to the default injector model.

Table 5. Overview, simplified injector models.

Model	m_01	m_02	m_03	m_04
Comment	no pilot stage, no rigid body dynamics; all objects use the same parameters as the default model	all *Pipe* objects use the same diameter as the connection pipe between rail and injector (otherwise same as m_01)	only single *Pipe* object between injector inlet and needle seat (length adapted to account for total distance); diameter same as connection pipe	same as m_03 but includes the flow restriction at the injector inlet (length adapted to new value, otherwise based on default settings)

It has to be emphasised that the simplified models are less accurate than the default model as they neglect various parts of the real injector. This is particularly true for the models m_02 to m_04. However, the simplification process aimed to omit only details that were believed to have a minor or no effect on the overall performance. It is therefore expected that the absolute values of, for example, the pressure amplitudes or oscillation frequency are somewhat higher or lower; the general trends, on the other hand, are conserved. The latter condition is essential, as it ensures the adequate representation of the injector characteristics.

Figure 102 compares as an example for the configuration l_p = 400 mm, d_p = 2.4 mm, p_{set} = 1000 bar, and t_{inj} = 700 µs the computed pressure history at the injector inlet. It is most evident that none of the simplified models is capable of reproducing the kink during the initial pressure drop. As m_01 to m_04 neglect the pilot stage altogether, this result is seen as further evidence that the very first negative slope is exclusively defined by pilot stage characteristics. Secondly, it is worth pointing out that m_03 is the only model that computes an almost vertical drop of *pII* due to valve activation. The other three models produce, in contrast, some reduction of the pressure gradient close to $p_{min,1}$. It is believed that this difference is due to the flow restriction at the injector inlet, as m_03 is the only model which neglects this component.

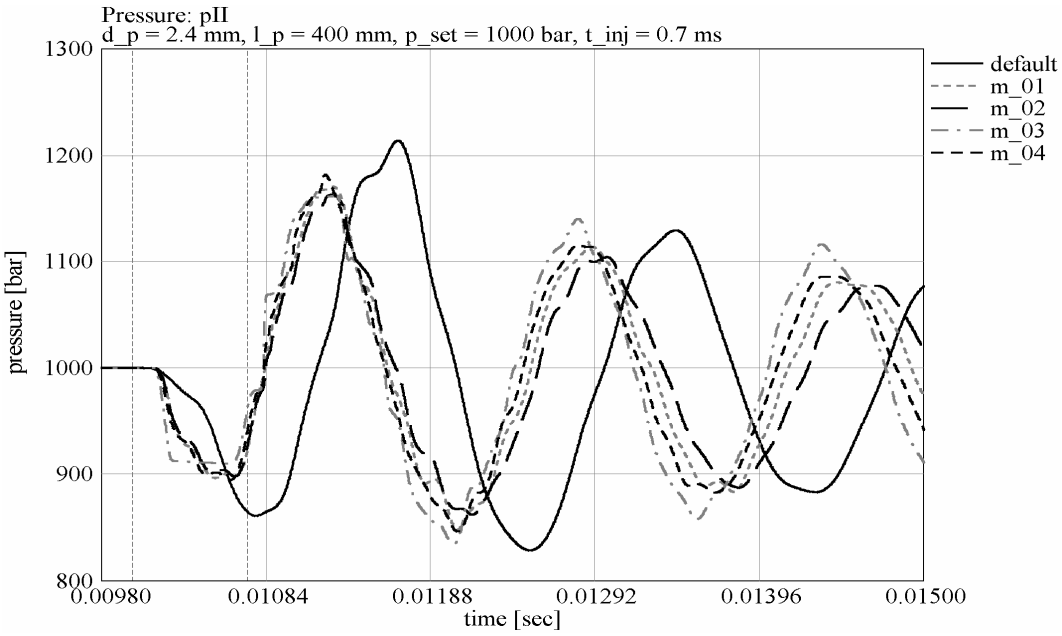

Figure 102. Example: comparison *pII*; default vs. simplified injector model.

In order to evaluate the quality of the models, each simplified setup was run for 81 different configurations. The connection pipe geometry considered 3 pipe lengths (l_p = 200 mm, 400 mm, and 600 mm) and 3 line diameters (d_p = 1.6 mm, 2.4 mm, 3.2 mm); the injection characteristics were defined by the 3 pressures p_{set} = 500 bar, 1000 bar, and 1500 bar and the 3 injection times t_{inj} = 400 µs, 700 µs, 1000 µs (only single injection). Just as in the analysis in chapter 3.2.5, the results are presented through the output parameters *f*, which denotes the frequency of the pressure oscillation at the injector inlet, and the extreme values of *pII*: p_{max} for the largest positive pressure amplitude and $p_{min,1}$, and $p_{min,2}$ for the first and second negative peak, respectively, after injector activation. Figure 103 shows for the two injection pressures p_{set} = 500 bar (left) and 1500 bar (right) the computed oscillation frequency as a function of the connection line geometry. Firstly, it can be seen that only the model m_01 is able to copy correctly the correlation between the oscillation frequency and the line diameter - generally, the oscillation frequency increases for a shift to a larger flow cross-section. All other models predict an opposite correlation of these two parameters. Because the setup of m_01 is relatively similar to m_02, but the findings are quite opposite, it can be concluded that this particular phenomenon is essentially defined by the variation of the flow cross-section from the injector inlet to the main flow split and along the main flow channel down to the needle seat (for a schematic of the injector, see Figure 15). The difference between the default model and m_01 must derive from the absence of the pilot stage in the latter model. An interesting observation can be made in respect of the flow restriction at the injector inlet.

Basically, m_03 and m_04 differ only by the omission and consideration, respectively, of this object. Concerning the oscillation frequency, Figure 103 reveals that a discrepancy between these two models may arise exclusively for short rail to injector connections that are characterised by a relatively large diameter.

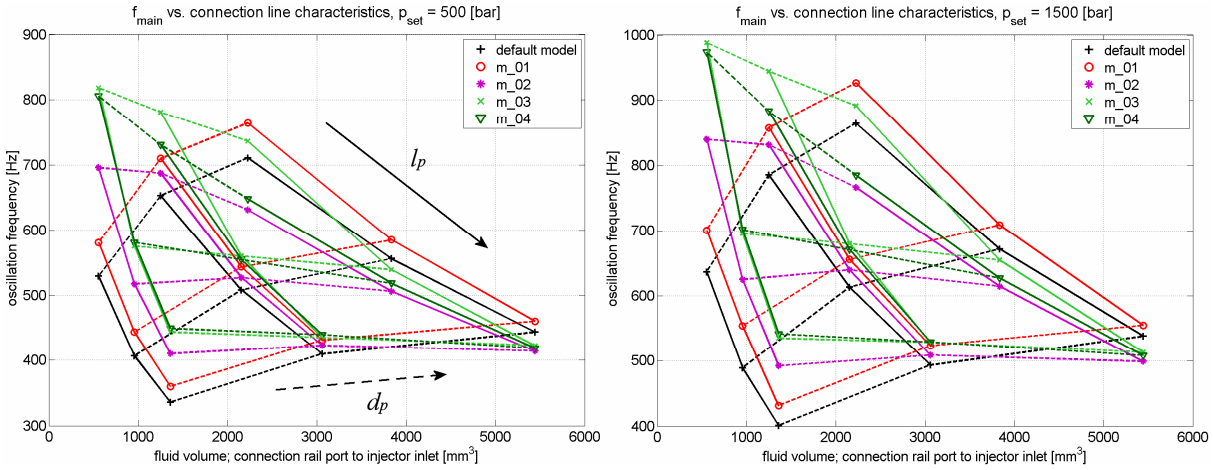

Figure 103. Comparison oscillation frequency as f(l_p, d_p) for p_{set} = 500 bar and 1500 bar.

Figure 104 presents for various configurations the computed maximum pressure amplitude, p_{max}, as a function of the simulation model. On the left hand side, the injection pressure is fixed to 1500 bar. From top to bottom the injection duration increases from 400 µs to 700 µs and 1000 µs. At the shortest injection time the biggest gap between the default simulation and a simplified injector model occurs for the models m_03 and m_04. If the smallest connection line diameter is selected, the amplitude of the latter approaches may exceed the default computation by up to 90 % (Figure 104, top-left, comparison default model to m_03 at d_p = 1.6 mm and l_p = 200 mm). For long injection times, that is, t_{inj} = 700 µs or longer, the discrepancy becomes smaller. The right hand side of Figure 104 shows p_{max}-values for some alternative setups with lower injection pressures. By comparing for the settings p_{set} = 1000 bar and t_{inj} = 700 µs (Figure 104, centre-right) for example the default simulation to the model m_01, it emerges that the latter approach significantly under-predicts the maximum pressure amplitude when a long connection line is used. Although all models can capture more or less the basic non-linear relation between the line geometry and the maximum pressure amplitude, it has to be said that an evaluation of p_{max} by a simplified model is rather problematic. Overall, the fit might be reasonably good at one operation point, but differ at some other configuration by 30 % or more. In light of the small total quantities that are injected and the generally high propagation velocity of a pressure pulse, it is more

than likely that such a model leads to findings that are not accurate enough for evaluating, for instance, the impact on the combustion process.

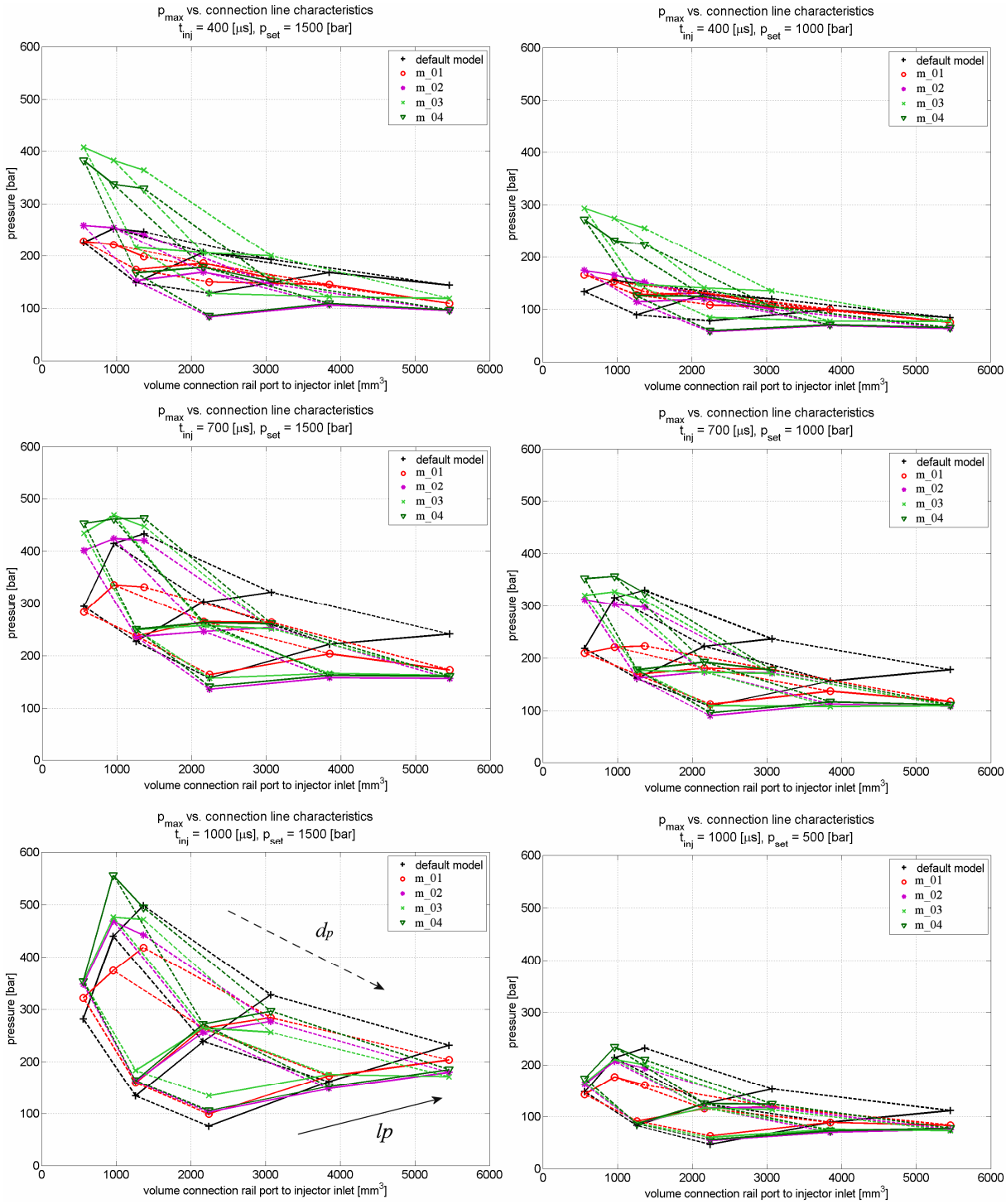

Figure 104. Comparison p_{max} as f(p_{set}, t_{inj}, l_p, d_p).

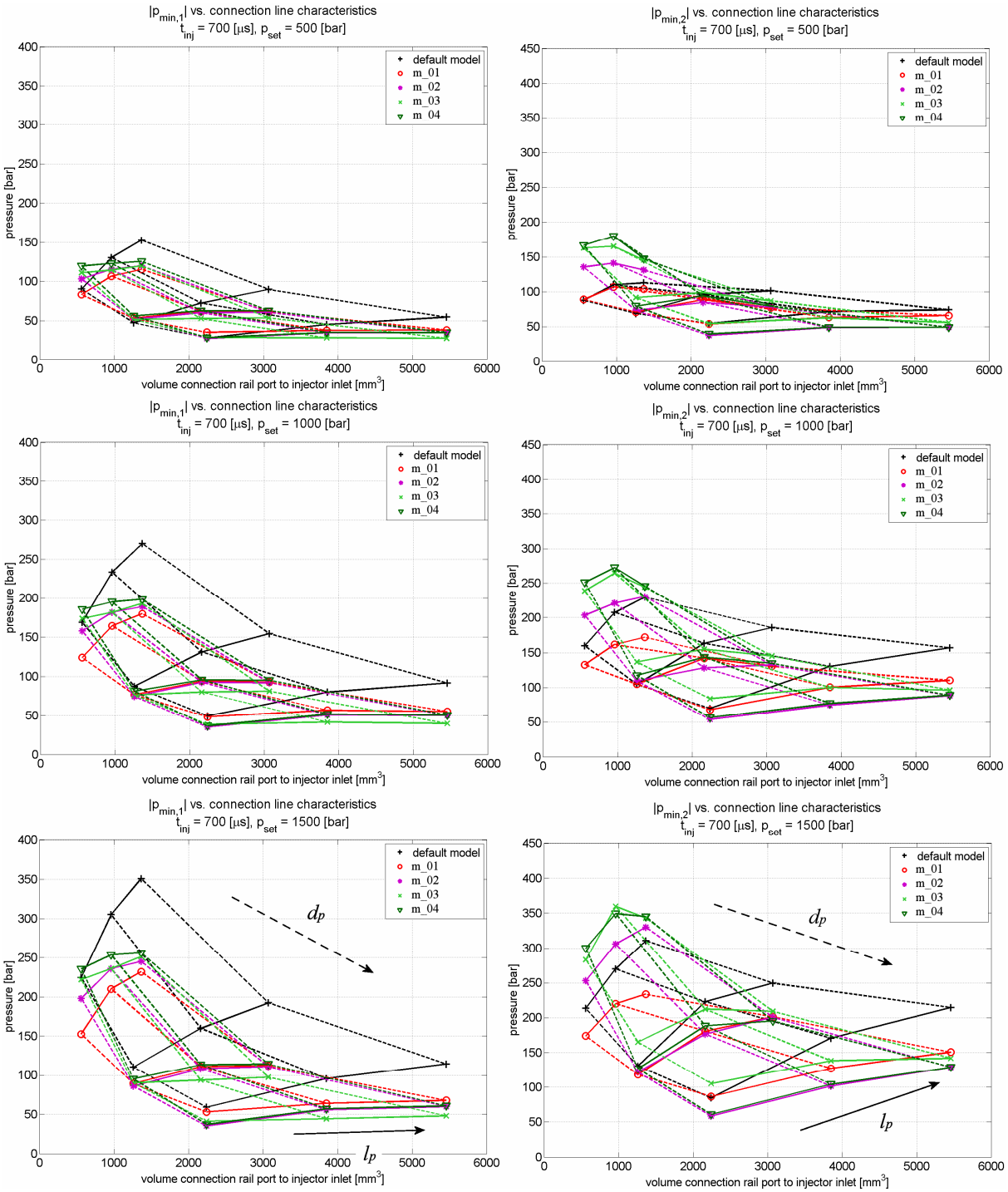

Figure 105. Comparison $p_{min,1}$ (left) and $p_{min,2}$ (right) as f(p_{set}, t_{inj}, l_p, d_p).

Figure 105 completes the previous figure through showing for the studied configurations the computed absolute amplitude of the first and second negative pressure peak at the injector inlet. The left hand side of Figure 105 demonstrates that all simplified models fail to accurately describe the increase of $p_{min,1}$ as a function of the connection pipe length, l_p. On the other hand, the values are, in the main, too small if the system is based on a small line diameter. Again, the closest match can be found for m_01 as the results suggest the same

trend as the default model. Concerning $p_{min,2}$, the right side of Figure 105 leads to similar findings. Firstly, the differences between the default simulation and the simplified models tend to increase for large distances between the rail and the injector. Secondly, the models m_02 to m_04 exceed the $p_{min,2}$ prediction of the default model if a small line diameter is used. The latter finding aligns with the result for p_{max}.

A presentation of the injection rate as a function of the injector model is omitted here. Due to the large discrepancy for the pressure signal *pII*, it is anticipated that the simplified models are not capable of adequately predicting the mass flow rate for single or multiple injection events.

3.3.3 Effect of wall flexibility on system characteristics

All materials are characterised by the fact that they deform if some load is applied. Usually, the dynamic behaviour of a system is strongly dependent on the component with the lowest stiffness. In low and medium pressure hydraulic circuits hoses define in most cases the objects with the largest flexibility. As explained at the beginning, high pressure fuel injection systems consist solely of steel pipes and connectors that are specially designed for this application. It is therefore expected that boundary flexibility has only a minor impact on the characteristics of the system. On the other hand, in order to evaluate the effect of the wall flexibility on the findings, the present analysis uses for the rail and connection lines a

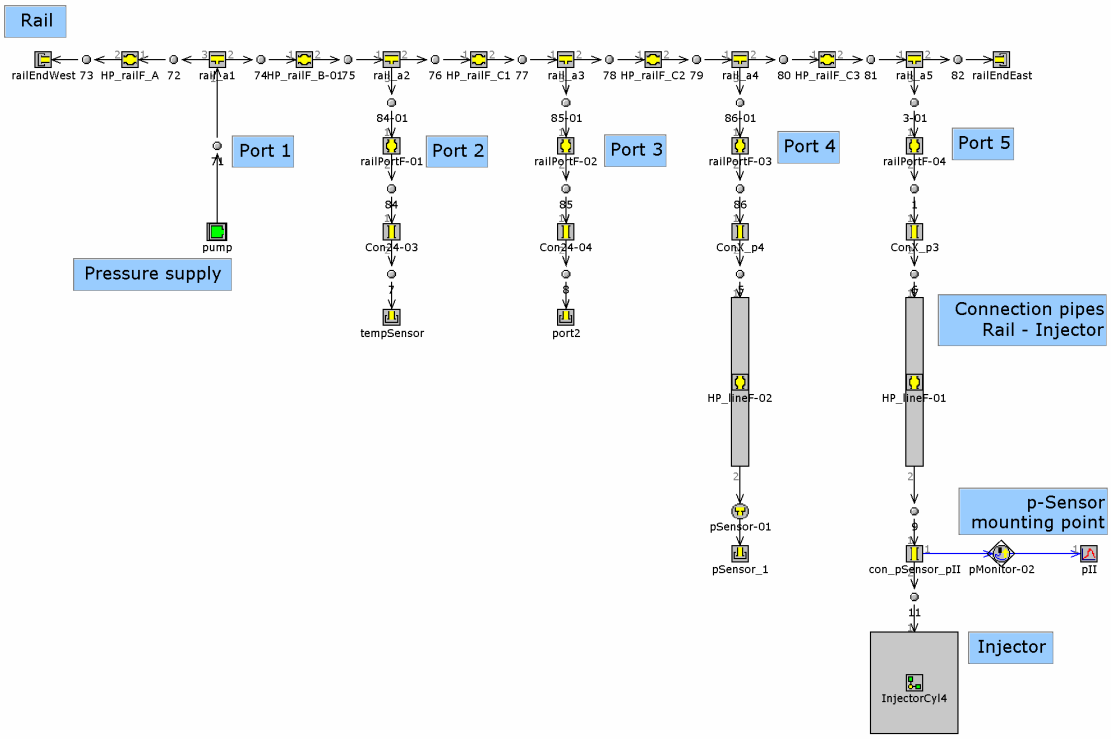

Figure 106. GT-Fuel model; main CR circuit with *PipeFlexibleWall* objects.

definition that accounts for the elasticity of the material. Figure 106 shows the modified model of the main CR circuit in the GT-Fuel environment. The injector model was not affected by this study. As opposed to the default model (see page 90, Figure 58), the present definition utilised *PipeFlexibleWall* objects instead of rigid *Pipe* elements. In addition to the equations for the flow field, the newly introduced objects account for FSI effects through solving the previously presented equations (108) to (110) in chapter 3.2.1. The simulation model used for the connection pipes a Young's modulus 196000 MPa and Poisson ration of 0.3; the numerical values for the rail elements were 207000 MPa and 0.285, respectively (for further details, see Appendix A, Table A 5).

For analysing the basic correlation between wall flexibility and system characteristics, only one configuration was studied. The injection parameters were p_{set} = 1000 bar and t_{inj} = 1000 µs; the connection line parameters were chosen as l_p = 200 mm and d_p = 1.6 mm. Analogous to the real system, the wall thickness of the rail was set to 6.95 mm. For the connection pipes the same parameter was set to 2.375 mm (see Appendix A, Table A 6).

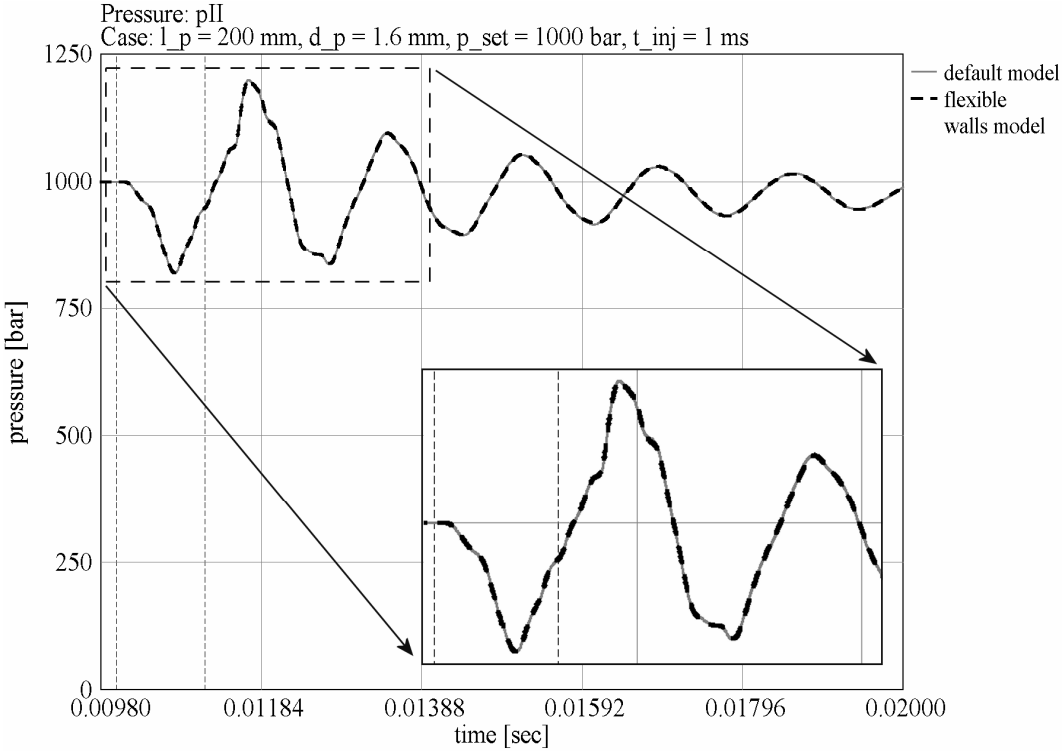

Figure 107. Example: impact of wall flexibility on pressure history *pII*.

Figure 107 presents the computed pressure history *pII* at the injector inlet for both the default model and the system with the flexible wall objects. From this plot it can be seen that actually both approaches lead to the same finding. The difference between the two cases is, in fact,

only marginal and not relevant for the evaluation of the system characteristics. It is therefore concluded that the earlier made assumption concerning the rigidity of the wall boundaries is applicable without compromising the quality of the simulated results. Accordingly, also no other plots of the flexible wall simulation model are presented here.

3.3.4 Analysis of rail properties

Up to this point, the geometry of the rail has been kept constant, that is, its length and diameter have not been considered in the analysis of the system. One reason for this strategy is based on the basic purpose of the rail and its requirements. From a fluid dynamics point of view, it is advantageous to use a large volume, as an increase of the hydraulic capacity supports the elimination of unwanted fluid transients in the system. On the other hand, a large volume under high pressure is not very economic to pressurise at start-up and during set pressure variations. Secondly, large volumes under high pressure load are subjected to higher stresses due to the bigger dimensions. Finally, the space in the engine compartment is commonly very limited. In light of these arguments, it can be summarised that the range of acceptable rail designs is very restricted. Potential modifications can only be made within narrow bounds unless the entire engine layout is completely reconsidered.

Table 6. Definition of main rail dimensions.

Configuration	Length [mm]	Diameter [mm]
default model	315.5	9.9
m_l1	268.175	9.9
m_l2	362.825	9.9
m_d1	315.5	8.415
m_d2	315.5	11.385

For evaluating the general impact of the rail properties on the dynamic characteristics of the hydraulic CR circuit, the present study investigated 4 additional configurations in the GT-Fuel environment. As presented in Table 6, the analysis was split into two parts; the first series studied the effect of the accumulator length (m_l1 and m_l2) and the second part the impact of the rail diameter on the system (m_d1 and m_d2). In both cases the new models were based on a 15 % increase or decrease, respectively, of the analysed parameter. The default model

was identical to the one that was used in the previous chapters. The main settings were defined by l_p = 200 mm, d_p = 2.4 mm, p_{set} = 1000 bar, and t_{inj} = 800 µs.

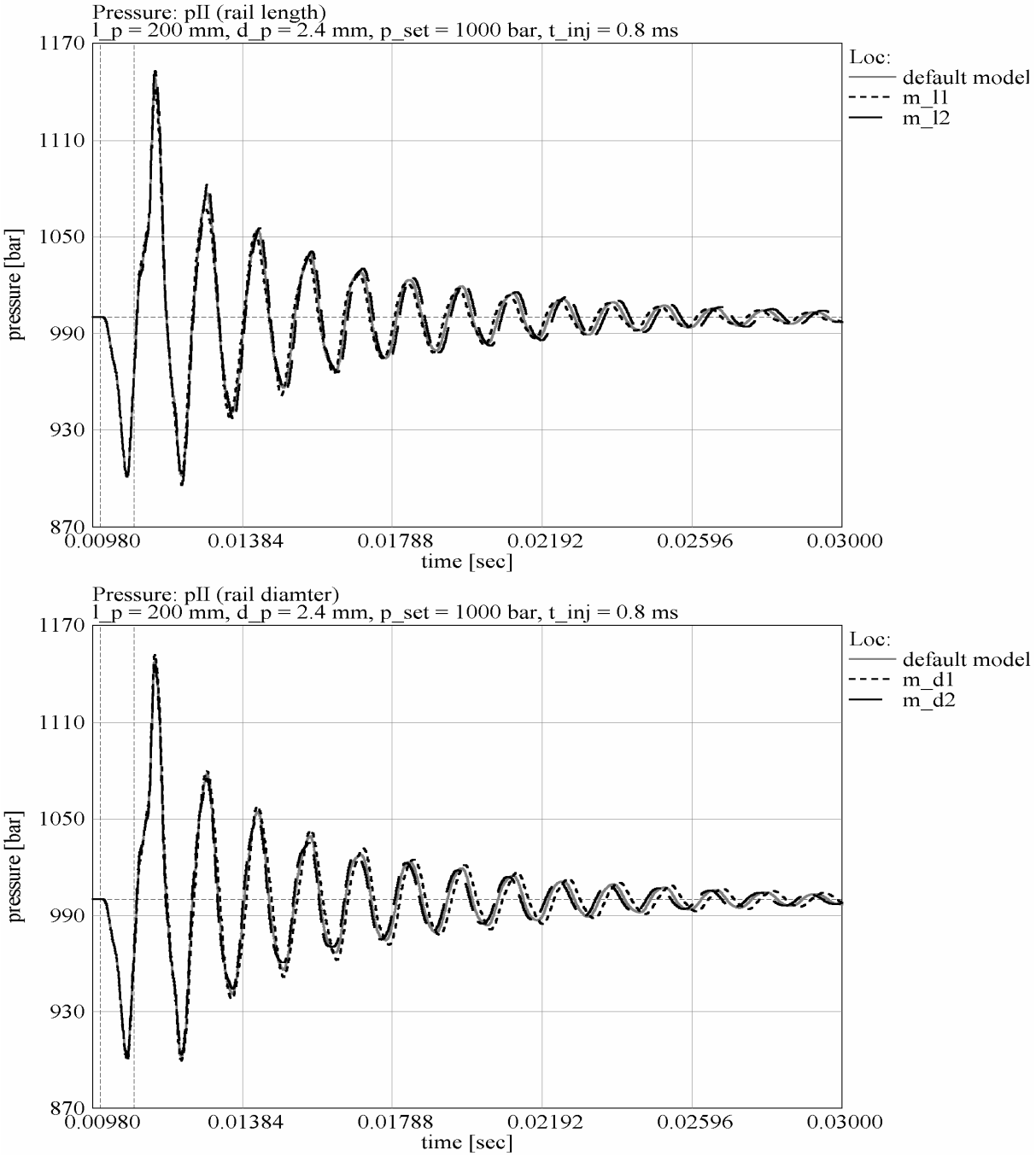

Figure 108. Comparison pressure *pII* as f(rail geometry); length (top) and diameter (bottom).

The pressure at the injector inlet, *pII*, is used to analyse the effect of the rail geometry variation on the hydraulic circuit characteristics. Figure 108 shows that on a large scale the curves of the new models are rather similar to the default setup. Indeed, it can be seen that all models lead to almost identical initial pressure peaks. This includes both the absolute values

of $p_{min,1}$, p_{max}, and $p_{min,2}$ and their respective time of appearance. It can be said that the geometrical characteristics of the rail are of secondary importance when optimising the dynamic characteristics of the system, as the time of a potential second injection start follows within one millisecond or slightly more after the first needle lift. The curves in both graphs suggest that the effect of the rail parameters causes a distinguishable difference to the default model only after about 5 ms to 10 ms after the first injection. Although the amplitudes of the oscillations remain nearly constant, it can be said that a shorter rail tends to increase the oscillation frequency *pII*, while a longer accumulator leads to the opposite result (Figure 108, top). Similarly, a 15 % larger rail diameter supports a faster propagation of the main pressure disturbance; the smaller diameter, on the other hand, causes the oscillation to slow down (Figure 108, bottom). It is interesting to notice that in the latter analysis the curve of the default model is not centred between the curve of the bigger and smaller diameter case. As a closer investigation shows, the difference between the 15 % larger rail setup and the default model is somewhat smaller than the gap towards the other extreme.

Overall, it can be said that the rail dimensions need to be changed significantly to cause a noticeable effect on the initial pressure history at the injector inlet and the injection rate, respectively (see analysis in chapter 3.2.5). Then again, as has been outlined in the beginning, the rail geometry is more restricted than, for example, the geometry of the connection lines between the rail and the injectors. A change to a different configuration might be therefore not feasible without requiring further adaptations of the engine layout.

3.3.5 Analysis of potential measures to minimize unwanted pressure oscillations

It is unmistakable that the pressure oscillation at the injector inlet has adverse consequences on the homogeneity of the fuel delivery during multiple injection events. Both experimental measurements (chapter 3.1.5) and simulation results (chapter 3.2.6) show that, for example, the mass flow rate of the second injection is strongly affected by the injection timing, that is, the instantaneous total pressure head over the injector. It is therefore desirable to minimise as much as possible any oscillation at the injector inlet. As has been indicated in the introduction, common measures for attenuating unwanted fluid transients in low and medium pressure hydraulics are not appropriate in high pressure applications due to the pressure level and the fast transients. Secondly, the limited space requirement enforces the use of solutions that can be integrated easily into existing systems. The present study aims to guide towards

potential methods that are suitable for minimising pressure and flow oscillations. In this sense, this investigation is not meant to be complete or more detailed than necessary.

Two concepts for damping unwanted fluid transients at the injector inlet are discussed in this study - Helmholtz resonator and in-line attenuator. The location of the damping devices was set as close as possible to the source of excitation. Generally, the injector dimensions are fixed, that is, the nozzle holder can not be enlarged to accommodate the required volume because of the limited space available at the injector mounting point. Consequently, the injector inlet defines the next possible location for the damper and attenuator position, respectively. The dimensions of both systems were adapted to the dynamic characteristics of the CR circuit (see Appendix E). In respect of the connection pipe geometry, the connection pipe length, l_p, shows a larger impact on the *pII* oscillation frequency than the line diameter, d_p (see, for example, page 111, Figure 76). This numerical study utilised accordingly a system configuration of d_p = 2.4 mm and l_p = 200 mm, 400 mm, and 600 mm. The injection pressure was varied between 500 bar, 1000 bar, and 1500 bar and the injection duration includes t_{inj} = 600 µs and 1000 µs. For each damping device two setups were considered. Figure 109 defines the main parameters and Table 7 lists the corresponding numerical values.

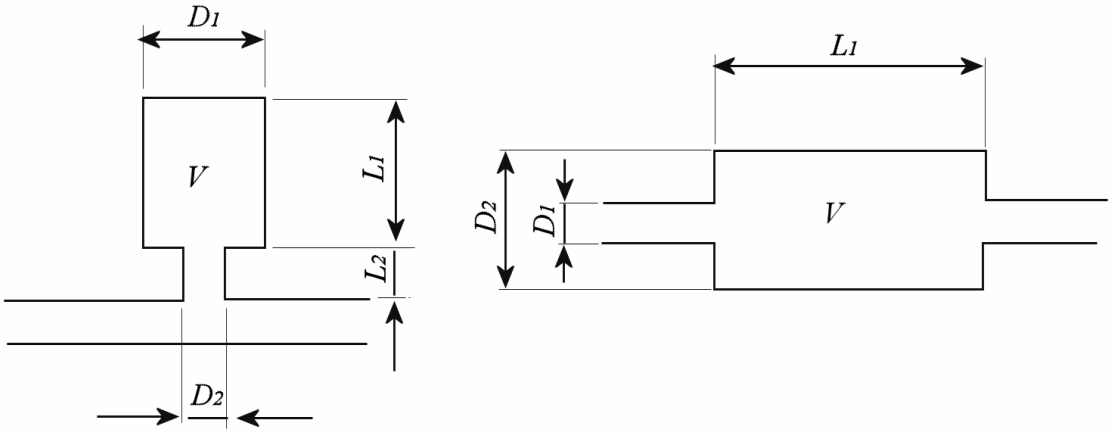

Figure 109. Geometry definition, Helmholtz resonator (left) and in-line attenuator (right).

Table 7. Numerical values for damping devices (internal dimensions).

Type	Model	V [mm^3]	L_1 [mm]	L_2 [mm]	D_1 [mm]	D_2 [mm]
Helmholtz	m_H01	65395	93	10	30	2
	m_H02	8174	46	20	15	1
In-line	m_L01	2356	30	-	2.4 (= d_p)	10
	m_L02	9425	30	-	2.4 (= d_p)	20

The implementation of the damping devices into the existing GT-Fuel model is straightforward and easy to accomplish. In the case of a Helmholtz resonator, a three-port flow split object was added at the injector inlet. The two main ports were connected to the connection pipe downstream end and injector inlet, respectively. The third port was perpendicular to the pipe axis and connects the actual resonator to the main flow path between rail and injector. Two pipe objects were used to represent the resonator geometry. The first object stands for the resonator throat, the second for the resonator volume. For completeness, the resonator volume could alternatively be represented by a simple volume object. Using a pipe object (with one termination) instead enables that the pressure inside the resonator volume is not uniform but a function of the axial pipe dimension. The implementation of the in-line attenuator followed the same concept. Based on the default geometry, a section of the original pipe connection between rail and injector was replaced by a new pipe object with the dimensions of the attenuator. It is emphasised at this point that no special treatment is necessary for the interfaces between resonator or attenuator and default model. This also includes potential assumptions for the upstream or downstream side of the damping device. Furthermore, no additional equations are necessary. As the damping devices are made of the same components as the remaining circuit, the same equations apply for modelling the fluid flow through the objects (see chapter 2.2.2, for example equations (45), (51), and (61)).

The effectiveness of each configuration is evaluated by comparing the computed results to the default simulation model (see chapter 3.2 for a model description).

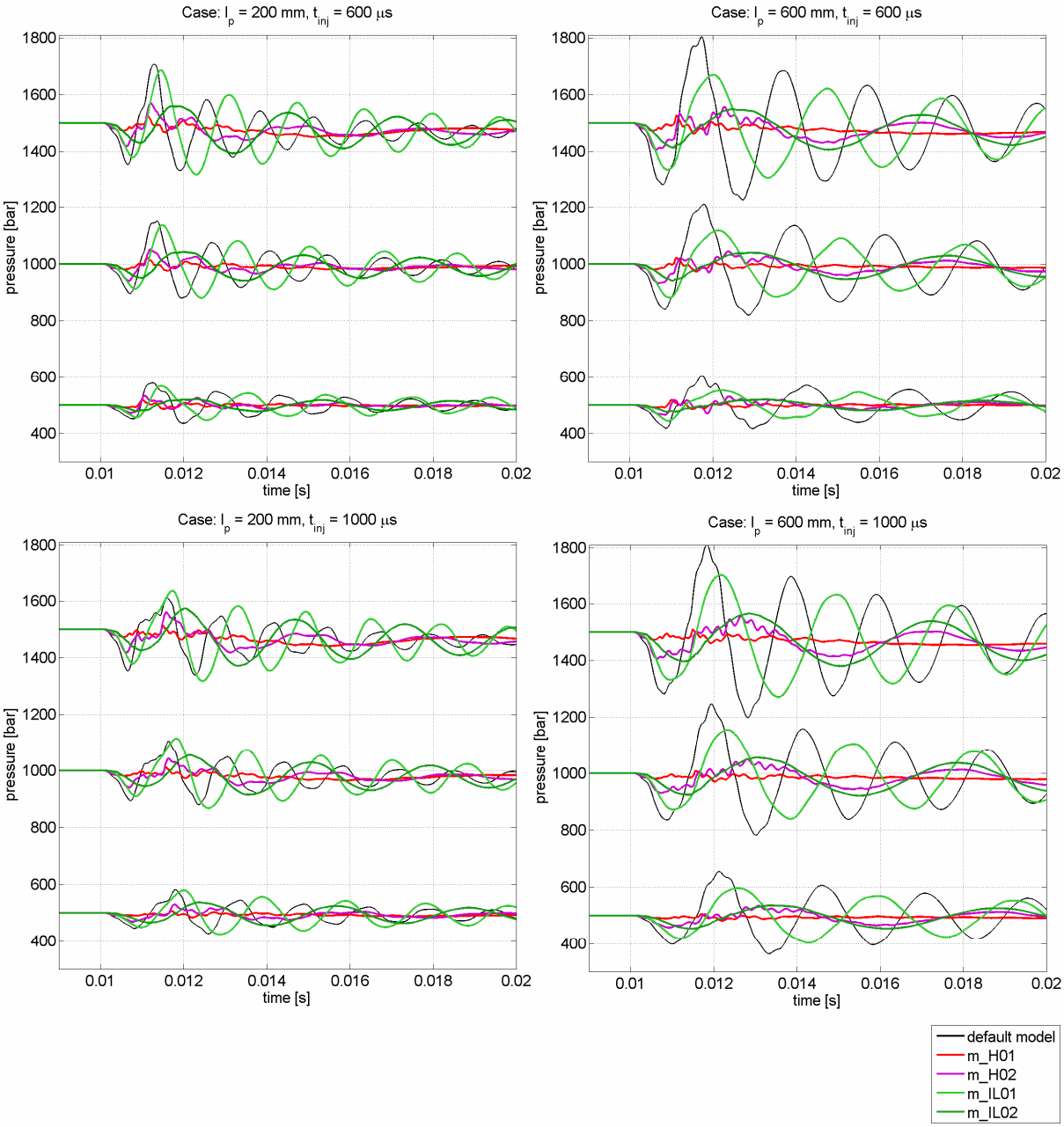

Figure 110. Comparison *pII* for various damping configurations as a function of injection parameters and connection pipe length.

Figure 110 shows for the shortest (left) and longest connection pipe setup (right) the pressure history at the injector inlet. It is apparent that best attenuation is achieved by the Helmholtz resonator with the largest volume (m_H01); the pressure remains nearly constant for all studied configurations. The smaller Helmholtz resonator (m_H02) is rated as the second best solution, as the fluctuations are only minor, that is, in direct comparison to the default model they tend to be negligible. The in-line attenuators, on the other hand, are less effective than the previous damper group. Particularly the setup with the smallest dimensions (m_L01) leads to pressure amplitudes in the range (Figure 110, l_p = 200 mm) or slightly below (l_p = 600 mm)

the predictions of the default model. The slightly bigger in-line damper (m_L02) is already noticeably better than its smaller version. While the improvement is relatively small for a setup with short connection pipe and long injection duration (Figure 110, bottom-left), the benefits become more apparent for the other system configurations. For the small Helmholtz resonator setup (m_H02) and both in-line attenuator models, it is observable that the frequency of the new oscillation is lower than for the default circuit configuration. The former case shows initially a pressure variation of high frequency that is superimposed on the frequency (see, for example, Figure 110, bottom-right, m_H02). The in-line attenuator curves, on the other hand, are characterised right from injection start solely by the new oscillation frequency. It is worth noting that for all three configurations (small Helmholtz resonator and both in-line attenuators) the oscillation decay appears to be smaller than for the default setup; the latter phenomenon is most evident for the case m_L01.

Figure 111 presents for various configurations and models the absolute pressure variation between the lowest and highest pressure level at the injector inlet. Firstly, the plots reveal in analogy to the previous Figure 110 that, generally, the Helmholtz resonator simulations lead to a smaller variation of *pII* than the in-line damper configurations. Secondly, both graphs clearly show that a damping device may support a uniform pressure level as a function of the input parameters. By taking, for example, the injection pressure as the main variable, the upper graph of Figure 111 shows that for a setup with l_p = 400 mm and t_{inj} = 600 µs the default model leads to Δp values of 400 bar and 550 bar for the injection pressures p_{set} = 1000 bar and 1500 bar, respectively. The same Δp values for the m_H02 model account for Δp = 100 bar and 150 bar as a function of p_{set}. In the former case the amplitude variation equals 150 bar, while for the small Helmholtz resonator setup the difference is only 50 bar. Similarly, Figure 111 demonstrates that for the models m_H01, m_H02, and m_L02 the calculated pressure variation is fairly independent of the connection line length. In all three cases the lines that connect the values of constant injection pressure are basically horizontal. In contrast, the default model predicts a considerable increase of Δp for large line lengths. It should be noted that not all tested damper configurations lead to a significant change from the default setup. As for the analysis of the *pII* histories in Figure 110, it can be summarised that the model m_L01 behaves quite similarly in respect of Δp compared with a circuit without any damping device. In fact, it can be seen that for a setup of l_p = 200 mm and t_{inj} = 1000 µs the small in-line attenuator causes a setback with respect to Δp.

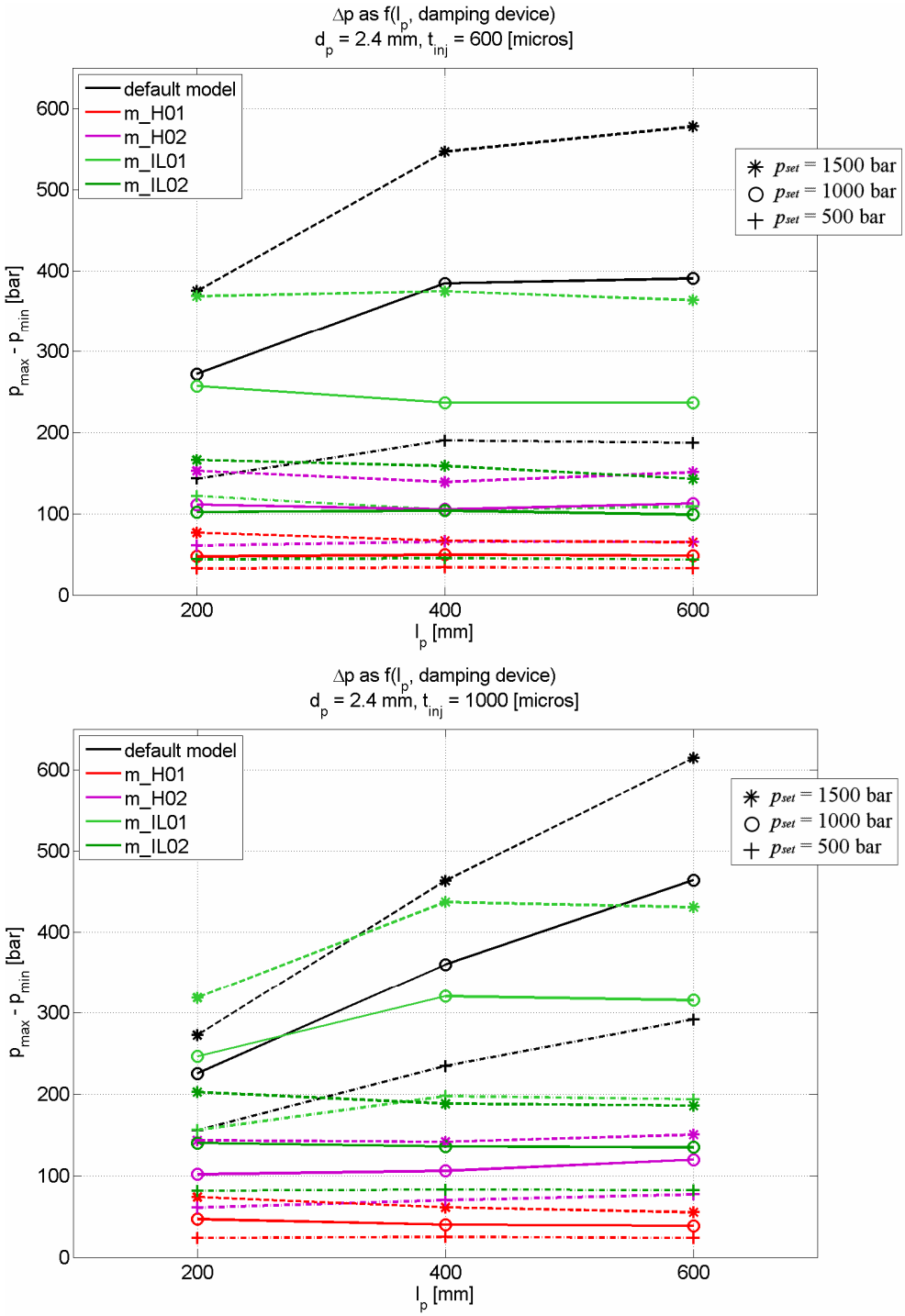

Figure 111. Comparison of Δp for various damping configurations as a f(l_p, p_{set}); t_{inj} = 600 µs (top) and t_{inj} = 1000 µs (bottom).

Because of the smaller impact of the injection pressure and the connection line length on the oscillation amplitudes, it can be concluded that a properly dimensioned Helmholtz resonator or in-line damper promotes a smaller pressure variation at the injector inlet. As the effect of the studied input parameters is reduced, it is to be expected that the injection process is more uniform over the input parameter range.

Figure 112 illustrates for the two example cases m_L02 and m_H02 the corresponding modifications to the hydraulic circuit. Based on this view, it can be said that an in-line attenuator usually fits well into an existing system, as the device is rather compact. On the other hand, the small Helmholtz resonator setup also appears not very large. It should be noted that both devices display their respective outer dimensions, that is, a reasonable wall thickness has been chosen for this presentation. Finally, by incorporating the damping device into the injector it is probably possible to further reduce the external dimensions.

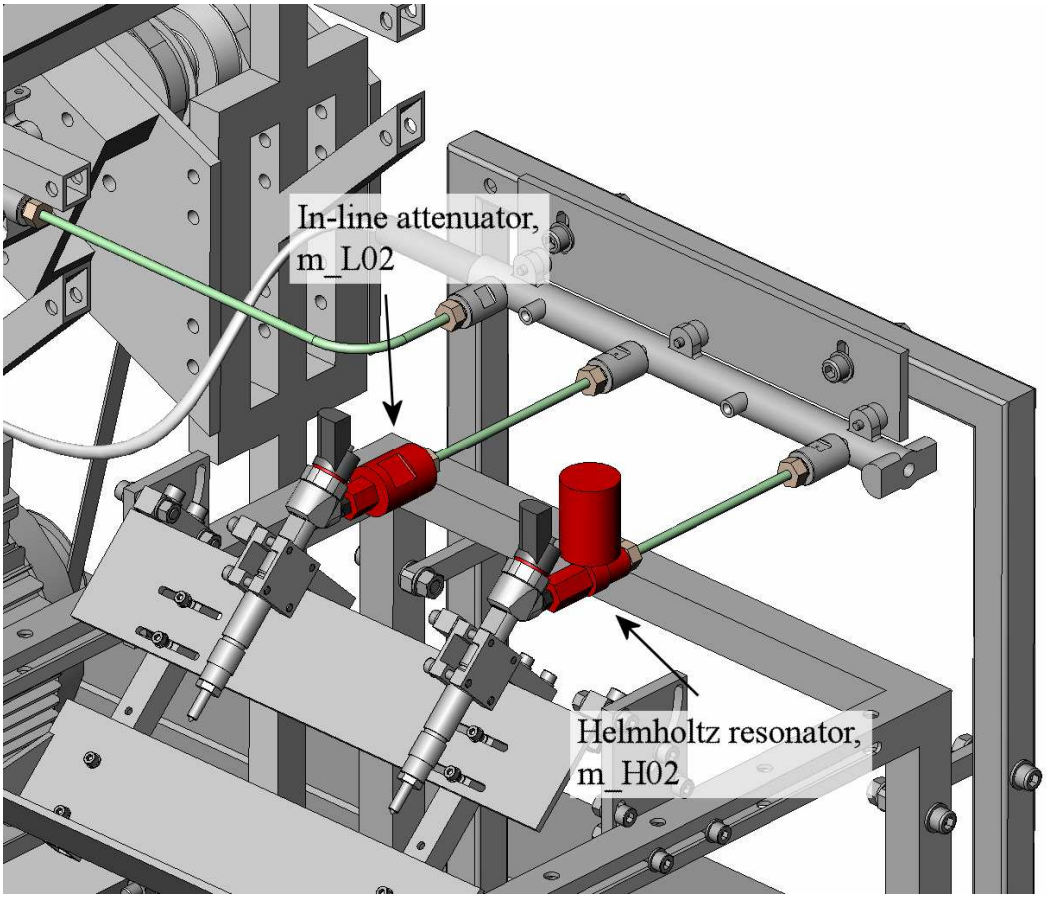

Figure 112. CAD drawing of CR test bench with m_L02 and m_H02.

4. DISCUSSION

This thesis closes the gap between research that concentrates on the combustion process and work that focuses on the fuel delivery process, that is, the performance of, for example, an explicit CR fuel injector design. The literature review in the introduction has stressed that, up to this point, basically no information is available in the literature discussing the impact of the dynamic characteristics of the hydraulic circuit of a high pressure CR system for fast running diesel engines on the overall injection performance. Accordingly, this thesis primarily addresses the need for a deeper knowledge in this area in order to optimise existing and future CR diesel fuel injection systems.

The research work carried out in this thesis involved the study of the theory for modelling fluid transients in hydraulic systems, the analysis of the dynamic characteristics of a commercial high pressure CR system by means of experimental measurements, the development of a numerical simulation model for extending and refining the range of the measurement results, and the utilization of the numerical model to obtain a better insight into local flow phenomena and to investigate the impact of individual parameters and components on the overall system behaviour.

The theoretical review of methods for modelling fluid transients briefly described the main aspects of various approaches that belong either to the group of frequency or time domain methods. The presentation of the basic governing equations for modelling fluid flow has served as a basis for the discussion of different aspects that are important when modelling fast transients in high pressure environments by GT-Fuel and ANSYS-CFX. This included the clarification of the main differences to other, classical methods for modelling fluid transients. The theoretical part ended with a presentation of two simple methods for approximating the main frequencies in primitive hydraulic systems. Consideration of the latter methods was included in this thesis to demonstrate the complexity of the hydraulic system and its effect on the modelling requirements. Based on a comparison of the results of the measurements and GT-Fuel model findings, respectively, it can be said that the predictions of the simplified approaches are less suited to model real-life problems than, for example, the presented CR fuel injection system.

The experimental measurement work was conducted on a hydraulic test bench, which had been designed to allow maximum flexibility with respect to the system layout. The main focus of the geometrical study was on the connection line geometry between rail and injector. In total six, signals were recorded during a measurement run: temperature (*T*), injector current signal, pressure at the injector inlet (*pII*), pressure at the dead end of the adjacent port (*pDE*), pressure at the rail (*pRa*), and mass per injection. From all three pressure signals the pressure at the injector inlet is characterised by considerably larger amplitudes than *pDE* and *pRa*. The latter two data arrays have been found to be very similar, which indicates that the mass flow oscillation in the small dead end branch is to some extent lower than in the relatively large rail (*small* and *large* refers to the corresponding diameters). The oscillation frequency of the *pRa* signal prior to an injection was analysed by DFT for three different injection pressures. It can be said that the frequency before an injection is solely defined through the characteristics of the high pressure pump. No evidence has been found of the pressure regulator valve dynamics having an impact on the overall system dynamics. The study on the effect of the injector mounting point has revealed that it is not important to which rail port the injector is connected.

The parameter analysis for a single injection event consisted of three connection pipe lengths (l_p), three line diameters (d_p), five injection pressures (p_{set}), and four different injection durations (t_{inj}). In respect of *pDE* it can be concluded that a long l_p supports large pressure amplitudes. It is expected that the capacitive effect of the rail volume on the pressure oscillation at the measurement point weakens for increasing connection pipe length. Hence, the oscillation at the end of a long pipe is only affected to a minor degree by the approximately constant pressure in the rail. The impact of d_p is negligible for long t_{inj}; for short injection times, a big d_p leads to larger initial *pDE* amplitudes than a setup with small pipe diameter. The latter finding is particular interesting, since a large flow cross-section is normally associated with smaller amplitudes. On the other hand, it has to be remembered that the rail volume is located between *pDE* and the source of the excitation. Since each flow split and restriction has an effect on the propagation of a pressure pulse, it is plausible that such effects lead to the observed result. The correlation between the dead end amplitudes and p_{set} has been found to depend in a non-linear way on t_{inj}. At the injector inlet, the measurements show that the line length l_p has no effect on *pII* if the injection time is short (t_{inj} = 400 µs). Otherwise, the amplitudes increase as a function of l_p. It has been noted that the setups with the longest pipe tend to be more uniform, that is, the amplitudes are less affected by, for

example, the injection duration. As for *pDE*, it is expected that this behaviour is related to the relative distance between the injector inlet (*pII*) and the rail volume. Concerning the line diameter, the results demonstrate that a larger d_p helps to reduce the amplitudes. This has been found to be true for all t_{inj}; a small exception represents the case for t_{inj} = 400 µs, as the phenomenon appears slightly reduced. It is very likely that this overall trend is related to the differences in instantaneous mass flow as a function of pipe diameter. By assuming approximately identical mass flows, the velocities in the small pipe are by physical law higher. This, on the other hand, leads to larger pressure amplitudes if the moving fluid column needs to be accelerated in either direction. Generally, the data have shown the largest pressure amplitudes for the highest injection pressure. This finding is, in fact, also expected as the volumetric flow through a restriction is connected to the pressure gradient (see, for example, equation (1)). An increase of the pressure gradient usually leads, if choked flow is not considered, to an increase of the flow velocity. By applying the water hammer theory for the d_p argument as above, it can be seen that the amplitude must increase for higher injection pressures. The frequency analysis of the *pII* signal reveals that this output parameter commonly increases for short l_p, large d_p, and high p_{set}. The trends for the first and last parameter, namely l_p and p_{set}, are anticipated. With respect to l_p, it can be said that the oscillation frequency, which is observed at *pII*, is related to the time a pressure pulse needs to travel up and down the connection pipe between rail and injector. The closer the injector is mounted to the rail, the shorter is the pressure pulse revolution and the higher the oscillation frequency. The injection pressure directly affects the fluid density and with it the speed of sound. In this sense, a high set pressure causes an increase of the speed of sound, which again supports a short revolution time of a pressure pulse. The impact of the connection pipe diameter on the oscillation frequency is, on the other hand, significant. Classical *Fluid Transients* theory shows no link between the oscillation frequency and the pipe diameter (see, for example, also the discussion in chapter 2.3). In fact, it makes no sense that the latter parameter has an effect on the fluid density (such as p_{set}) or the revolution time of a pressure pulse (see for example l_p). Accordingly, the explicit phenomenon that has been observed in the measurements and simulations must be based on the fact that the oscillation frequency is the result of a combination of different dynamic systems, that is, the rail, the connection pipe, and the injector. The circumstance that the characteristic oscillation frequency at *pII* is significantly lower than the reciprocal of the connection pipe time constant shows that the statement in the previous sentence is unquestionable. Finally, the measurements have shown that the characteristic time constant of the oscillation is not affected by t_{inj}. The initial pressure

drop is initiated by lifting the injector needle; the needle seat characteristics, on the other hand, define the first pressure minimum, $p_{min,1}$ (see page, 133, Figure 98). In respect of the mean pressure drop (Δp_{mean}) of *pII* due to the needle opening, the measurements have indicated that the pressure drop does not change linearly with p_{set}. Basically, the real CR system behaves similarly in this respect to the classical case of flow out of a pressurised container. The main difference, however, is the fact that the rail is continuously fed by the pump with a specific mass flow and that the system elasticity changes as a function of set pressure. Both contributions may lead to the particular observation that is presented in this thesis. As a function of t_{inj}, the same parameter shows non-linear behaviour. The impact of the connection pipe geometry on the pressure drop is negligible within the studied limits. A small correlation might be found that supports a reduction of Δp_{mean} for long l_p and large d_p. Nevertheless, if larger fuel injection systems, for example, medium speed diesel engines are analysed, it might be sensible to also consider the parameters d_p and l_p. The mass weight measurements have revealed that a large injection pressure and long injection duration support large injection amounts. For injection times longer 600 µs the results have indicated that in the range of the analysed parameters the mass flow rate through the injector tends to be independent of the pressure drop over the injector (see, for example, Figure 49 on page 81). On a cautious note, however, it must be stressed that the quality of this statement is dependent on the number of utilised observation points. Further phenomena need to be considered in order to make a more accurate prediction (see discussion of simulation results). If the injection parameters p_{set} and t_{inj} are kept constant, the measurement data document that long connection lines lead to a reduction of the injected mass per injection. This has been found to be particularly true if the diameter d_p is chosen to be small. Similarly, large line diameters support an increase of the mass flow rate, which was especially evident when long l_p has been used. Overall, the impact of the connection line on the mass per injection diminishes for short injection times. The last findings are believed to be result of the combined system characteristics. Depending on the hydraulic circuit configuration and operating conditions it is likely that the dynamic properties are changing. Thus, the combination of all contributions leads to the observed result.

The experimental analysis of double injection events covered five injection periods or dwell times, respectively. Both injections were conducted with an identical injection time of t_{inj} = 600 µs. The output parameters included the study of pressure histories at the injector

inlet (*pII*), the frequency of *pII*, and the comparison of the mass flow rates for the first and second injection. In respect of the first parameter, it has been found that the final pressure oscillation is significantly larger than for the single injection case, if the start of the second injection is in phase with the positive pressure peak of the previous injection. Conversely, an injection that starts on the second negative amplitude of the oscillation leads to peaks that are only slightly higher or lower than the single injection extreme values. If the start is set on the first negative slope (not counting the initial pressure drop due to valve opening) at about the same p_{set}-level as the first injection ("case A"), the amplitudes are significantly larger than for the default case. Conversely, for the second injection starting on the second positive slope and at the same injection pressure level ("case B"), the resultant oscillation has been recorded as smaller than for the single injection event. Based on these findings, it can be argued that the final pressure amplitudes are the result of both the static and dynamic pressure head. Both contributions define the final outcome, that is, if the effects of each injection support or oppose each other. With respect to the oscillation frequency, the measurements show that the timing of the second injection has no effect on the final frequency; a slight exception to this rule can be found for the setup with the first and second wave being in opposite phase. Together with the findings for the single injection measurements, it can be speculated that also double injections with different t_{inj} lead to the same result. The analysis of the individual mass flow rate results shows a strong correlation to the injection period. The lowest injection rate for the second injection is recorded for "case A"; an injection at the first positive peak and at "case B" has led, on the other hand, to maxima of the same parameter. Just as for the pressure amplitudes, the total amount of mass that is injected during the second needle opening is dependent on the total pressure head.

The main settings and definitions for modelling the CR system by means of GT-Fuel were presented. This included the presentation of the basic concept for modelling fluid transients in GT-Fuel and the implementation of the real system into the code. The presence of special flow phenomena inside the fuel injector was emphasised. A three-dimensional transient CFD analysis in ANSYS-CFX was conducted to obtain knowledge about the flow field inside the injector pilot stage. The results have confirmed that the pressure field and streamlines vary strongly during the plunger lift phase. This information has been used to enhance the one-dimensional simulation model in order to obtain better correlation with the real system.

The GT-Fuel simulation model of the CR system was validated with experimental data. The comparison was not restricted to a few operating points, but included the complete range that had been investigated during the measurements. For evaluation, the *pII* data array and the mass flow rate were chosen as comparison parameters. The simulation model has shown overall good agreement with the measurement data. Some discrepancy has been found for the mass rate per injection for the smallest injection time (t_{inj} = 400 µs). However, the impact of the difference on the overall results has been judged to be acceptable. It should be noted at this point that due to the good agreement between measurements and simulations, the subsequently following summary of the simulation results omits a discussion of the findings if they are commented on in the previous sections of the measurement results.

The simulation model was used to extend the parameter study of the experimental measurement, that is, to refine and widen the range of considered parameters. With emphasis placed on the connection pipe geometry and the injection parameters p_{set} and t_{inj}, a total of 1050 configurations were investigated. The output parameters included the pressure history at *pII* and the injection rate per injection. The former parameter considered explicitly the extreme values p_{max}, $p_{min,1}$, and $p_{min,2}$. Secondly, the oscillation frequency, f, and the attenuation of the oscillation were studied. Concerning the latter analysis, two methods were presented and utilised. In respect of the maximum pressure level in the system, the simulations show that generally long injection durations support a high value for p_{max}. This correlation is emphasised for low injection pressures. It has been further found that the p_{max} values align for long t_{inj} and in conjunction with long l_p and large d_p. Overall, it is evident that the connection line geometry affects the impact of t_{inj} on p_{max}. If, for example, a short pipe length is used, it can be seen that the weight of t_{inj} is reduced. By speaking for the impact of p_{set} on p_{max}, the results confirm that the maximum positive amplitude increases as a function of injection pressure. It has been found that this correlation is non-linear. The situation is similar for the link between connection line geometry and p_{max}. Firstly, the parameters l_p and d_p are connected to p_{max} in a non-linear way. Secondly, the simulations demonstrate that some small impact of the pipe geometry is present for very short injection times. The rate of change of p_{max} as a function of l_p increases if the line diameter is set to a small value. On the other hand, the relative impact of d_p reduces for long connection pipes. With reference to the minimum pressures $p_{min,1}$ and $p_{min,2}$, the results have been in alignment with the p_{max} findings. Generally, the absolute value of the first downwards pointing peak is bigger than the second, if the injection pressure is high and a small line diameter is chosen. It can also be seen that the

first pressure undershoot becomes independent of the injection duration in the case of t_{inj} > 500 µs. The frequency analysis of the *pII* pressure oscillation has extended the measurement data discussion by showing clearly the non-linear relation between p_{set} and f. The calculations have indicated that the impact of p_{set} depends on the connection pipe geometry. Particularly for small connection line diameters, the weight of p_{set} appears reduced. In respect of the connection between pipe geometry and f, the simulation adds that the impact of d_p decreases for long l_p. In fact, the results indicate that f tends to a finite value for large d_p. The normalised comparison of the data has revealed that p_{set} has no impact on the relative variation of f due to l_p and d_p. In this context, the results of the simplified methods for estimating the basic frequency of a hydraulic system did not match with the findings of the GT-Fuel simulation and measurements, respectively. This shows that none of the presented simplified methods is capable of predicting the main characteristics of the hydraulic CR circuit. For completeness, it should be added that the approaches might perform somewhat better if more detail is added to the models. This would, however, not overcome the general deficiency when representing large pressure gradients. Secondly, both methods would become significantly more complex, which undermines the initial idea of using a quick and simple method. With respect to the oscillation damping, a trend emerges that supports higher damping for higher injection pressures. Overall, the differences as a function of the studied parameters are small. The simulation results for the mass rate per injection confirm the measurement findings. Because of the finer parameter definition, it is found, in fact, that the impact of the connection line geometry on the injection rate diminishes for injection times equal or less than t_{inj} = 600 µs. The analysis of the mass rate per injection, together with the needle lift, has shown that the injection amount is primarily a combination of injection duration, instantaneous pressure at the needle seat and needle opening area. The last two parameters are directly linked to each other, since the static needle seat pressure acts on the needle tip surface; most interestingly, it has been found that the needle does not necessarily reach its full lift, but performs only partial lifts. This latter circumstance, which depends on the injection parameters p_{set} and t_{inj}, is to a great extent responsible for the observed results (see, for example, Figure 49 and Figure 100).

The numerical study of the double injection event was defined in accordance with the experimental measurements. In total, nine injection periods were analysed. The geometry study included two additional connection pipe lengths and line diameters. The output parameters were based on the pressure history at the injector inlet, mass flow rates, and

computed needle lifts. Firstly, a comparison of the simulated data to the experiment has shown good agreement between the pressure histories *pII* and the mass flow rates. Secondly, the geometry analysis confirms that the injection amount of the second injection is, the same as the *pII* pressure characteristics, a function of the pipe geometry, l_p and d_p. The characteristic delivery curve shifts left or right on the time axis and is compressed or stretched as a function of the pipe length and line diameter. With reference to the pressure amplitudes, the computations have underlined the strong impact of the injection period on the pressure history *pII*. The needle lift analysis reveals that the second needle opening depends on the dwell time between the first and second injection. It has been emphasised in the text that the smallest needle lift and the smallest delivery rate do not occur for the same injection period. The last two findings can be supported by the same argument as for the discussion of, for example, the mass rate per injection for a single injection event. While the needle displacement is solely defined by the forces that act on the needle mass, that is, forces based on the static pressure, the mass flow rate is to a great extent also dependent on the instantaneous motion of the fluid column.

In a further analysis of the CR circuit, parameters have been studied that are not accessible through measurements. Firstly, a comparison of the pressures at the injector inlet and inside the sac volume has confirmed that a discussion of the system characteristics (initial pressure amplitudes, frequency and decay of the oscillation) based on *pII* is justified. Secondly, it has been presented that the temperature variation due to compression and rarefaction waves is considerable. The same is true for the calculated speed of sound in the fluid. Because both variables are linked together via the fluid density, which is dependent on the instantaneous temperature, it has been shown that this effect should not be neglected in the presence of large pressure gradients. The computation of the instantaneous *Re* number and fluid velocity at two different locations in the circuit and for various injection settings underline that both variables are not constant. Certainly, this finding has been anticipated due to the nature of the involved physics. The presented plots, therefore, stress that it is not sensible to apply the same categorisation of, for example, laminar versus turbulent flow when dealing with this kind of hydraulic system. An analysis of the pressure histories at various locations inside the injector was used together with the computed needle lift profile to discuss explicit injector phenomena. In this context, it has been found that the initial pressure history at the injector inlet is strongly affected by the internal design of the injector. The review of computed needle lifts as a function of the input parameters has revealed that the injector opening is based on

p_{set} and t_{inj}. At short injection times the needle usually does not reach its full stroke length. In fact, a large injection pressure supports fast valve activation and large needle displacement. Conversely, the simulation results reveal that the connection line geometry has basically no effect on the needle lift.

Four additional models were compared to the default simulation setup in order to investigate the effect of the injector on the overall system behaviour. All new models were characterised by a simplified representation of the injector; for example, in all cases the needle movement was defined through a look-up table of the needle seat flow cross-section. The comparison of the cases concentrated on the pressure signal at the injector inlet. This included the *pII* history, the extreme values of *pII*, and the main frequency of the same data array. In respect of the first comparison criteria, the simulation results have shown that none of the simplified models can reproduce the typical shape of the initial pressure drop. Similarly, the simplified models lack the capability to predict the initial extreme values of the *pII* signal. Although the results are acceptable for some operating points, the overall accuracy over the complete parameter range is not satisfactory. Only the model that shows the highest similarity to the default setup can correctly predict the correlation between oscillation frequency and connection line diameter. The reasons for the latter observations are already given in earlier sections. The overall dynamic behaviour of the hydraulic CR circuit is the sum of individual components. One such component is the fuel injector. If it is changed, for example, by neglecting some of its flow paths, the resultant dynamic behaviour is different and with it the characteristics of the complete circuit.

A simulation model was developed to investigate the impact of wall flexibility on the dynamic characteristics of the system. For this purpose, all *Pipe* objects of the rail and the connection lines in the GT-Fuel model were enhanced to includ FSI effects. A comparison of the injector inlet pressure signal has revealed that both FSI and rigid wall simulation basically lead to the same findings. One explanation that speaks for this observation is the fact that the individual components are specially designed for this application. Because of the relatively large wall thickness and material selection, the deformation of the components is basically negligible. In order to study the effect of the rail properties on the system, four additional rail geometries were simulated together with the default injector model. The main output parameter was given the same as for the FSI analysis by the *pII* history. It has been summarised that the initial pressure history at the injector inlet is not affected by the rail

geometry; both initial minimum and maximum pressure values are very similar to the default simulation result. Indeed, it has been shown that the diameter and length of the rail only has a slight effect on the main oscillation frequency. This result underlines that, within the studied parameters, the rail volume has only a minor impact on the overall dynamic characteristics of the hydraulic circuit.

The final chapter of this research work briefly investigated the possibilities of minimising unwanted pressure oscillations at the injector inlet. Two dampers of passive interference and wave reflection type were studied: Helmholtz resonator and in-line attenuator. The numerical analysis was based on the study of two designs for each damper. The simulation setup considered three different connection pipe lengths and six injection parameters. By considering exclusively the pressure history at the injector inlet and the total pressure variation at the same location, it has been observed that the best attenuation can be achieved through implementing a Helmholtz resonator. The results for the in-line resonator have been mixed. For a too small damper configuration, the attenuation has been found to be not satisfactory. The second, slightly bigger design, however, has led to an acceptable attenuation rate of the oscillation. This last analysis has shown that it is in general possible to optimise an existing system by relatively small modifications. It should be stressed, however, that the damper study was intended to provide only a rough presentation of some potential solution. Before adapting such a device to an existing system, more analysis is required.

5. CONCLUSIONS AND SUGGESTIONS FOR FURTHER RESEARCH

The research contributions of this thesis regarding the analysis of the hydraulic circuit of a high pressure CR diesel fuel injection system by means of experimental measurements and numerical simulations are:

- Fuel injection by an injector that is connected to the accumulator of a CR system triggers fluid transients in the hydraulic circuit. Primarily, the transients have a negative effect on subsequent injections at the same injector as they considerably alter the initial conditions. In the same way, it is also possible that the injection at an adjacent injector is affected negatively through wave transmission.
- The fluid transients at the injector inlet are a function of the injection parameters and the connection line geometry between rail and injector.
- A simulation model of the CR system is a very valuable tool to gain better insight into local flow phenomena that ultimately define the behaviour of the total system.

In detail, it can be concluded that:

- The regulator valve has no impact on the dynamic characteristics of the CR circuit studied here. It can therefore be omitted in the simulation model of the hydraulic system.
- It is adequate to study the system on a test bench by mounting only one injector to the rail. The other ports can be used, for example, to connect sensors to the system.
- The internal flow field of the injector is rather complex. As experimental measurements are extremely difficult, or even impossible, to conduct, a three-dimensional analysis of the internal flow physics by CFD can help to optimise the one-dimensional simulation model of the complete circuit.
- Fluid flow in CR circuits can not be described by classical dimensionless numbers like for example the *Re*.
- The measured and simulated mass flow rates per injection show that this variable is strongly connected to the explicit needle lift. Secondly, it is believed that, particularly for high injection pressures and long needle openings, there develops a choked flow condition inside of the nozzle holes. The latter argument supports the finding that the

flow rate through the injector tends to be independent of the pressure gradient (within the studied limits).

- The mass flow rate during injection is not exclusively defined by the instantaneous static pressure head at the needle seat, but also the dynamic pressure, that is, the fluid inertia and the needle lift.
- By modifying the internal restrictions of the injector, it is possible to adjust the first negative peak of the oscillation at the injector inlet. For example, the pressure level is defined by the needle seat geometry; the initial slope of the first pressure undershoot is based on the pilot stage characteristics.
- The dimensions of the main flow path inside the injector, that is, the variations of the flow cross-sections from injector inlet to needle seat are responsible for the typical correlation between main oscillation frequency of the complete circuit, which is, for example, measured at the injector inlet, and the connection line diameter.
- For analysing the attenuation of the pressure oscillation, the step-response method should not be used exclusively, as uncertainties may have a significant effect on the final result. This output parameter is generally seen as less important than the other parameters for evaluating the characteristics of the fluid transients in a high pressure CR system.
- The simulation model has confirmed that fluid compression and rarefaction leads to considerable changes of the instantaneous fluid temperature. It is therefore sensible to include the energy equation in the basic set of governing equations for the modelling of high pressure systems.
- It is adequate to use rigid walls for the analysis of the high pressure CR system. Generally, uncertainties in, for example, the injector model definition surpass the impact of the wall flexibility on the analysed parameters.
- The rail dimensions, if modified within the studied range, play only a minor role for optimization of the dynamic characteristics of the complete system.
- Based on a properly designed Helmholtz resonator or in-line damper, it is possible to reduce significantly the fluid transients at the injector inlet. It is very likely that such measure leads to a more uniform injection pattern and a more predictable combustion process.

For more precise statements concerning the impact of the total pressure at the needle seat and the needle lift on the mass flow rate per injection, it would be advantageous to extend the double injection study to include a wider range of parameter settings. Clearly, such work should be made on the basis of a given engine layout. Only in this way is it possible to reduce the amount of parameters to a manageable size. In respect of the injector model, it can be said that the development of a new system could certainly benefit from measured needle lift data. It is emphasised at this point that such information is not compulsory for model accuracy reasons. In fact, it is believed that measured needle lift data can help to accelerate the model development time by shortening the trial and error phase. The present model of the CR system could eventually be further advanced by adapting the fluid properties of the simulation model to the fluid properties of the hydraulic test bench. Although both fluids belong to the same standard, it is conceivable that small differences are a source of the observed discrepancies.

REFERENCES

1. Accessory for Test Benches, Injection Quantity Indicator - EMI21. Moehwald GmbH, product data sheet.
2. Ahlin, K. Modelling of Pressure Waves in Common Rail Diesel Injection Systems. Department of Electrical Engineering - Vehicular Systems, University of Linköping, Masters Thesis, 2000, Linköping, Sweden.
3. Altstadt, E., H. Carl, R. Weiss. "Fluid-Structure Interaction Experiments at the Cold Water Hammer Test Facility (CWHTF) of Forschungszentrum Rossendorf." Annual Meeting on Nuclear Technology, Stuttgart, Germany, 14-16 May 2002.
4. American Society of Mechanical Engineers. Symposium on Water Hammer, Arranged by the ASME Committee on Water Hammer for Presentation June 30, 1933 at the Century of Progress Exposition, Chicago. 1949.
5. Anderson Jr., J. D. Computational Fluid Dynamics. International ed. New York, USA: McGraw-Hill, Inc., 1995.
6. Angermann, A., M. Beuschel, M. Rau, U. Wohlfarth. Simulation mit Simulink/Matlab, Skriptum mit Uebungsaufgaben. Lehrstuhl fuer Elektrische Antriebssystems - Technische Universitaet Muenchen (November 2001).
7. ANSYS CFX-10.0. ANSYS CFX-Solver, Release 10.0: Theory. ANSYS Inc. 2005.
8. Axworthy, D. H., M. S. Ghidaoui, D. A. McInnis. "Extended Thermodynamics Derivation of Energy Dissipation in Unsteady Pipe Flow." Journal of Hydraulic Engineering, American Society of Civil Engineers, 4 (2000): 276-287.
9. Backé, W. Grundlagen der Ölhydraulik (Umdruck zur Vorlesung). 4th ed. Rheinisch-Westfaelische Technische Hochschule Aachen, Institut fuer hydraulische und pneumatische Anlagen, Germany (1979).
10. Bargende, M., U. Esser. eds. Dieselmotorentechnik 2000. Volume 580. Renningen, Germany: Expert Verlag GmbH, 2000: 230-239.
11. Bauer, H. ed. Diesel Engine Management. 2nd ed. Stuttgart, Germany: Robert Bosch GmbH, 1999.
12. Beierer, P. "Pressure Transient in Conduits – A Numerical Study." Report 91, Institute of Hydraulics and Automation, Tampere University of Technology, 2006.
13. Beierer, P., K. Huhtala, E. Lehto, M. Vilenius. "Study of the Impact of System Characteristics on Pressure Oscillations in a Common Rail Diesel Fuel Injection System." SAE Paper 2005-01-0910 2005.
14. Beierer, P., K. Huhtala, M. Vilenius. "Effect of Model Characteristics on Numerical Results for a Hydraulic High-Pressure Nozzle System." Bath Workshop on Power Transmission and Motion Control, Bath 2003. Bath, UK.
15. Beierer, P., K. Huhtala, M. Vilenius. "Experimental Study of the Hydraulic Circuit of a Commercial Common Rail Diesel Fuel Injection System." SAE Paper 2007-01-0487 2007.

16. Beierer, P., K. Huhtala, M. Vilenius. “Numerical Analysis of the Hydraulic Circuit of a Commercial Common Rail Diesel Fuel Injection System.” Bath Workshop on Power Transmission and Motion Control, Bath 2007. Bath, UK.

17. Beierer, P., K. Huhtala, M. Vilenius. “Study of Various Fluid Flow Models and their Impact on Numerical Predictions for a High-Pressure Diesel Fuel Injector.” Proceedings of the Fourth International Fluid Power Conference - IFK, Dresden. Dresden, Germany (2004).

18. Bianchi, G. M., P. Pelloni, S. Falfari, F. Brusiani, G. Osbat, M. Parotto, C. Lamberti. Speech. “Advanced Modelling of a New Diesel Fast Solenoid Injector and Comparison with Experiments.” AMESim Users’ Conference, 2004.

19. Bianchi, G. M., S. Falfari, F. Brusiani, P. Pelloni, G. Osbat, M. Parotto. “Numerical Investigation of Critical Issues in Multiple-Injection Strategy Operated by a New C.R. Fast-Actuation Solenoid Injector.” SAE Paper 2005-01-1236 2005

20. Brennen, C. E. Hydrodynamics of Pumps. White River Junction, USA: Concepts NREC, 1994.

21. Bronstein, I. N., K. A. Semendjajew, G. Musiol, H. Muehlig. Taschenbuch der Mathematik. 5th ed. Frankfurt am Main, Germany: Verlag Harri Deutsch, 2001.

22. Brown, F. T. “A Quasi Method of Characteristics with Application to Fluid Lines with Frequency dependent Wall Shear and Heat Transfer.” Journal of Basic Engineering, Transactions of the ASME, Volume 91 (1969): 217-227.

23. Brown, G. W., H. McCallion. “Simulation of an Injection System with Delivery Pipe Cavitation using a Digital Computer.” Proceedings of the Institution of Mechanical Engineers, Conference Proceedings 1964-1970 (1967): 182-206.

24. Brunone, B., B. W. Karney, M. Mecarelli, M. Ferrante. “Velocity Profiles and Unsteady Pipe Friction in Transient Flow.” Journal of Hydraulic Engineering, American Society of Civil Engineers, 7-8 (2000): 236-244.

25. Brunone, B., U. M. Golia, M. Greco. “Effects of Two-Dimensionality on Pipe Transients Modeling.” Journal of Hydraulic Engineering, American Society of Civil Engineers, 12 (1995): 906-912.

26. Carlucci, A. P., N. Panarese, D. Laforgia. “Experimental Characterization of Diesel Fuel Pulsed Sprays.” SAE Paper 2007-01-0664 2007

27. Casoli, P., A. Vacca. “Modelling of an Axial Piston Pump for Pressure Ripple Analysis.” Proceedings of the 8th Scandinavian International Conference on Fluid Power, Tampere 2003 Volume 1 (2003): 207-221.

28. Catania, A. E., A. Ferrari, A. Mittica, E. Spessa. “Common Rail Without Accumulator: Development, Theoretical-Experimental Analysis and Performance Enhancement at DI-HCCI Level of a New Generation FIS.” SAE Paper 2007-01-1258 2007.

29. Catania, A. E., A. Ferrari, M. Manno, E. Spessa. “Thermal Effect Simulation in High-Pressure Injection System Transient Flow.” SAE Paper 2004-01-0532 2004.

30. Catania, A. E., C. Dongiovanni, A. Mittica, M. Badami, F. Lovisolo. “Numerical Analysis Versus Experimental Investigation of a Distributor-Type Diesel Fuel-Injection System“ Journal of Engineering for Gas Turbines and Power Volume 116, Issue 4: 1994

31. Cerbe, G., G. Wilhelms. Technische Thermodynamik. 14th ed. Muenchen, Germany: Carl Hanser Verlag, 2005.

32. Chilton, T. H., A. P. Colburn. “Mass Transfer (Absorption) Coefficients Prediction from Data on Heat Transfer and Fluid Friction.” Journal of Industrial and Engineering Chemistry *(today: Industrial & Engineering Chemistry)*, Volume 26, Issue 11 (1934): 1183-1187.

33. Coppo, M., C. Dongiovanni, C. Negri. “Numerical Analysis and Experimental Investigation of a Common Rail-Type Diesel Injector.” Transactions of the ASME Volume 126 (October 2004): 874-885.

34. D’Souza, A. F., R. Oldenburger. „Dynamic Response of Fluid Lines.“ Journal of Basic Engineering, Transactions of the ASME (1964): 589-598.

35. Dietsche, K.-H., M. Kingebiel, R. Mueller. eds. Diesel Fuel-Injection System Common Rail. 2nd ed. Stuttgart, Germany: Robert Bosch GmbH, 2005.

36. Edge, K. A., D. N. Johnston. “The Impedance Characteristics of Fluid Power Components: Relief Valves and Accumulators.” Journal of Systems and Control Engineering, Proceedings of the Institution of Mechanical Engineers, Volume 205, No. I1 (1991): 11-22.

37. Edge, K. A., F. J. T. de Freitas. “A Study of Pressure Fluctuations in the Suction Lines of Positive Displacement Pumps.” Management and Engineering Manufacture, Proceedings of the Institution of Mechanical Engineers, Vol 199, Part B (1985): 211-217.

38. Ehrenfried, K. Skrip zur Vorlesung Stroemungsakustik 1 und 2. Technische Universitaet Berlin, Germany (2003).

39. Esser, U., ed. Dieselmotorentechnik 98. Volume 553. Renningen, Germany: Expert Verlag GmbH, 1998: 71-78.

40. Esser, U., K. H. Prescher. eds. Dieselmotorentechnik 96. Volume 505. Renningen, Germany: Expert Verlag GmbH, 1996: 137-153.

41. Favennec A.-G., M. Lebrun, “Models for Injector Nozzles.” Proceedings of the 6th Scandinavien International Conference on Fluid Power, Tampere 1999 Volume 1 (2003): 583-596.

42. Favennec, A. G., P. Minier, M. Lebrun. "Analysis of the Dynamic Behaviour of the Circuit of a Common Rail Direct Injection System" Proceedings of the Fourth JHPS International Symposium on Fluid Power, Tokyo 1999 (1999): 543-548.

43. Gamma Technologies, Inc. GT-FUEL User’s Manual and Tutorial. Version 6.2. Gamma Technologies, Inc., September 2006.

44. Ghidaoui, M. S., B. W. Karney, D. A. McInnis. “Energy Estimates for Discretization Errors in Water Hammer Problems.” Journal of Hydraulic Engineering, American Society of Civil Engineers, 4 (1998): 384-393.

45. Ghidaoui, M. S., A. A. Kolyshkin. “Stability Analysis of Velocity Profiles in Water Hammer Flows.” Journal of Hydraulic Engineering, American Society of Civil Engineers, 6 (2001): 499-512.

46. Giannadakis, E., D. Papoulias, M. Gavaises, C. Arcoumanis, C. Soteriou, W. Tang. “Evaluation of Predictive Capability of Diesel Nozzle Cavitation Models.” SAE Paper 2007-01-0245 2007.

47. Gullaksen, J. Simulation of Diesel Fuel Injection Dynamics. Department of Mechanical Engineering, Technical University of Denmark, Masters Thesis, 2003, Lyngby, Denmark.

48. Haikio, S., K. Huhtala, S. Tikkanen, M, Lammila, Erkki Lehto, and Matti Vilenius. "Effect of Number of Pumping Elements on Pressure Ripple in High Pressure System." Proceedings of the 8th Scandinavien International Conference on Fluid Power, Tampere 2003 Volume 2 (2003): 1277-1288.

49. Harrison, K. A., K. A. Edge. "Reduction of Axial Piston Pump Pressure Ripple." Journal of Systems Control Engineering, Proceedings of the Institution of Mechanical Engineers, Vol 214, Part 1 (2000): 53-63.

50. Hersey, M. D. "Viscosity of Diesel Engine Fuel Oil under Pressure." Technical Notes National Advisory Committee for Aeronautics NASA Technical Library, No. 315: 1929.

51. Herwig, H. Strömungsmechanik: Eine Einführung in die Physik und die mathematische Modellierung von Strömungen. Berlin, Germany: Springer-Verlag, 2002.

52. Hountalas, D. T., A. D. Kouremenos. "Development of a fast and simple simulation model for the fuel injection of system of diesel engines." Advances in Engineering Software Volume 29, No. 1 (1998): 13-28

53. Hu, Q., S. F. Wu, S. Stottler, R. Raghupathi. "Modelling of Dynamic Responses of an Automotive Fuel Rail System, Part 1: Injector" Journal of Sound and Vibration Volume 245, No. 5 (2001): 801-814.

54. Huttunen, H. Signaalinkaesittelyn menetelmaet (in Finnish language). Institute of Signal Processing - Tampere University of Technology (2005:1).

55. Implicit versus Explicit Methods. Flow Science Inc. 16 May 2007 <http:// www.flow3d.com/cfd101/cfd101_impl_expl.html>

56. Ivantysyn, J. and M. Ivantysynova. Hydrostatische Pumpen und Motoren: Konstruktion und Berechnung. 1st ed. Würzburg, Germany: Vogel Verlag und Druck KG, 1993.

57. Johnston, D. N. "Prediction of Fluid Inertance in Non-uniform Passageways." Journal of Fluids Engineering, Transactions of the ASME, Volume 128 (2006): 266-275.

58. Johnston, D. N., K. A. Edge. "The Impedance Characteristics of Fluid Power Components: Restrictor and Flow Control Valves." Journal of Systems and Control Engineering, Proceedings of the Institution of Mechanical Engineers, Volume 205, No. I1 (1991): 3-10.

59. Johnston, D. N., K. A. Edge., M. Brunelli. "Impedance and Stability Characteristics of a Relief Valve." Journal of Systems and Control Engineering, Proceedings of the Institution of Mechanical Engineers, Volume 216, Part I (2002): 371-382.

60. Keller, F. J., W. E. Gettys, M. J. Skove. Physics: Classical and Modern. 2nd ed. New York, USA: McGraw-Hill, Inc., 1993.

61. Knight, B. E. "Fuel Injection Systems Calculations." Proceedings of the Institution of Mechanical Engineers, Automobile Division 1947-1970 (1960): 25-33.

62. Kojima, E., M. Shinada, J. Yu. "Development of Accurate and Practical Simulation Technique Based on the Modal Approximations for Fluid Transients in Compound Fluid-Line Systems." International Journal of Fluid Power 3 (2002) No. 2: 5-15.

63. Laamanen, A., M. Linjama, M. Vilenius. “Pressure peak phenomenon in digital hydraulics - a theoretical study.” Bath Workshop on Power Transmission and Motion Control, Bath 2005. Bath, UK: 91-104.

64. Laamanen, A., M. Linjama, M. Vilenius. “The effect of coding method on pressure peaks in digital hydraulic system.” Proceedings of the 4th FPNI - PhD Symposium, Sarasota 2006 Volume 1 (2006): 285-295.

65. Larock, B. E., R. W. Jeppson, G. Z. Watters. Hydraulics of Pipeline Systems. Boca Raton, USA: CRC Press LLC, 2000.

66. Lehto, E., M. Lammila, K. Huhtala, T. Virvalo. “Influence of Solenoid Current Format on Common Rail Fuel Injection.” Proceedings of the 8th Mechatronics Forum International Conference. University of Twente, Netherlands, 24-26 June 2002: 251-258.

67. Maekinen, J., R. Piché, A. Ellman. “Fluid Transmission Line Modelling Using a Variational Method.” Journal of Dynamic Systems, Measurement, and Control, Transactions of the ASME, Volume 122, Issue 1 (2000): 153-162.

68. Marcic, M., “A new Method for Measuring Fuel-Injection Rate.” Flow Measurement and Instrumentation, 10 (1999): 159-165.

69. Marriott, C. D.. "Distributed Accumulator for Hydraulic Camless Valve Activation System." US Patent 6755162. 2004.

70. Matsuoka, S., K. Yokota, T. Kamimoto, M. Igoshi. “A study of Fuel Injection Systems in Diesel Engines - Part 1” SAE Paper 760550 1976.

71. Matsuoka, S., K. Yokota, T. Kamimoto, M. Igoshi. “A study of Fuel Injection Systems in Diesel Engines - Part 2” SAE Paper 760551 1976.

72. Merritt, H. E. Hydraulic Control Systems. New York, USA: John Wiley & Sons, Inc., 1967.

73. Miller, D. S., Internal Flow Systems. 2nd ed. Bedford, England: BHRA - The Fluid Engineering Centre, (1990).

74. Mueller, B. Einsatz der Simulation zur Pulsations- und Geraeuschminderung hydraulischer Anlagen. Institut fuer fluidtechnische Antriebe und Steuerungen, Rheinisch-Westfaelische Technische Hochschule Aachen, Doctoral Thesis, 2002, Aachen, Germany.

75. PONSSE Beaver C33 – photo gallery. Ponsse Group. 9 May 2007 <http://www.ponsse.com/gallery/view_album.php?set_albumName=Beaver&newlang=en_US>

76. Pontoppidan, M., F. Ausiello, G. Bella, and S. Ubertini. “Study of the impact on the spray shape stability and the combustion process of supply pressure fluctuations in CR-diesel injectors.” SAE Paper 2004-01-0023 2004

77. Rakopoulos, C. D., D. T. Hountalas. “A Simulation Analysis of a DI Diesel Engine Fuel Injection System Fitted with a constant Pressure Valve.” Elsevier: Energy Conversion and Management Volume 37, No. 2 (1996): 135-150.

78. Rébel, J. “Systematische Uebersicht ueber Daempfungsmassnahmen in Druckleitungen.” Oelhydraulik und Pneumatik, 20, Nr. 7 (1976): 461-465.

79. Rodriguez-Anton, L. M., J. Casanova-Kindelan, G. Tardajos. “High Pressure Physical Properties of Fluids used in Diesel Injection Systems.” SAE Paper 2000-01-2046 2000.

80. Roth, H., E. Giannadakis, M. Gavaises, C. Arcoumanis, K. Omae, I. Sakata, M. Nakamura, H. Yanagihara. “Effect of Multi-Injection Strategy on Cavitation Development in Diesel Injector Nozzle Holes.” SAE Paper 2005-01-1237 2005.

81. Russell, M. F., G. Greeves, N. Guerrassi. “More Torque, Less Emissions and Less Noise.” SAE Paper 2000-01-0942 2000.

82. Scheidl R., B. Manhartsgruber, G. Mikota, B. Winkler. “State of the Art in Hydraulic Switching Control - Components, Systems, Applications.” Proceedings of the 9th Scandinavien International Conference on Fluid Power, Linkoeping 2005 (2005).

83. Schlichting, H., K. Gersten. Boundary Layer Theory. 8th ed. Berlin, Germany: Springer-Verlag, 2000.

84. Shu, J.-J., C. R. Burrows, K. A. Edge. “Pressure Pulsations in Reciprocating Pump Piping Systems, Part 1: Modelling.” Journal of Systems and Control Engineering, Proceedings of the Institution of Mechanical Engineers, Vol 211, Part 1 (1997): 229-237.

85. Siekmann, H. E. Strömungslehre - Grundlagen. Berlin, Germany: Springer-Verlag, 2000.

86. Stecki, J., D. Davis. “Fluid Transmission Lines-Distributed Parameter Models, Part 1: A review of the State of the Art.” Power and Process Engineering 1983-1988, Proceedings of the Institution of Mechanical Engineers, Part A (1986): 215-228.

87. Streeter, V. L., ed. Handbook of Fluid Dynamics. 1st ed. New York, USA: McGraw-Hill Book Company, Inc., 1961.

88. Systems for Diesel Fuel Injection. Stuttgart, Germany: Robert Bosch GmbH, 2000.

89. Taylor, S. E. M., D. N. Johnston, D. K. Longmore. “Modelling of Transient Flow in Hydraulic Pipelines.” Journal of Systems and Control Engineering, Proceedings of the Institution of Mechanical Engineers, Vol 211, Part I (1997): 447-456.

90. Technologien - Hydraulik. Rexroth Bosch Group. 9 May 2007 <http:// www.boschrexroth.com/country_units/europe/germany/de/products/technologiefelder/index.jsp>

91. The MathWorks, Inc. Matlab User’s Manual. Release R2006a.

92. Tijsseling, A. S., A. E. Vardy, D. Fan. “Fluid-Structure Interaction and Cavitation in a Single-Elbow Pipe System.” Journal of Fluid and Structures, Academic PressLimited, 10 (1996): 395-420.

93. van Basshuysen, R., F. Schaefer, eds. Handbuch Verbrennungsmotoren. 2nd ed. Braunschweig, Germany: Vieweg & Sohn Verlagsgesellschaft mbH, 2002.

94. van Bebber, D. “Reduction of Pressure Waves in Common Rail Systems by Improving System Design Parameters.” Proceedings of the Fifth International Fluid Power Conference - IFK, Aachen. Aachen, Germany (2006).

95. Versteeg, H. K., W. Malalasekera. An Introduction to Computational Fluid Dynamics: The Finite Volume Method. Edinburgh Gate, Harlow, Essex, London: Pearson Education, Ltd, 1995.

96. Wang, H., G. H. Priestman, S. B. M. Beck, R. F. Boucher. “Pressure Wave Attenuation in an Air Pipe Flow.” Journal of Mechanical Engineering Science, Proceedings of the Institution of Mechanical Engineers, Vol 214, Part C (2000): 619-632.

97. Watton, J., M. J. Tadmori. “A Comparison of Techniques for the analysis of Transmission Line Dynamics in Electrohydraulic Control Systems.” Applied Mathematical Modelling Volume 12, No. 5 (1988): 457-466.

98. Wiggert, D. C., A. S. Tijsseling. “Fluid Transients and Fluid-Structure Interaction in Flexible Liquid-Filled Piping.” Applied Mechanics Reviews, Transactions of the ASME, 54 (2001): 455-481.

99. Wilcox, D. C. Basic Fluid Mechanics. 2nd ed. La Cañada, USA: DCW Industries, Inc., 2000.

100. Wylie, E. B., J. A. Bolt, M. F. El-Erian. “Diesel Fuel Injection System Simulation and Experimental Correlation.” SAE Paper 710569 1971.

101. Wylie, E. B., V. L. Streeter, L. Suo. Fluid Transients in Systems. Englewood Cliffs, USA: Prentice-Hall, Inc., 1993.

102. Zielke, W. “Frequency-Dependent Friction in Transient Pipe Flow.” Journal of Basic Engineering, Transactions of the ASME (1968): 109-115.

APPENDIX A. NUMERICAL PARAMETERS OF HIGH PRESSURE CR TEST BENCH

Figure A 1 presents the variation of ISO 4113 oil density as a function of pressure and temperature.

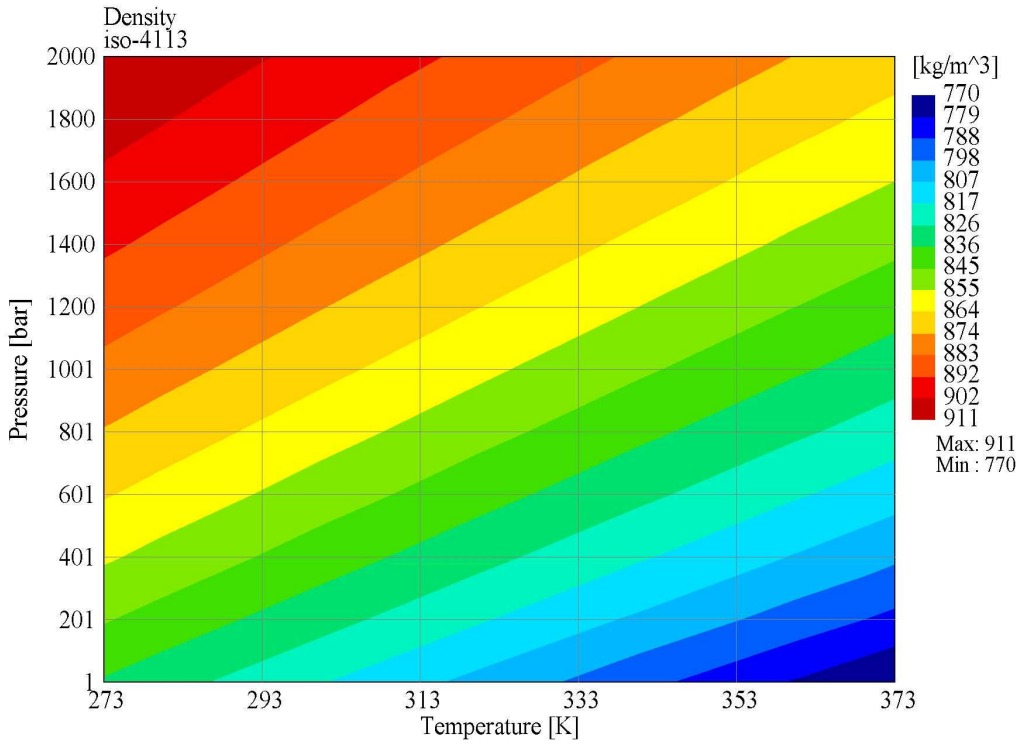

Figure A 1. ISO 4113 oil, ρ(p, T) [43].

The main properties of Shell calibration fluid S-9365 are defined in the ISO 4113 standard. The following table summarises the most important characteristics of the oil (Table A 1).

Table A 1. Fluid properties Shell calibration oil (ISO 4113 oil).

Characteristic	Unit	Value
Density at 15 °C	g/ml	0.827
Flash point	°C	+ 75 min.
Kinematic viscosity at 40 °C	mm^2/s	2.6
Cloud point	°C	- 27 max
Water content	-	free from undissolved water

Particular attention was paid for the placement of the pressure sensor at the injector inlet. Firstly, the sensor and its connector have to act neutral with respect to the main flow path. For each diameter of the high pressure line an individual sensor connector was used during the measurements. Secondly, the sensor membrane was placed as near as possible to the point of interest in order to minimize any unwanted interference due to resonance effects of liquid filled cavities. Figure A 2 shows a lateral cut through the injector inlet pressure connector for a high pressure pipe diameter of 2.4 mm. With the exception of the main flow path diameter, it is emphasised at this point that all geometrical characteristics of the various injector inlet connectors are identical, that is, the length of the main flow path through the injector is about 76.5 mm and the placement of the sensor axis is approximately 45.5 mm upstream of the injector inlet.

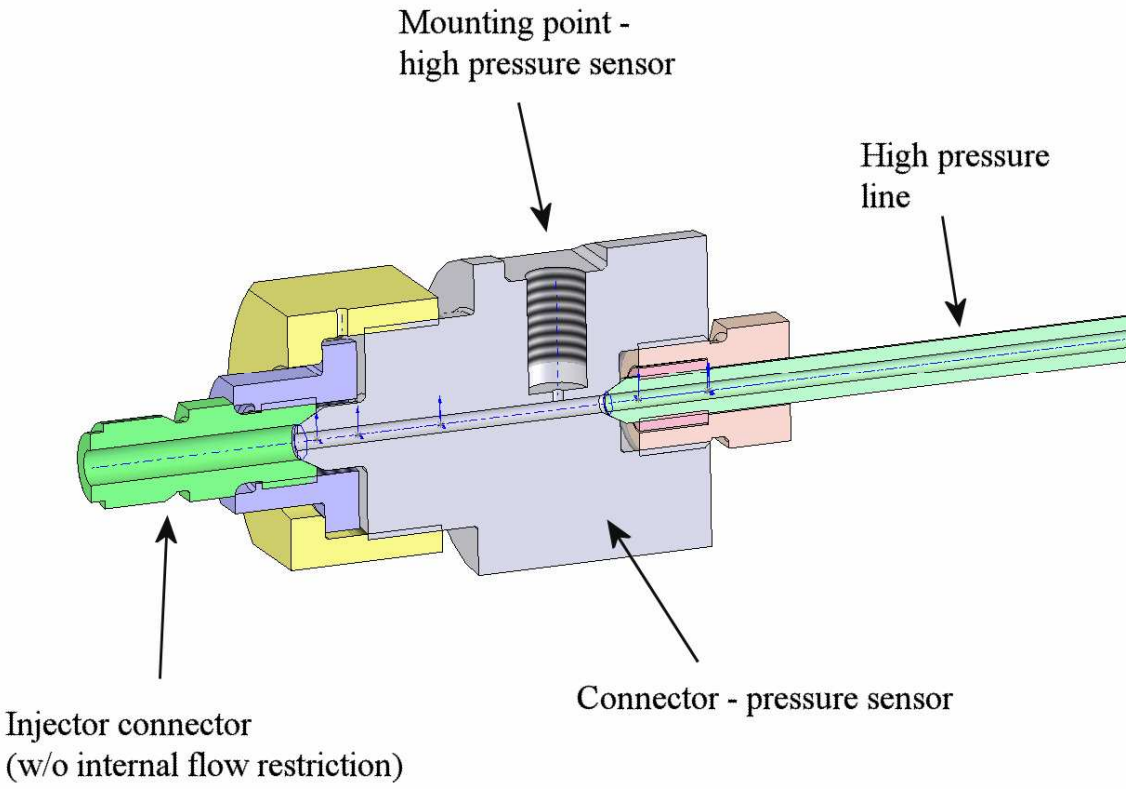

Figure A 2. Cross-section of connector pressure sensor, injector inlet (d_p = 2.4 mm).

The pressure sensor that is mounted to the upstream end of the rail is part of the original CR system. Flow acts on a steel diaphragm with deformation resistors. The latter form a bridge circuit and generate an output voltage between 0…80 mV. An evaluation circuit amplifies the signal further to 0…5 V [35]. No information is available about the accuracy of the sensor.

The two other sensors that were attached to the dead end and injector inlet are Kistler high pressure sensors type 4067 A 2000. Both are piezoresistive absolute pressure sensors that are specially designed for fuel injection systems. The corresponding amplifiers 4618A0 generate an output signal of 0…10 V to represent a pressure range of 0…2000 bar. Table A 2 lists the main characteristics of the pressure sensors.

Table A 2. Pressure sensor characteristics.

Rail sensor	Bosch high pressure rail sensor with amplifier Output signal: 0…5 V Accuracy: - Not known
Injector inlet sensor	Kistler 4067 A 2000, piezoresistive type, range: 0…2000 bar Amplifier: Kistler 4618A0, output signal: 0…10 V Accuracy: ±0.5 % FS = ±10 bar, natural frequency: >100 KHz
Dead end sensor	see data 'Injector inlet sensor'

Figure A 3 shows a typical plot of the sensor calibration curves. Each point in the graph corresponds to an average of 15 measurements. The temperature level during calibration was the same as for the measurements between 35 and 39 °C.

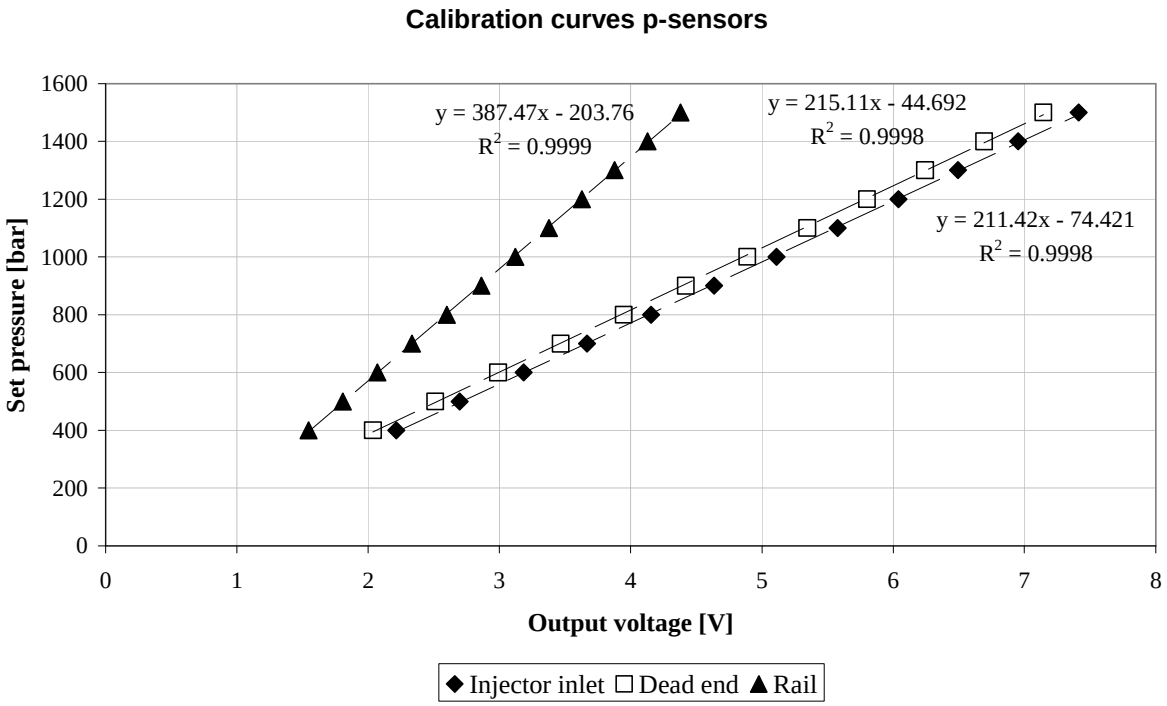

Figure A 3. Typical calibration curves for pressure sensors.

Temperature measurement was based on a K-type thermocouple for high pressure applications. The main characteristics are specified in Table A 3.

Table A 3. Temperature sensor characteristics.

Temperature sensor	Sitec thermocouple, type K (Ni/Cr - Ni), class 1 Maximum temperature: 500 °C Accuracy (DIN EN 60584-2): 0.4 % FS = ±2 °C Nokeval 2021 panelmeter Range: -150…1350 °C Accuracy: 0.1 % FS = 1.5 °C

Mass measurements were conducted on a high precision scale Mettler Toledo PR1203. Table A 4 defines the main characteristics of the scale.

Table A 4. Scale characteristics.

Mass measurement	Mettler Toledo PR1203 Range: 0…1210 g Linearity: ±2 mg Reading precision: 1 mg

The high pressure pipe connections of the hydraulic test bench are seamless made steel tubing in killed cast steel. No explicit information is available for the rail material. The latter properties are, however, believed to be similar as for the connection pipes (Table A 5).

Table A 5. High pressure pipe and rail characteristics.

Material (pipe): 1.4435 (DIN 17411 / EN 10 088-2)		
Tensile strength (EN 10 088-2)	N/mm^2	550…700
Elongation after fracture (EN 10 088-2)	%	≥ 40
Density	kg/dm^3	7.98
Young's modulus (20 °C)	MPa	196000 (rail: 207000)
Poisson ratio	-	0.3 (rail: 0.285)

The wall thicknesses of the individual pipes depend on the inner diameter of the connection line (d_p). Table A 6 lists beside the pipe dimensions also some characteristic numbers for the rail.

Table A 6. Characteristic dimensions of pipe (rail to injector and dead end, respectively) and rail.

	Inner diameter [mm]	Wall thickness [mm]	Length [mm]
Pipe	1.6	2.375	200, 400, 600
	2.4	1.975	200, 400, 600
	3.2	3.16	200, 400, 600
Rail	≈ 9.9	≈ 6.95	≈ 315.5

A standard three-phase Brook Crompton AC motor, type T-DA112 M4/01, was used for driving the low and high pressure pump of the CR system. The rotational speed of the motor was controlled via a Fuji FVR 110 G7S-4EX converter. If not otherwise specified, the electrical engine was operated at a rotational speed of 600 rpm at all operating points.

The data acquisition hardware for electrical signals consisted of a National Instrument NI BNC-2110 adapter board and a NI PCI-6251 high speed data acquisition device. The NI PCI-6251 card was build into a standard personal computer. It features 16 ADC channels (16 bit, 1.25 MS/s, ±0.1…±10V) and 2 DAC channels (16 bit, ±5 and ±10V). Analog and digital triggering is also supported. The former capability was employed in conjunction with the analysis software LabView 7.1 to define the time window for data storage. Finally, data handling and processing was carried out by using C++ and Matlab routines.

APPENDIX B. NUMERICAL PARAMETERS OF GT-FUEL MODEL

Due to the vast amount of parameters used in the modelling of the CR fuel injection system only the significant settings are presented at this place. The nomenclature that is used in this chapter aligns with the remarks in chapter 3.1.1, for example, Figure 15, and chapter 3.2.2, Figure 58. Table B 1 summarises the most important solver settings that are used during the simulations.

Table B 1. General code settings.

Definition	Setting		Comment
time control	continuous [s]		simulation is continuous and includes no periodicity
initialisation	user imposed		definition of system state at simulation start
flow control	time step multiplier	0.7	multiplier to the explicit solution time step
	global friction multiplier (constant)	1	multiplier to scale the calculated friction losses, steady term
	global friction multiplier (unsteady)	1	multiplier to scale the calculated friction losses, unsteady term
mechanical control	default settings		parameters to adjust the accuracy of the integration of the mechanical governing equations
thermal control	wall temperature solver	off	wall temperature is not calculated (isothermal condition)
plot setup	maximum plot points vary between 1000, 5000, and 20000		selection of resolution depends on the studied parameter and location, respectively

In the following Table B 2 the main parameter settings of the simulation model are presented. The table includes both general parameters and definitions for the transient arrays. It is emphasised at this point that the set pressure is adapted in accordance with the measurements.

Table B 2. Main model settings.

Object	Name	Value	Comment
general	discretization length [mm]	3	axial dimension of pipe CV
	air mass fraction []	1E-6	mass content of air in fluid
	exit pressure [bar]	1	cylinder volume and return line pressure
	wall temperature [K]	310.5	temperature of all boundaries
	total simulation time [s]	0.03	minimum total time for a single simulation run
pilot activation	t_0 [s]	0.01	start ball valve lift
	t_1 [s]	0.01026	ball valve fully lifted
	t_2 [s]	0.01082	start ball valve close; t_2 depends on t_{inj}, in this case t_{inj} = 800 µs
	t_3 [s]	0.01092	ball valve fully closed; $t_3 = t_2$ + 100 µs
time profile p_{set}	t_{0X1} [s]	0.011	start drop p_{set}
	t_{0X2} [s]	0.012	end drop p_{set}
	t_{0X3} [s]	0.03	equal to total simulation time

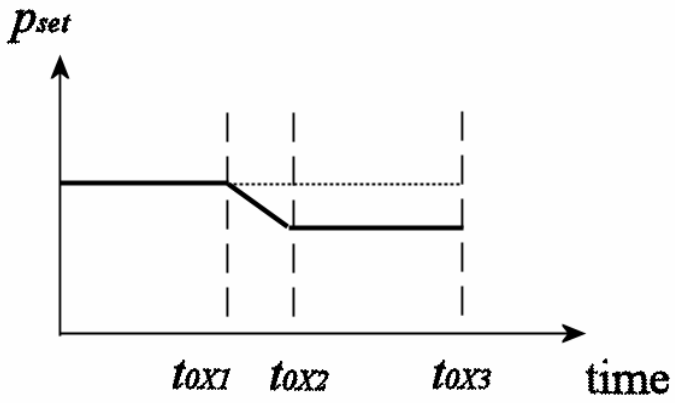

Figure B 1. Time profile p_{set}.

Table B 2 continued:

Object	Name	Value	Comment
moving injector mass	plunger [g]	11.197	for modelling the three masses are represented by a single object with a total mass of 15.65 g
	pin [g]	1.239	
	needle [g]	3.213	
injector spring	stiffness [N/mm]	30	stiffness of injector spring (assumption)
	pretension [N]	-30	spring is pre-compressed
plunger and needle contact surfaces	contact stiffness [N/m]	10E+9	stiffness of material
	contact damping coefficient [N s/m]	400	damping properties of material
	maximum gap for damping [µm]	10	parameter is used to add effects such as film squeezing

The geometrical parameters of key objects are shown in Table B 3. As the fuel injector defines to a great extent the dynamic characteristics of the system, the majority of the subsequently following parameters are related to an injector attribute.

Table B 3. Geometrical parameters and dimensions of the main objects.

Object	Name	Value	Comment
rail	axial dimension	-	rail consists of several pipe segments
	diameter [mm]	9.9	constant value for all segments
	surface roughness [µm]	10	-
maximum lift	z_{max} [mm]	0.27	maximum lift of injector mass
lines, volumes	surface roughness [µm]	2	surface roughness of all line and volume elements, except rail components
injector inlet	volume [mm^3]	40	cavity at the inlet of the injector
injector inlet restriction	diameter [mm]	0.9	the injector inlet restriction is modelled by a long , thin pipe
	length [mm]	28	

Table B 3 continued:

Object	Name	Value	Comment
main flow split, injector	volume [mm^3]	30	main characteristics of main injector flow split
	port characteristics	angles to x, y, z [°]	characteristic length, expansion diameter [mm]
	upstream	90, 180, 90	2, 4
	downstream to pilot	70, 20, 90	2, 4
	downstream to needle	100, 20, 107	2, 4
VuZ, injector	volume [mm^3]	184	volume between main flow split and Z-nozzle
	port characteristics	angles to x, y, z [°]	characteristic length, expansion diameter [mm]
	upstream	0, 90, 90	3, 4
	downstream	170, 90, 80	1, 3
Z-nozzle, injector	diameter [mm]	0.27	characteristics of Z-nozzle
	discharge coefficient []	0.85	
VdZ, injector	volume [mm^3]	f(lift)	volume between z- and A-nozzle, function of mass lift
	port characteristics	angles to x, y, z [°]	characteristic length, expansion diameter [mm]
	upstream	0, 90, 90	0.8, 2
	downstream to pilot	90, 90, 0	z_{max}, 4.3
	area, plunger top	90, 90, 180	z_{max}, 4.3
	plunger leakage	90, 90, 180	z_{max}, 4.3
plunger-top orifice, injector	diameter [mm]	f(lift)	diameter is calculated by shell surface of flow passage; forward and backward discharge coefficient are based on array pair: lift: (0, z_1, z_2, z_{max}) CD: (0.64, 0.64, 0.2, 0)
	discharge coefficient []	f(lift)	

Table B 3 continued:

Object	Name	Value	Comment
A-nozzle, injector	diameter [mm]	0.3	characteristics of A-nozzle
	discharge coefficient []	0.9	
ball valve, injector	diameter [mm]	-	characteristics of ball valve; diameter is based on time profile: time: (t_0, t_1, t_2, t_3) diameter: (0, 0.3, 0.3, 0.3)
	discharge coefficient []	0.95	
internal injector channels, injector	top [mm]	2, 11	internal injector channels: diameter, length
	middle [mm]	2.2, 104	
	bottom [mm]	1.7, 12	
gallery, injector	volume [mm^3]	120	volume of fuel gallery (port characteristics are neglected at this place)
lBottom, injector	area [mm^2]: in, out	7.16, 4.52	ring passage between gallery and needle seat
	wetted perimeter [mm]: in, out	23.9, 22.62	
	length [mm]	25	
needleSeat, injector	diameter [mm]	f(lift)	needle seat area is replaced by an orifice with variable diameter (see equation (B1))
	discharge coefficient []	0.9	
sacVolume, injector	volume [mm^3]	4	volume of sac between needle seat and nozzle holes
nozzle holes, injector	number of holes	6	nozzle hole characteristics
	diameter [mm]	0.15	
	length [mm]	1	

The equivalent diameter of the needle seat orifice is based on the equation:

$$d = 0.9 \cdot \left(-145.14 \cdot lift^4 + 116.73 \cdot lift^3 - 31.603 \cdot lift^2 + 6.3402 \cdot lift\right) \quad \text{(B1)}$$

Figure B 2 presents the above equation in a graphical way. The curve is characterised by a disproportionately high increase of the equivalent diameter at small lifts. For larger values of the same parameter the curve bends and the diameter increases at a slower rate than before.

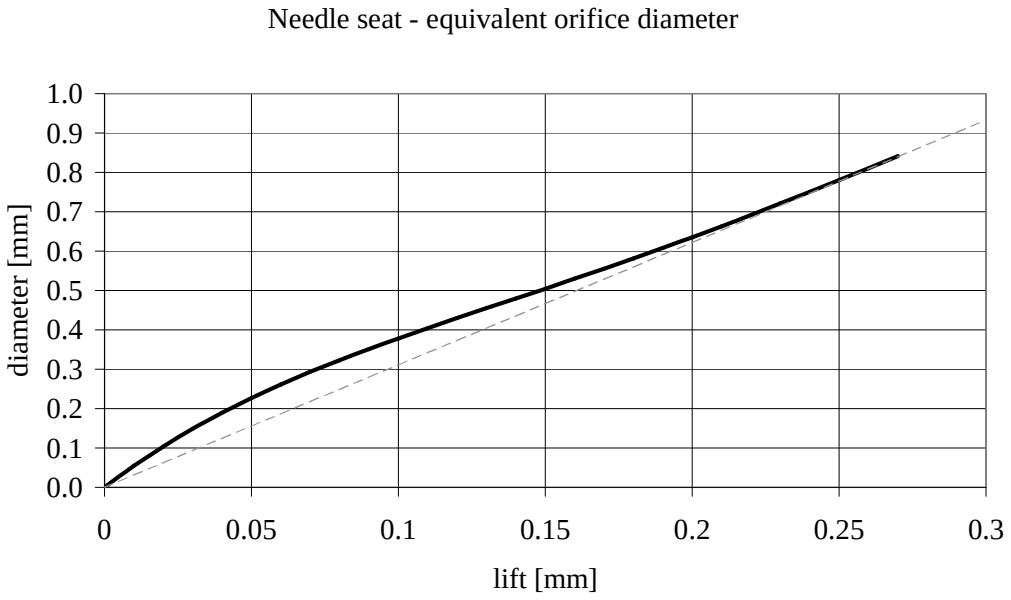

Figure B 2. Equivalent diameter needle seat as f(lift).

It has been found that the overall appearance of the pressure curve at, for example, *pII* is strongly affected by the utilised equation. The equivalent diameter can be computed in principle by two different methods. Firstly, it is possible to compute the diameter by applying the concept of the hydraulic radius (for example [99]). In this particular case this approach however has shown to lead to too small values. Secondly, the equivalent diameter can be computed by relating simply the flow cross-section at the needle seat to the diameter of an equivalent circular area. The latter approach leads to the typical shape of the diameter curve with an upwards pointing bend at small lifts (see the initial shape of Figure B 2). On the other hand, at large lifts this method tends to assume too big diameters for the needle seat restriction. The equation (B 1) that is finally used in this study represents a compromise. It includes the particular shape of the curve at small lifts, but restricts the diameter for large displacements.

APPENDIX C. MODEL SETTINGS AND ANALYSIS OF 3D PILOT STAGE SIMULATION

Table C 1 summarises the most important settings for the three-dimensional computation of the pilot stage flow field.

Table C 1. Summary of main ANSYS-CFX settings.

Name		Value / Setting	Comment
Solver	advection scheme	upwind	main solver setting
	transient scheme	1st order backward Euler	
	timescale control	coefficient loops (max. 10)	
	convergence criteria	RMS normalisation (residual target: 1E-4)	
Simulation type	total simulation time [s]	0.0009	transient run definition with turbulence model enabled
	time step [s]	2E-06	
	turbulent flow	k-ε model, scalable wall functions	
Fluid	density [kg/m^3]	see page 44, equation (70)	constant values correspond to reference pressure p_{ref} = 1000 bar and reference temperature T_{ref} = 310 K
	reference density [kg/m^3]	861.5	
	dynamic viscosity [Pa s]	0.006	
	bulk modulus [MPa]	2345	
Boundary conditions	flow inlet/outlet at upstream VuZ and downstream A-nozzle	opening, pressure = f(time)	all boundary conditions vary as f(time)
	mass displacement	body force = f(time)	

Because of geometrical symmetry the domain is represented by a 180° model with a symmetry boundary condition. The mesh of the model is block-structured and consists of 26216 hexahedral cells. Although attention has been paid to ensure appropriate grid resolution

for accurate gradient representation, the mesh is not fine-tuned to satisfy the near-wall criteria at all locations (Figure C 1).

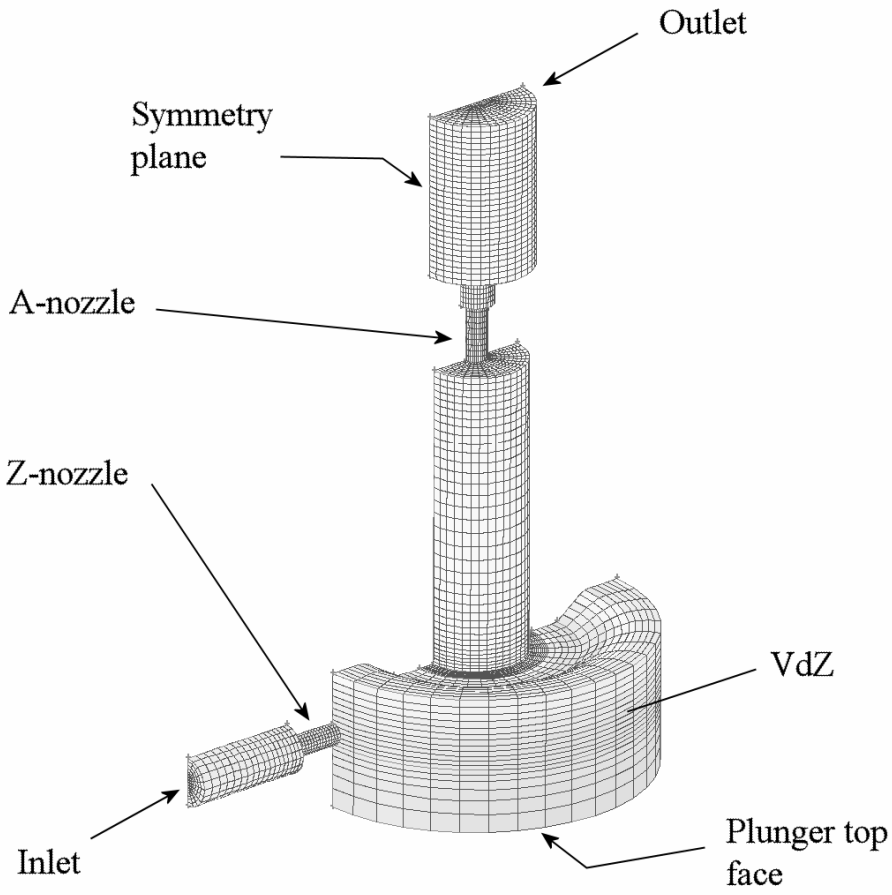

Figure C 1. Computational mesh (180°) ANSYS-CFX, pilot stage

Various parameters were monitored during the simulation process. Table C 2 gives an overview of the monitor point definitions as they are, for example, presented in Figure C 2.

Table C 2. Pilot stage, definition of monitor points.

Name	X [mm]	Y [mm]	Z [mm]
1	0.002	0	-0.00075
2	0	-0.002	-0.00075
3	-0.002	0	-0.00075
4	-0.004	0	-0.00047
5	0	0	0.002
6	0	0	0.006

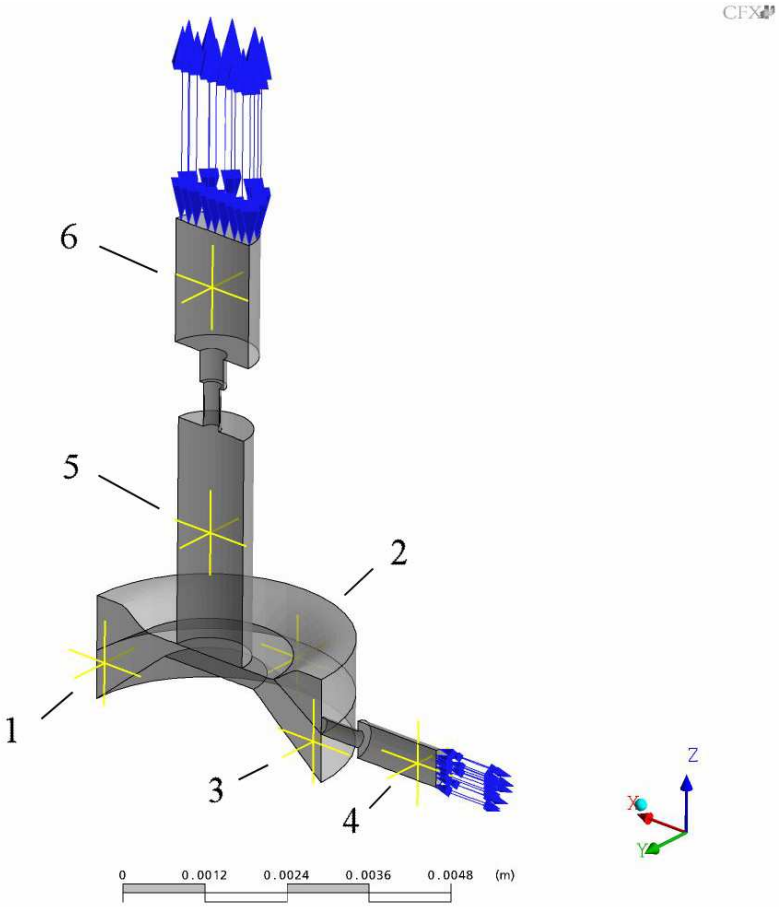

Figure C 2. Pilot stage, definition of monitor points.

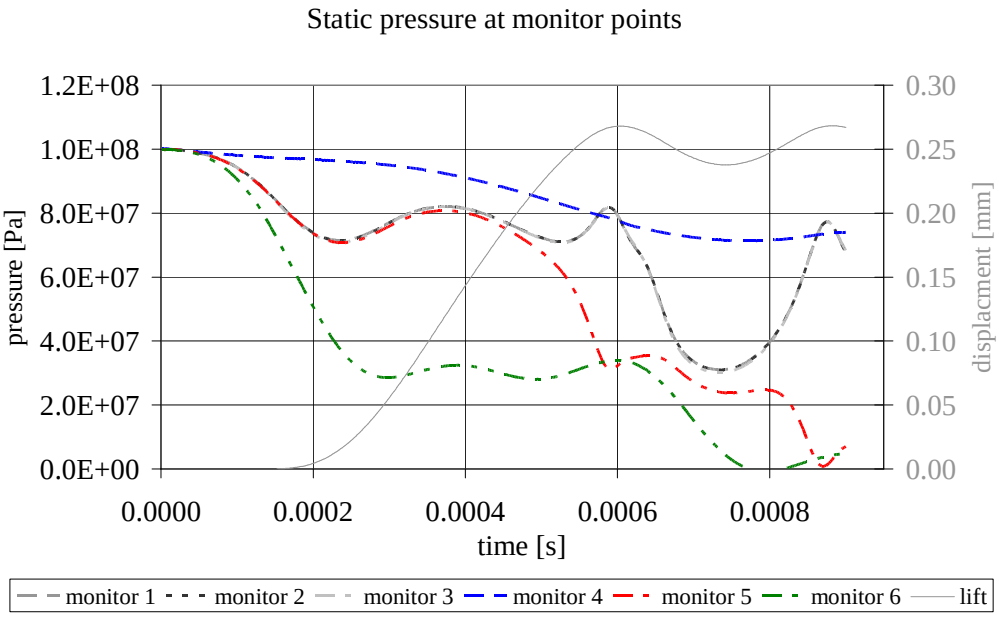

Figure C 3. Pilot stage, static pressure at monitor points (vs. lift).

Figure C 3 exemplifies the static pressure values at the 6 monitor points versus time and in comparison to the plunger displacement. Firstly, it can be seen that the pressure inside the volume *VdZ* is rather uniform, that is, monitors 1 to 3 predict basically the same pressure throughout the run. By comparing the progress of this pressure to, for example, monitor 5, it is interesting to notice that in a fluid dynamic sense the two volumes *VdZ* and *VuA* separate at about t = 500 µs or a plunger displacement of approximately 210 µm. For times later than that the pressure in *VuA* drops, while it increases in the chamber downstream of the Z-nozzle (monitor 1 to 3, t = 600 µs). As the plunger reverses its motion, the flow passage increases and the pressure in *VdZ* decreases to almost the same level as upstream of the A-nozzle (t = 700 µs). Towards the end of the simulation the plunger moves upwards again. The restriction becomes smaller, which leads to another pressure increase in *VdZ* due to fluid squeezing.

APPENDIX D. SETUP - SIMPLIFIED INJECTOR MODELS

The profile for controlling the fuel delivery is presented in Figure D 1. Altogether, three injection durations were investigated in this study. Table D 1 gives a summary of the main settings.

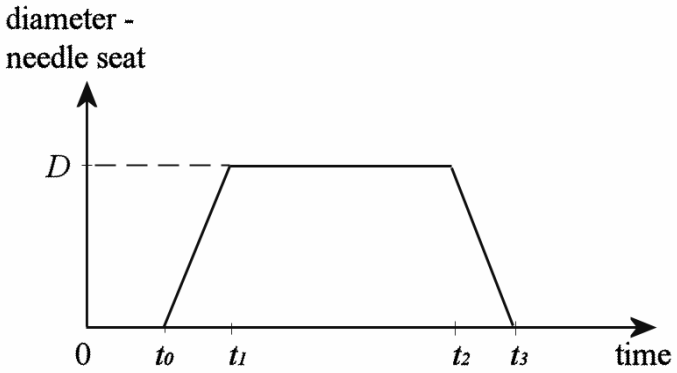

Figure D 1. Simplified GT-Fuel injector model; profile: effective needle seat diameter.

Table D 1. Simplified GT-Fuel injector model; injection control.

Needle seat: D_{max} [mm]	0.34			
Time	t_0 [s]	t_1 [s]	t_2 [s]	t_3 [s]
t_{inj} = 400 µs	0.01	0.0101	0.01039	0.0104
t_{inj} = 700 µs	0.01	0.0101	0.01069	0.0107
t_{inj} = 1000 µs	0.01	0.0101	0.01099	0.011

Figure D 2 presents the schematic GT-Fuel model layout of the simplified injector model m_01 and m_02. The most obvious difference between this plot and the default model (see page 90, Figure 58) is the absence of the pilot stage, the mass that represents the needle, pin, and plunger, and any leakage paths. While m_01 employs the same parameters as the default model, the m_02 configuration utilises for all pipe objects the same diameter as the connection pipe between rail and injector inlet. This modification includes the channels between the “Main flow split” and the “Fuel gallery” and one object between the “Fuel gallery” and the “Sac volume”.

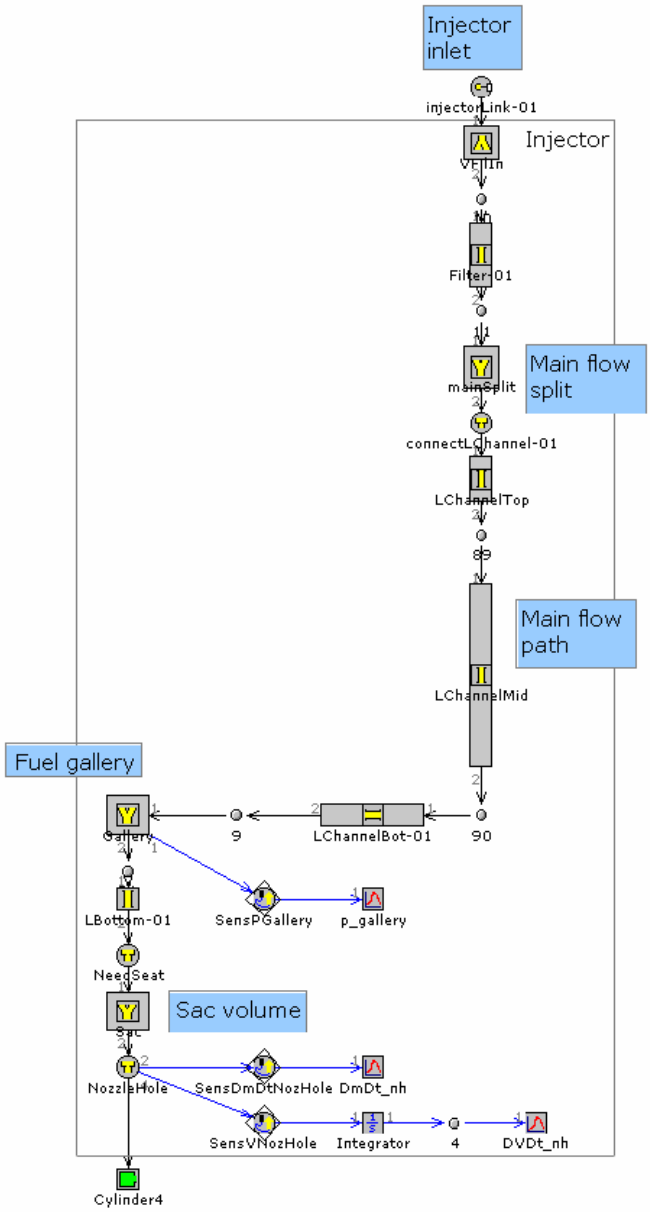

Figure D 2. Simplified GT-Fuel injector model, m_01 and m_02.

The model m_03 and m_04 represent a further simplification of the injector model. In fact, m_03 is basically a single connection line with a valve at the downstream end. The diameter of the “Main flow path”-pipe is set identically to the one of the connection line between rail and injector. The length is chosen to represent approximately the distance from the injector inlet to the needle seat (L = 190 mm). Only the elements downstream of the needle seat, that is, the sac volume and the nozzle hole object use the same settings as the default model. The schematic layout of this model is presented on the left side of Figure D 3.

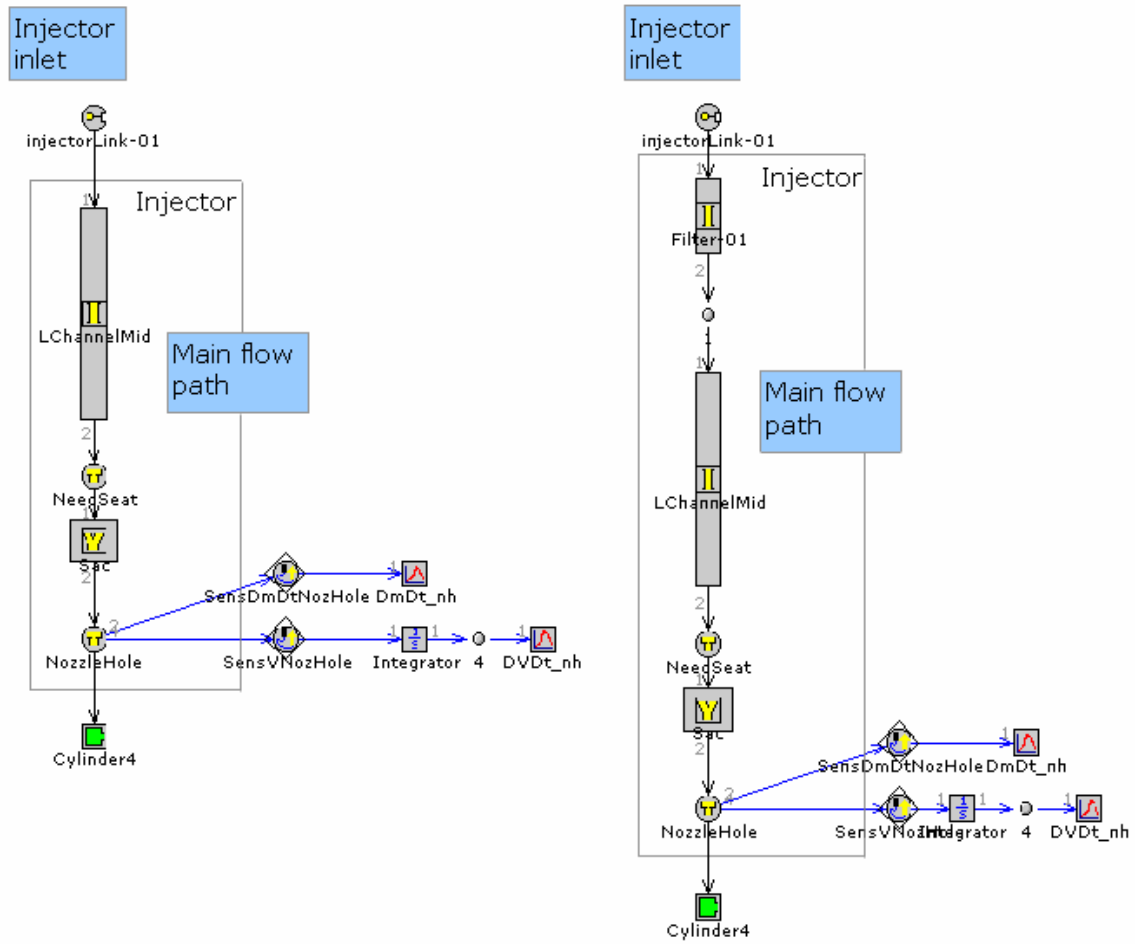

Figure D 3. Simplified GT-Fuel injector model, m_03 (left) and m_04 (right).

The right hand side of Figure D 3 shows the layout of the model m_04. Essentially, this model is identical to the m_03 setup. Exceptions include the flow restriction object right after the injector inlet and the adapted length of the "Main flow path" pipe object (L = 162 mm). Again, the flow restriction object uses the same parameters as the default simulation model.

APPENDIX E. ATTENUATION OF PRESSURE OSCILLATIONS AT INJECTOR INLET

Both in-line attenuator and Helmholtz resonators belong to the group of passive interference and wave reflection damper [78]. To ensure optimum performance, both damping devices need to be adapted to the dynamic characteristics of the hydraulic circuit. In this study the theoretical background is based on the science of acoustics [38]. Beside the inviscid flow assumption, further simplifications were applied in this basic evaluation. It is stressed at this point that the subsequent following derivation and discussion serves only the determination of the preliminary damping device layout. In other words, the thus obtained results were solely used to define the range of reasonable dimensions, which were then used to specify the model in the GT-Fuel environment. As also explained in chapter 3.3.5, no equations or assumptions of this discussion were utilised in the final simulation model.

The working principle of a Helmholtz resonator rests on the excitation of the fluid column at the resonator throat (Figure E 1, position “S”) and the compensation of the fluctuation by its volume (position “1”). In the ideal case, that is, at the resonance frequency of the damper, the resonator acts as a switch that prevents the transmission of this particular frequency.

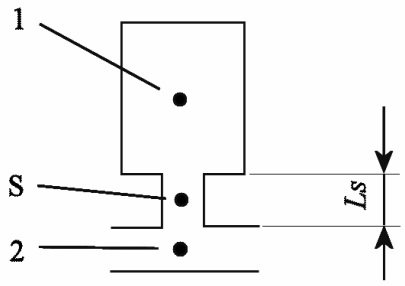

Figure E 1. Helmholtz resonator; definition of main parameters.

It is assumed for simplicity reasons that the fluid can be described through lumped parameters. Secondly, all geometrical dimensions are considerably smaller than the wave length of the oscillation. The change of mass in the resonator volume equals the change of mass flow into the volume:

$$\frac{dm}{dt} = V_1 \cdot \frac{d\rho_1}{dt} = \rho_S \cdot u_S(t) \cdot A_S \qquad \text{(E1)}$$

where ρ denotes the density, $u_S(t)$ the instantaneous velocity in the throat, and A_S the flow area at the same location. The product of the latter two parameters is subsequently replaced by the

volumetric flow, $U_S(t)$. In the case of a harmonic excitation with the radial frequency ω, the density at "1" and the flow at "S" can be written in complex form as:

$$\rho_1(t) = \hat{\rho}_1 \cdot e^{i \cdot \varpi \cdot t} \tag{E2}$$

$$U_S(t) = \hat{U}_S \cdot e^{i \cdot \varpi \cdot t} \tag{E3}$$

For both equation (E2) and (E3) the first parameter on the right hand side describes the complex amplitude of the density and flow, respectively. An equation for the mass conservation is obtained by putting (E2) and (E3) into (E1). It follows that:

$$i \cdot \varpi \cdot V_1 \cdot \hat{\rho}_1 = \rho_S \cdot \hat{U}_S \tag{E4}$$

The force balance is obtained by computing the pressure and inertia force at the resonator inlet. As friction and any throttling effects at the throat are omitted, the momentum equation is:

$$A_S \cdot (p_2 - p_1) = \rho_S \cdot L_S \cdot \frac{dU_S}{dt} \tag{E5}$$

As before, the instantaneous pressure at "1" and "2" is described by:

$$p_1(t) = \hat{p}_1 \cdot e^{i \cdot \varpi \cdot t} \text{ and } p_2(t) = \hat{p}_2 \cdot e^{i \cdot \varpi \cdot t} \tag{E6}$$

If equations (E3) and (E6) are put into (E5), the final momentum equation becomes:

$$A_S \cdot (\hat{p}_2 - \hat{p}_1) = \rho_S \cdot L_S \cdot i \cdot \omega \cdot \hat{U}_S \tag{E7}$$

Equation (E7) and (E4) represent a system of two expressions for three unknowns. Usually, the pressure outside of the resonator, $\hat{p}_2$, is known and therefore not part of the solution. For only modest density variations, that is, the case of an ideal pressure wave transmission, the pressure can be related to the density via the speed of sound in the medium, a:

$$p_1 = a^2 \cdot \rho_1 \text{ and } \hat{p}_1 = a^2 \cdot \hat{\rho}_1 \tag{E8}$$

Equation (E8) can be combined with the equation for mass conservation (E4) to lead to:

$$\hat{p}_1 = \frac{a^2 \cdot \rho_S \cdot \hat{U}_S}{i \cdot \varpi \cdot V_1} \tag{E9}$$

If $\hat{p}_1$ in equation (E7) is substituted with (E9) it follows:

$$\hat{p}_2 = \left(\frac{i \cdot \omega \cdot \rho_S \cdot L_S}{A_S} + \frac{a^2 \cdot \rho_S}{i \cdot \varpi \cdot V_1} \right) \cdot \hat{U}_S \tag{E10}$$

The bracket term represents a complex number that is a function of the oscillation frequency, ω, the resonator variables L_1, A_S, and V_1, and the fluid state ρ_S (and a). With p_2 constant across the inlet of the resonator throat, the pressure outside of the damper equals the pressure at the

resonator inlet, p_S. Hence, the sum can be interpreted as the hydraulic impedance of the Helmholtz resonator, $Z_{S,H}$, at the damper inlet. Equation (E10) can be rewritten in the form:

$$Z_{S,H} = \frac{\hat{p}_S}{\hat{U}_S} = \frac{i \cdot \rho_S \cdot L_S}{\omega \cdot A_S}\left(\omega^2 - \frac{a^2 \cdot A_S}{V_1 \cdot L_S}\right) \tag{E11}$$

If $Z_{S,H} = 0$, some infinitesimal small pressure disturbance at the damper inlet ($p_2 = p_S$) is sufficient to cause infinite large flow amplitudes at the same location. This condition, which is also termed resonance condition, is met if the bracket term in equation (E11) cancels out; by setting the bracket term to 0 and solving for ω, it follows that:

$$\omega_{res} = \sqrt{\frac{a^2 \cdot A_S}{V_1 \cdot L_S}} \tag{E12}$$

Equation (E12) defines the resonance frequency, ω_{res}, of the Helmholtz resonator. For the excitation frequency identical to the resonance frequency of the damper, all incoming waves are reflected at the resonator connection.

An in-line attenuator is purely based on the wave cancellation through reflection effects inside of the damper. The diameters and diameter steps are assumed to be considerably smaller than the wave length. No restriction applies to the damper length. Figure E 2 depicts the main parameters for an in-line attenuator. The variable I denotes the complex amplitudes of incoming wave; R stands for the reflected wave amplitudes. For simplicity reasons it is assumed that the reflection at the downstream end can be omitted ($R_3 = 0$). Generally, such an assumption can be made as long as the flow domain downstream the attenuator behaves neutrally towards any incoming wave I_3.

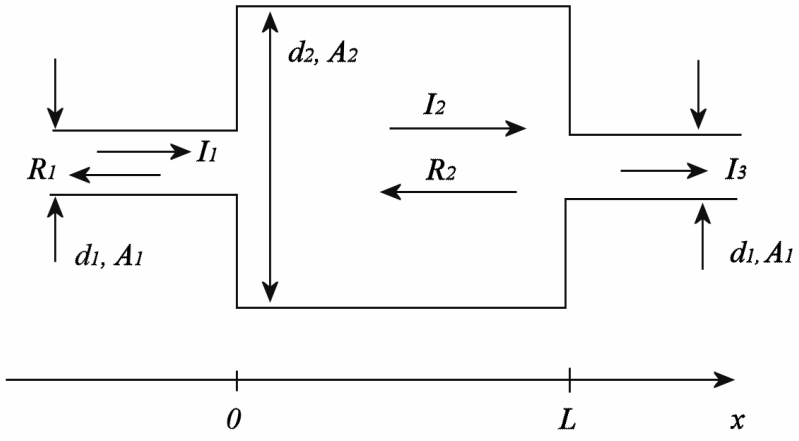

Figure E 2. In-line attenuator; definition of main parameters.

The pressure distribution along the damper can be written as:

$$p(x,t) = \begin{cases} p_1(x,t), \text{ for } x < 0 \\ p_2(x,t), \text{ for } 0 < x < L \\ p_3(x,t), \text{ for } L < x \end{cases} \quad \text{(E13)}$$

and, by employing the general form of the wave equation:

$$\begin{aligned} p_1(x,t) &= I_1 \cdot e^{i\cdot(\varpi\cdot t - k\cdot x)} + R_1 \cdot e^{i\cdot(\varpi\cdot t + k\cdot x)} \\ p_2(x,t) &= I_2 \cdot e^{i\cdot(\varpi\cdot t - k\cdot x)} + R_2 \cdot e^{i\cdot(\varpi\cdot t + k\cdot x)} \\ p_3(x,t) &= I_3 \cdot e^{i\cdot(\varpi\cdot t - k\cdot x)} \end{aligned} \quad \text{(E14)}$$

In the same way, the fluid velocity in each section can be defined by:

$$u(x,t) = \begin{cases} u_1(x,t), \text{ for } x < 0 \\ u_2(x,t), \text{ for } 0 < x < L \\ u_3(x,t), \text{ for } L < x \end{cases} \quad \text{(E15)}$$

and

$$\begin{aligned} u_1(x,t) &= \frac{I_1}{\rho\cdot a}\cdot e^{i\cdot(\varpi\cdot t - k\cdot x)} - \frac{R_1}{\rho\cdot a}\cdot e^{i\cdot(\varpi\cdot t + k\cdot x)} \\ u_2(x,t) &= \frac{I_2}{\rho\cdot a}\cdot e^{i\cdot(\varpi\cdot t - k\cdot x)} - \frac{R_2}{\rho\cdot a}\cdot e^{i\cdot(\varpi\cdot t + k\cdot x)} \\ u_3(x,t) &= \frac{I_3}{\rho\cdot a}\cdot e^{i\cdot(\varpi\cdot t - k\cdot x)} \end{aligned} \quad \text{(E16)}$$

The only known variable is I_1; R_1, I_3, I_2, and R_2 are part of the solution. In fact, only the former two variables are of interest. The boundary condition at the diameter steps state that for low frequency oscillations it can be written:

$$p_1(0,t) = p_2(0,t) \quad \text{(E17)}$$

$$p_2(L,t) = p_3(L,t) \quad \text{(E18)}$$

On the other hand, mass conservation requires:

$$A_1 \cdot u_1(0,t) = A_2 \cdot u_2(0,t) \quad \text{(E19)}$$

$$A_2 \cdot u_2(L,t) = A_3 \cdot u_3(L,t) \quad \text{(E20)}$$

By combining the equations (E14) with (E17), (E14) with (E18), (E16) with (E19), and (E16) with (E20), a system of four new equations with four unknowns is created:

$$I_1 + R_1 = I_2 + R_2 \quad \text{(E21)}$$

$$I_2 \cdot e^{-i\cdot k\cdot L} + R_2 \cdot e^{i\cdot k\cdot L} = I_3 \cdot e^{-i\cdot k\cdot L} \quad \text{(E22)}$$

$$A_1 \cdot (I_1 - R_1) = A_2 \cdot (I_2 - R_2) \quad \text{(E23)}$$

$$A_2 \cdot \left(I_2 \cdot e^{-i \cdot k \cdot L} - R_2 \cdot e^{i \cdot k \cdot L}\right) = A_1 \cdot I_3 \cdot e^{-i \cdot k \cdot L} \tag{E24}$$

Through substitution and elimination, it can be shown that:

$$R_1 = R_C \cdot I_1 \tag{E25}$$

with R_C being defined as the reflection coefficient:

$$R_C = \frac{i \cdot \left(\frac{A_1}{A_2} - \frac{A_2}{A_1}\right) \cdot sin(k \cdot L)}{2 \cdot cos(k \cdot L) + i \cdot \left(\frac{A_1}{A_2} + \frac{A_2}{A_1}\right) \cdot sin(k \cdot L)} \tag{E26}$$

Similarly, a transmission coefficient, T_C, relates the incoming wave I_1 with the transmitted wave I_3:

$$I_3 = T_C \cdot I_1 \text{ (E27)}$$

and

$$T_C = \frac{2 \cdot e^{i \cdot k \cdot L}}{2 \cdot cos(k \cdot L) + i \cdot \left(\frac{A_1}{A_2} + \frac{A_2}{A_1}\right) \cdot sin(k \cdot L)} \tag{E28}$$

It should be noted that the reflection and transmission coefficients depend not only on the ratio of the areas, but also on the factor:

$$k \cdot L = \frac{\varpi \cdot L}{a} \tag{E29}$$

The variable k represents the wave number. Equation (E29) underlines that R_C and T_C are also a function of the oscillation frequency. If the product of k and L equals π, or an integer multiple of it, the reflection coefficient becomes 0 and the transmission coefficient 1. The corresponding angular frequency is calculated by:

$$\varpi = \frac{n \cdot \pi \cdot a}{L}, \text{ and n = 0, 1, 2, 3, …} \tag{E30}$$

For evaluating the effectiveness of in-line attenuators, a new variable is defined that describes the transmission loss between damper inlet and outlet:

$$T_L = 10 \cdot log_{10}\left(\frac{I_1^2}{I_3^2}\right) \tag{E31}$$

Together with (E27) and (E28), it follows that:

$$T_L = 10 \cdot log_{10}\left(1 + \frac{1}{4} \cdot \left(\frac{A_1}{A_2} - \frac{A_2}{A_1}\right)^2 \cdot sin^2(k \cdot L)\right) \tag{E32}$$

The unit of the transmission loss coefficient is [dB]. From equation (E32) it can be seen that T_L is maximum when the sine-term on the right hand side is maximum. In other words, the highest damping rate can be achieved if:

$$k \cdot L = \frac{n}{2} \cdot \pi \text{, and n = 1, 3, 5, 7, …} \quad \text{(E31)}$$

Putting equation (E31) into (E29), it can be calculated that an in-line attenuator is most effective if the damper length stays in the following relation to the speed of sound in the fluid, *a*, and the excitation frequency, *f*:

$$L = \frac{n}{4} \cdot \frac{a}{f} \quad \text{(E32)}$$

By reviewing the main equations for the Helmholtz resonator and in-line damper, it is comprehensible that the performance of both devices is not simply a function of the respective geometry, but also depends on the environment into which they are planted. As an unfortunate fact, the properties in high pressure CR systems are not constant. As has been shown in this thesis, the fluid properties and the dynamic characteristics of the system are strongly dependent on the circuit layout and injection settings. Particularly the injection pressure is permanently adjusted to new engine conditions. Consequently, it is not possible to design a passive damper that works at its optimum at all conditions. It is, in fact, necessary to find a good compromise that serves all operating points. For the present CR system, it is assumed that the target oscillation frequency is about 600 Hz (see, for example, page 111, Figure 76). The speed of sound in the liquid is assumed to be fixed to 1720 m/s, which is a compromise between the lowest ($\approx$1500 m/s) and highest ($\approx$1920 m/s) computed values. For the Helmholtz resonator equation (E12) applies, which leads after some re-arrangement to:

$$V_1 = \frac{a^2 \cdot A_S}{4 \cdot \pi^2 \cdot f^2 \cdot L_S} \quad \text{(E33)}$$

By assuming some values for the resonator throat geometry, equation (E33) computes the volume of the damper. In this sense, the data in Table 7 on page 149 represent two example configurations. Figure E 3 presents graphically the performance of the in-line attenuator. The plot clearly shows that it is not possible to take full advantage of this type of damper if it is build into a CR system. By looking firstly at the damper length, the graph indicates that the axial extension of the attenuator should be beyond 250 mm. In fact, an optimum is reached at around 750 mm; for larger damper lengths T_L starts to decrease again (not shown). In contrast, it is more promising to increase the attenuator diameter. Based on the shape of the surface, the

transmission loss rises faster as a function of diameter than as a function of length. Just as for the Helmholtz resonator, the in-line attenuator data (Table 7 on page 149) represent a compromise and an example from the various possibilities.

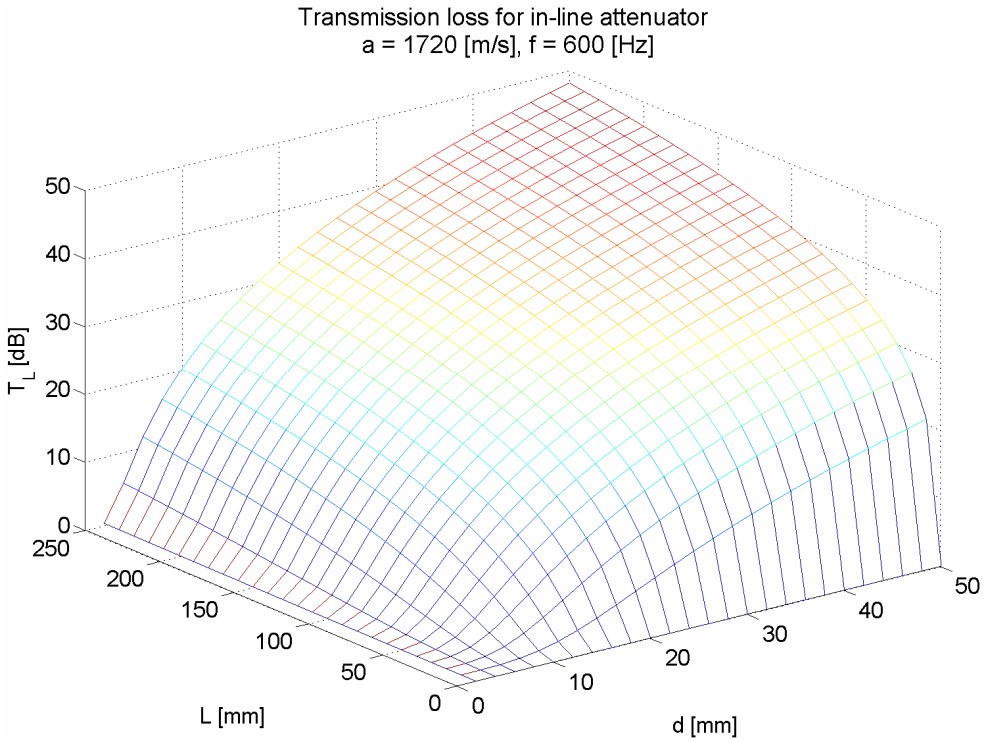

Figure E 3. Transmission loss of in-line attenuator as f(geometry); l_p = 1.6 mm.

Tampereen teknillinen yliopisto
PL 527
33101 Tampere

Tampere University of Technology
P.O. Box 527
FIN-33101 Tampere, Finland